

A novel approach for integrating concentrated solar energy with biomass thermochemical conversion processes

MUKTAR ABDULLAHI BASHIR

Doctor of Philosophy

ASTON UNIVERSITY

September 2016

© Muktar Bashir, 2016

Muktar Bashir asserts his moral right to be identified as the author of this thesis

This copy of the thesis has been supplied on condition that anyone who consults it is understood to recognise that its copyright rests with its author and that no quotation from the thesis and no information derived from it may be published without appropriate permission or acknowledgement

Aston University

A novel approach for integrating concentrated solar energy with biomass thermochemical processes

MUKTAR ABDULLAHI BASHIR

Doctor of Philosophy

SUMMARY

Concentrated solar energy provides thermal energy that can be utilised for thermochemical conversion of biomass to produce liquid fuel and gases. This creates an efficient and a carbon-free process. The fast pyrolysis of biomass is an endothermic thermal process that occurs within 400-550°C at fast heating rates of >300 °C/second in the absence of oxygen. This temperature is within the range produced in a parabolic trough arrangement. The process of biomass gasification is the conversion of biomass fuels to non-condensable gases usually for chemical feedstock or as fuel using a fluidising medium. Solar intermittence is a major issue; this can be resolved by proposing a continuous process from concentrated solar energy to fuels or chemical feedstock. Computational fluid dynamics has proven to be a tool for design and optimisation of reactors. The Eulerian-Eulerian multiphase model using ANSYS Fluent has shown to be cost-effective at describing the characteristics of complex processes.

The project entails using parabolic trough for fast pyrolysis of biomass; it is integrated with a gasification process with utilities produced entirely from solar energy. The scope of the project are: (i) A Computational fluid dynamic (CFD) model analysis of the novel reactor is to be developed to model biomass pyrolysis (ii) Investigate the potentials of integrating the proposed solar reactor with a conventional circulating fluidised bed (CFB) gasifier to create a highly efficient and sustainable closed loop thermo-solar process (iii) Validate the circulating fluidised bed model with an experimental scale Circulating fluidised bed (CFB) gasifier at Aston University's European Bioenergy Research Institute.

The report studied the use of CFD modelling to investigate fast pyrolysis of switch grass biomass using a solar parabolic trough receiver/reactor equipped with a novel gas-separation system. The separator controls the effect of tar-cracking reactions and achieves high separation efficiency compared to other gas-solid separation methods. The study assumes an average heat flux concentrated along the receiver/reactor. Pyrolysis reaction was represented as a single global first order Arrhenius type reaction with volatiles separated into condensable (bio-oil) and non-condensable products. The drying of moisture of the switch grass was represented as a mass transfer process. The separation efficiency achieved by the conical deflector was about 99%. The proposed reactor at the considered operating conditions can achieve overall energy efficiency of 42%; the product yield consist of 51.5% bio-oil, 43.7% char and 4.8% non-condensable gases. The average reactor temperature, gas residence time, and maximum devolatilisation efficiency were 450 °C, 1.5 s, and 60% respectively. There was good agreement in comparison with experimental

findings from literature. A sensitivity analysis was conducted to study the effect of heat flux conditions, heat transfer, sweeping gas temperature, and particle size. The heat flux distribution showed that non-homogeneous provides a greater heating rate and temperature compared to the homogeneous flux. Radiation negligibly affects the final product composition; the radiation heats the biomass mainly rather than cause devolatilisation. The larger the biomass diameter the more bio-oil is produced, when a uniform particle temperature is assumed.

An experimental study was conducted for the validation of the hydrodynamic model of a circulating fluidised bed. The experiment measured the pressure profiles and the solid recirculation rate. The experiment result showed that particle size has a negative correlation to the ease of fluidisation. High fluidising gas flowrate has a positive impact on the fluidising regime and pressure in the riser. The following parameters were compared with experimental results: grid size, turbulence model, drag laws, wall treatment, and wall shear properties (specularity coefficient and restitution coefficient). The results proved the optimum hydrodynamic model through comparison of pressure profiles of the model with experimental results.

The gasification of char in a circulating fluidised was studied using the optimum hydrodynamic model validated from experiment. The model considered the effect of turbulence on the species evolution and tar reforming with char. Over the range of operating conditions, the results looked into the hydrodynamics and product yield of the gasifier. The product yields obtained for the base case was CO (12%), CO₂ (19%), H₂ (6%), CH₄ (0.7%), and N₂ (63%). The results proved that for smaller particles the evolution of species are dominated by kinetics. The catalytic effect of char showed improvement in tar yield and CGE to 15.12g/Nm³ and 67.74%. The product yields showed improvement with the compositions of CO₂ and H₂ due to reforming reactions. The yields and efficiency were in qualitative agreement with results from literature. The proposed models described will provide details on the procedures for future design of integrated solar biomass thermochemical conversion systems.

Keywords: Computational fluid dynamics, solar thermochemical conversion, solar pyrolysis, biomass fast pyrolysis, char gasification, circulating fluidised bed

ACKNOWLEDGEMENTS

I will first like to thank GOD for life and my family especially my parents for their love, support, and guidance.

I would also like to thank my external supervisor Dr. Yassir Makkawi for his leadership, help, and suggestions without whom it will not have been possible to complete this project.

I would also like to thank my Supervisor Dr. Sotos Generalis who took over after Dr. Yassir Makkawi's departure. He has helped tremendously in providing great guidance and made a huge impact to the completion of this project.

Finally, I would like to dedicate this thesis to my friends that were around throughout this journey.

LIST OF CONTENTS

SUMMARY	ii
ACKNOWLEDGEMENTS	iv
LIST OF CONTENTS	v
NOTATIONS	ix
LIST OF FIGURES	xi
LIST OF TABLES	xiv
Chapter 1 : Introduction	16
1.1. Bioenergy and Climate change	16
1.2. Pyrolysis	17
1.2.1. Concentrated solar energy	18
1.3. Gasification	19
1.3.1. Fluidised beds	20
1.4. Modelling	20
1.5. Thesis Novelty	21
1.5.1. Original proposed concept	21
1.5.2. Modified concept	22
1.6. Thesis objectives	24
1.7. Thesis outline	24
Chapter 2 : Computational fluid dynamics	26
2.1. Hydrodynamic model	26
2.1.1. Background theory	26
2.1.1.1. Eulerian-Lagrangian model	26
2.1.1.2. Eulerian-Eulerian model	27
2.1.2. Literature review	27
2.1.2.1. Studies of gas-solid flow in pipes	27
2.1.2.2. Studies of circulating fluidised bed risers	36
2.1.3. Governing equations	43
2.1.3.1. Conservation of mass	43
2.1.3.2. Conservation of momentum	44
2.1.3.3. Kinetic theory of granular flow	44
2.1.3.4. Turbulence models	49
2.1.4. Boundary conditions	53
2.2. Heat transfer model	54
2.2.1. Conservation of energy	54

2.2.2.	Heat transfer coefficients	55
2.2.3.	Radiation model	56
2.3.	Reaction model.....	57
2.3.1.	Literature review	57
2.3.1.1.	Pyrolysis	57
2.3.1.2.	Secondary reactions	62
2.3.1.3.	Gasification.....	65
2.3.2.	Model formulation	70
2.3.2.1.	Species transport equation	70
2.3.2.2.	Laminar finite rate model	70
2.3.2.3.	Surface reaction model	71
2.4.	Numerical model.....	72
2.4.1.	Solver	72
2.4.2.	Discretisation.....	73
2.5.	Conclusion	74
Chapter 3 :	Modelling of biomass fast pyrolysis in a solar trough reactor	75
3.1.	Background theory	75
3.1.1.	Solar thermochemical conversion	75
3.1.2.	Parabolic trough.....	76
3.1.2.1.	Types of solar receivers.....	78
3.1.3.	Biomass fast pyrolysis	81
3.2.	Literature review	82
3.2.1.	Studies on solar thermochemical conversion.....	82
3.2.2.	Studies on biomass fast pyrolysis	88
3.3.	Model formulation	90
3.3.1.	Preliminary simple model.....	90
3.3.2.	Proposed model for base case.....	96
3.3.2.1.	Boundary/operating conditions	100
3.3.2.2.	Numerical procedure.....	102
3.4.	Results and Discussion	103
3.4.1.	Hydrodynamics	103
3.4.2.	Residence time distribution	106
3.4.3.	Separation efficiency	108
3.4.4.	Heat distribution and Energy efficiency	109
3.4.5.	Reaction Rate and devolatilisation efficiency.....	112

3.4.6.	Heterogeneous Reactions and Product gas composition.....	114
3.5.	Conclusion	118
Chapter 4 :	Sensitivity analysis of solar pyrolysis model	119
4.1.	Literature review	119
4.1.1.	Studies on sensitivity analysis of tubular solar receiver/reactors	119
4.1.2.	Studies on sensitivity analysis of biomass fast pyrolysis.....	121
4.2.	Results and discussion	125
4.2.1.	Heat flux distribution	125
4.2.2.	Heat transfer mechanisms	129
4.2.3.	Effect of sweeping gas temperature.....	132
4.2.4.	Effect of particle size	135
4.3.	Conclusion.....	139
5. :	Hydrodynamics of a circulating fluidised bed riser	140
5.1.	Background theory	140
5.2.	Experimental settings and procedure	143
5.2.1.	Experiment setup.....	143
5.2.2.	Operating conditions.....	147
5.2.3.	Procedure	148
5.3.	Proposed CFD Model.....	149
5.4.	Results and Discussion	152
5.4.1.	Experimental results	152
5.4.1.1.	Solid circulation rate.....	152
5.4.1.2.	Pressure Profiles.....	153
5.4.2.	Modelling results	156
5.4.2.1.	Effect of Grid size.....	156
5.4.2.2.	Effect of drag laws.....	157
5.4.2.3.	Effect of turbulence model	158
5.4.2.4.	Effect of wall treatment	159
5.4.2.5.	Effect of particle-wall restitution coefficient	160
5.4.2.6.	Effect of specularity coefficient	161
5.5.	Conclusion	162
Chapter 6 :	Modelling of circulating fluidised bed gasification of char	164
6.1.	Background theory	164
6.1.1.	Gasification	164
6.1.1.1.	Gasification process.....	165

6.1.1.2. Tars	167
6.1.2. Gasification reactors	169
6.1.2.1. Fixed bed Reactors	169
6.1.2.2. Fluidised bed	171
6.2. Literature review	175
6.2.1. Experimental studies on biomass gasification	175
6.2.2. Numerical studies on biomass gasification	179
6.3. Proposed CFD Model	184
6.3.1. Species rate model and reaction kinetics	184
6.3.2. Boundary/Operating conditions	187
6.4. Results and Discussion	189
6.4.1. Hydrodynamics	189
6.4.2. Heat distribution and rate of reactions	192
6.4.3. Product composition and Efficiencies	195
6.5. Conclusion	198
Chapter 7 : Conclusion	200
7.1. Conclusions	200
7.1.1. Solar trough biomass fast pyrolysis	201
7.1.2. Circulating fluidised bed gasification of char	201
7.2. Summary of contributions	203
7.3. Future work	204
REFERENCES	206
APPENDIX	231
APPENDIX A: UDF codes	231
APPENDIX B: List of Publications	240

NOTATIONS

Letters and Symbols

\vec{u}_g, \vec{u}_{s_i}	Gas and solid velocity vector	m/s
C_D	Drag coefficient	
C_R	Concentration Ratio	Suns
\bar{D}	Duct length	m
\dot{Q}	Heat flux	W/m
Q''	Heat flux	W/m ²
U_i	Superficial velocity	m/s
U_{mf}	Minimum fluidization velocity	m/s
e_s	Particle-Particle restitution	
e_w	Particle-Wall restitution	
f_{drag}	Drag force	N
g_o	Radial Distribution	
k_o	Arrhenius constant	s ⁻¹ , s ⁻¹ bar ⁻ⁿ
\dot{m}	Mass flow rate	Kg/s
\dot{n}	Mole rate	mol/s
h	Heat transfer coefficient	W m ⁻² K ⁻¹
P	Pressure	Pa
ΔH	Enthalpy Change	J/mol
ΔG_{rxn}	Gibbs free energy	J/mol
A	Kinetic constant	s ⁻¹
A	Area	m ²
C	Mass concentration	kg m ⁻³
E	Activation Energy	KJ/mol
$F(X)$	Function	
I	Irradiation	W/ m ²
K	Equilibrium Constant	
L	Length	m
Nu	Nusselts Number	
Pr	Prandtl Number	
Q	Heat	W
R	Gas Constant	m ² kg s ⁻² K ⁻¹ mol ⁻¹
Ra	Rayleigh Number	
Re	Reynolds Number	
S	Source of enthalpy due to exchange	kJ m ⁻³ s ⁻¹
T	Temperature	K
U	Internal energy	J
W	Dry weight	Kg
X	Mole Conversion	
Y	Mass Fraction	
c/c_p	Specific heat capacity	J/K
k	Thermal Conductivity	W m ⁻¹ K ⁻¹
m	Mass	Kg
n	Reaction order	
p	Partial Pressure	kg m ⁻¹ s ⁻² (Pa)
r	Reaction rate	
t	Time	s
y	Position	m

Greek and Latin letters

$\bar{\tau}$	Shear stress tensor	$\text{kg m}^{-1} \text{s}^{-2}$
$\gamma_{\theta_{s_i}}$	Collisional energy dissipation	$\text{kg m}^{-1} \text{s}^{-3}$
Θ_s	Granular temperature	$\text{m}^2 \text{s}^{-2}$
$\alpha_{s,max}$	Packing limit	
$\kappa_{\theta_{s_i}}$	Diffusion coefficient of granular energy	$\text{kg m}^{-1} \text{s}^{-1}$
λ_{s_i}	Particle bulk viscosity	$\text{kg m}^{-1} \text{s}^{-1}$
λ_{eff}	Effective Conductivity	$\text{Wm}^{-1} \text{K}^{-1}$
Φ	Flux	
α	Volume fraction	
β	Momentum exchange coefficient	$\text{kg m}^{-3} \text{s}^{-1}$
γ	Energy Dissipation rate	J/kg s
η	Efficiency	
θ	Incident Angle	o
λ	Bulk viscosity	Pa.s
μ	Viscosity	Pa.s
π	Pi	
ρ	Density	kg/m^3
σ	Stefan-Boltzmann Constant	$\text{Wm}^{-2} \text{K}^{-4}$
v	Velocity	m/s
ϵ	Emissivity	
ϕ	Porosity	

Abbreviations

<i>2D</i>	Two dimensional
<i>3D</i>	Three dimensional
<i>BFB</i>	Bubbling fluidised bed
<i>CFB</i>	Circulating fluidised bed
<i>CFD</i>	Computational fluid dynamics
<i>CPC</i>	Compound parabolic concentrator
<i>CSE</i>	Concentrated Solar energy
<i>HHV</i>	High heating value
<i>LHV</i>	Low heating value
<i>TG</i>	Thermogravimetric
<i>UDF</i>	User defined function

Subscripts and superscripts

<i>Stag</i>	Stagnant
<i>ab</i>	Absorber
<i>b</i>	Bubble
<i>e</i>	Emulsion
<i>eff</i>	Effective
<i>f</i>	Fluid
<i>i</i>	species
<i>j</i>	Segment
<i>m</i>	Material
<i>n</i>	Number of components
<i>p</i>	Particle

<i>r</i>	Reactor
<i>s</i>	Solid
<i>v</i>	Volatiles
<i>w</i>	Wall
<i>g</i>	gas

LIST OF FIGURES

Figure 1.1: Thermochemical biomass conversion using solar energy as heat source (Shakya 2007).	18
Figure 1.2: Concentrated solar heated particle for integration in circulating fluidised bed gasification.	21
Figure 1.3: Description of modified integrated solar biomass thermochemical conversion process.....	23
Figure 1.4: Description of modified integrated solar biomass thermochemical conversion process the absence of solar energy.	23
Figure 2.1: a) The time averaged -particle concentration in a 45° inclined flow b) ECT image for flow at 45° inclined pneumatic conveying (Zhu et al. 2003).....	29
Figure 2.2: A layout of experimental equipment with the pressure transducer at different points along the pipe (Mason & Li 2000).....	29
Figure 2.3: The mean air velocity of at different solid loading ratios (0.75,1.43, and 2.0) and bulk velocity of 8.9m/s compared with experiment (Lun & Liu 1997).	31
Figure 2.4: The particle concentration at different solid loading ratios (0.45, 1.5, and 3.2) and bulk velocity of 15m/s compared with experiment (Lun & Liu 1997).	31
Figure 2.5: Particle concentration distribution for comparison of calculated flow structure in a particle-laden developed channel and pipe flow for high roughness, $\Delta\gamma = 5^\circ$; left column: two-way coupling; right column: four-way coupling (Laín & Sommerfeld 2012).....	32
Figure 2.6: Distribution of stream-wise particle velocity for comparison of calculated flow structure in a particle-laden developed channel and pipe flow for high roughness, $\Delta\gamma = 5^\circ$; left column: two-way coupling; right column: four-way coupling (Laín & Sommerfeld 2012). 32	32
Figure 2.7: Influence of inclination angle on the flow quantities along line L of pneumatic conveying of 3.0-mm particles in a pipe with a diameter of 8.0 cm. (a) Particle concentration; (b) mean gas velocity; (c) mean solid velocity ($m = 3.85 \text{ m/s}$, $es = 0.9$, $ew = 0.7$, $\phi = 0.02$) (Zhu et al. 2004).	33
Figure 2.8: Gas pressure drop as function of the gas flux: (a) schematic representation of experimental observation and (b) model predictions at a fixed solid mass flux, mass flux= $150\text{kgm}^{-2}\text{s}$ (Makkawi & Ocone 2006).....	34
Figure 2.9: Solids fluxes, G_s , vs. velocity in the CFB. The maximum and minimum solids fluxes were obtained by control of the purge air to the inlet of the recycled solids. The terminal velocity of an average size bed particle (ut) and the transport velocity (utr) are indicated (Johnsson et al. 2000).....	38
Figure 2.10: Mean cluster descent velocities vs. mean solid concentration compared with different experimental data (Liu & Lu 2009).	39
Figure 2.11: Time-averaged data of mas flux with superficial velocity of 1.1m/s for 3-D (0.645cmx0.645cmx1.33cm) and 2-D(0.645cmx1.333cm) simulations (Zhang & VanderHeyden 2001).....	40
Figure 2.12: Particle concentration predicted with and without turbulent transfer compared with experimental techniques (Alves et al. 2001).....	42
Figure 2.13: Sub-divisions of the near wall-region (ANSYS 2009).....	52
Figure 2.14: Single Step Pyrolysis Reaction (Prakash & Karunanithi 2009).....	59

Figure 2.15: Three-Parallel reaction model (Prakash & Karunanithi 2009).....	60
Figure 2.16: Competing Reaction Model (Thurner & Mann 1981).....	61
Figure 2.17. Competing and Parallel Model with Secondary Tar Cracking (Sinha et al. 2000).	63
Figure 2.18. Single step primary reaction with secondary reactions (Prakash & Karunanithi 2009).	64
Figure 2.19. Broido-shafizadeh Multi-step Scheme (Di Blasi 1996).	64
Figure 2.20: Pressure based coupled solver iterative procedure (ANSYS 2009).	72
Figure 3.1: Ray Concentration on a Parabola (Stine 2001).	76
Figure 3.2: Schematic diagram of parabolic trough (Volker Quaschnig 2003).	77
Figure 3.3: Schematic diagram of linear Fresnel reflector (Volker Quaschnig 2003).	78
Figure 3.4: Diagram of Heat Collection Element (Forristall 2003).	79
Figure 3.5: Temperature profile in a Tubular Solar Receiver (Fend 2010).	79
Figure 3.6: Temperature profile in a Volumetric Receiver (Fend 2010).	80
Figure 3.7: The different solar thermochemical conversion process to produce synthesis gas(adapted from Steinfeld (2005)).	83
Figure 3.8: Influence of the mean solar flux on the temperature of the solar receiver/reactor (Sui et al. 2011).	84
Figure 3.9: Comparison of experimental and theoretical values for the relative upgrade in energy level of solar thermal energy at different mean solar flux at methanol feeding rate of 2.1L/h(Jin et al. 2009).	84
Figure 3.10: Heat balance containing heat fluxes and losses in a solar pyrolysis process (Morales et al. 2014).	86
Figure 3.11: Temperature distribution along the centerline of porous medium solar thermochemical reactor for both the non-reactive and SMR reactive conditions (F. Wang et al. 2014).	87
Figure 3.12: One dimensional Simple Energy balance in a parabolic trough(adapted from Gong et al. 2010)	91
Figure 3.13: The parabolic trough outlet temperature change with length of the receiver.....	94
Figure 3.14: Pressure drop relationship between length and superficial gas velocity for a solid flowrate of 1g/s.	95
Figure 3.15: Schematic of solar pyrolysis reactor	98
Figure 3.16: Cross-sectional view of mesh and computational domain	99
Figure 3.17: Gas velocity distribution (a) Radial velocity profile at 3.5 m from the entrance (b) radial cross-section of velocity contour at 3.5 m from the entrance (c) axial cross-section vectors over the entire simulation domain (d) axial cross-section of velocity vectors around the separator zone.	103
Figure 3.18: Solid (biomass) concentration (a) axial cross-section concentration profile over the entire simulation domain (concentration restricted to 2×10^{-4} to allow better visualization) (b) radial profile at 3.5 m from the entrance (c) radial cross-section contour at 3.5 m from the entrance.	104
Figure 3.19: Axial granular temperature at points along the domain.....	106
Figure 3.20: Pathlines of gas velocity distribution. This indicates the average residence time of the gas particles.....	107
Figure 3.21: Residence time distribution of the gas phase.....	108
Figure 3.22: Timed evolution of Separation efficiency of the gas-solid conical deflector separation mechanism.....	109
Figure 3.23: Average biomass and gas temperature distribution along the riser.....	110
Figure 3.24: Greenhouse gas emissions for heat needed supplied by switch grass combustion and electricity.	111
Figure 3.25: The drying and devolatilisation rate for the pyrolysis process along the domain	113

Figure 3.26: The devolatilisation efficiency at localised zones along the reactor.....	114
Figure 3.27: Timed evolved product yield composition.....	115
Figure 3.28: Composition of bio oil yields with solar pyrolysers.	116
Figure 3.29: Comparison of products yield with other fluid-particle reactors.	117
Figure 3.30: Comparison of non-condensable gases compositions.....	117
Figure 4.1: Heat flux distribution in the absorber tube of a parabolic trough solar collector (modified from Wang et al. (2014)).....	125
Figure 4.2: Parametric results for non-homogeneous flux and homogeneous flux for exit temperature of the gas and solid phases.	127
Figure 4.3: Parametric results for non-homogeneous flux and homogeneous flux a) Devolatilisation efficiency b) final product composition.....	128
Figure 4.4: Parametric results for (conduction+convection only) and complete model (conduction+convection+radiation) a) exit temperature of the gas and solid phases b) average temperature of the solid phase.....	130
Figure 4.5: Parametric results for cases of wall model (conduction+convection only) and complete model (conduction+convection+radiation) a) devolatilisation efficiency b) final product composition.....	131
Figure 4.6: Parametric results for cases of 300°C and 200°C sweeping gas temperatures a) outlet temperature at the gas and solid outlet b) average biomass solid temperature	133
Figure 4.7: Parametric results for cases of 300°C and 200°C sweeping gas temperatures at the gas outlet for a) devolatilisation efficiency b) final product composition.....	135
Figure 4.14: A timed variation of separation efficiency with respect to temperature for 250µm and 1mm biomass particles undergoing fast pyrolysis.	136
Figure 4.15: Gas phase residence time distribution for 250µm and 1mm biomass particles undergoing fast pyrolysis.	137
Figure 4.16: Devolatilisation efficiency for 250µm and 1mm biomass particles undergoing fast pyrolysis.	138
Figure 4.17: Product composition 250µm and 1mm biomass particles undergoing fast pyrolysis.	139
Figure 5.1: The transition regimes of fluidization (Almutter 2006).....	141
Figure 5.2: Geldart classification of powders (Geldart 1973).....	142
Figure 5.3: Picture and diagram of the Experimental CFB at Aston University's EBRI.	145
Figure 5.4: Diagram of the primary cyclone.	146
Figure 5.5: Picture of the primary and secondary rotameters used for the experiment.	147
Figure 5.6: Geometry and mesh of the CFB gasifier.	150
Figure 5.7: A graph showing the effect of particle size on the solid circulation rate for 0.3mm and 0.4mm particle diameters.	152
Figure 5.8: Time series raw experimental values from pressure measurement a) 0.3mm sand particle diameter b) 0.4mm sand particle diameter.....	153
Figure 5.9: Pressure values at different air flowrate in the riser for 0.3mm particle size.	154
Figure 5.10: A comparison of pressure values at 260L/min and 200L/min along the riser for 0.3mm and 0.4mm particle sizes.....	155
Figure 5.11: Pressure profiles for experiment and simulation of different grid sizes.	156
Figure 5.12: Pressure profiles for experiment and simulation of different drag laws.	157
Figure 5.13: Pressure profiles for experiment and simulation of different turbulence models.	158
Figure 5.14: Pressure profiles for experiment and simulation of different near-wall treatment models.....	160
Figure 5.15: Pressure profiles for experiment and simulation for particle-wall restitution of 0.4, 0.9, and 1	161
Figure 5.16: Pressure profiles for experiment and simulation of different turbulence models	162

Figure 6.1: C-H-O diagram of the gasification process (Basu 2010).....	165
Figure 6.2: Imbert downdraft gasifier (Warnecke 2000).	169
Figure 6.3: Updraft Gasifier (Warnecke 2000).	170
Figure 6.4: Bubbling fluidised bed (Geldart 1986).	171
Figure 6.5. Circulating Fluidised bed (Bridgwater 1984).....	172
Figure 6.6: Dual circulating fluidised bed (modified from Bridgwater & Peacocke (2000)) ..	173
Figure 6.7: Model setup for the circulating fluidised bed gasifier (diagram and computational mesh domain).	187
Figure 6.8: Solid volume fraction distribution along the riser.	190
Figure 6.9: Axial velocity distribution of char, sand and gas phases.	191
Figure 6.10: Entrance and exit regions for the solid velocity (sand).....	192
Figure 6.11: Axial Temperature profile along the riser height.	193
Figure 6.12: Axial profile contour of rate of reaction for heterogeneous reactions.	194
Figure 6.13: Axial profile contour of rate of reaction for homogeneous reactions.....	195
Figure 6.14: Outlet gas composition along the riser height for CO, CO ₂ , CH ₄ , H ₂ , O ₂ , H ₂ O, and N ₂	196
Figure 6.15: Outlet gas composition compared with char cracking reactions.	197
Figure 7.1: Integrated solar biomass thermochemical conversion process	203

LIST OF TABLES

Table 1.1. Pyrolysis methods and their Variants (Demirbas 2005)	17
Table 1.2: Characteristics of solar collectors (Luzzi & Lovegrove 2004).....	19
Table 2.1: Comparison between Two-fluid and discrete model (Pepiot et al. 2010).....	27
Table 2.2: Experimental techniques in multiphase gas-solid flow (Silva et al. 2012).....	36
Table 2.3: Correlations of the different viscosities of the solid phase	47
Table 2.4: Drag models for gas-solid momentum exchange	48
Table 2.5: Chemical kinetics of Parallel reaction model (Larfeldt et al. 2000)	61
Table 2.6: Chemical kinetics of competing reaction model (Turner & Mann 1981)	62
Table 2.7: Kinetics of secondary reaction	63
Table 2.8. Kinetics of boudouard reaction.....	65
Table 2.9. Kinetics of water-gas reaction	66
Table 2.10. Kinetics of hydrogasification.....	67
Table 2.11. Kinetics of water-gas shift reaction	68
Table 2.12. Kinetics of water-gas shift reaction	68
Table 2.13. Kinetics of Combustion Reactions (Pasangulapati 2012)	69
Table 2.14. Kinetics of Char Combustion Reactions	69
Table 3.1: Main types of pyrolysis reactors (Bridgwater 1999).....	81
Table 3.2: Properties of the gas and solid phases.....	94
Table 3.3: Values of the different heat parameters and material savings	96
Table 3.4: Dimensions of simulation domain	98
Table 3.5: Proximate and ultimate analysis of switch grass (Boateng et al. 2007)	100
Table 3.6. Operating conditions.....	102
Table 3.7: The thermodynamics and performance of solar parabolic trough pyrolyser	111
Table 3.8: GHG emission factors(Deru & Torcellini 2007)(Saidur & Abdelaziz 2011)	112
Table 5.1: Dimensions of the primary cyclone.	146
Table 5.2: Operating conditions for the CFB gasifier process.	148
Table 5.3: Operating conditions of CFD model.	151
Table 6.1: Summary of Gasification (Shinya & Yukihiro 2008).	164

Table 6.2: Summary of Gasification Reactions (Basu 2010).....	166
Table 6.3: Classification of biomass tars (Paasen & Kiel 2004).	167
Table 6.4: Advantages and Disadvantages of Reactors in a gasification process (Warnecke 2000).	174
Table 6.5: Proximate analysis of switch grass char	185
Table 6.6: Kinetic rate equations of Primary and secondary reactions	185
Table 6.7: Rate of reaction equations for heterogeneous reactions (Pasangulapati 2012).	186
Table 6.8: Kinetic rate equations for homogeneous gasification reactions (Miao et al. 2013).	186
Table 6.9: Properties and operating conditions of the domain	189
Table 6.10: Outlet gas composition of reported literature values for gasification in a CFB compared with the tar reforming case (Case 3).	198
Table 7.1: Summary of hydrodynamic model for a CFB riser	202

CHAPTER 1 : INTRODUCTION

This chapter presents the background of the research, research objectives and outline of this thesis for integrating of concentrated solar energy with biomass thermochemical conversion processes.

1.1. Bioenergy and Climate change

The climate change phenomenon has been one of the major issues of the 21st century with regards to energy production and utilisation. Fossil fuels form a bulk of the world's energy supply; they are limited resources and their excessive consumption leads to climate change. Renewable energy usage is growing and progresses in innovation have driven efficiency much significantly. Sustainability is a huge issue for the future to drive growth in the world; renewable energy technologies of mainly wind, bioenergy, solar are being developed extensively to complement fossil fuels.

Bioenergy is a non-fossilized biodegradable organic matter from plant, microorganisms and animal origin including products, by-products, residues and waste from forestry, agriculture, and biodegradable materials from industrial and municipal waste (UNFCCC 2005). It requires extensive amount of land though a very diverse resource. If only 5% about 3.5 billion tons can be utilized for energy production; this is equivalent to 6 billion tons of oil clearly 26% of the world energy consumption (Basu 2010). The sources of biomass are categorized into virgin (i.e. food crops, energy crops, or perennial grasses) or waste (i.e. Municipal waste, Forest and agricultural residues or Industrial waste).

Biomass consists of lignin, hemi-cellulose, cellulose, organic extractives and inorganic minerals. Lignin, hemi-cellulose, and cellulose are the major component which form the structure of the biomass. The organic extractives (e.g. starch, protein, simple sugars and fatty acids etc.) are present in small quantities (2-3% in wood); they are normally extracted using solvents. The inorganic extractives (such as Calcium (Ca), Potassium (K), and Magnesium (Mg)) end up as ash in thermochemical conversion processes. The composition of biomass is analysed using the proximate and ultimate analysis. The proximate analysis consists of the bulk composition of fixed carbon, volatile matter, moisture content and ash. The ultimate analysis represents the elemental composition of the biomass as Carbon (C), Hydrogen (H), Oxygen (O), Nitrogen (N), Sulphur(S) and Ash.

Combustion is regarded as an inefficient method for biomass utilization due to the low energy density of biomass. Pyrolysis and gasification are alternatives that overcome the

storage and transport issues relating to biomass utilization. They produce higher heating value gas and provide feedstock to other fuels and chemicals.

1.2. Pyrolysis

Pyrolysis is a thermochemical decomposition of an organic matter in the absence of air or oxygen; it usually takes place at temperatures between 300 °C- 650 °C. Biomass is usually decomposed to mainly gases (CO, H₂, CH₄, CO₂, C_xH_y), bio-oil, and char in a heterogeneous (solid-gas) reaction. The fraction of the final product yield is heavily dependent on the feedstock and operating conditions. The temperature, heating rate and residence time are the most important operational characteristics that distinguish the different pyrolysis process. Heating rate is defined based on the difference between the time required for heating the fuel and the reaction time. Biomass fast or flash pyrolysis produces mainly bio-oil while slow processes produce chars. The characteristics of the different variant of pyrolysis are shown in Table 1.1.

Table 1.1. Pyrolysis methods and their Variants (Demirbas 2005)

Process	Residence time	Heating rate	Final temperature(°C)
Carbonisation	1800s-Days	Very low	400
Intermediate	300-1800 s	Low	600
Fast	0.5-5 s	Very High	~500
Flash	Less than 1 s	High	<650
Ultra-rapid	Less than 0.5 s	Very High	~1000

The main aim of fast pyrolysis is to produce pyrolysis liquid or bio-oil. This happens at higher pyrolysis temperatures less than 500 °C preferably with a short residence time producing high quality bio-oil; the heating rates are >200 °C/s. The ability to produce high quality products is attributed to its high heating rate, shorter residence time and quick heat transfer rate. The reactors used for pyrolysis represent just 10-15% of the cost of pyrolysis; most of the cost is attributed to the pre-processing and utilization steps of the process (Bridgwater 2012). The usual auto thermal gasification and pyrolysis are endothermic reactions that require heat to be supplied by either combustion of by-products, or some form of fuel (30% of biomass, fossil fuels etc.). This reduces the heating value of the final product and loss of material due to exothermic combustion reactions. Solar energy is able to provide cleaner and environmentally sound products. The combustion of part of the feedstock is avoided replacing contamination caused by air and oxygen combustion; this improves the heating value of the final products is significantly. The main pyrolysis reactors are categorized into

the following: Bubbling fluidised bed, Circulating and transporting beds, ablative, rotating cone and vacuum. The mechanism of ablative reactors (sweeping or centrifugal effect) can be implemented to solar reactors to eliminate the primary products as they are formed to avoid the formation of high charred products.

1.2.1. Concentrated solar energy

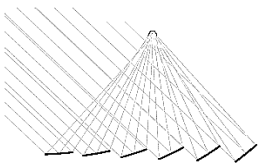
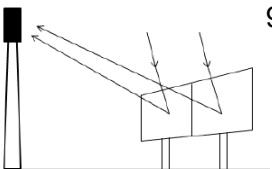
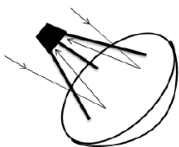
Solar energy is an unlimited energy resource which is can be utilised for thermal purposes using concentrated solar technologies. Concentrated solar technologies are solar thermal systems, which use mirrors to focus solar radiation to an absorbing medium or receiver. It can be used to drive endothermic reactions using thermal energy. They have capabilities when coupled with chemical reactions to reach solar –fuel efficiency exceeding 50% making the process hugely economical. Concentrated solar energy is utilised for biomass thermochemical conversion either using an integrated or separated system in Figure 1.1.



Figure 1.1: Thermochemical biomass conversion using solar energy as heat source (Shakya 2007).

Concentrated solar energy can be used to provide fast heating rates and high biomass conversion. Concentrated solar energy is exploited using different technologies either line focusing (parabolic trough and linear Fresnel) or point (dish and solar tower) focusing systems as shown in Table 1.2.

Table 1.2: Characteristics of solar collectors (Luzzi & Lovegrove 2004)

Solar collector	Diagram	Temperature(°C)	characteristics
Parabolic trough		601	Focuses along a cylindrical surface. Single-axis tracking.
Linear Fresnel		350	Focuses on multiple absorbers using alternating mirrors Single-axis tracking
Heliostat		900	Point concentration using multiple heliostats. Two-axis tracking
Parabolic dish		1200	Point focus using a dish Two-axis tracking

The problem of intermittence and dilute nature of solar energy is complemented by using concentrated solar energy and an energy storage mechanism. Parabolic trough can be used feasibly for processes with temperature up to 600 °C. It is the most mature technology and has the capability to be integrated to a pyrolysis process. This provides an efficient path for solar energy storage and transport for long term use in terms of processed biomass.

1.3. Gasification

Gasification is the conversion of biomass fuels to non-condensable gases usually for chemical feedstock or as fuel. Most of the progresses in gasification were done mostly using coal or natural gas as raw material. It converts the fuel to gaseous fuels with the purpose of either increasing the heating value, removal of gases that produce pollutant when burnt or

increasing the hydrogen-carbon ratio. It requires a gasifying medium mainly air, oxygen, steam or a mixture.

The gasifying agent affects the heating value of the product, the reaction pathways and the final product gases. The gasification products are mainly CO and CO₂ when the gasifying agent is oxygen. When the proportion keeps increasing, it reaches a point where the amount is sufficient to produce only combustion products; these products have no significant heating value. Steam as a gasifying agent shift the reaction towards the production of H₂ at the expense of CO. Air as a gasifying agent dilutes the final product and produces other contaminants from nitrogen. The most frequently used reactor types for gasification are fixed bed, fluidised bed and entrained flow. An entrained flow reactor requires high temperatures, small biomass particles and high concentration of oxygen to maintain the process. Fixed bed reactors compared to fluidised bed produce low heating value gas.

1.3.1. Fluidised beds

Fluidised bed gasifiers are widely employed, particularly for large scale systems. Fluidised beds are used because there is a high solid-to-solid interaction rate in the fluidized bed that makes it well suited for the gasification process. The commonly used fluidised beds are bubbling and circulating fluidised beds. The bubbling beds often have a heat carrier constrained within the reactor as a bed material. There is need to operate at a higher temperature and issues with regards to bed agglomeration and sintering and limits to particle size or type of biomass that can be utilised. Circulating fluidised bed operates at extremely high fluidising velocity based on a regime of fast fluidization above the terminal velocity of the solid. There exist two flow regimes an upward flow of solids and gases and downward flow of the particles along the walls with the solids being entrained out of the reactor. This creates a high mass and heat transfer with uniform distribution of flow properties. The reaction rate becomes really fast and gasification can be achieved at lower temperatures. The gasification of carbonaceous material in fluidized beds and transport reactors is a series of different processes. Therefore, the operation and design of several gasifiers require an understanding of different parameters and operating conditions that affect the performance of the process. These parameters are mainly type of biomass feed, reactor temperature, flow rates of biomass, fluidizing agents (air, oxygen, carbon dioxide or steam), type and amount of catalysts, and biomass type and properties.

1.4. Modelling

Computational fluid dynamics, commonly abbreviated by CFD, is a method used to simulate and predict the behaviour of multiphase flow mixture. In the application of CFD models in multiphase flow systems, such as gas-solid flow, the model provides microscopic and

transient prediction of the flow in two and three dimensional coordinate. For reactive multiphase flow systems, such as fluidized bed reactors, the CFD system allows for incorporating heat transfer and chemical reactions to be solved simultaneously with the flow equations. However, technical challenges arise in adding the correct reactive system, constitutive relations, and additional equation for each case. This usually require development of user defined functions. The two main CFD methods for multiphase flow modelling and simulation are the two-fluid model (also refered to as Eulerian-Eulerian model) and the discrete particle methods (sometimes refered to as Eulerian-Lagrangian model). Currently, the main commercially available CFD softwares used for multiphase flow system simulations are CPFDF Baracuda[®](CPFDF 2014), open-source OPENFOAM[®](CFD Direct 2014), ANSYS Fluent[®](ANSYS 2014), and open source NETL MFIX[®](NETL 2014). In describing the fluid flow, the latter software uses the Eulerian-Eulerian (two-fluid model) modelling approach, while the former applies the Eulerian-Lagrangian approach.

1.5. Thesis Novelty

1.5.1. Original proposed concept

The initial problem at hand was to heat supply from a concentrated trough arrangement to biomass gasification in circulating fluidised bed (CFB). The solar heated particle (sand or suitable metal catalyst) is heated in the trough system and the heated particle enhances thermal performance and hydrodynamic mixing in a circulating fluidised bed. This is shown in the diagram below:

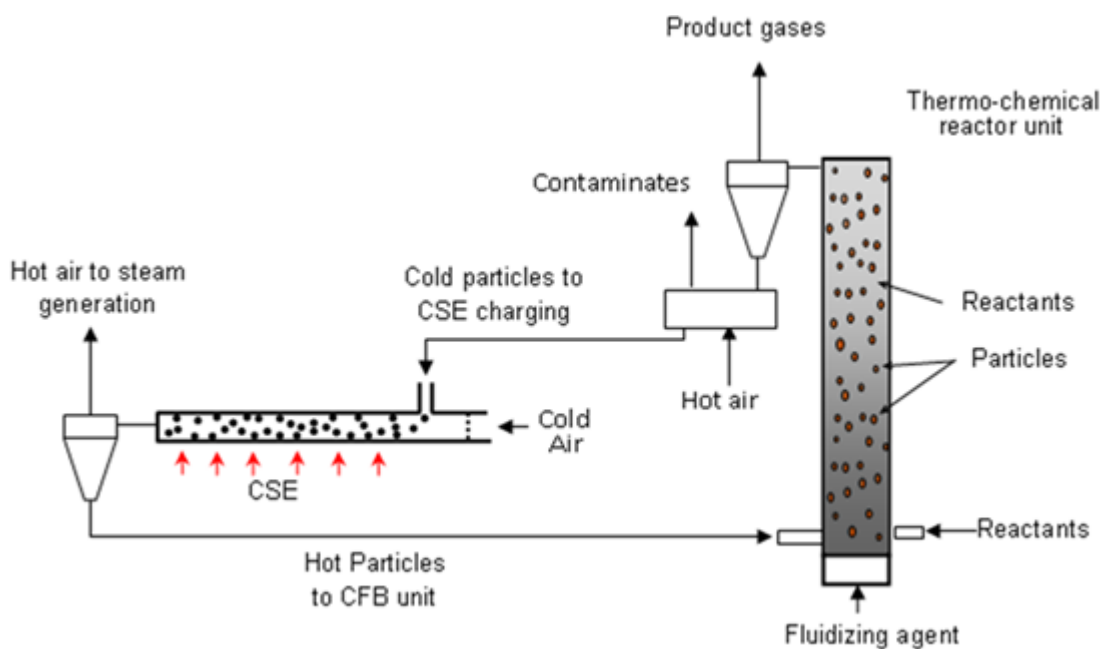


Figure 1.2: Concentrated solar heated particle for integration in circulating fluidised bed gasification.

The problem with the process is the parabolic trough cannot heat the particles to extremely high temperature for the gasification to be self-sustaining. Though air can be used as a fluidizing agent to increase the performance of the process, this creates a duplication of process as the cost of implementing the first process outweighs the savings from it by using purely air.

1.5.2. Modified concept

The concept of recovery and storage of solar energy is utilised in the process to create high value products. The process was optimised so that pyrolysis process is initiated using the solar parabolic trough receiver (See Figure 1.3). Biomass instead of sand is heated to temperatures up to 450°C in an ablative process. This process eliminates the bio-oil and reduces the amount of high molecular mass weight tar being formed in the process. This makes gasification much more efficient. Also, as char have catalytic tendencies on tar; this increases the product gas composition of hydrogen. In the absence of solar energy, the heat for the gasification process is supplied from the pyrolysis gas stored from the pyrolysis process (See Figure 1.4). The remaining biochar is mixed with fresh biomass in a conventional gasification process until spent and only fresh biomass is added into the process. This allows for high throughput of biomass feed.

The present work expands on work carried out in solar trough receiver/reactors and circulating fluidised bed gasification. The method of Eulerian-Eulerian modelling has been implemented severally to fluidised bed reactors and solar reactor modelling. A problem solving approach was used to study the dynamics of solar fast pyrolysis in a parabolic trough receiver. The model has an advantage in leveraging extensive research on parabolic trough, fast pyrolysis, and Eulerian-Eulerian modelling. There has been several research on Eulerian-Eulerian modelling of circulating fluidised bed gasification. The catalytic activity of char during gasification has rarely been implemented in existing research though being referenced extensively using CFD models. A catalytic model is implemented as a particle-surface reaction to report the effect of char on tar catalytic conversion.

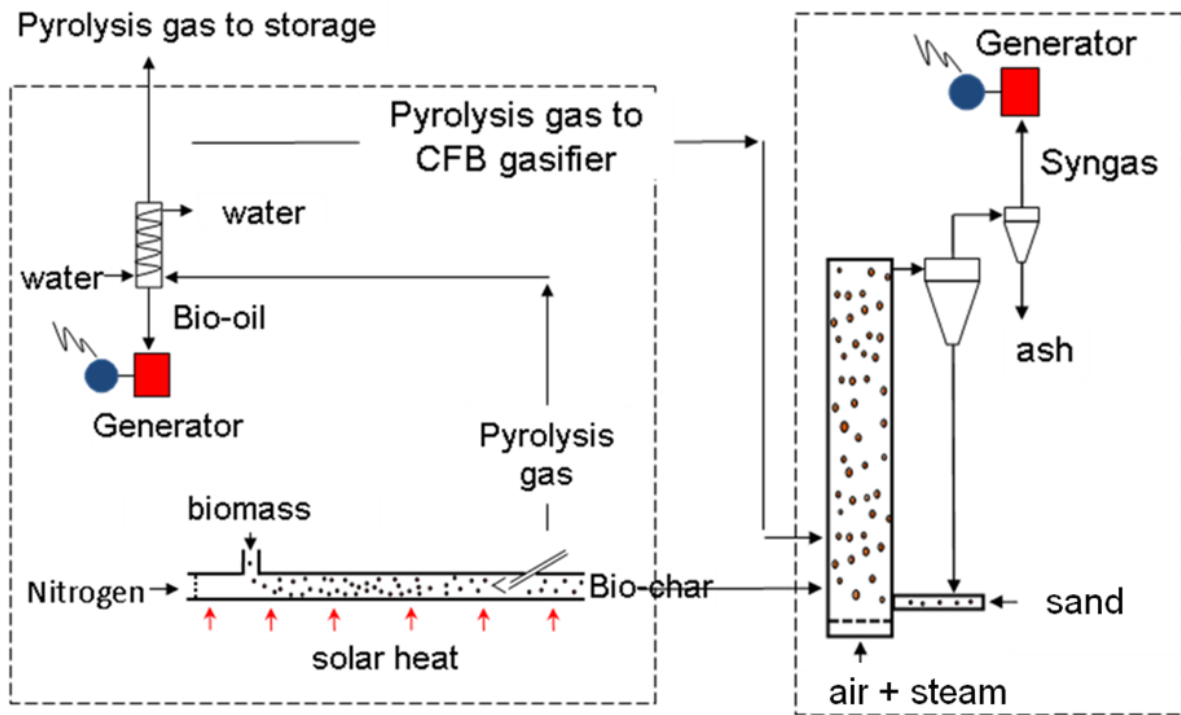


Figure 1.3: Description of modified integrated solar biomass thermochemical conversion process.

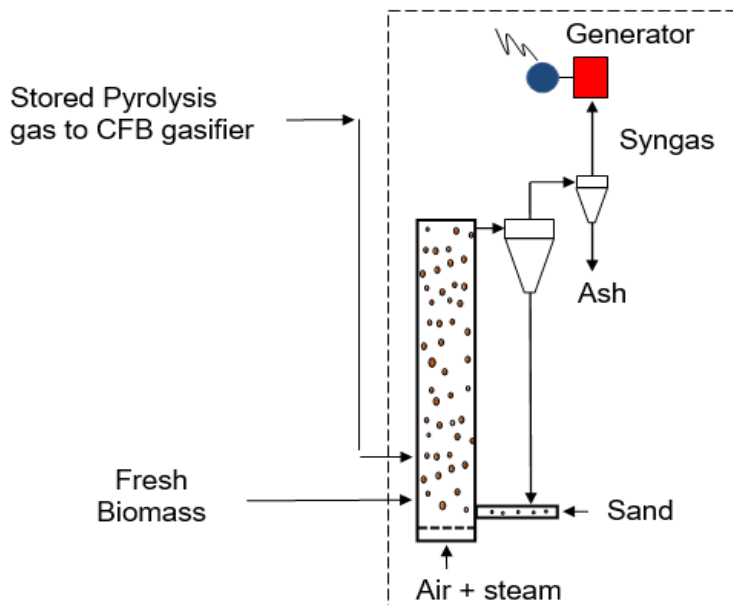


Figure 1.4: Description of modified integrated solar biomass thermochemical conversion process the absence of solar energy.

1.6. Thesis objectives

The main project objective is to develop a model for biomass fast pyrolysis in a parabolic trough receiver/reactor and char gasification in a circulating fluidised bed. The simulation is to be carried out based on numerical hydrodynamics approaches and optimization. This is a theoretical study and the objectives highlighted below are to be achieved using CFD modelling:

- Develop a three-dimensional model to predict biomass fast pyrolysis in a solar-thermal reactor
- Investigate the potentials of implementing steam-air char gasification in a conventional Circulating fluidised bed (CFB)
- Validate the circulating fluidised bed model with an experimental scale circulating fluidised bed (CFB) gasifier at Aston University's European Bioenergy Research Institute

1.7. Thesis outline

The thesis is composed of CFD models for thermal conversion processes (gasification and pyrolysis) integrated with solar conversion techniques.

Chapter 1: Introduction

The chapter presents the concept and idea of the project and how computational fluid dynamics can be implemented to solve the problem at hand. It shows the modified project and the final objectives of the PhD.

Chapter 2: Computational fluid dynamics

This chapter provides the general theoretical and literature background of the thesis regarding computational fluid dynamics. The knowledge regarding the modelling the hydrodynamics, heat transfer and reaction model. The importance of the different correlation and techniques used have been highlighted. The discretisation scheme used by FLUENT was also provided in brief.

Chapter 3: CFD modelling of biomass fast pyrolysis in a solar/receiver reactor

The chapter is initiated with a background and literature review. The Eulerian-Eulerian modelling of a solar receiver/reactor was described in detail including the drying and pyrolysis models implemented. Finally, the hydrodynamics, energy efficiency, heat distribution and product compositions were described with reference to literature findings.

Chapter 4: Sensitivity analysis of CFD modelling of biomass fast pyrolysis in a solar/receiver reactor

This chapter presents a continuation of research from chapter 3. The model has been advanced to include the effect of different heat flux and heat mechanisms. The effect of operating conditions were also investigated. The performance of gasifier and quality of product gas compositions was tested based on the effect of particle size, sweeping gas flowrate, and sweeping gas temperature. These changes were described and compared to literature findings.

Chapter 5: Hydrodynamics of a circulating fluidised bed riser

The chapter presents an experimental pressure measurement technique in a circulating fluidised bed riser. The experimental pressure gradient in the riser is described for different particle sizes. The measurement was used to model the hydrodynamics of the gasifier. The effect of grid size, different drag laws, turbulence models, wall treatment, and wall shear models were reported.

Chapter 6: CFD modelling of char gasification in a circulating fluidised bed

The chapter is an extension of the modelling of the experimental circulating fluidised bed riser. A reaction model is included for a poly-disperse solid phase mixture of sand and char for a gasification process. The reaction model included both the heterogeneous and homogeneous model using a UDF for the gasification code. The species rate model was also looked into using both laminar finite rate and finite rate/eddy dissipation model for the reactions. The catalytic effect of char was explored with respect to tar reforming reactions.

Chapter 7: Conclusion and recommendation

The final conclusions to all the chapters is discussed and the achievements of this thesis. Further recommendations were presented for future research.

CHAPTER 2 : COMPUTATIONAL FLUID DYNAMICS

Gas-solid multiphase flow in chemical reactors commonly takes the form of solids suspended in gases. This phenomenon has been implemented in many industrial applications to allow enhanced heat and mass transfer between the solid and gas phases. The most prevalent of these reactors are fluidised beds and they operate based on this principle. This chapter contains mainly the methodologies for modelling the gas-solid flow in a tubular solar/receiver reactor using the commercial CFD software ANSYS FLUENT. The first section describes the numerical approaches to modelling flow hydrodynamics and heat transfer. The governing equations of mass, momentum, granular temperature and heat balance, in addition to the relevant model parameters and closure equations are presented. A full description of the reaction kinetics and rate equations for biomass pyrolysis and gasification are also presented. Finally, this chapter present the numerical procedure, assumptions and solution procedure for the coupled hydrodynamic, heat transfer and reaction equations.

2.1. Hydrodynamic model

2.1.1. Background theory

The classification of gas-solid flow models is attributed to either the particles being treated as a continuum or as single particles. The former is usually referred to as “Eulerian-Eulerian” while the latter is usually referred to as “Eulerian-Lagrangian”. The gas phase is normally implemented as a continuous phase in the both numerical approaches. There is need to solve the gas-solid phases interactions as well as the particle-particle interactions in terms of mass, momentum and energy exchanges. These approaches are discussed further in the following sections.

2.1.1.1. *Eulerian-Lagrangian model*

The discrete particle phase (Eulerian-Lagrangian) model uses the newton’s law of motion to describe the solid phase dynamics, while the gas phase is described as a continuous medium to solve Navier-stokes equations. The model provides a microscale dynamic flow behaviour and details complex interactions between the gas and solid phases. The particle location is tracked to predict the mass, energy and momentum within the gas phase. The exchanges between the phases are treated as source terms in the transport equation.

2.1.1.2. Eulerian-Eulerian model

The two-fluid (Eulerian-Eulerian) model treats the solid and fluid phases as interpenetrating continuum described by Navier-stokes equations with volume fraction specifying the cell occupied by the fluid as continuous in space and time (Gidaspow 1994). The model involves solving continuity, momentum and energy equations. The particle-particle interactions are determined using the principles of kinetic theory of granular flow (KTGF). The two-fluid method is relatively computationally fast and more suitable for the simulation of real scale processing units. The particle interactions are estimated using effective solid pressure (p_s), shear (μ_s), and bulk viscosity (λ_s). The model can confidently be used to predict the distribution of phases and velocities. The advantages and disadvantages of two fluid and discrete phase models is given in Table 2.1.

Table 2.1: Comparison between Two-fluid and discrete model (Pepiot et al. 2010)

Fluid Model	Advantages	Disadvantages
Two-fluid Model	Typically used in dilute solid-gas phases Simulates larger reactor, therefore suitable for scale up and reactor design	Less closure in dense flows Over-prediction of temperature and composition profiles
Discrete - particle Model	Analysis at an individual particle level (Particle-particle collisions are considered). Model typical bed features Eliminates error in mass and energy calculations.	Large number of particles in fluidised beds makes it expensive. Applied to mostly 2D configurations due computational expense. Limit on particles analysed due to computational cost

2.1.2. Literature review

2.1.2.1. Studies of gas-solid flow in pipes

Tsuji & Morikawa (1982) used Laser-Doppler anemometry (LDA) to measure fluid velocities rather than conventional pitot tubes and hot wire anemometer due to its inability to obstruct

flow movements. Pressure drop inherently gives the power needed for transport though these techniques are not very satisfactory with regards to gas-solid flows. The aim was to replace pressure measurement techniques that are one-dimensional and cannot be used to understand the internal structure of the flow. LDA has been used by several researchers such as Birchenough & Mason (1976) and Kulick et al. (2006) to measure velocity, concentration and particle size in gas-solid flows. Sommerfeld & Huber (1999) also used it to measure effect of particle-wall collisions such as wall roughness and sphericity of particles in particle laden flows. There was good agreement for both particle and wall properties when compared with numerical models.

Electric capacitance tomography (ECT) to study horizontal and inclined flows has been evaluated by Rao et al. (2001) and Zhu et al. (2003). Rao et al. (2001) studied the flow patterns in various regimes in horizontal pneumatic flow. A single phase ECT was used to measure the particle concentration and a twin phase ECT to measure the velocity across the pipe. The different regimes of homogeneous, dune, settled, and plug flows was observed in horizontal flows. Zhu et al. (2003) showed that in 45° inclined riser showed a settled flow with ECT measurements. The effect was due to particle sedimentation caused by gravitational force as shown in Figure 2.1. This showed initial particle sparsing due to acceleration and then it levels off due to gravitational sedimentation; further downstream the flow becomes fully developed. ECT has been used to validate CFD models both for horizontal flows and fluidised beds. Other authors that have used ECT to evaluate pneumatic conveying flows such as McKee et al. (1995) and Jaworski & Dyakowski (2001).





Figure 2.1: a) The time averaged -particle concentration in a 45° inclined flow b) ECT image for flow at 45° inclined pneumatic conveying (Zhu et al. 2003).

Pneumatic conveying experiments have also been conducted using probing and sampling techniques. The pressure measurement technique is relatively common technique of analysing gas-solid flows. The pressure drop in horizontal pipes has been studied using a novel method by modelling an actual section of large scale installation (Mason & Li 2000). A parametric analysis was done in a controlled environment and compared with other pressure measurement techniques. A layout of the experiment is given in Figure 2.2.



Figure 2.2: A layout of experimental equipment with the pressure transducer at different points along the pipe (Mason & Li 2000).

There was constant change in pressure due to the wave like behaviour of particles suspended in air. They found out the flow in a pipe changes from a dense to dilute flow

along the pipe. They concluded the method is applicable to reduce uncertainties in scale up of pilot plants. Tomita et al. (2008) implement low velocity conveying of polyethylene pellets and fluidised horizontal conveying down a slope. There were small fluctuations in suspension flow in pressure drop than with slug flow. The hard particles have a high pressure drop than soft particles due to a reduction in wall friction coefficient. The concept of fluidised horizontal conveying of particles was proposed through which they found out that other forces except gravity are capable of moving the particle even when the ratio of superficial velocity to minimum fluidisation velocity was less than unity (Gupta et al. 2006). Hirota et al. (2002) studied the effect of mechanical properties and inclination in an inclined pipe. They used fly ash, silica, and flour at different inclinations of 0°, 20°, 30°, 45°, 60° and 90°. They found that the pressure drop coefficient of flow in an inclined pipe can be obtained from the inclination angle and dynamic internal friction factor. They concluded that inclination angle has no effect on the mechanical properties of powder conveying.

There have been several researches in multiphase gas-solid flows in circular ducts framed based on Eulerian-Lagrangian or Eulerian-Eulerian models as a numerical approach. Tsuji et al. (1991) implemented a Lagrangian simulation in a horizontal pipe. The methods of particle-wall collisions and particle-fluid interactions were adjusted for a 3D simulation. The equations were solved using finite difference method of approximation and compared with experiment done using an optical fibre probe. It was shown that the particles disperse more in experiments than in simulations due to the model neglecting turbulent diffusion. The small particles concentrate near the bottom wall due to low inertia from the particle-wall collisions. It shows that mean velocity increases with increasing particle loading. Oesterle & Petitjean (1993) compared dense gas-solid flow with dilute gas solid flows in a horizontal pipe. They found that the Lagrangian model has shown that particle-particle effect is negligible so long the loading is below unity. Lun & Liu (1997) developed a two-dimensional numerical simulation for a Lagrangian model in channel flows. The simulation model was compared with experimental results using glass beads, the concentration and velocity are shown in Figure 2.3 and Figure 2.4. The particle concentration increases from top to bottom due to the effect of gravity and asymmetry of air velocity becomes more pronounced as particle loading increases along the channel. Particle-wall collisions only regime has shown that the particles deposit at the bottom of the channel, when inter-particle collisions are considered a steady suspension is observed.



Figure 2.3: The mean air velocity of at different solid loading ratios (0.75,1.43, and 2.0) and bulk velocity of 8.9m/s compared with experiment (Lun & Liu 1997).



Figure 2.4: The particle concentration at different solid loading ratios (0.45, 1.5, and 3.2) and bulk velocity of 15m/s compared with experiment (Lun & Liu 1997).

Huber & Sommerfeld (1998) used a two way coupling (without particle-particle interactions) and observed the effect of wall roughness on the gravitational settling of particles. The inter-particle collisions disperse high particle concentration regions in particle-laden flows. Also, Laín & Sommerfeld (2012) studied using the Lagrangian method by means of four-way coupling (particle-particle and wall-particles collisions) of k-e and Reynold stress turbulence models. This model considered the particle motion with all the forces subjected to it. They

compared four-way and two-way coupling methods. The contours for concentration and particle velocity are given in Figure 2.6 and Figure 2.6.



Figure 2.5: Particle concentration distribution for comparison of calculated flow structure in a particle-laden developed channel and pipe flow for high roughness, $\Delta\gamma = 5^\circ$; left column: two-way coupling; right column: four-way coupling (Lain & Sommerfeld 2012).



Figure 2.6: Distribution of stream-wise particle velocity for comparison of calculated flow structure in a particle-laden developed channel and pipe flow for high roughness, $\Delta\gamma = 5^\circ$; left column: two-way coupling; right column: four-way coupling (Lain & Sommerfeld 2012).

They concluded that particles focus at the core region after colliding with the wall and this effect is reduced with the addition of particle-particle collisions. Zhu et al. (2004) reported using a similar method for horizontal and inclined pipes that the effect of particle-wall interactions on the solid distribution was considerably significant. They compared different inclination angles with to measure its effect on solids distribution and velocity.



Figure 2.7: Influence of inclination angle on the flow quantities along line L of pneumatic conveying of 3.0-mm particles in a pipe with a diameter of 8.0 cm. (a) Particle concentration; (b) mean gas velocity; (c) mean solid velocity ($m = 3.85 \text{ m/s}$, $e_s = 0.9$, $e_w = 0.7$, $\phi = 0.02$) (Zhu et al. 2004).

It is shown in Figure 2.7a that inclination angle affects the solids distribution. The solid volume fraction increases with increasing inclination up the horizontal plane. This leads to an asymmetric particle distribution due to the effect of gravitational force. The velocity of the gas and solid become more symmetric with inclination till it reaches a vertical angle parallel to

gravity; this is similar to other reported literatures as shown in Figure 2.7b. The solid velocity in Figure 2.7c displays a decreasing effect with inclination towards gravity plane. This is due to the lift effect caused by momentum interaction between the solid and the gas phase. Kuang et al. (2012) obtained similar effect with regards to inclination when compared with vertical or horizontal systems. They showed that inclination angle affects the pressure drop thereby increasing the gravitational effects on the solids. The majority of literature on horizontal and inclined pneumatic conveying used the Lagrangian-Lagrangian models as are suitable for showing particle-particle and particle-wall interactions when compared to Eulerian-Eulerian models. Microscale observation of particle interactions is not applicable to this work as these models are computationally expensive for complex interactions.

Ocone et al. (1993) applied a one dimensional kinetic theory model for an inclined duct to study its hydrodynamics. A two-way coupling method was implemented and the effect of turbulence was considered due to the nature of the process. Makkawi & Ocone (2006) studied gas-solid flow in a horizontal duct covering a range of flow regimes (rapid, intermediate and dense). The model showed good correlation with experimental and a modified version of the kinetic theory model as shown in Figure 2.8.



Figure 2.8: Gas pressure drop as function of the gas flux: (a) schematic representation of experimental observation and (b) model predictions at a fixed solid mass flux, mass flux=150kgm⁻²s (Makkawi & Ocone 2006).

The model merges all the three regimes and provided boundaries at which each regime occurs expressed as a factor of shear rate and Reynolds number. They concluded that kinetic and collisional shear rates are prevalent in rapid regimes. Levy et al. (1997) compared numerical and experimental methods using the two-fluid model in vertical and inclined pipes; they had satisfactory correlation between both methods. They compared the effect of inclination to pressure gradient at different solid loading to ascertain the effect of the critical angle. They found that at the critical angle the maximum pressure drop is attained. Hong & Zhu (1997) also found that pressure drop in upward inclined transport is greater than that of horizontal transport. They both concluded that a low solid mass flowrate and loading ratio leads to a high critical angle. Levy (2000) extended it to a 3D Eulerian-Eulerian model to study pneumatic conveying in a horizontal pipe. It showed that this model was capable of predicting flow dynamics in gas-solid pneumatic conveying.

McGlinchey & Cowell (2007) also employed using FLUENT, 3D Eulerian-Eulerian model to predict pressure drop in a horizontal to vertical bend pneumatic conveying. They reported qualitative agreement between experimental and the CFD models. Also, pressure gradient was found to be proportional to the particle diameter. The total pressure drop is affected by the difference between the solid and the gas velocity at the inlet.

Kartushinsky et al. (2011) did a 3D simulation of gas-solid flows in a horizontal pipe using a Reynolds Averaged Navier-Stokes method. The results were validated with experiment to understand the flow structure based on velocity and turbulence kinetic energy. The initial comparison showed good agreement for normalized velocity profiles; the presence of gravity gives it an asymmetric behaviour. There is increase in particle concentration moving through rolling and saltation at the bottom the lower the gas velocity. There is good agreement between the experiment and velocity. The fluid velocity is lower near the walls of the pipe. The effect of gravity leads to asymmetric distribution of velocities, turbulent kinetic energy, and concentration. The absence of gravity result in symmetric particle distribution as there is no particle sedimentation.

Patro & Dash (2013) used Eulerian-Eulerian approach to study the hydrodynamics and pressure characteristics in a horizontal pipe. They understood the effect of gravity induced particle settling and the effect of other forces such as antiparticle collisions. The solid was modelled based on kinetic theory of granular flow. The Standard turbulence k-e model was used to treat the turbulence phenomenon for stability and smooth convergence; the drag force was based on a correlation by Gidaspow (1994). The model showed good agreement with experimental data. It was shown that Particle-wall collisions and friction are dominating mechanisms that affect pressure drop. It also covered a parametric analysis of the effect of

particle diameter, gas velocity and particle loading on the pressure drop. The extensive literature concluded that Eulerian-Eulerian can be used to describe the hydrodynamic behaviour of horizontal and inclined gas-solid flows.

2.1.2.2. *Studies of circulating fluidised bed risers*

Multiphase gas-solid flow in a circulating fluidised riser has been implemented using different experimental techniques individually or in conjunction with other techniques to measure different quantities (velocity, pressure, and concentration). The general techniques for capturing two-phase flows are either intrusive measuring techniques (IMT) or non-intrusive measuring techniques (NMT). These techniques are explained in Table 2.2.

Table 2.2: Experimental techniques in multiphase gas-solid flow (Silva et al. 2012)

Technique	Type of technique	Description
NMT	Laser Doppler anemometry	Laser light is scattered by particles that pass through a series of interference fringes. This light oscillates with a specific frequency relative to the velocity of the particles.
	Radioactive techniques	The transmission of X-rays or γ -rays through a medium causes an attenuation of the incident radiation; this attenuation measurement provides the local mass density distribution.
	Radioactive particle tracking	The motion of a single tracer particle emitting γ -rays as a marker of the solids phase is tracked. This radiation is received by an ensemble of specific detector to measure the velocity field and turbulent parameters.
	Particle velocimetry	The displacement of a particle is used to determine whole velocity fields through taking two images shortly after each other and calculating the distance the individual particles travelled within this time.
IMT	Differential pressure probes/pitot tubes	Mechanical method based on determination of momentum by means of differential pressure measurements
	Fibre optic probes	It is used to measure the local porosity in fluidized beds
	Capacitance probes	The local dielectric constant of the gas-solid suspension measured is linked to the local volume fraction of solids

Samuelsberg & Hjertager (1996) used laser Doppler anemometry (LDA) to measure root mean and axial solid velocities in a circulating fluidised bed. They confirmed the presence of upward flow of gas and downward flow of solids along the walls. Mathiesen et al. (2000) also used a laser Doppler and phase Doppler anemometry (PDA) to measure velocity diameter and volume concentration of particles simultaneously in a circulating fluidised bed. They

concluded a core annulus flow structure similar to Samuelsberg & Hjertager (1996) in a circulating fluidised beds; with the solid concentration dilute in the core and dense in the annular region. These are the same technique discussed for horizontal and inclined pneumatic conveying. Circulating fluidised beds has a close similarity in terms of techniques used to vertical pneumatic conveying. Liu et al. (2005) also reported using ECT measurements for small scale experiments. They concluded ECT produces blurred images for large scale applications.

Hassan (2013) compared experiments using pressure probe techniques and Positron emission particle tracking (PEPT) to measure the pressure and velocity of the particle in the riser. This is similar to the technique implemented by Van de Velden et al. (2007), Hoomans et al. (2001), and Chan et al. (2009). They reported the presence of asymmetric velocity profile behaviours in the riser. They concluded the pressure measured was in correlation with analytical models. Ersoy et al. (2004) implemented a pressure and optical fibre probe technique to study the effect of mode of injection on the hydrodynamics of a circulating fluidised bed. The injection modes were radial, tangential and 45° angle. The pressure measurement was only measured at the secondary injection points. They found out that secondary injection reduces the superficial velocity of the primary fluidizing gas. The time-series fluctuations of pressure measurement has been done in a fluidized bed to cover three fluidizing regimes in a CFB (Johnsson et al. 2000). The bed operates according to Figure 2.9 to describe flow conditions. They found out that amplitude in pressure fluctuations does not give details in determining the change in flow regime. Oelfke et al. (2006) used sampling probes, pressure probes, electrical capacitance and radiation probes to measure the different parameters in a fluidized bed. He obtained a detailed analysis of the particle behaviour and dynamics for validation of CFD models.



Figure 2.9: Solids fluxes, G_s , vs. velocity in the CFB. The maximum and minimum solids fluxes were obtained by control of the purge air to the inlet of the recycled solids. The terminal velocity of an average size bed particle (u_t) and the transport velocity (u_{tr}) are indicated (Johnsson et al. 2000).

The discrete particle model which forms part of the Eulerian-Lagrange models has been implemented to calculate the particle motion under inter-particle collisions (Tsuji et al. 1998). The discrete model (Lagrangian) was compared with the two-fluid (Eulerian) model. They reported larger clusters being formed in the discrete model than the two-fluid model. The results were qualitatively similar the only difference they found was as duct size increases the two fluid model has clusters only near wall region while the discrete model has clusters at the core region. Helland et al. (2000) performed a Lagrangian simulation in a 2D circulating fluidised bed riser to study fluctuating gas-solid motion and flow instabilities using porosity function. They found out that inelasticity and friction affect the formation of clusters in circulating fluidised beds. The core annular structure in fluidised beds was attributed to clusters formed at the core region being moved closer to the wall. Zhou et al. (2002) also used Lagrangian model to simulate the clusters formed in a 2D circulating fluidised bed risers. The particle-particle and particle-wall interactions are responsible for forming this heterogeneous structures.

Liu & Lu (2009) implemented an extended method for the identification of clusters in a Lagrangian model. They observed high solid concentrations at the bottom of the riser

compared to the top which was dilute. Figure 2.10 shows the variation of cluster velocities to the mean particle concentration. The experimental data was qualitatively similar to the simulation. The descent velocities of clusters near the wall increase with increase in cross-sectional solid concentration (Liu & Lu 2009) .



Figure 2.10: Mean cluster descent velocities vs. mean solid concentration compared with different experimental data (Liu & Lu 2009).

They concluded the presence of horse shoe shaped at the upward direction of flow and the downward clusters exhibit inverse-v shaped clusters. Lagrangian models have been modelled in fluidised beds to track single particle or a collection of particles. The model is sparsely used as though it simulates properly the particle clusters formation characteristic of circulating fluidised beds and prevalent in 2D models. There was good qualitative agreement at low restitution coefficient for a dense phase fluidised bed when comparing Eulerian and Lagrangian models; this shows the extension of kinetic theory of granular flow beyond dilute flow. The Eulerian-Eulerian model predicts the particle-particle interactions relatively, which shows its significance for industrial applications due to low computational demand. The drawback is the converging flow that fails to predict particle trajectory crossing effect in dilute systems (Chen & Wang 2014). Ibsen et al. (2004) concluded the superiority of Eulerian to discrete particle models with regards to computational time. Sufficient improvement in drag models would improve its ability to predict realistic hydrodynamics of CFB. The Eulerian-Eulerian model provides good approximation of the particle discretisation.

Jin et al. (2010) demonstrated Eulerian-Eulerian approach for Geldart B particles in a circulating fluidised bed. They studied the effect of restitution coefficients and specularly

coefficients on gas velocity, solids velocity, and solids volume fraction. A multiple phase Eulerian-Eulerian modelling in a circulating fluidised bed has been reported with good agreement with laser phase anemometry experimental measurements (Mathiesen et al. 2000). The model was made up of a single gas phase and three solid phases. It predicted the core-annular structure correctly with the solid concentration close to experimental values. A similar study extended it to six solid phases for close representation of particle size and non-uniform diameter distribution present in a circulating fluidised bed (C. Ibsen et al. 2001). They showed that the results correlate better with experimental values the more the number of Eulerian phases.

Zhang & VanderHeyden (2001) compared 3D vs 2D simulations with experimental measurements. As shown in Figure 2.11, the 2-D simulation under predicts the particle mass flux by a third compared to the 3-D model being as accurate as experimental results. They concluded the presence of meso-scale structures or clusters in circulating fluidised bed dynamics.



Figure 2.11: Time-averaged data of mas flux with superficial velocity of 1.1m/s for 3-D (0.645cmx0.645cmx1.33cm) and 2-D(0.645cmx1.333cm) simulations (Zhang & VanderHeyden 2001).

Drag models have been extensively studied for cases of Bubbling and circulating fluidised beds. The development of drag models started with the Ergun Equation to describe the interaction between gas-solid momentum in a packed bed. The nature of fluidised beds requires a more detailed drag model. Gidaspow et al. (1991) combined the correlation by

Wen & Yu (1966) and the Ergun & Orning (1949) to describe fluidised beds. This model has the capability to be implemented over a range of phases from dilute to dense beds. The problem with this model is in transitioning from dilute to dense phase; the model loses coherence. Circulating fluidised bed risers contains dense regions at the riser bottom/ near walls and dilute region at the top/core regions leading to clustering of particles.

Almuttahir & Taghipour (2008a) compared the different drag models of Syamlal & O'Brien (1987), Arastoopour et al. (1990), and Gidaspow et al. (1991) in circulating fluidised bed. These drag models do not consider the presence of meso-scale structures through provide good correlations with experimental data. Eulerian-Eulerian model using kinetic theory of granular flow has been implemented to predict solid clusters and there was good agreement with experiment for different fluidizing conditions (Almuttahir 2006). These meso-scale structures were predicted by Agrawal et al. (2001); they observed the need to be resolved in simulations to obtain accurate particle-drag, dissipation rate, particle pressure and effective particle viscosities. Syamlal & O'Brien (1987) considered the effect of meso-scale in predicting drag in a circulating bed. Li et al. (1993) implemented the energy minimisation multi scale (EMMS) to describe the different scales of clustering in circulating fluidised bed. The model showed the different heterogeneous regions in the riser. The EMMS and Wen Yu/Ergun was compared in a circulating fluidised bed using FLUENT (Yang et al. 2003). It predicted the homogeneous structure of the Wen Yu model in relation to the EMMS. The Gidaspow model did not predict the behaviour accurately. Gujjula & Mangadoddy (2015) compared the drag model from Arastoopour et al. (1990), Syamlal & O'Brien (1987), Gidaspow et al. (1991), and Gibilaro et al. (1985). The drag force predicted by Arastoopour et al. (1990) and Gibilaro et al. (1985) in areas of higher solid concentration (near walls and bottom region) were larger compared to the other models. Syamlal & O'Brien (1987) drag model was used extensively in this work due to its ability to predict the nature of flow in a circulating fluidised beds.

The Reynolds number in a circulating fluidised bed is considerably high. There is need to consider the effect of turbulence. The turbulence models have been implemented in very dilute flows. These models for gas turbulence are mostly derived from single phase flow applications. Neri & Gidaspow (2000) considered turbulence in a vertical pipe using the single equation model. Samuelsberg & Hjertager (1996b) used the large eddy simulation turbulence model to study the characteristics of a circulating fluidised bed. The gas-phase turbulence is modelled using the Sub-grid scale (SGS) model. The results agreed well with experimental finding excluding at the inlet due to the simplification of boundary conditions and inlet characteristics in the domain. Ibsen et al. (2001) evaluated a numerical model of a scaled gas-solid flow in circulating fluidised bed using the same SGS model as Samuelsberg

& Hjertager (1996b) . They compared 2D and 3D models with experimental measurement conducted with laser Doppler measurement. It shows that the nature of 2D models limits prediction of turbulence behaviour. Alves et al. (2001) used standard k-e model to analyse the effect of turbulence between phases. It predicted high concentration of particles at the wall and internal recirculation points in a CFB. Figure 2.12 compared models for turbulence with and without interface transfer with experimental data. The model without interface transfer underestimates the particle concentration. It shows qualitative agreement with experimental data better for particle concentration when interphase turbulence was considered in a 2D model. They concluded that better agreement could be achieved for 3D models.



Figure 2.12: Particle concentration predicted with and without turbulent transfer compared with experimental techniques (Alves et al. 2001).

The dispersed standard k-e model was used by Jin et al. (2010) to study the hydrodynamics of a CFB in Geldart B particles as stated earlier. Ansart et al. (2013) validated experimental measurement for pressure and mass flux with Eulerian model. They showed that the boundary conditions of wall and solid have an impact on the measurement of pressure and mass flux using the dispersed k-e model. This concluded the strength of k-e models to predict experimental measurements accurately. The several authors reviewed above implemented the k-e model for Eulerian-Eulerian phases due to its simplicity and reasonable

accuracy it provides with a wide array of turbulence flows. However, the effect of turbulence models is mostly observed in 3D models as turbulence has a 3D character attributed to it.

2.1.3. Governing equations

The governing equations are based on the principles of the laws of physics as mass, rate of momentum change, and energy are conserved in each control volume. The gas and particle phases are expressed as a continuous phase in the form of their properties modelled over spatial or time constraints. The energy conservation equation is discussed in the Heat modelling section.

2.1.3.1. Conservation of mass

The conservation of mass is the sum of the total mass entering the control volume to that of the mass leaving it. The concept of volume fraction is introduced to show the fraction each phase occupies within the volume. The rate of mass change in a control volume V and its surface Φ from a single particle perspective is given as (Armstrong 2011):

$$\frac{\partial}{\partial t} \int \rho \, dV + \int \rho (\vec{v} \cdot \vec{n}) \, d\Phi = \sum \text{external}, \quad (2.1)$$

where \vec{v} as phase velocity, and ρ as density. This equation is solved using divergence theorem to give the continuity equation for a single particle as follows:

$$\frac{\partial}{\partial t} (\rho) + \nabla(\rho \vec{v}) = \sum \text{external} \quad (2.2)$$

Therefore, the continuity equations for the solid and gas phase is adjusted with the introduction of volume fraction and the Source term S_i :

$$\frac{\partial}{\partial t} (\alpha_i \rho_i) + \nabla(\alpha_i \rho_i \vec{v}_i) = S_i \quad (i = \text{gas, solid}), \quad (2.3)$$

where α_i as volume fraction, and $S_i = S_{gs} = -S_{sg}$ as source term due to external influences (i.e. mass transfer or chemical reaction). The source term applies to heterogeneous char reaction in pyrolysis and gasification which changes the composition of the gas and particulate phase; the value is zero in the absence of external influences.

2.1.3.2. Conservation of momentum

According to Newton's 2nd law; the rate of change of momentum is directly proportional to the forces acting on it. The rate of momentum change per unit volume and its surface from a single fluid perspective is given as (Armstrong 2011):

$$\frac{\partial}{\partial t} \int \rho \vec{v} dV + \int \rho (\vec{v}\vec{v}) d\Phi = \sum \text{Body forces} + \text{surface forces} \quad (2.4)$$

The solving of this equation using the same process as the continuity equations gives the momentum equation for a single fluid:

$$\frac{\partial}{\partial t}(\rho \vec{v}) + \nabla(\rho \vec{v} \vec{v}) = -\nabla P + \nabla \bar{\tau} + \rho \vec{g}, \quad (2.5)$$

where $\bar{\tau}$ as stress tensors, p as pressure forces, and \vec{g} as gravitational force. The equation is adjusted with the addition of the volume fraction of phases and interaction between the particulate and gas phase. The source term is introduced for mass exchanges with regards to chemical reaction. The momentum equation for the gas and solid phases are given below:

$$\frac{\partial}{\partial t}(\alpha_g \rho_g \vec{v}_g) + \nabla(\alpha_g \rho_g \vec{v}_g \vec{v}_g) = -\alpha_g \nabla P + \alpha_g \nabla \bar{\tau}_g - \sum_{s=1}^N \beta(v_g - v_{si}) + \alpha_g \rho_g \vec{g} + \vec{S}_{g si} \vec{v}_g, \quad (2.6)$$

$$\frac{\partial}{\partial t}(\alpha_{sn} \rho_{sn} \vec{v}_{sn}) + \nabla(\alpha_{sn} \rho_{sn} \vec{v}_{sn} \vec{v}_{sn}) = -\alpha_{sn} \nabla P - \nabla P_{sn} + \alpha_{sn} \nabla \bar{\tau}_{sn} - \sum_{s,g=1}^N \beta(v_{s,g} - v_{sn}) + \alpha_{sn} \rho_{sn} \vec{g} + \vec{S}_{sn g} \vec{v}_{sn}, \quad (2.7)$$

where β represents gas-solid momentum exchanges, P_s represents the solid pressure and $\vec{S}_{gs} = -\vec{S}_{sg}$ is the source term which is zero when there are no external influences. The momentum equation requires constitutive equations as closure to describe the particulate phase that is implemented from by kinetic theory of granular flow.

2.1.3.3. Kinetic theory of granular flow

The analogy of kinetic theory of gases states that molecules randomly collide in a fixed space. It provides averaging techniques to determine the properties of a fluid. Particles have a similar inherent behaviour of random collisional and kinetic behaviour. The kinetic theory of granular flow implies that the random motion of particles is measured using granular temperature. This kinetic energy of particle is lost due to random oscillatory motion. This collision is measured using the coefficient of restitution of particles with zero being equal to an inelastic collisions and one is elastic collisions. There have been several applications of

kinetic theory to pneumatic conveying and circulating fluidised beds as discussed earlier. The granular particles have a collisional and kinetic behaviour; hence kinetic theory represent the fluid properties at a macroscopic scale. The different particle loading has to be considered in kinetic theory of granular flow. The collisional, kinetic and frictional need closure terms to account for the different phenomena. The conservative equation for the kinetic theory of granular flow is represented by Gidaspow (1994):

$$\frac{3}{2} \left(\frac{\partial}{\partial t} (\alpha_s \rho_s \theta_s) + \nabla (\alpha_s \rho_s \vec{v}_s \theta_s) \right) = (-P_s \bar{I} + \bar{\tau}_s) : \nabla \vec{v}_s - \nabla (k_{\theta_s} \nabla \theta_s) - \gamma_{\theta_s} + \phi_{gs} \quad (2.8)$$

The first term represents the energy generation in terms of pressure and stress forces. The second term which is the energy diffusion term represents the granular temperature vector and granular conductivity k_{θ_s} . The granular conductivity is made up of a kinetic term and collisional term for particle velocity fluctuation and particle collisions as follows:

$$k_{\theta_s} = \frac{150 \rho_s d_s (\theta_s \pi)^{1/2}}{384 (1 + e) g_o} \left[1 + \frac{6}{5} \alpha_s (1 + e) g_o \right]^2 + 2 \alpha_s^2 \rho_s d_s (1 + e) g_o \left(\frac{\theta_s}{\pi} \right)^{1/2} \quad (2.9)$$

The energy collision dissipation γ_{θ_s} term is taken into account from Ding & Gidaspow (1990):

$$\gamma_{\theta_s} = \frac{12(1 - e^2)}{d_s (\pi)^{1/2}} \alpha_s^2 \rho_s \theta_s^{3/2} \quad (2.10)$$

The energy exchange coefficient which represents the dissipation of fluctuating kinetic energy due to particle interaction ϕ_{gs} (Gidaspow (1994)):

$$\phi_{gs} = -3\beta\theta_s \quad (2.11)$$

2.1.3.3.1. Constitutive equations

The solid phase in Eulerian-Eulerian model requires closure equations for the conservation of momentum. The equations explain the flow dynamics of the gas and particulate phases based on the kinetic theory of granular flow.

Stress tensors for the viscous forces are related to the gradient velocity of the corresponding phases. The stress tensors for the gas phase and the solid phase are given in Equation (2.12) and Equation (2.13).

$$\bar{\tau}_i = \left(\lambda_i - \frac{2}{3} \mu_i \right) \lambda_i (\nabla \cdot \vec{v}_i) \bar{I} + 2 \mu_i \bar{S}_i \quad (2)$$

.12)

$$\bar{S}_i = \frac{1}{2}(\nabla \cdot \vec{v}_i + (\nabla \vec{v}_i)^T) \quad (2.13)$$

Bulk viscosity λ_i is accounted for in resistance to compression and expansion of particles to during random collisions. The bulk viscosity λ_g for the gas phase is zero as the compressibility of the gas is assumed negligible. The expression for bulk viscosity in the solid phase is given from Lun et al. (1984). The effect of shear viscosity μ_i is accounted for both phases. The gas shear viscosity is dependent on the viscosity of the laminar and the turbulence present in the system. Circulating fluidised beds have high Reynolds number and significant turbulence, therefore turbulence have to be considered. The shear viscosity of the gas is shown in Equation (2.14), which includes the laminar μ_l and turbulent viscosity μ_t .

$$\mu_g = \mu_l + \mu_t \quad (2.14)$$

$$\mu_t = C_\mu \alpha_g \rho_g \frac{k_g^2}{\varepsilon_g} \quad (2.15)$$

The turbulent viscosity μ_t is expressed based on the turbulent kinetic energy k and energy dissipation rate ε . The different regimes of friction, kinetic, and collisional are considered especially in complex gas-solid flows like fluidised beds. The shear viscosity of the solid is given as a combination of all the different regimes:

$$\mu_s = \mu_{kinetic} + \mu_{coll} + \mu_{fric} \quad (2.16)$$

The kinetic shear viscosity $\mu_{kinetic}$ generally considered in models for gas-solid flows has been applied to bubbling and circulating fluidised bed. Dilute flows are normally dominated by kinetic forces; as the particulate phase becomes dense there is a possibility of more random particle collisions which can be accounted for by the collisional shear viscosity. As the particulate phase becomes denser, friction occurs between the particles during collisions. The frictional shear viscosity μ_{fric} is accounted for as it nears the packing limit. The different correlations for the solid shear viscosity is given in Table 2.3.

Table 2.3: Correlations of the different viscosities of the solid phase

Viscosity term	Equation	Reference
Bulk viscosity	$\lambda_s = \frac{4}{3} \alpha_s \rho_s d_s g_o (1 + e_s) \left(\frac{\theta_s}{\pi}\right)^{1/2}$	Lun et al. (1984)
Kinetic viscosity	$\mu_{kinetic} = \frac{\alpha_s \rho_s d_s (\theta_s \pi)^{1/2}}{6(3 - e_s)} \left(1 + \frac{2}{5} (1 + e_s)(3e_s - 1) g_o \alpha_s\right)$	Syamlal et al. (1993)
Collisional viscosity	$\mu_{coll} = \frac{4}{5} \alpha_s \rho_s d_s g_o (1 + e_s) \left(\frac{\theta_s}{\pi}\right)^{1/2} \alpha_s$	Syamlal et al. (1993)
Frictional viscosity	$\mu_{fric} = \frac{p_s \sin \phi}{2(I_{2D})^{1/2}}$	Johnson et al. (1990)

Solid pressure is a form of pressure similar to the van der waals equation of state for gases. It is the pressure exerted on the wall by the particulate phase. It combines the kinetic and collisional aspects of the particle. The expression for solid pressure for more than two phases is given by Lun et al. (1984):

$$P_s = \alpha_s \rho_s \theta_s + \sum_{n=1}^N 2 \frac{d_{n,s}^3}{d_s^3} \alpha_s \rho_s g_o \alpha_n \theta_s (1 + e_{n,s}) \quad (2.17)$$

The kinetic term is deemed negligible in cases where there is a dense solid phase. This was proposed by Syamlal et al. (1993). The radial distribution function accounts for the probability of particle collisions when the solid phase concentration becomes dense. This parameter is prevalent in several constitutive equations and the correlations is given in Equation (2.18). The radial distribution function works better in dense regimes where the probability of collisions is adjusted. The several correlations have shown good agreement with experimental values especially in bubbling fluidised beds. Lun et al. (1984) model have shown its applicability with regards to dilute gas solid flows as presented in Armstrong (2011).

$$g_o(\alpha_s) = \left(1 - \left(\frac{\alpha_s}{\alpha_{s,max}}\right)^{1/2}\right)^{-1} + \frac{1}{2} d_{n,s} \sum_{n=1}^N \frac{\alpha_{n,s}}{d_{n,s}} \quad (2.18)$$

Drag models predict the momentum interphase exchanges β between the particles and the gas. There are different drag models used in computational fluid models. In a fluidised bed drag model is considered based on pressure drop of the bed or the drag coefficient C_D of a

single particle in the bed. Stokes introduced an analytical expression of drag model using the Reynolds number Re_s for solid spheres. These are represented in Equation (2.19) and Equation (2.20).

$$C_D = \frac{24}{Re_s} \quad (2.19)$$

$$Re_s = (1 - \alpha_s)\rho_g d_s \frac{(\vec{v}_s - \vec{v}_g)}{2\mu_g} \quad (2.20)$$

The drag coefficient has been modified to accommodate different flow regimes from very dilute to dense phenomena. The main drag models used to study gas-solid flow hydrodynamics are given in Table 2.4.

Table 2.4: Drag models for gas-solid momentum exchange

Drag models	Equations	Referen ce
Wen Yu	$\beta = \frac{3}{4} C_D \frac{\alpha_s \rho_g (\vec{v}_s - \vec{v}_g)}{d_s} \omega(\alpha) \text{ for } \alpha_g > 0.8$	
Gidaspow model	$\beta = \frac{3}{4} C_D \frac{\alpha_s \alpha_g \rho_g (\vec{v}_s - \vec{v}_g)}{d_s} \alpha_g^{-2.65} \text{ for } \alpha_g > 0.8$ $\beta = 150 \frac{\alpha_s^2 \mu_g}{d_s^2 \alpha_g} + 1.75 \frac{\alpha_s \rho_g (\vec{v}_s - \vec{v}_g)}{d_s} \text{ for } \alpha_g \leq 0.8$ $C_D = \frac{24}{\alpha_g Re_s} \left[1 + 0.15 (\alpha_g Re_s)^{0.687} \right]$	Gidaspow et al. (1991)
Syamlal Obrien model	$\beta = \frac{3}{4} \frac{\alpha_s \alpha_g \rho_g (Re_s)}{v_{r,s}^2 d_s} \frac{(\vec{v}_s - \vec{v}_g)}{v_{r,s}}$ $C_D = \left[0.63 + \frac{4.8}{v_{r,s} (Re_s)^{1/2}} \right]^2$ $v_{r,s} = 0.5 \left(A - 0.06 Re_s + \sqrt{A^2 + (0.06 Re_s)^2 + 0.12 Re_s (2B - A)} \right)$ $A = \alpha_g^{4.14} \quad B = \alpha_g^{2.65} \text{ for } \alpha_g > 0.8$ $A = \alpha_g^{4.14} \quad B = 0.8 \alpha_g^{1.28} \text{ for } \alpha_g > 0.8$	Syamlal & O'Brien (1987)
Gibilaro model	$\beta = \left(\frac{17.5}{Re_s} + 0.336 \right) \frac{\alpha_s \rho_g (\vec{v}_s - \vec{v}_g) \alpha_g^{-1.80}}{d_s}$	Gibilaro et al. (1985)

The Syamlal and O'Brien drag model was developed based on terminal velocities of single particles considering the drag force to be same as the buoyant weight. Therefore, the Archimedes number, which is a ratio of external to viscous forces, is the same for single and multiparticle as the terminal velocity. The expression relates void fraction with settling velocities. This model was used extensively due to its applicability to display particle clustering near the walls.

In fluid dynamics model with a polydisperse phase, the interactions between different solids have to be taken into consideration. The solid –solid momentum exchange is implemented from Syamlal (1987) based on the expression given below:

$$\beta_s = \frac{3(1+e)\left(\frac{\pi}{2} + C_{fr,sn} \frac{\pi^2}{8}\right) \alpha_s \rho_s \alpha_n \rho_n (d_s + d_{n,s})^2 g_o(\alpha_{s,n})}{2\pi(\rho_s d_s^3 + \rho_n d_{n,s}^3)} |\vec{v}_s - \vec{v}_{s,n}|, \quad (2.21)$$

where β_s represents solid-solid momentum exchanges, and $C_{fr,sn}$ is coefficient of friction between the s^{th} solid phase and the n^{th} solid phase.

2.1.3.4. Turbulence models

The flow in a control volume is either laminar or turbulent. The turbulent model provides a closure in the momentum equation to obtain the Reynolds stress. There are different varieties of turbulence model but the most widely used is the k-ε model. These models solve the equation through the introduction of the turbulence kinetic energy and turbulence dissipation rate. The turbulence is modelled as a standard k-ε two equation model for better flow prediction in pipes, it takes swirl into account and has the dissipation rate improved. This improvement will provide a detail description of turbulence especially in the tubular reactor such as the one subject of this study, the flow is expected to be highly turbulent around the gas stripping pipe associate with sudden pressure drop and swirling effect. It is very applicable in fully turbulent flow especially gas-solid flows. The equations for the standard k-ε model is represented below (ANSYS 2009):

$$\frac{\partial}{\partial t} (\rho k) + \frac{\partial}{\partial x_i} (\rho k \vec{v}_i) = \frac{\partial}{\partial x_j} \left[\left(\mu + \frac{\mu_t}{\sigma_k} \right) \frac{\partial k}{\partial x_j} \right] + G_k + G_b - \rho \varepsilon - Y_M + S_k, \quad (2.22)$$

$$\frac{\partial}{\partial t} (\rho \varepsilon) + \frac{\partial}{\partial x_i} (\rho \varepsilon \vec{v}_i) = \frac{\partial}{\partial x_j} \left[\left(\mu + \frac{\mu_t}{\sigma_\varepsilon} \right) \frac{\partial \varepsilon}{\partial x_j} \right] + C_{1\varepsilon} \frac{\varepsilon}{k} (G_k + C_{3\varepsilon} G_b) - C_{2\varepsilon} \rho \frac{\varepsilon^2}{k} + S_\varepsilon, \quad (2.23)$$

$$G_k = \mu_t (\nabla \cdot \vec{v}_k + (\nabla \vec{v}_k)^T) : \vec{v}_k, \quad (2.24)$$

where μ_t is turbulence viscosity, k is the turbulence kinetic energy, ε is the turbulence kinetic energy's dissipation rate, G_k is the generation of turbulence kinetic energy due to the

mean velocity gradients, G_b is the generation of turbulence kinetic energy due to buoyancy, Y_M represents the contribution of the fluctuating dilatation in compressible turbulence to the overall dissipation rate, $C_{1\varepsilon}$, $C_{2\varepsilon}$, and $C_{3\varepsilon}$ are constants, σ_k and σ_ε are the turbulent Prandtl numbers for k and ε , S_k and S_ε are user-defined source terms. The Re-Normalisation Group (RNG) model is a refined version of the standard model. It contains additional terms to improve accuracy in strained flows, enhances the effect of swirl, and has analytical formula values for turbulent Prandtl numbers rather than constants. The equations for the RNG k- ε model is represented below (ANSYS 2009):

$$\frac{\partial}{\partial t} (\rho k) + \frac{\partial}{\partial x_i} (\rho k u_i) = \frac{\partial}{\partial x_j} \left(\alpha_k \mu_{eff} \frac{\partial k}{\partial x_j} \right) + G_k + G_b - \rho \varepsilon - Y_M + S_K \quad (2.25)$$

$$\frac{\partial}{\partial t} (\rho \varepsilon) + \frac{\partial}{\partial x_i} (\rho \varepsilon u_i) = \frac{\partial}{\partial x_j} \left(\alpha_k \mu_{eff} \frac{\partial \varepsilon}{\partial x_j} \right) + C_{1\varepsilon} \frac{\varepsilon}{k} + (G_k + C_{3\varepsilon} G_b) - C_{2\varepsilon} \rho \frac{\varepsilon^2}{k} - R_\varepsilon + S_\varepsilon \quad (2.26)$$

While the standard - model is a high Reynolds number model, the RNG theory provides an analytically- derived differential formula for effective viscosity that accounts for low Reynolds number effects. These features make the RNG model more accurate and reliable for a wider class of flows than the standard model. The realizable model contains an alternative formulation for the turbulent viscosity. A modified transport equation for the dissipation rate, has been derived from an exact equation for the transport of the mean-square vorticity fluctuation. Realizable defines that the model satisfies certain mathematical constraints on the Reynolds stresses, consistent with the physics of turbulent flows. The equations for the realizable k- ε model is represented below (ANSYS 2009):

$$\frac{\partial}{\partial t} (\rho k) + \frac{\partial}{\partial x_j} (\rho k u_j) = \frac{\partial}{\partial x_j} \left[\left(\mu + \frac{\mu_t}{\sigma_k} \right) \frac{\partial k}{\partial x_j} \right] + G_k + G_b - \rho \varepsilon - Y_M + S_K \quad (2.27)$$

$$\frac{\partial}{\partial t} (\rho \varepsilon) + \frac{\partial}{\partial x_j} (\rho \varepsilon u_j) = \frac{\partial}{\partial x_j} \left[\left(\mu + \frac{\mu_t}{\sigma_\varepsilon} \right) \frac{\partial \varepsilon}{\partial x_j} \right] + \rho C_{1\varepsilon} S_\varepsilon - \rho C_{2\varepsilon} \frac{\varepsilon^2}{k + \sqrt{\nu \varepsilon}} + C_{1\varepsilon} \frac{\varepsilon}{k} C_{3\varepsilon} G_b + S_\varepsilon \quad (2.28)$$

$$C_1 = \max \left[0.43, \frac{\eta}{\eta + 5} \right], \quad \eta = S \frac{k}{\varepsilon}, \quad S = \sqrt{2S_{ij}S_{ij}} \quad (2.29)$$

The turbulence models for gas-solid phases are normally divided into mixture, dispersed and per phase formulations. The mixture model uses an averaging method and is mostly suitable for phases with similar properties. Also, the model ignores interphase momentum transfer therefore not suitable for non-interpenetrating phases (Hartge et al. 2009). The per-phase approach describes each phase separately and applicable to cases where turbulence transfer plays a major role, it has no assumptions or limitations. The problem with the model

is its reliability as transport equations were originally developed for fluid phases. Therefore, uncertain to use them directly without modification for solid phases. The dispersed model is based on a dispersion theory of discrete particles by homogeneous turbulence (Hinze 1975). The assumptions in the dispersed model is applicable for cases where the inter-particle collisions are limited. This formulation is suitable for dilute suspension where motion of phases are dominated by the gas phase and the dispersed phase is estimated using characteristics ratio as is the case of this study (Hartge et al. 2009) .

The Large eddy simulation (LES) model is a filtered model which resolves only large eddies directly and models small eddies. This model provides a detailed representation of two phase flows in comparison to experimental data. It characterises the different regions in a two phase flow and considered valuable for complex industrial system. The LES conservation equations have been modified to include filtered terms are given as:

$$\frac{\partial}{\partial t}(\tilde{\alpha}_i \rho_i) + \nabla(\tilde{\alpha}_i \rho_i \tilde{v}_i) = 0 \quad (2.30)$$

$$\frac{\partial}{\partial t}(\tilde{\alpha}_i \rho_i \tilde{v}_i) + \nabla(\tilde{\alpha}_i \rho_i \tilde{v}_i \tilde{v}_i) = -\tilde{\alpha}_g \nabla \tilde{P} + \tilde{\alpha}_g \nabla \tilde{\tau}_g - \sum_{s=1}^N \beta(\tilde{v}_g - \tilde{v}_s) + \alpha_g \rho_g \tilde{g} + \nabla^2(\alpha_g \tilde{v}_i) \quad (2.31)$$

Sub grid scale models are used to define the filtered stresses based on Boussinesq hypothesis. In ANSYS Fluent there are different LES models offered such as the Smagorinsky-Lilly model, the dynamic Smagorinsky-Lilly model, the WALE model, and the dynamic kinetic energy subgrid-scale model. The stress tensor term $\tilde{\alpha}_g \nabla \tilde{\tau}_g$ is modified as a filtered form termed as the subgrid stress tensor. The Smagorinsky-lilly model implies that the eddy viscosity is proportional to characteristic length and to the turbulent velocity centred on second invariant of the filtered-field deformation (Luo et al. 2013).

$$T_{ij,f} = 2\mu_t \tilde{S}_{ij} + \frac{1}{3} T_{ii} \delta_{ij}, \quad (2.32)$$

$$\mu_t = \rho_f (C_s \Delta)^2 \sqrt{2\tilde{S}_{ij}\tilde{S}_{ij}} \quad \tilde{S}_{ij} = \frac{1}{2} \left[\frac{\partial \tilde{U}_i}{\partial x_j} + \frac{\partial \tilde{U}_j}{\partial x_i} \right], \quad \Delta = (\Delta x \Delta y \Delta z)^{1/3}, \quad (2.33)$$

$$C_s \approx (3C_K/2)^{-3/4} / \pi, \quad (2.34)$$

where μ_t is turbulent viscosity, \tilde{S}_{ij} deformation tensor of the filtered field, Δ is deformation tensor of the filtered field and characteristic length scale, C_s is the constant and C_K is Kolmogorov constant. Turbulence is heavily influenced by walls; these wall bounded flows

need to consider its effect in the near-wall region. The near-wall region is subdivided into three layers: the viscous layer which is the innermost layer, fully-turbulent layer which is the outermost layer, and buffer layer which is the interim layer. These subdivisions are illustrated in Figure 2.13.



Figure 2.13: Sub-divisions of the near wall-region (ANSYS 2009).

The approach to modelling near wall region is through using wall functions or near wall treatment. These wall functions are semi empirical formulas that bridge the viscous sub layer and buffer region with the fully turbulent region without it being resolved. These provides the need not to modify turbulence models to account for the presence of walls. The standard wall function is based on Launder & Spalding (1974) gives good prediction of the wall effect for high Reynolds number and can be extended to non-equilibrium cases. They are reliable as long as the flow is within ideal conditions. The equations for standard wall function are given below:

$$U^* = \frac{1}{\kappa} \cdot \ln(Ey^*) \quad \text{at } 11.225 < y^* < 300, \quad (2.35)$$

$$U^* \equiv \frac{\rho U_p C_{1\varepsilon}^{0.25} K_p^{0.50}}{\tau_\omega}, \quad (2.36)$$

$$y^* \equiv \frac{\rho y_p C_{1\varepsilon}^{0.25} K_p^{0.50}}{\mu}, \quad (2.37)$$

$E = 9.793$ represents empirical constant, $K = 0.4187$ is the Von Kármán, U^* is the non-dimensional mean velocity of the flow at the wall, U_p is the mean velocity at the nodal point P of the wall-adjacent cell, y^* is the non-dimensional distance from the wall, y_p is the distance between the point P and the wall. In the viscous sublayer ($y^* < 11.225$) the value of the mean velocity is:

$$U^* = y^* \quad (2.38)$$

In non-equilibrium cases where the effects of pressure gradient and strong non-equilibrium lead to unideal conditions the near wall treatment is applicable. The near wall models have the viscous layer and the buffer region resolved using near wall mesh. The enhanced wall treatment suggested by Kader (1981) combines the two layer model and the enhanced wall functions. The equations for the enhanced wall treatment is as follows:

$$u^+ = e^\Gamma u_l^+ + e^{1/\Gamma} u_t^+ \quad (2.39)$$

$$\Gamma = -a \left(\frac{y^+}{1 + by^+} \right)^4, \quad (2.40)$$

$$\frac{du^+}{dy^+} = \frac{e^\Gamma du_{lam}^+}{dy^+} + \frac{e^{1/\Gamma} du_{turb}^+}{dy^+}, \quad (2.41)$$

where the + signifies a dimensionless quantity with the longitudinal and vertical flow velocity components, Γ is the blending function, a and b are constants respectively with values 0.01 and 5.00, and e is the natural logarithm constant. The method agrees for the fully turbulent law to be adapted to take into account certain effects such as pressure gradients and non-equilibrium conditions.

2.1.4. Boundary conditions

The solving of the kinetic theory of granular flow equations require boundary condition to function. Boundary conditions are essential for solving the partial differential equation describing the gas-solid flow. A no-slip boundary condition is used for the gas flow in an impenetrable wall, this different for the solid phase. The solid phase velocity normal to the wall is at zero and wall shear condition for the particles is introduced based on Johnson & Jackson (1987) :

$$u_{s_i,w} = - \frac{6\mu_{s_i} \alpha_{s,max}}{\sqrt{3\theta_{s_i} \pi \phi \rho_s \alpha_{s_i} g_{0,s_i s_i}}} \frac{\delta u_{s_i,w}}{\delta n} \quad (2.42)$$

The granular temperature is represented through the flux and generation terms to the energy dissipation due to collision caused by the wall-particle:

$$\theta_{s_i} = -\frac{k_{s_i}\theta_{s_i}}{\gamma_w} \frac{\delta\theta_{s_i,w}}{\delta n} + \frac{\sqrt{3}\pi\varphi\rho_s\alpha_{s_i}u_{s_i,slip}^2g_{0,s_i s_i}\theta_{s_i}^{\frac{3}{2}}}{6\alpha_{s,max}\gamma_w}, \quad (2.43)$$

$$\gamma_w = \frac{\sqrt{3}\pi(1 - e_{s_i,w}^2)\rho_s\alpha_{s_i}g_{0,s_i s_i}\theta_{s_i}^{\frac{3}{2}}}{4\alpha_{s,max}}, \quad (2.44)$$

where φ is the specularity coefficient and $e_{s_i,w}$ is the particle–wall restitution coefficient. The particle–wall restitution coefficient and the specularity coefficient are significant in determining the dynamics of particles at the wall region. The specularity coefficient is introduced based on a smooth or frictionless wall boundary condition where a value of one relates to a rough wall. The boundary condition at the solid/gas outlet is assumed at atmospheric pressure for all cases in this report.

2.2. Heat transfer model

2.2.1. Conservation of energy

The rate of change of energy is equal to the sum of added heat rate and the work carried on the fluid. The enthalpy is used to express the energy conservation equation of both phases as follows:

$$\left(\frac{\partial}{\partial t}(\alpha_g\rho_g h_g) + \nabla(\alpha_g\rho_g\vec{v}_g h_g)\right) = \alpha_g \frac{dp}{dt} + \bar{\tau}_g : \nabla\vec{v}_g + \nabla k_{eff,g} \nabla T_g - \nabla\vec{q}_g + Q_{gs} + S_{gs} h_g, \quad (2.45)$$

$$\left(\frac{\partial}{\partial t}(\alpha_{sn}\rho_{sn} h_{sn}) + \nabla(\alpha_{sn}\rho_{sn}\vec{v}_{sn} h_{sn})\right) = \alpha_{si} \frac{dp}{dt} + \bar{\tau}_{si} : \nabla\vec{v}_{si} + \nabla k_{eff,s} \nabla T_s - \nabla\vec{q}_{si} + Q_{sgi} + S_{sig} h_{si}, \quad (2.46)$$

where h_g is the specific enthalpy of the gas phase, \vec{q}_i is the heat flux, Q_{gs} and Q_{sg} is the intensity of heat exchange between the gas and solid phases and S_{gs} is zero with no external influences. k_{eff} is the effective thermal conductivity of the phases given below with the turbulent Prandtl number set at 0.85:

$$k_{eff} = k + \frac{c_p^t}{pr^t} \quad (2.47)$$

The intensity of heat exchange Q_{gs} is given as the temperature difference between the two phases as:

$$Q_{gs} = -Q_{sgi} = a_{gs}h_{gs}(T_g - T_s) \quad (2.48)$$

The specific enthalpy of the individual phases in the mixture is given from:

$$h(T) = H_{f,0} + \int_{298.15}^T C_p dT \quad (2.49)$$

The specific heat capacity C_p is the measure of the energy required to change the species temperature of 1kg of material by 1°C. The heat of formation $H_{f,0}$ is the energy needed for the formation of 1 mole of a substance in its standard state from its constituent element at standard state.

2.2.2. Heat transfer coefficients

The convective heat transfer coefficient h_{sg} between the particles and gas is expressed as:

$$h_{sg} = \frac{6k_g\alpha_g\alpha_s Nu_s}{d_p^2}, \quad (2.50)$$

where Nu_s is the Nusselts number and k_g is the thermal conductivity of gas. The thermal conductivities of a phase are used to describe the phase's ability to conduct heat. This is given for a mixture of species as:

$$k_g = \sum_j \frac{x_j k_j}{\sum_j x_j \phi_j}, \quad (2.51)$$

$$\phi_j = \left[1 + \left(\frac{\mu_i}{\mu_j} \right)^{1/2} \left(\frac{mw_i}{mw_j} \right)^{1/4} \right] \left[8 \left(1 + \frac{mw_i}{mw_j} \right) \right]^{1/2}, \quad (2.52)$$

where, x_j is the mass fraction of the individual species in the phases and mw_j is the molecular weight of species. The Nusselts number is estimated from the correlation which includes the Reynolds Re and Prandtl number Pr (Gunn 1978):

$$Nu_s = (7 - 10\alpha_g + 5\alpha_g^2) \left(1 + 0.7Re_s^{0.2}Pr^{\frac{1}{3}}\right) + (1.33 - 2.4\alpha_g + 1.2\alpha_g^2)Re_s^{0.7}Pr^{\frac{1}{3}} \quad (2.53)$$

This correlation is applicable for multiphase flow with wide range of porosity in the range of 0.35-1 and Reynolds number less than 10^5 . The prandtl number is calculated from the equation below:

$$Pr = \frac{c_{p,g}\mu_g}{k_g} \quad (2.54)$$

2.2.3. Radiation model

Electromagnetic radiation is emitted continuously due to molecular and atomic agitation connected to its internal energy. The emitted radiation within the wavelength range of 10–1 μ m and 103 μ m is termed as thermal radiation. Thermal radiation affects pyrolysis and gasification due to their dependence on temperature for chemical reactions. The thermal radiation is given as:

$$Q_{rad} = \sigma(T_{max}^4 - T_{min}^4) \quad (2.55)$$

This shows that radiation is significant in high absolute temperature difference levels such as combustion and solar induced processes. The governing equation for radiation transfer is shown in Equation (2.56).

$$\frac{dI(\vec{r}, \vec{s})}{ds} = -(a + \sigma_s)I(\vec{r}, \vec{s}) + a\frac{\sigma T^4}{\pi} + \frac{\sigma_s}{4\pi} \int_0^{4\pi} \Phi(\mathbf{s}', \mathbf{s})I(\mathbf{r}, \mathbf{s}')d\Omega', \quad (2.56)$$

where a the absorption coefficient, σ_s is the scattering coefficient, $(a + \sigma_s)$ is the extinction coefficient (optical thickness), I is the radiation intensity, Φ is the phase function, and Ω' is the solid angle. The radiation transfer need to be solved with the governing Navier stokes equations. There have been different methods for solving the radiative transfer equation such as the P1 method, monte-carlo method, discrete transfer and discrete ordinate method. The discrete ordinate (DO) method is used to solve the radiative transport equation over an entire range of optical thicknesses and has the ability to solve a range of radiation problems

from surface-to-surface to participating radiation. The radiative transfer equation (RTE) is solved in the \vec{s} direction:

$$(\vec{s} \cdot \nabla)I(\vec{r}, \vec{s}) + (a + \sigma_s)I(\vec{r}, \vec{s}) = a \frac{\sigma T^4}{\pi} + \frac{\sigma_s}{4\pi} \int_0^{4\pi} \Phi(\mathbf{s}', \mathbf{s})I(\mathbf{r}, \mathbf{s}')d\Omega' \quad (2.57)$$

The transport equation is then solved for a set of discrete solid angles directions represented by its direction cosines spanning the total solid angle.

2.3. Reaction model

2.3.1. Literature review

2.3.1.1. Pyrolysis

2.3.1.1.1. Drying kinetic model

The drying process is the initial stage of a pyrolysis process occurring from 100-200C before the pyrolysis process. Generally, biomass has a higher water content than fossil fuels or municipal solid waste. The drying models have been categorised into three different types; heat sink model, equilibrium model and first order rate model.

The first order rate kinetic model assumes the rate of drying as a chemical reaction. The model ignores condensation and evaporation is independent of saturation pressure. Chan et al. (1985) modelled biomass drying in the pyrolysis of using an Arrhenius type chemical reaction.



$$r_{h_2o} = 0 \quad T < 95^\circ C \quad (2.59)$$

$$r_{h_2o} = k\rho_m \quad T > 95^\circ C \quad (2.60)$$

$$k = A \exp\left(\frac{-E}{RT}\right), \quad (2.61)$$

where k is the Kinetic constant, A is the Arrhenius constant, E is the Activation energy, R is the gas constant, T is the temperature. The rate parameters used for drying were $A = 5.13 \times 10^6$ and $E = 88 \text{ KJ/mol}$. This resulted in a higher temperature for optimum drying. This was adjusted by modifying the pre-exponential factor to achieve drying between 100°C

and 120°C (Bryden et al. 2002). Tinaut et al. (2008) used a similar model for a one dimensional drying model in a biomass gasifier and combustor. Miltner et al. (2008) has analysed from TGA measurements drying of biomass which is assumed as a first order reaction. The model was extended to include the effect of biomass solid temperature. This model increases computational time when coupled with pyrolysis reactions; thus convergence is difficult to be achieved.

Heat sink model implies that drying occurs at boiling temperature and is mainly dependent on heat transfer. Peters et al. (2002) used a constant evaporation model based on a thermodynamic balance of the amount of energy for evaporation and the amount evaporated. The terms are given below:

$$r_{h_2o} = \begin{cases} \frac{(T - T_{vap})\rho c_p}{H_{vap}\delta t} & \text{if } T \geq T_{vap}, \\ 0 & \text{if } T < T_{vap} \end{cases} \quad (2.62)$$

where, r_{h_2o} is the vaporisation rate, H_{vap} is the evaporation enthalpy, and T_{vap} is the evaporation temperature. Equilibrium models depends on both heat and mass transfer. The evaporation/condensation model was earlier implemented by Blasi (2004) as a process dependent on diffusion as follows:

$$H_2O_{(l)} \rightarrow H_2O_{(g)}, \quad (2.63)$$

$$r_{H_2O} = k_d \cdot S \cdot (C_{w,s} - C_{w,g}), \quad (2.64)$$

$$S = \frac{2\rho_s r_p}{\rho_{biomass}(r_p^2 - r_{p,in}^2)}, \quad (2.65)$$

where, k_d is the mass transfer coefficient, ρ_s is the bulk density of biomass in the bed, $\rho_{biomass}$ is the density of biomass wall, r_p is the external radius of the biomass, $r_{p,in}$ is the internal radius of the hollow biomass, $C_{w,s}$ is the concentrations of moisture at the biomass surface $C_{w,g}$ is the concentrations of moisture in the gas.

Jurena et al. (2009) modified the drying rate including the moisture mass fraction $Y_{h_2o,s}$ to prevent shock fluctuations in the rate when the moisture has evaporated completely from the solid as follows:

$$r_{H_2O} = k_d \cdot S \cdot (C_{w,s} - C_{w,g}) Y_{H_2O,s}, \quad (2.66)$$

In this study, a drying model similar to Kaushal et al. (2011) and Hassan (2013) is adopted. The drying occurs as a mass transfer process from liquid to gas at temperatures greater than the saturation temperature (100°C). The method retains heat and mass transfer characteristics associated with drying without the complexity of reactions when compared to other drying models. The model simplifies certain aspects of drying process which are considered in the diffusion dependent model discussed earlier for modelling purposes to ease convergence and fasten numerical solution.

$$r_{H_2O} = k_d \times \alpha_m \rho_m \frac{(T - T_{sat})}{T_{sat}} \text{ at } T > T_{sat}(100^\circ\text{C}), \quad (2.67)$$

where, \dot{r} is the mass transfer rate from the liquid phase to the vapour phase, α_m and ρ_m are the volume fraction and density of liquid moisture respectively, T is the vapour phase temperature and T_{sat} is the saturation temperature.

2.3.1.1.2. Pyrolysis kinetic models

The pyrolysis of biomass undergoes many complex reactions; its kinetics are not very precise. The reactions are heavily interlinked making modelling them difficult, this complexity is simplified by kinetic models. Several researchers developed kinetic models to usually account for the primary reactions only or with secondary reactions.

Kinetic models represent pyrolysis reactions and physical factors in mathematical representation. Several other factors affect the kinetic models of the process even with experimental analysis. The single step model considers pyrolysis as being a first order single reaction, the final products are the volatiles and fixed char (see Figure 2.14).

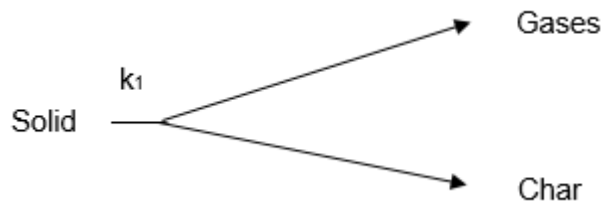


Figure 2.14: Single Step Pyrolysis Reaction (Prakash & Karunanithi 2009).

Bamford et al. (1946) produced the earlier use of pyrolysis single order model of wood assuming an isenthalpic process. The single reaction is given by:

$$\frac{dm}{dt} = mA \exp\left(\frac{-E}{RT}\right), \quad (2.68)$$

where, m is the mass of reactant. Investigations by Bilbao et al. (1996) have showed a good trend with predicted and experimental results using wet wood as a starting material and a single step kinetic model. The single step model has also been validated experimentally using thermo-gravimetric analysis with cellulose (Antal & Varhegyi 1995). Boateng & Mtui (2012) used the model for biomass pyrolysis and modified the kinetics from coal pyrolysis using pre-exponential constants. They seemed reasonable to provide accurate results and reduce computational time required for other complex models.

Parallel reactions model is made up of independent pyrolysis reactions occurring parallel to each other. Tinney (1965) studied the decomposition of wooden dowels in a furnace using a two parallel first order reaction. He observed a change in activation energy, reaction-velocity constant, and heat of reaction with the decomposition of structural constituents of wood.

However, Many et al. (2003) reformulated thermal decomposition of sugar cane bagasse to a three-parallel reaction model; thermo-gravimetric curves showed a misfit with earlier experimental results by several researchers at low heating rates with only cellulose. This explained the presence of lignin decomposition reactions as the third pseudo component.

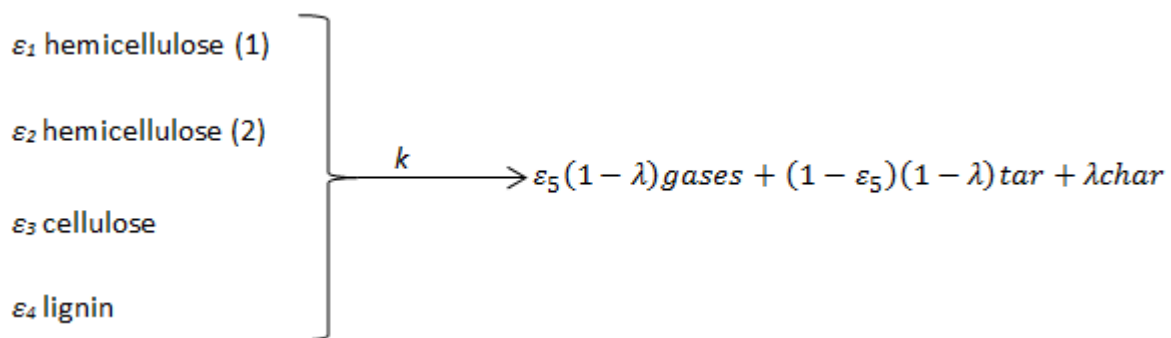


Figure 2.15: Three-Parallel reaction model (Prakash & Karunanithi 2009).

Grønli (1996) developed a four parallel model using birch wood as biomass material as represented in Figure 2.15. This model has five predetermined mass fraction values, the four values are given in Table 2.5 and the final value ϵ_5 is 0.68. The char fraction λ is assumed

to be constant at 0.21. The disadvantage of the parallel model is the Heat of reaction and stoichiometric coefficients have to be arbitrary chosen in advance and a constant char yield assumed. The parallel model was used by Xue et al. (2012) to describe in biomass fast pyrolysis using the Eulerian-Eulerian model.

Table 2.5: Chemical kinetics of Parallel reaction model (Larfeldt et al. 2000)

Reactions	E(KJ/mol)	A (s ⁻¹)	fractions
Hemicellulose 1	159.2	7.24x10 ¹²	0.11
Hemicellulose 2	118.2	1.26x10 ⁸	0.29
Cellulose	287.6	7.59x10 ²¹	0.31
Lignin	49.9	1.12x10	0.09

The competing model has the char yield varying in the primary reactions. The reactions are assumed to occur at a narrow temperature range.

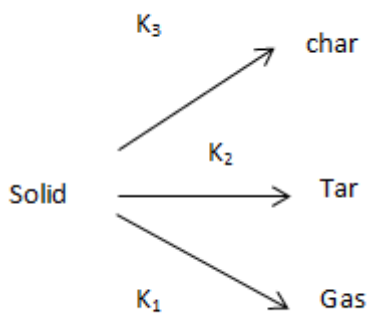


Figure 2.16: Competing Reaction Model (Thurner & Mann 1981).

Thurner & Mann (1981) studied pyrolysis in sawdust Oakwood using the competing reactions at 300-400 °C (see Figure 2.16). It showed that pyrolysis reactions are the rate controlling step within this temperature range. At higher temperature, he observed that the reaction is controlled mainly by effective thermal and mass diffusivities. The rate equation for the competing reaction is represented below:

$$\frac{dY_i}{dt} = -k_i Y_i, \quad (2.69)$$

where, Y_i is the fraction of component, and k_i is the kinetic rate of component. They showed that the fraction of pyrolysis gases, mainly CO_2 and CO , increase at higher temperatures and short residence times; this was validated by experimental results. The chemical kinetics of the competing reaction is given in Table 2.6.

Table 2.6: Chemical kinetics of competing reaction model (Turner & Mann 1981)

Reactions	E(KJ/mol)	A (s ⁻¹)
k_1	84	5.16×10^6
k_2	112.7	1.48×10^{10}
k_3	106.5	2.66×10^{10}

Ranganathan & Gu (2016) used the competing, parallel, and a detailed chemistry of the parallel scheme. A similar detailed chemistry model was used by Mellin et al. (2014) to model a pyrolysis process using CFD. These advanced models provided more accuracy though they contain several equations, which when incorporated to CFD models they lead to a computational expense and complex models.

2.3.1.2. Secondary reactions

The review of the existing literature indicted a single, competing, and parallel chemical kinetics models are weak alone as they ignore the complexities of the secondary reactions. The secondary reactions of biomass pyrolysis describe the thermal tar cracking reactions. The rate equation for the secondary reaction is represented below:

$$\frac{dC}{dt} = -k_i C_{tar,i} \quad (2.70)$$

The different kinetics for the secondary reactions with different biomass is given in Table 2.7. The kinetics of thermal cracking of tar was studied by Kosstrin (1980) in a fluidised bed regime. They reported Arrhenius constant of 3.26×10^4 and activation energies of 72.8KJ/mol at isothermal conditions. Boroson et al. (1989) assumed tar breakdowns into gases and inert tar. Rath et al. (2002) predicted the composition of the tar inert to be 22% with remaining being the non-condensable gas composition. Diebold (1985) and Liden et al. (1988) also predicted their results under a fluidised bed condition. Fagbemi et al. (2001) predicted general kinetics of tar independent on biomass type. Their predictions were lower than other

model shown in Table 2.7 . It also showed the dependence of the kinetics on the biomass type, conditions, and geometry.

Table 2.7: Kinetics of secondary reaction

Tar origin	A (s^{-1})	E (kJ/mol)	Reference
Spruce wood	3.076×10^3 1.13×10^6	66.3 109	Rath & Staudinger (2001)
Poplar wood	4.28×10^6	107.5	Liden et al. (1988)
Cellulosic biomass	1.55×10^5	87.6	Diebold (1985)
Biomass	4.43	23.4	Fagbemi et al. (2001)
Hard wood	$10^{4.98}$	99.3	Boroson et al. (1989)
Beech wood	$10^{5.14}$	99.3	Rath et al. (2002)

In order to improve the predictive capabilities of pyrolysis models, researchers tend to compile the primary models to secondary reactions. As an example, Chan et al. (1985) assimilated the competing model with the secondary cracking and dehydration reactions as shown in Figure 2.17. This model was used by Papadikis et al. (2009) to describe particle shrinkage during biomass pyrolysis in a Eulerian-Eulerian multiphase flow. The secondary reaction used a model by Liden et al. (1988). Sharma et al. (2015) also used the same model for a multiphase reactive model to predict devolatilisation.

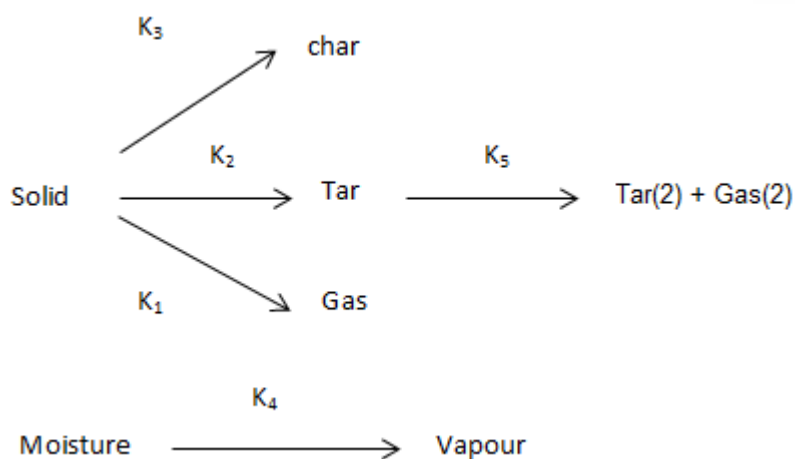


Figure 2.17. Competing and Parallel Model with Secondary Tar Cracking (Sinha et al. 2000).

Another model incorporating secondary reactions is the so called Koufopoulos model. This is a two-step reaction model-relating rate of pyrolysis to composition (Prakash & Karunanithi 2009). The first order model described all the reactions in this model. The model is given in Figure 2.18.

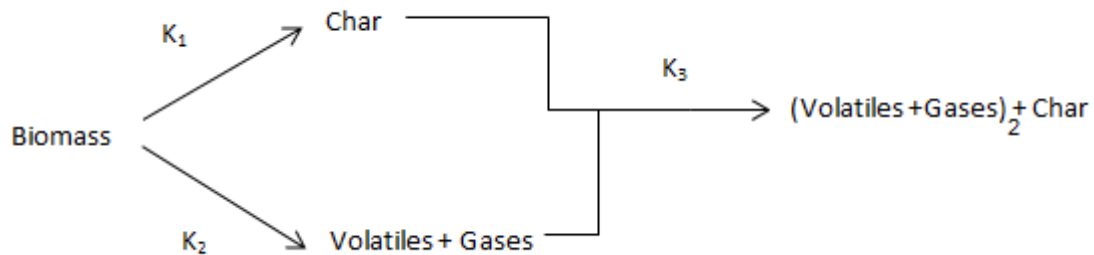


Figure 2.18. Single step primary reaction with secondary reactions (Prakash & Karunanithi 2009).

The global multi-step competing mechanism approach is simplified as the broido-shafizadeh model (Di Blasi 1996). An active solid is formed before polymerization reactions as given in Figure 2.19.

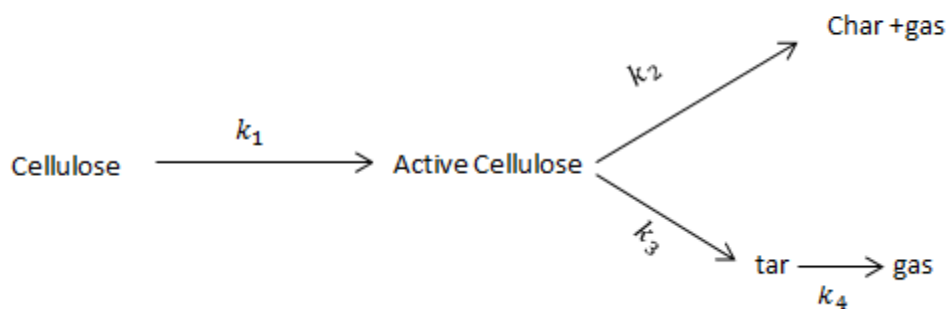
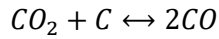


Figure 2.19. Broido-shafizadeh Multi-step Scheme (Di Blasi 1996).

2.3.1.3. Gasification

2.3.1.3.1. Boudouard reaction

This reaction is given by:



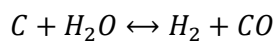
The kinetics of boudouard reaction has been studied for different biomass samples of pine, eucalyptus, and sugarcane bagasse chars in circulating fluidised bed conditions (Cetin et al. 2005). He found that pressure has no effect on the reactivity of the char conversion process. The different kinetics char reactions for different biomass samples are represented in Table 2.8. It is observed that at low temperature CO inhibition occurs lowering the gasification rate of the boudouard reaction (Mitsuoka et al. 2011):

Table 2.8. Kinetics of boudouard reaction

Char reaction	A(s ⁻¹ bar ⁻ⁿ)	E(kJ/mol)	n	Equation	Reference
Olive residue(0.15mm)	168.28	133.33	0.43	$\frac{dX}{dt} = r_b F(X)$	Ollero et al. (2003)
Cotton trash	36.2	77.32	1	$\frac{dX}{dt} = r_b F(X)$	Pasangulapati (2012)
Birch Wood(0032-0.045mm)	3.1x10 ⁶	215	0.38	$\frac{dX}{dt} = r_b F(X)$	Barrio & Hustad (2008)
Refuse Derived Fuel	4.2x10 ⁷	221	0.72	$\frac{dX}{dt} = \frac{r_b}{T} (1 - X)$	Cozzani (2000)
Wood	3.42	129	1	$\frac{dX}{dt} = r_b$	Gerber et al. (2010)

2.3.1.3.2. Water-gas reaction

This reaction is given by:



The effect of the equilibrium of CO₂, H₂, CO in water gas shift reaction increases to its complexity. The rate of this reaction can be described by the Langmuir-Hinshelwood rate equation as follows:

$$r_s = \frac{k_1 p_{H_2O}}{1 + \left(\frac{k_1}{k_3}\right) p_{H_2O} + f(p_{H_2})} \quad f(p_{H_2}) = \frac{k_2}{k_3} p_{H_2} + \frac{k_4}{k_5} p_{H_2} + \frac{k_6}{k_7} p_{H_2}^{0.5} \quad (2.71)$$

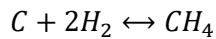
In the Langmuir-Hinshelwood rate in Equation (2.71); the function $f(p_{H_2})$ has several forms depending on part taken for the mechanism. The kinetics of water-gas gasification reactions for different feedstocks is given in Table 2.9.

Table 2.9. Kinetics of water-gas reaction

Char reaction	k_o ($s^{-1}bar^{-n}$)	E (kJ/mol)	n	Equation	Reference
Rice-husk powder	5.53×10^6	82.9	1	$\frac{dX}{dt} = \frac{r_b}{T}(1 - X)$	Bhat et al. (2001)
Cotton trash	1.52×10^4	121.6	1	$\frac{dX}{dt} = r_b F(X)$	Pasangulapati (2012)
Poplar Wood	6.57×10^3	156	1	$\frac{dX}{dt} = \frac{r_b}{T}(1 - X)$	Hawley et al. (1983)
Wood char	1.79×10^3	138	1	$\frac{dX}{dt} = r_b F(X)$	Barrio et al. (2001)

2.3.1.3.3. Hydrogasification reaction

This reaction is given by:



The reaction is much slower than the boudouard or gas-shift reaction. It requires a hydrogen environment. The equilibrium reaction proceeds with increasing hydrogen pressure to overcome thermodynamic limitation. The reaction decreases with char consumption as inactive hydrogen molecules block the active site; the reaction rate proceeds with increasing temperature up to 850 °C (González et al. 2002). The kinetics of this reaction is given in Table 2.10.

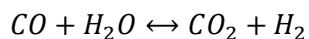
Table 2.10. Kinetics of hydrogasification

Char reaction	$k_o(s^{-1})$	E(kJ/mol)	n	Equation	Reference
Almond shells char	-	94.8 103.1	0.93 1.02	Surface reaction: $1 - (1 - X)^{\frac{1}{3}} = kt$	González et al. (2002)
Biomass ₃	4.19×10^{-3}	19.21	1	Diffusion controlled reaction: $1 - (1 - X)^{\frac{2}{3}} = kt$ Volume of reaction	Babu & Sheth (2006)
Wood ₃	3.42×10^{-3}	129.7	1	model: $-\ln(1 - X) = kt$	Gerber et al. (2010)

In Table 2.10, the shrinking core model is applied when the reaction proceeds at the surface under experimental conditions. The surface reaction equation is used when chemical reaction at the surface controls the process and the diffusion equation is used when the gas film diffusion controls the reaction. The volume reaction model is applied when the reaction is assumed to proceed uniformly.

2.3.1.3.4. Water –gas shift reaction

This reaction is given by:



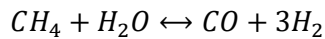
The reaction is reversible at standard condition. It is classified as exothermic homogeneous gas phase reaction; however, it is sensitive to increase in temperature. The various reaction rates and Kinetics are given in Table 2.11. The water gas shift reaction kinetics are mostly from catalytic reactions, this reduces the reliability of the kinetics. Liu et al. (2013) reported the effect of water gas shift on the gasification reaction. They concluded that the reaction affects the CO concentration and in a gasifier the reaction is far from equilibrium.

Table 2.11. Kinetics of water-gas shift reaction

k_o (s ⁻¹)	E (kJ/mol)	Equation	Reference
10 ^{12.7}	283	$\frac{dC_{CO}}{dt} = -kC_{CO}^{0.5}C_{H_2O}$	Graven & Long (1954)
2.78x10 ⁶	12.6	$\frac{dC_{CO}}{dt} = -kC_{CO}C_{H_2O} + \frac{C_{CO_2}C_{H_2}}{K_p(T)}$ $K_p(T) = 0.0265exp^{3958/T}$	Gerber et al. (2010)
2.512x10 ⁵	132.5	$\frac{dC_{CO}}{dt} = -kC_{CO}C_{H_2O}$	Picou et al. (2008)
1.52x10 ⁴	121.62	$\frac{dC_{CO}}{dt} = -kC_{CO}$	Sato et al. (2004)

2.3.1.3.5. Steam reforming reaction

This reaction is given by:



The steam reforming reaction is highly endothermic which produces hydrogen. This is a reversible reaction and the reaction is followed by water-gas shift reaction. The various reaction rates and Kinetics are given in Table 2.12. This reaction is rarely used in gasification models though a process that occurs in steam gasification process.

Table 2.12. Kinetics of water-gas shift reaction

k_o (s ⁻¹)	E (kJ/mol)	Equation	Reference
0.0265	65	$\frac{dC_{CH_4}}{dt} = -kC_{CH_4}C_{H_2O}$	Pasangulapati (2012)
3x10 ⁵	125.5	$\frac{dC_{CH_4}}{dt} = -kC_{CH_4}C_{H_2O}$ $K_p(T) = 0.0265exp^{3958/T}$	Gerber, et al., (2010)
2.78x10 ³	125.5	$\frac{dC_{CO}}{dt} = -kC_{CO}C_{H_2O}$	Miao et al. (2013)

2.3.1.3.6. Combustion reactions

The oxidation of char and other gases, i.e. CO, CH₄, and H₂, comprises the main combustion reactions. The gas phase reactions and their reported rate equations and kinetics are given in Table 2.13.

Table 2.13. Kinetics of Combustion Reactions (Pasangulapati 2012)

Reaction	k_o (s ⁻¹)	E(KJ/mol)	Equation
$\text{CH}_4 + 1.5\text{O}_2 \rightarrow \text{CO} + \text{H}_2\text{O}$	1.58x10 ⁸	202.39	$\frac{dC_{\text{CH}_4}}{dt} = -kC_{\text{CH}_4}^{0.7}C_{\text{O}_2}^{0.8}$
$\text{H}_2 + 0.5\text{O}_2 \rightarrow \text{H}_2\text{O}$	3.09x10 ¹¹	100	$\frac{dC_{\text{H}_2}}{dt} = -kC_{\text{H}_2}C_{\text{O}_2}$
$\text{CO} + 0.5\text{O}_2 \rightarrow \text{CO}_2$	8.83x10 ¹¹	100	$\frac{dC_{\text{CO}}}{dt} = -kC_{\text{CO}}C_{\text{O}_2}^{0.25}$

The char oxidation reaction is dependent on remaining gas specie available; this can also be the reaction that provides heat in an autothermal process. The reaction is assumed to occur as a similar process for coal (Blasi 2009). The reaction rates and kinetics of the combustion reactions for various types of chars are given in Table 2.14.

Table 2.14. Kinetics of Char Combustion Reactions

Char reactions	k_o (s ⁻¹ bar ⁻ⁿ)	E(kJ/mol)	n	Equation	Reference
Hardwood	-	125	0.85	$\frac{dX}{dt} = kP_{\text{O}_2}^n [S/S_o]$	Magnaterra et al. (1993)
Wood	-	-	-	$\frac{dc_c}{dt} = \frac{-fP_{\text{O}_2}}{\frac{1}{k_1} + \frac{1}{k_2}}$ $k_1 = \frac{0.292(1-\varepsilon)D_g}{2d_p T_g}$ $D = 4.26 \left(\frac{T_g}{1800}\right)^{1.75}$ $k_2 = k_1 \varepsilon^{2.5} \frac{dc_c}{1-d_c}$	Syamlal & Bissett (1992)
Straw	1.31x10 ⁸	134		$\frac{dX}{dt} = k$	Zolin et al. (2001)
Corncob	8.12x10 ⁸	151	0.53	$\frac{dX}{dt} = kP_{\text{O}_2}^n [F(X)]$	Várhegyi et al. (2006)

2.3.2. Model formulation

2.3.2.1. Species transport equation

The species exchanges are represented from the mass of species to express the conservation of species transport as follows:

$$\frac{\partial(\alpha_g \rho_g Y_{i,g})}{\partial t} + \nabla(\alpha_g \rho_g \bar{u}_g Y_{i,g}) = -\nabla \cdot \alpha_g \vec{J}_{i,g} + R_{i,g} + S_{gs}, \quad (2.72)$$

$$\vec{J}_{i,g} = -\left(\rho_g D_{i,g} + \frac{\mu_t}{Sc_t}\right) \nabla Y_{i,g} - D_{T,i,g} \frac{\nabla T}{T}, \quad (2.73)$$

where $Y_{i,g}=1, 2, \dots, n_g$ is the mass fraction of species i in the gas phase, $\vec{J}_{i,g}$ is diffusion flux of species i , $R_{i,g}$ are the mass transfer due to reactions, $D_{i,g}$ is the mass diffusion coefficient for species i in the gas phase, and $D_{T,i,g}$ is the thermal diffusion coefficient.

2.3.2.2. Laminar finite rate model

The model implements the reaction rate based on Arrhenius rate only. This model is applicable for small combustion reactions where the chemistry-turbulence interaction is negligible. The chemical species term R_i are represented based on a sum of Arrhenius reactions over the number of reactions computed as follows:

$$R_i = mw_i \sum_{n=1}^n R_{i,n}, \quad (2.74)$$

$$R_{i,n} = (\tilde{\nu}_{i,r} - \bar{\nu}_{i,r}) (k_{f,r} \prod_{j=1}^n (C_{j,r})^{\tilde{\eta}_{j,r} + \bar{\eta}_{j,r}}), \quad (2.75)$$

$$k_{f,r} = A_r T^\beta e^{-E/RT}, \quad (2.76)$$

where $R_{i,n}$, $\tilde{\nu}_{i,r}$, $\bar{\nu}_{i,r}$, $k_{f,r}$, $C_{j,r}$, and T^β is the molar rate of species, stoichiometric coefficient for reactant i in reaction r , stoichiometric coefficient for product specie i in reaction r , forward rate constant for reaction, molar concentration of species j in reaction r , and temperature exponent. The equations above represent the forward only reaction. The molar rate of species for backward reaction needs to be considered for reversible reaction as follows:

$$R_{i,n} = (\tilde{v}_{i,r} - \bar{v}_{i,r})(k_{f,r} \prod_{j=1}^n (C_{j,r})^{\tilde{\eta}_{j,r}} - k_{b,r} \prod_{j=1}^n (C_{j,r})^{\bar{\eta}_{j,r}}), \quad (2.77)$$

where, $k_{b,r}$ is the backward rate constant which is given as:

$$k_{b,r} = \frac{k_{f,r}}{K_r}, \quad (2.78)$$

$$K_r = \exp\left(\frac{\Delta S_r^o}{R} - \frac{\Delta H_r^o}{RT}\right) \left(\frac{P_{atm}}{RT}\right)^{\sum_{i=1}^n (\tilde{v}_{i,r} - \bar{v}_{i,r})}, \quad (2.79)$$

where K_r , ΔS_r^o , ΔH_r^o , P_{atm} are the equilibrium constant, the total change in standard state entropy of reaction r, the total change in standard state enthalpy of reaction r, and atmospheric pressure. The exponential terms are change due to Gibbs free energy and are presented based on the standard state entropy S_i^o and standard state enthalpy H_i^o in Equation (2.80) and (2.81).

$$\frac{\Delta S_r^o}{R} = \sum_{i=1}^n (\tilde{v}_{i,r} - \bar{v}_{i,r}) \frac{\Delta S_i^o}{R}, \quad (2.80)$$

$$\frac{\Delta H_r^o}{R} = \sum_{i=1}^n (\tilde{v}_{i,r} - \bar{v}_{i,r}) \frac{\Delta H_i^o}{R}, \quad (2.81)$$

2.3.2.3. Surface reaction model

The particle surface reaction is implemented by the following equation:

$$\mathcal{R} = D_0(C_g - C_s) = R_c(C_s)^N, \quad (2.82)$$

where D_0 is the bulk diffusion coefficient, C_g mean reacting gas species concentration in the bulk, C_s is the mean reacting gas species concentration at the surface, R_c is the chemical reaction rate coefficient, N is the apparent reaction order. The particle concentration term is re-expressed based on the mean gas concentration of species and bulk diffusion coefficient and the rate of reaction of a particle surface species with a gas species are given below:

$$\mathcal{R} = R_c \left(C_g - \frac{\mathcal{R}}{D_0}\right)^N, \quad (2.83)$$

$$\bar{\mathcal{R}}_{j,r} = A_p \eta_r Y_j \mathcal{R}_{j,r}, \quad (2.84)$$

$$\mathcal{R}_{j,r} = \mathcal{R}_{kin} \left(P_n - \frac{\mathcal{R}_{j,r}}{D_{0,r}} \right)^N, \quad (2.85)$$

where $\bar{\mathcal{R}}_{j,r}$ Rate of particle surface species depletion, A_p particle surface area, Y_j mass fraction of surface species.

2.4. Numerical model

2.4.1. Solver

The solver used in FLUENT is based on either the pressure based solver or the density based solver. The pressure based solver generally is for low velocity incompressible flows and the density based is for high velocity compressible flow. The solver has been modified and adjusted for a wide range of problems. The continuity equation is used to obtain the density field and the pressure is obtained from equation of state. The pressure-based solves the pressure field through the continuity and momentum equations. The pressure based coupled solver solves the momentum and continuity equation simultaneously when compared to the segregated solver. The iterative procedure is shown in Figure 2.20



Figure 2.20: Pressure based coupled solver iterative procedure (ANSYS 2009).

The coupling nature of the pressure coupled solver leads to a faster rate of convergence, though it consumes more memory. The linearization of partial differential equation takes two forms implicit or explicit.

2.4.2. Discretisation

The solution discretization procedure is based on the finite volume method. This method is similar to the finite element and finite difference approximation methods that solve partial differential equations. It is based on a cell average value as compared to the finite element or finite difference that uses a local function values at the mesh point. These cell averaging value is the fundamental aspect of CFD where the flow variable is at the centre of the computational cell.

The finite volume is more flexible robust and allows solution in complicated geometry using simple algorithmisation. The nodal field values are calculated based on a linearized set of algebraic equations of the governing equations. The linearization of the governing equations may take an implicit or explicit form. The implicit form of linearization takes the form that for a given variable the value is calculated from existing and unknown values from neighbouring cells. This gives a set of simultaneous equations for the unknown quantities which are solved to find the solution. The explicit form takes the form by which the variable unknown value using existing cells only. Therefore, the unknown value is solved one at a time for the solution of the unknown quantities. The discretization is based on one steady state solution for scalar quantity ϕ :

$$\underbrace{\frac{\partial(\rho\phi)}{\partial t}}_{transient} + \underbrace{\nabla \cdot (\rho\phi\vec{v})}_{convective} = \underbrace{\nabla \cdot (\Gamma\nabla\phi)}_{diffusion} + S, \quad (2.86)$$

$$\int \frac{\partial(\rho\phi)}{\partial t} dV + \oint (\rho\phi\vec{v}) \cdot d\vec{A} = \oint (\Gamma\nabla\phi) \cdot d\vec{A} + \int S dV, \quad (2.87)$$

$$\frac{\partial(\rho\phi)}{\partial t} V + \sum_f^{n_{faces}} \rho\phi_f \vec{v} \cdot \vec{A} = \sum_f^{n_{faces}} \Gamma\nabla\phi_f \cdot \vec{A} + SV, \quad (2.88)$$

where, Γ is the diffusion coefficient, n_{faces} is the number of faces enclosing the cell, ϕ_f and amount of scalar through the face. The face value of the scalar quantity is calculated using discretisation schemes. The different schemes could be used such as the first, second and third order upwind, the hybrid scheme (central plus upwind differentiating scheme), and the quick upwind differencing scheme (QUICK). The detailed process of discretization of the different schemes can be found in the Fluent theory guide (ANSYS 2009).

2.5. Conclusion

The chapter introduces the hydrodynamics, Energy, chemical kinetic, and numerical models for implementing solar thermal conversion of biomass using Computational fluid dynamics. In a fluidized bed biomass thermal conversion reactors such information are of vital importance to gain insight and predict overall reactor performance. There is huge computational cost in implementing the Lagrangian modelling approach for large scale systems therefore limited to experimental or small prototypes. This is even worse when adding heat transfer and reactions equations, such as in the case for the simulation of biomass thermal conversion. The Eulerian modelling approach seemed convenient to describe complex process more efficiently. They both allow prediction of different velocity, composition and temperature profiles. The different drag laws and turbulence models used for the Eulerian-Eulerian multiphase model were reviewed and illustrated. The heat transfer model was made up of the convection and radiation heat transfer models. The chemical reaction kinetics model for devolatilisation and gasification reactions were described. The process of modelling the species transport and the species rate model was explored; and the particle surface reaction model. The process of discretisation of the governing equations and the different solver used for the numerical process were also reviewed. This chapter provided an overview of the methodology required for CFD modelling using FLUENT for biomass thermochemical conversion.

CHAPTER 3 : MODELLING OF BIOMASS FAST PYROLYSIS IN A SOLAR TROUGH REACTOR

This chapter contains the theory and a literature review of different solar thermochemical processes and fast pyrolysis in several types of reactors. Biomass fast pyrolysis with the exploitation of solar thermal collectors to provide heat is an unconventional way to convert energy into liquid fuel, gas and bio-char. The process of biomass pyrolysis in a solar reactor using a trough arrangement can be implemented using the CFD software Fluent 14.0. Fluent can model both Eulerian-Eulerian and Eulerian-Lagrangian models; the Eulerian-Lagrangian models are generally computationally intensive. In this work, biomass pyrolysis was investigated using Eulerian-Eulerian multiphase flow model with the inclusion of a heat transfer and heterogeneous pyrolysis model. A performance analysis of the process was conducted and the results were analysed to reach final conclusion on the efficiency and future development of this novel process.

3.1. Background theory

3.1.1. Solar thermochemical conversion

Solar radiation reaching the earth surface can be either direct or diffused solar radiation. The direct solar radiation radiates from the sun, while the diffused radiation is a form of reflected, deflected, or absorbed and retransmitted radiation by particles or gases in the atmosphere, before it reaches the earths' surface. The total radiation reaching the earth surface is given by Iqbal (1983):

$$I_b = I_n \cos \theta_{inc}, \quad (3.1)$$

$$I_d = I_n \cos^2 \theta, \quad (3.2)$$

$$I = I_b + I_d, \quad (3.3)$$

where I_n as nominal Irradiation (W/m^2), I_b as beam Irradiation (W/m^2), I_d as diffuse Irradiation (W/m^2), θ_{inc} as Incident angle (0-90°), and θ as Inclination angle (preferably 0-12°). The concentrated solar energy technology converts' direct solar radiation to thermal energy that can be used for a wide range of energy conversion processes. The amount of direct nominal irradiation (I_n) incident on the earth surface is a measure of solar flux incident on a surface perpendicular to the beam radiation. Its value is usually about 0.9-1.1KW/m² in broad daylight (Raja et al. 2006).

The basic principle of concentrating thermal energy is by collecting substantial beam radiation over a huge area and concentrating it to a smaller one by using parabolic mirrors. This parabolic mirror focuses sunrays parallel to its axis into its focal point; these rays are usually 0.5° off point from Parallel. The reflection of the rays at the focal plane is shown in Figure 3.1.



Figure 3.1: Ray Concentration on a Parabola (Stine 2001).

The intensity of concentrated rays incident on the solar receiver is dependent on the concentration ratio. The concentration ratio is the amount of energy that a solar collector can concentrate at any given time. This can be either defined as optical or geometric concentration. Optical concentration ratio is the ratio of radiation flux intensity over the receiver to the normal direct radiation. The geometric concentration ratio is the ratio of aperture area to collector area; those losses not accounted for in the optical concentration ratio are considered. The unit for concentration ratio is given as suns. The concentration ratio has a maximum limit according to law of thermodynamics as light concentration. The value is calculated from $1/\sin^2(\Theta)$ in point focus systems and for a line-focus is $1/\sin(\Theta)$ with Θ as 0.27rad . The maximum concentration ratio is 46211 suns for point focus and 200 suns for line concentration.

3.1.2. Parabolic trough

This is a two-dimensional concentrator that has parabolic reflectors, which focus solar radiation on a receiver along its focal line. This receiver is an evacuated tube made up of concentric tube with annulus being vacuumed. The inner tube contains the heat transfer fluid and is made up of high conducting material with the outer surface being coated with a material to reduce heat loss and increase absorption (see Figure 3.2).



Figure 3.2: Schematic diagram of parabolic trough (Volker Quaschnig 2003).

This type of concentrator can be used for both low temperature and high temperature applications. The maximum temperature it achieves is mostly from 400-550°C without significant heat losses. The possible concentration ratios are from 30-100 suns; the temperature is limited by the heat transfer fluid (mostly used HPV-oil, steam and molten salt) and the rigidity of materials used for the receivers. Also the stagnation temperature is about 565°C, this limits its possibility for very high temperature processes. The power available in a parabolic trough is calculated from the concentration ratio and the proposed beam radiation. The maximum concentration ratio achievable by a parabolic trough is about 212 suns. The concentrated solar energy is calculated from the equation below:

$$Q_{parabolic} = I_b C_R, \quad (3.4)$$

where, $Q_{parabolic}$ is parabolic Irradiation and C_R is the concentration ratio. Parabolic trough is commonly designed to track the sun in a single axis with either axes in the north to south direction (seasonal) or east to west direction (daily) depending on the location. The north south tracking concentrates more energy in the winter, while the east west concentrates more in summer. The former requires more adjustment and there are large incident angles (cosine loss) at peak times.



Figure 3.3: Schematic diagram of linear Fresnel reflector (Volker Quaschnig 2003).

Another concentrator that is similar to parabolic trough is the Fresnel reflectors, which have the absorber tube above the reflectors (see Figure 3.3). This reduces the wind load and makes vacuumed inner tubes unnecessary. However, the Fresnel reflectors have less concentration ratios than parabolic trough and cannot be used for medium-high temperature applications.

3.1.2.1. *Types of solar receivers*

Evacuated and Tubular Receivers

These types of receivers are used in line or plane focusing technologies; they are made up of steel or copper pipes surrounded by a vacuumed glass to minimize convectional losses. The inner pipes are selectively coated with high absorptivity (>90%) and low emissivity (<30%) in the infrared region for radiation loss; also the glass is coated with an anti-reflective coating to improve efficiency. Glass coatings have constant absorptance and emissivity of 0.02 and 0.86 (Zarza 2009). The coatings are made of black-nickel and black-chrome coating for below 290 °C; for high temperature applications selective cermet coatings become necessary. The diagram of a tubular receiver is shown below:



Figure 3.4: Diagram of Heat Collection Element (Forristall 2003).

The inner tube and glass have bellows to compensate for thermal expansion of the materials. The welding is coated with aluminium to protect from high temperature and pressure effect. The temperature profile in a tubular receiver is shown in Figure 3.5. The typical length is below 6 m due to manufacturing limitations; the parts are mostly adjoined together to create a trough field (see Figure 3.2). Heat transfer fluids have less effect on the heat transfer performance; it only limits the temperature of operation.



Figure 3.5: Temperature profile in a Tubular Solar Receiver (Fend 2010).

Tubular receivers have low pressure drop; the receivers are very important in determining its performance. They are vital for energy collection and transformation, and the thermal losses associated with it in high temperature influence operation of the trough.

Volumetric Receivers

These receivers are made up of high porosity material for the ease of radiative and conductive heat transfer. Air is normally used as a heat transfer medium through the material in solar towers to provide heat to a process or particle. The concentrated radiation usually enters at the front of these absorbers as shown in Figure 3.7; hence the material can be easily cooled. The flow through the material is dependent on thermal conductivity and permeability. The temperature difference between the inlet and the outlet creates minimal heat losses so that temperatures over 1000 °C is possible.



Figure 3.6: Temperature profile in a Volumetric Receiver (Fend 2010).

Some extensive literature exists on volumetric receivers for solar thermochemical conversion processes this work only focused on using tubular receiver. Additionally, as volumetric receivers are rarely used in a parabolic trough. Hoffschmidt et al. (1999) reported maximum temperature achieved was about 250°C for volumetric receivers in a parabolic trough, which is below energy needed for biomass fast pyrolysis.

3.1.3. Biomass fast pyrolysis

Biomass is decomposed at moderate temperature and short residence time to generate mainly vapours and aerosols. The products are cooled and condensed rapidly to form bio oil and char is rapidly extracted to avoid vapour cracking to gas. The process efficiency is improved by using smaller particles, as they are easily controllable. Also, the rate of heat transfer has to be high, which makes ablation a suitable process for pyrolysis (Lédé 1999). A detailed background of kinetics for pyrolysis is given in chapter 2. The main pyrolysis reactors are categorized into the following: Bubbling fluidised bed, Circulating and transporting beds, ablative, rotating cone and vacuum (Bridgwater & Peacocke 2000). The characteristics of these reactors are given in Table 3.1 .

Table 3.1: Main types of pyrolysis reactors (Bridgwater 1999)

Reactor Types	Mode of heating	Heat transfer
Auger	Wall	Conduction 95%
	Auger screw	Convection 4%
Ablative	Wall	Radiation 1%
CFB and transported bed	Char gasification	Conduction 80%
	Sand	Convection 19%
		Radiation 1%
Entrained flow	Sand	Conduction 4%
	Carbon Combustion products	Convection 95%
		Radiation 1%
Fluidised bed	Recycle gas/Inert gas	Conduction 90%
		Convection 9%
		Radiation 1%
Rotating cone	Wall and Sand	Conduction 80%
		Convection 19%
		Radiation 1%
Vacuum	Direct contact	Radiation 1%

Concentrated solar energy has also been used to provide heat for pyrolysis processes. It provides high heat transfer rate due to its high flux density. The mode of transfer is either mainly by radiation or conduction depending on the solar reactor. The radiation mode of transfer has issues due to the optical properties of biomass not favourable for absorbing radiation. Biomass is a highly reflective and semi absorbing material so most of the radiation is lost. These properties change at each reaction step as the feed material changes to char, vapour and gases therefore difficult to model the process. The solar reactors that operate using a transparent window have the products forming a screen to radiation due to low mass

transfer efficiencies. This leads to the biomass receiving very low solar flux. The vapours and aerosols react due to the effect of radiation to crack these primary vapours into secondary species. A process relying on indirect heating by an intermediate wall can be an advantage to these issues, though there is a partial loss of high quality solar energy due to heat transfer.

3.2. Literature review

3.2.1. Studies on solar thermochemical conversion

There have been several applications of solar to thermochemical conversion processes. A review of the thermodynamics and reactors for the processes has been done by Steinfeld (2005) and Fletcher (2001). The different solar thermochemical conversion processes from carbonaceous fuels and metallic oxides are given in Figure 3.7.



Figure 3.7: The different solar thermochemical conversion process to produce synthesis gas (adapted from Steinfeld (2005)).

Solar thermolysis is the decomposition of a compound to its constituent molecules at high temperatures. Earlier experiments of solar thermolysis of water using a point focused system in a volumetric receiver/reactor have been implemented by Bilgen et al. (1977) at very high temperatures of 2000-2500°C. They observed that there were problems with reactor design and separation of dissociated products. Two-step solar thermochemical cycles have made it more possible to solve the issue of dissociated product separation and it occurs at a moderate temperature compared to thermolysis (Joshi et al. 2011). Cracking is the thermal decomposition of carbonaceous fuels such as fossil fuels and biomass. It requires a very fast residence time, the by-products are mainly carbon black, hydrogen or other hydrocarbons. Jin et al. (2007) demonstrated the possibility of using parabolic trough for methanol decomposition at temperatures within 200-300 °C. They obtained solar to chemical efficiencies of 30-60% using a mean solar flux of 300-800W/m². The results prove that solar parabolic trough can be utilized to provide energy for a thermochemical conversion process. Sui et al. (2011) used a concentrator with one-axis tracking. The receiver/reactor was made up of a tubular packed bed of dimension 4m length and 2.5m width. The concentration ratio was set to 70 delivering up to 5KW at a mean solar flux of 1000W/m². They obtained solar-chemical efficiency of 60% with 90% methanol conversion. They established a linear relationship between reactor temperature and mean solar flux incident on the collector as shown in Figure 3.8.



Figure 3.8: Influence of the mean solar flux on the temperature of the solar receiver/reactor (Sui et al. 2011).

Solar reforming of methane has been demonstrated successfully in a parabolic dish using a volumetric absorber by Buck et al. (1991). The solar to chemical efficiency of the process was 54% and almost 70% methane conversion. Jin et al. (2009) applied a solar flux of about 630W/m^2 to achieve temperatures up to $280\text{ }^\circ\text{C}$ in a parabolic trough. The mechanism integrated a solar/methanol fuel hybrid thermal power plant and a solar-hybrid combined cycle to upgrade the process into a high-grade thermal conversion unit. They achieved a correlation between theoretical and experimental values for the solar upgrade factor. The value reaches a peak maximum at about 600W/m^2 as shown in Figure 3.9. Hong et al. (2009) used the same solar receiver/reactor for solar methane reforming at 700W/m^2 with 90% hydrogen production at temperatures up to 300°C .



Figure 3.9: Comparison of experimental and theoretical values for the relative upgrade in energy level of solar thermal energy at different mean solar flux at methanol feeding rate of 2.1L/h (Jin et al. 2009).

The auto thermal gasification and pyrolysis are endothermic reactions that require heat to be supplied by either combustion of by products, or some form of fuel (30% of biomass, fossil fuels, etc.). This reduces the heating value of the final product and loss of material due to exothermic combustion reactions. Solar energy is able to provide cleaner and environmentally sound products. Research was mostly carried out for gasification rather than pyrolysis due to the nature of the reactors used mainly either free falling or fluidised bed

systems and the characteristics of gasification reactions (Murray & Fletcher, 1994). The concentrated solar energy can achieve high temperature gasification with less tar above 1473K. Steam is normally used as the gasifying medium to avoid the presence of nitrogen and costly oxygen systems. Gasification in a solar reactor was experimented by slowly focusing the wood at the concentrator's focus and moving the wood as it is consumed. This showed a fast pyrolysis reaction producing char followed by a slow steam gasification reaction. Heat transfer problems were prevalent and slow gas-solid reactions were observed. The majority of experimental setups for solar gasification were implemented using the point focused solar tower receivers. These processes are meant to produce hydrogen as one of the by products. Taylor et al. (1983) compared a packed bed and fluidised bed incident with solar energy for gasification of wood, paper and charcoal. The packed bed utilized more than 30% of the solar radiation compared to the fluidized bed. Piatkowski, et al (2009) studied the gasification of different carbonaceous feedstocks (sewage sludge, industrial sludge, scarp tire, fluff, coal and charcoal) in a packed bed using an indirectly irradiated window reactor design. The reactor configuration is meant to solve the problem of tar and ash deposition at the window; rather inefficient heat transfer occurred with minimal heat distribution to the bottom even with added wall heating. Adinberg et al. (2004) and Hathaway et al. (2014) used molten salt as a heat carrier for biomass gasification. It provided effective heat transfer and thermal storage compared to directly irradiated processes.

Lincoln (1980) realised flash pyrolysis as the first step to providing products for combustion. Cellulose was seeded with carbon particles to provide an absorbance of 90% due to the reflectivity of cellulose and exposed to thermal radiation. They concluded that thermal cracking occurs with increase irradiance. Tabatabaie-Raissi (1989) conducted a thermogravimetric analysis of pyrolysis kinetics on a solar environment and compared them with recently conducted kinetics results. They proved the presence of catalytic secondary reactions occurring in the process in the presence of high flux and high heating rate. They concluded that single-step first order reactions are suitable for qualitative prediction of biomass pyrolysis. Boutin et al. (2002) implemented solar pyrolysis using a parabolic concentrator for flux ranging from 2×10^5 to 4×10^6 Wm^{-2} . The cellulose particles were irradiated directly on the cellulose sample. They confirmed that cellulose decomposes into intermediate species of vapours and aerosols. The intermediate specie forms a protective thin layer coating as the cellulose is heated this changes the mode of heating to conduction. This led to the production of 80% char residue due to the condition being favourable to slow pyrolysis. Shakya (2007) designed a 3KW solar receiver/reactor for pyrolysis of waste plastics. He reported the several steps needed to design a solar receiver/reactor which are i)

determine the kinetics ii) develop a reactor concept and iii) modelling reactor concept. Anderson et al. (2011) investigated pyrolysis in parabolic trough using an auger trough receiver/reactor. The auger system though produces ablative effect which is highly desirable, it increases the residence times of both solid and gas. This produces more bio char product therefore, it is more suitable for slow pyrolysis. Morales et al. (2014) reported pyrolysis of orange peels using a parabolic trough reactor made of borosilicate glass material. A heat balance was implemented to calculate the heat fluxes and losses obtained during the process as shown in Figure 3.10.



Figure 3.10: Heat balance containing heat fluxes and losses in a solar pyrolysis process (Morales et al. 2014).

The percentage of solar radiation absorbed was only 0.72%, about 74% of most the heat was lost to the environment or reflected on the biomass sample. This showed the low absorptivity of biomass with regards to absorption of solar flux. The product yield was 77.64% bio-oil, 20.93% char, and 1.43% non-condensable gases. Similarly a comparison of both radiative and contact ablative pyrolysis in solar reactor have been reported (Lédé 2003). It was discussed that high char content produced by radiant pyrolysis. The need for an ablative effect was required to remove primary liquids to avoid secondary reactions and successive flash radiant heating. The contact ablative method avoids the reflectivity issue of biomass and secondary reactions. The flux densities of the radiative and contact ablative processes are very similar. The contact method produces 3-5% hydrogen compared with 26% for the radiative pyrolysis. This is due to the catalytic effect of radiation on the intermediate liquid compound to favour hydrogen producing reactions. Grassmann & Boaro (2015) concluded char in solar pyrolysis is a mixture of transition or amorphous char with the inherent properties of biomass still intact. The char sample contained 30% volatiles and 60% carbon remaining using wheat straw. The high heating value (HHV) was between 24.5 to 28.2 MJ/kg. Badarayani (2015) did solar pyrolysis of cellulose at a flux of 10^7 W/m². It shows

the formation of intermediate liquid phase before the vapour and gases are produced similar to the broido-Shafizadeh model.

Modelling provides experience and data for parametric evaluation and design necessary for reactor optimisation and performance. There have been several numerical techniques used for solar thermochemical conversion processes. Computational fluid dynamics have been employed for the design and optimisation of solar thermal reactors for thermal reduction of zinc oxide (Abanades et al. 2007). A Eulerian-Lagrangian method was used to couple hydrodynamics, heat transfer, mass transfer, and chemical reaction. They emphasized the need to optimize geometry and operating conditions to achieve maximum conversion. Abanades & Flamant (2007) reported solar methane cracking in graphite tube reactor comparing CFD model and experimental results with good agreement. They concluded that changes in the temperature of the reactor and residence time of the process are proportional to the conversion efficiencies of the product.

Wang et al. (2014) investigated steam methane reforming in a steady state CFD model coupled with chemical reaction kinetics developed for a solar thermochemical reactor. They compared reactive and non-reactive models and obtained similar temperature distributions.



Figure 3.11: Temperature distribution along the centreline of porous medium solar thermochemical reactor for both the non-reactive and SMR reactive conditions (F. Wang et al. 2014).

The temperature for the reactive phase is lower than the non-reactive phase due to the endothermic nature of steam reforming reactions (see Figure 3.11). The effect of incidence solar radiation, mean cell size, fluid velocity, heat transfer model and porosity were

investigated extensively. The temperature of the solid phase increases with increase in the solar irradiance therefore increasing the hydrogen yield.

CFD models for solar gasification and pyrolysis are relatively rare. Z'Graggen & Steinfeld (2008) modelled steam gasification of carbonaceous materials subjected to concentrated solar energy. The governing equations were solved by finite volume method for mass, momentum, energy and chemical reactions. The heat transfer mechanism by conduction, convection and radiation were considered. They obtained good agreement with experimental results for steam conversion, hydrogen and CO produced. Janajreh & Syed (2010) used a Eulerian-Lagrangian method to model steam gasification of coal in a solar receiver/reactor. The radiation model was based on Discrete Ordinate (DO) to solve the radiative transport equation.

The results show that all the volatiles were converted to gases through thermal degradation by radiation at high temperatures. The steam gasification reaction favours the shift reaction which increases the concentration of hydrogen in the products.

Hofmann & Antal (1984) modelled pyrolysis of cellulose in a solar environment. They found that the presence of two temperature effect is attributed to the solar energy creating a cooling effect. This effect inhibits high temperature gas reactions as only the biomass is heated. They observed the benefits of solar as compared to auto thermal process. All the feedstock is used thereby increasing value and Greater efficiencies than auto thermal conversion systems. Solar intermittence makes shutdown and start up to be achievable easily due to low thermal mass system associated with radiant energy. The liquid products serve as a solar storage system; this also solves the low concentration per area problem of biomass. Zeng et al. (2015) reported solar pyrolysis of beech wood in a point focused solar receiver/reactor. The heating rate was kept constant and the effect of temperature, sweeping gas flowrate was investigated. The experimental results were compared with a CFD model in Fluent 14.0 under steady state conditions. The model showed the presence of a two temperature effect attributed to solar radiative pyrolysis processes with mainly high temperatures at the surface of the beech wood. The liquid yields obtained were up to 70.5% at temperature of 600°C. The cracking of tars occurs at temperatures lower than 450°C.

3.2.2. Studies on biomass fast pyrolysis

The Eulerian-Lagrangian and Eulerian-Eulerian have been reported extensively in different reactors for fast pyrolysis of biomass. Eulerian-Lagrangian method has been implemented with small or single biomass particle models due to the computational expenses of modelling

the vast amount of particles. The momentum, heat and mass transfer for a single particle in a 2D Eulerian gas phase has been studied using this model (Papadikis et al. 2008). The pyrolysis model was incorporated as a UDF (User-defined function) based on a semi global pyrolysis model. The product yields obtained were 45% bio-oil, gases 10% and char 15% based on an unreacted biomass of 30%. They took into account the presence of tar cracking reactions which lowered the percentage of bio-oil produced in the model. It was found that the model can predict the residence time of vapours and biomass particle. Therefore, it predicts more realistic particle behaviour.

Papadikis & Gu (2009) studied fast pyrolysis of biomass using Eulerian-Lagrangian approach to show the effect of biomass shrinkage at a particle scale. The surface and centre of the particle was analysed by this model. It shows that shrinkage of biomass has no effect on the yield and pyrolysis time at small particle diameters. The rate of the process was only dependent on heat transfer inside the biomass particle. Therefore, uniform particle diameter in Eulerian-Eulerian phases predicts fast pyrolysis accurately for small particle diameter. They concluded that discrete phase models are computationally expensive especially with regards to 3D simulations.

The multiphase Eulerian-Eulerian model shows good results with fast pyrolysis and has a considerably less computational cost. The pyrolysis of cellulose and red oak was developed using a multicomponent, multi kinetic model (Xue et al. 2011). The experimental values were used to validate the model at different operating conditions based on the biomass conversion and product yield. The final products at a temperature of about 500°C were bio-oil 76.59%, 19.75%, and 3.39%. The same model was applied to bagasse with high lignin content; this produced high char content from the parallel model.

Boateng & Mtui (2012) developed Eulerian model using one-step global reaction kinetics. They compared switchgrass, corn cob, and soya beans pyrolysis results from experiment with a 3D CFD model. The pyrolysis and drying kinetics was based on a first order global model. The limitation of this rate is they are heating rate specific and not applicable over a confined operating range. The model is oversimplified, though it provides a robust design for modelling pyrolysis. The bio-oil yield was as follows switchgrass (71.58%), corncob (65.45%), and soybeans (68.89%). They predicted strong correlation between experiment and model for all the biomass samples. The model has the ability to be extended to several biomass models with data from experiment. This has been implemented by Simanungkalit & Rinaldi (2013) for fruit bunches and Mtui (2013) for palm fruit pyrolysis.

Yu et al. (2015) also reported Eulerian-Eulerian pyrolysis in a downer reactor using one-step global reaction model. The reactor leverages a novel design for rapid gas-particle residence

time and high separation efficiency to prevent char cracking reactions. The model uses sand as a heat transfer mechanism in a dual fluidised bed arrangement. They obtained a devolatilisation efficiency of over 60% and the product composition was bio-oil (56.85%), bio-char (37.87%), and gas (5.28%). The maximum residence time was <2s for the gas phases species. The CFD model has been proven computationally fast and reasonably accurate in evaluating hydrodynamics characteristics and thermochemical performance. The model has flexibility to be able to predict fast pyrolysis of a wide range of biomass from experimental values.

A comprehensive fast pyrolysis model in a fluidised bed was developed to show the intermediates and final products formed in a complex pyrolysis process (Mellin et al. 2014). The model was a laminar flow model due to the nature of fluidised bed. They considered both primary and secondary reaction scheme of the pyrolysis process using the model from Ranzi et al. (2008). This model has been used by Norinaga et al. (2013) to analyse the different reaction pathways for tar products. The cases were compared with experimental values for no tar cracking, with tar cracking, and tar cracking including unreacted biomass. They obtained bio-oil yields of 44%, 42% and 34% for the corresponding cases. There was a low water content in bio-oil prediction compared to that of other publications but the pyrolysis product composition was similar to experiment result. The maximum residence time was about 1.8s for gas species. They concluded that cracking reactions will be the more accurate if in parallel with primary reaction. However, to the best knowledge of authors there has not been much CFD modelling of solar pyrolysis in a parabolic trough receiver/reactor.

3.3. Model formulation

3.3.1. Preliminary simple model

A 1-D and 2-D energy balance was conducted to find the optimum length of the receiver. The parabolic trough receiver is normally made up of the glass envelope and the receiver. Generally, the heat losses in the glass envelope are the most prevalent. The general heat fluxes are given in Figure 3.12.

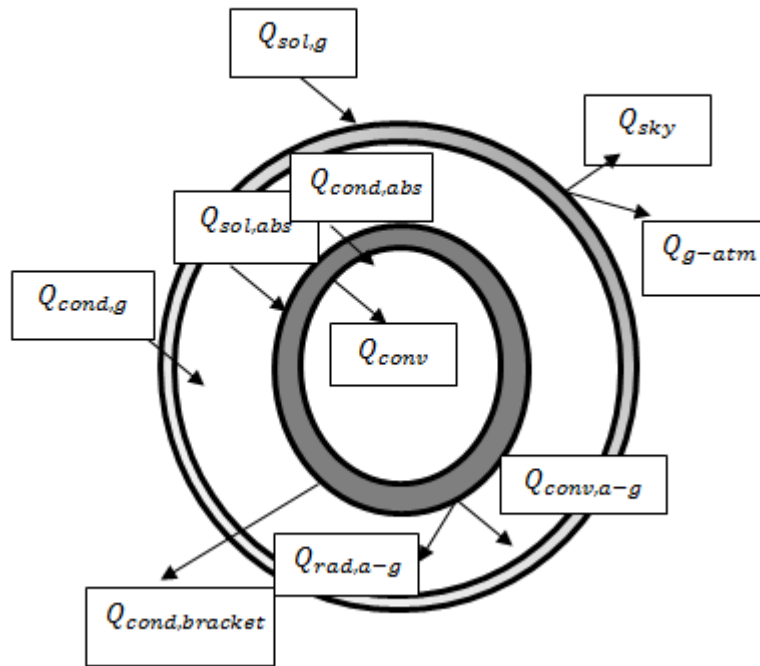


Figure 3.12: One dimensional Simple Energy balance in a parabolic trough(adapted from Gong et al. 2010)

The general energy balance is given in Equation 3.15 from analysis by Forristall (2003).

$$Q_{g-atm} + Q_{sky} = Q_{cond,g} = Q_{rad,a-g} + Q_{conv,a-g} = Q_{sol,abs} = Q_{cond,abs} = Q_{conv}, \quad (3.5)$$

where Q_{sky} is the heat of radiation from the glass to the sky, Q_{g-atm} is the heat of convection from the glass to the atmosphere, $Q_{cond,g}$ is the heat of conduction in the glass surface, $Q_{rad,a-g}$ is the heat loss due to radiation from the absorber surface to $Q_{sol,abs}$ is the solar heat flux at the absorber Q_{conv} is the heat of convection of the heat transfer fluid. The effect of the glass part of the receiver was accounted for in a limited role in this work. The heat loss due to convection between the receiver and the annulus space $Q_{conv,a-g}$ is assumed to operate in a very good vacuum (annulus pressure $<10^{-4}$ torr). The effect of conductive resistance within the absorber tube $Q_{cond,abs}$ was neglected. This is a simple energy calculation, it does not consider heat losses through conduction and convection. Therefore, the actual final temperature might be less.

The proposed receiver was assumed to operate at 12.533kW/m^2 with a diameter of 0.066m . The model assumes uniform heat flux both radially and along the receiver. This assumption leads to the flow being uniform, which is not the case as the non-uniform flux heats the fluid

asymmetrically leading to non-uniform flow in the receiver. This non-uniformity in flow affects heat transfer, this causes an over estimation in the circumferential heat flux. The heat losses along the bracket and other radiative losses were not considered. These assumptions make the model very simple. The arbitrary length needed for the reaction is calculated from the equations given below (Burkholder & Kutscher 2009):

$$Q_{sol,abs} = Q''_{solar} A_i - \dot{Q}_{losses} \Delta L, \quad (3.6)$$

$$\dot{Q}_{losses} = 0.141 * (T_{abs}) + (6.48 \times 10^{-9}) * (T_{abs}^4), \quad (3.7)$$

$$Q_{sol,abs} = \dot{m} \left[c_{p,i} (T_{out,i} - T_{in,i}) + \frac{1}{2} (v_{out,i}^2 - v_{in,i}^2) \right], \quad (3.8)$$

where \dot{m}_i is the mass flowrate assumed to be constant, \dot{Q}_{losses} is the heat losses due to radiation, convection and other applicable losses, Q''_{solar} is the solar radiation heat flux, $c_{p,i}$ is specific heat capacity, T_{abs} is the absorber outer temperature assumed as 600°C, $v_{in,i}$ represent the inlet which is calculated from the initial volume flowrate and A the cross-sectional area, $v_{out,i}$ is the outlet velocity given below (Forristall 2003):

$$v_{out} = \frac{\dot{m}}{\rho_{avg,i} A}, \quad (3.9)$$

where \dot{m} is assumed constant and the value of the outlet density $\rho_{out,i}$ depends on the outlet temperature $T_{out,i}$. The density of the gas is used as the velocity of solid is hugely dependent on the gas velocity based on incompressible ideal gas characteristics.

The length was calculated based on a segmental increase of 0.5m length at each segment and the initial outlet velocity was assumed. The outlet temperature for the biomass phase is calculated from Equation (3.8). The pressure drop is assumed to be a fluid flow in an inclined pneumatic conveying pipe for fully developed turbulent flow as follow:

$$\Delta P_{t,i} = \Delta P_{acc,i} + \Delta P_{g,i} + \Delta P_{s,i} + \Delta H_{g,i} + \Delta H_{s,i}, \quad (3.10)$$

where $\Delta P_{acc,i}$, $\Delta P_{g,i}$, $\Delta P_{s,i}$, $\Delta H_{g,i}$, $\Delta H_{s,i}$ are the pressure due to acceleration of particles, pressure drop of gas due to frictional losses, pressure drop of solids, pressure drop due to elevation of gas and solid. The pressure due to acceleration of particles is given below:

$$\Delta P_{acc,i} = \frac{G_s u_{avg,s}}{144 g \sin \theta}, \quad (3.11)$$

$$u_{avg,s} = 0.8 u_{avg,g}, \quad (3.12)$$

where, G_s is the mass flux, u_s is the solid velocity, g is the acceleration due to gravity. The pressure of gas due to frictional losses is given as:

$$\Delta P_{g,i} = 4 \frac{f \Delta L \rho_g u_{avg,g}}{2 g \sin \theta d \times 144}, \quad (3.13)$$

where, f is the fanning friction factor, u_g is the velocity of the gas, d is the internal diameter, and ΔL is the change in aperture length. The friction factor for turbulent flow in a pipe is estimated based on the Crane equation (Agarwal 2005):

$$f = \frac{0.331}{\text{Log} \left(\frac{\varepsilon}{3.7d} + \frac{7}{Re_i} \right)^2}, \quad (3.14)$$

where ε is the roughness factor given as $\sim 1.5E-6$ for drawn pipes and Re_i is the average Reynolds number estimated from the average bulk temperature of the fluid at each ΔL . The solid pressure drop is given in Equation (3.15).

$$\Delta P_{s,i} = \Delta P_{g,i} K R, \quad (3.15)$$

where K is a physical and frictional constant given as 1.2, R is the ratio of solid to gas mass flowrate given as $R = G_s / u_{avg,g} \rho_g$. The pressure loss due to elevation for the gas $\Delta H_{g,i}$ and solid $\Delta H_{s,i}$ phases are given as follows:

$$\Delta H_{g,i} = \frac{\Delta z \rho_g g}{144 g_c}, \quad (3.16)$$

$$\Delta H_{s,i} = \frac{\Delta z G_s g}{144 u_{avg,s} g_c}, \quad (3.17)$$

where, Δz is the elevation change and g_c is a constant (32.174). The properties and operating conditions for the biomass phase is given in Table 3.2.

Table 3.2: Properties of the gas and solid phases

Properties	Biomass	Gas
$c_{p,i}(J/kgK)$	$5.34(T) - 299$	104
$T_{in,i}(^{\circ}C)$	25	400
$\dot{m}_i(g/s)$	1	3.9
$\rho(kg/m^3)$	223	Incompressible ideal gas

The change in outlet temperature with length is given in Figure 3.13. The temperature increases with an increase in length. This is attributed to the flux build up along the receiver, therefore there is heat gain along the length of the receiver. The non-linear behaviour of the temperature is captured in the model displaying a behaviour that at some point further increases in length will give a constant outlet temperature. The heat losses increase significantly as the point that the heat loss nets the heat gain. The heat losses in a complex model are more significant; stagnation temperature and material limitations become applicable. This shows that the 2D model over predicts the temperature though it predicts efficiently the behaviour of parabolic trough collectors. The length of the receiver will be adjusted after a pre-analysis in FLUENT to the required length to achieve optimum temperature.

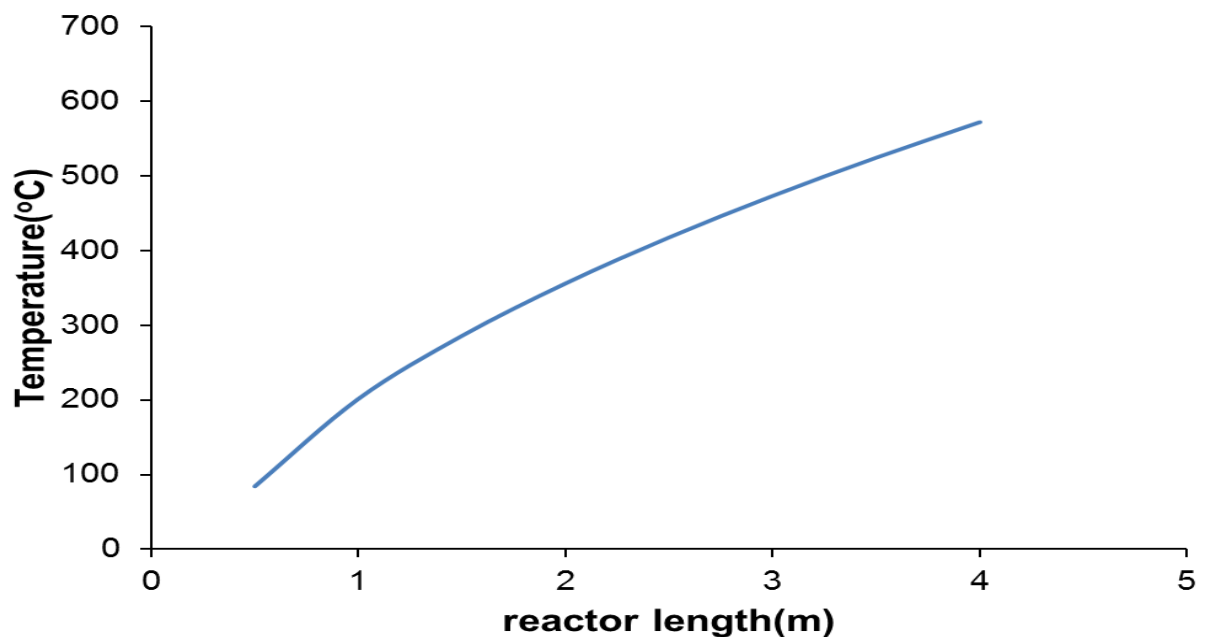


Figure 3.13: The parabolic trough outlet temperature changes with length of the receiver

The total pressure drop for a 4m receiver was about 9.82Psi. The pressure drop behaviour in the receiver is shown in Figure 3.14. The pressure drop decreases as the particles flow along the receiver length. At low superficial velocity of the gas the pressure drop increases. The relationship is not linear in nature. Makkawi & Ocone (2006) observed similar behaviour for suspended flow over a bed in a dilute flow regime.

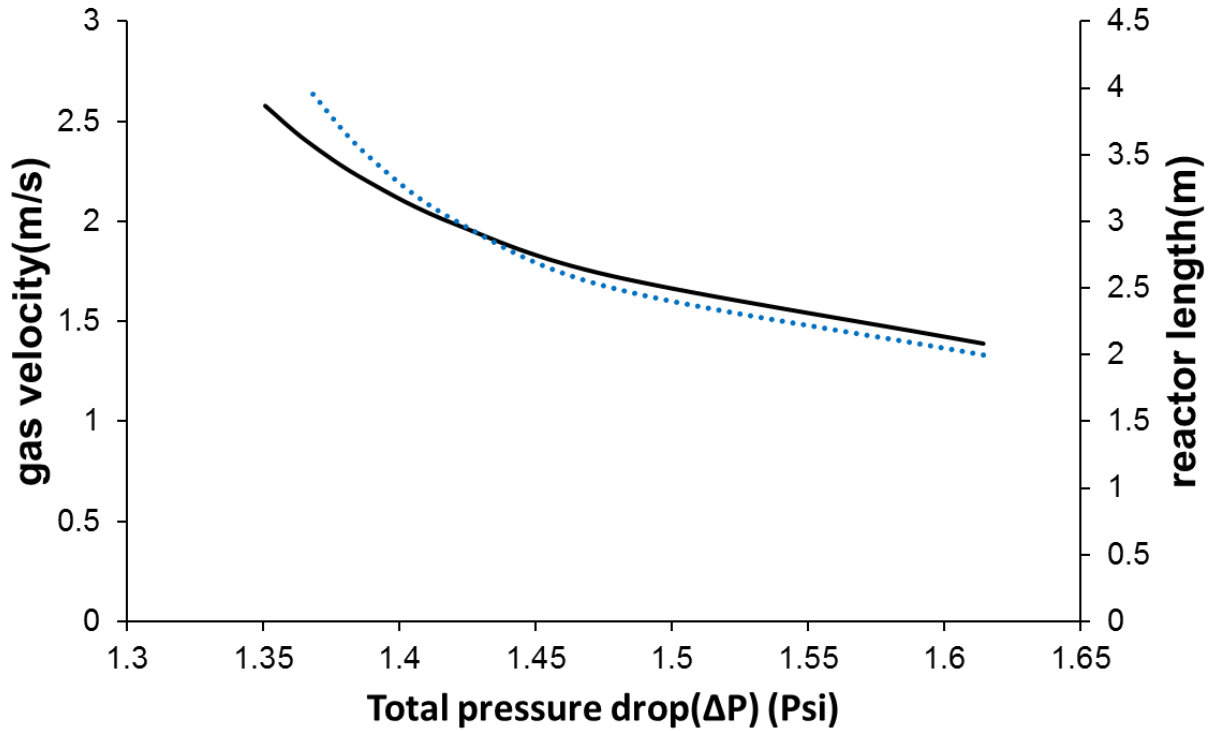


Figure 3.14: Pressure drop relationship between length and superficial gas velocity for a solid flowrate of 1g/s.

The energy needed for the receiver/reactor to pyrolyse sufficient biomass is given by the equation below:

$$Q_{process} = Q_{pyrolysis} + Q_{heating} + Q_{drying} + Q_{losses} , \quad (3.18)$$

where $Q_{pyrolysis}$ is the heat needed for pyrolysis, $Q_{heating}$ is the heat needed for biomass and gas, Q_{drying} is the heat needed for drying moisture, Q_{losses} is the other heat losses to the environment. The equations for the heat parameters are given below:

$$Q_{pyrolysis} = X_{biomass} * \dot{m}E, \quad (3.19)$$

$$Q_{heating} = \dot{m}c_p\Delta T + \dot{m}_{gas}c_{p,gas}\Delta T \quad (3.20)$$

$$Q_{drying} = X_{H_2}\dot{m}(L_{vap} + c_p\Delta T), \quad (3.21)$$

$$Q_{losses} = hA\Delta T, \quad (3.22)$$

Where E is the energy required to pyrolyse the biomass given as 768KJ/Kg, L_{vap} is the latent heat of vaporization is 2258kJ/kg, and $h = 0.0001(T)+0.0358(T)+12.192$ as the heat loss coefficient. The receiver temperature was assumed to be 450 °C. The values of the heat balance parameters are given in Table 3.3. The amount of sand and biomass needed to heat the process without using solar energy was 37g/s and 0.28g/s. This is about 30% of the biomass that is consumed to heat the process. This is avoided by using solar energy to heat the process.

Table 3.3: Values of the different heat parameters and material savings

Parameter	Value
$Q_{pyrolysis}(KW)$	0.75
$Q_{heating}(KW)$	0.98
$Q_{drying}(KW)$	0.11
$Q_{losses}(KW)$	2.79
$Q_{process}(KW)$	4.63
$Q_{solar}(KW)$	4.82
Equivalent sand (g/s)	36
Equivalent biomass(g/s)	0.28

The majority of the energy is lost to the environment or heating the process. The heat exchanges and fluid flow in a parabolic trough is better accurately predicted using computational fluid dynamics (Forristall 2003).

3.3.2. Proposed model for base case

The model presents the hydrodynamics, heat transfer and chemical reactions kinetic model for biomass fast pyrolysis in a parabolic trough receiver/reactor. The switch grass sample is injected into a solar reactor inclined horizontally similar to a parabolic trough orientation. The solar energy is implemented as a heat flux around the wall of the reactor. The model includes a separation section using a novel gas-solid separator and stripping mechanism developed by Huard et al. (2010). The separator has been reported to achieve separation efficiencies up to 99.9%. The governing equations have been modified to include the effect of drying, heterogeneous pyrolysis and inclination as shown below: -

Momentum equation:

$$\frac{\partial}{\partial t}(\alpha_g \rho_g \vec{v}_g) + \nabla(\alpha_g \rho_g \vec{v}_g \vec{v}_g) \quad (3.23)$$

$$= -\alpha_g \nabla P + \nabla \bar{\tau}_g - \beta(v_g - v_s) + \alpha_g \rho_g \vec{g} \cos \theta + \dot{m}_{sg} \vec{v}_{sg} + \vec{R}_{sg}$$

$$\frac{\partial}{\partial t}(\alpha_s \rho_s \vec{v}_s) + \nabla(\alpha_s \rho_s \vec{v}_s \vec{v}_s) \quad (3.24)$$

$$= -\alpha_s \nabla P - \nabla P_s + \nabla \bar{\tau}_s - \beta(\vec{v}_g - \vec{v}_s) + \alpha_s \rho_s \vec{g} \cos \theta - \dot{m}_{sg} \vec{v}_{sg} + \vec{R}_{gs}$$

Energy Equation:

$$\frac{\partial(\alpha_g \rho_g h_g)}{\partial t} + \nabla(\alpha_g \rho_g \vec{v}_g h_g) \quad (3.25)$$

$$= \alpha_g \frac{\partial P_g}{\partial t} + \bar{\tau}_g : \nabla \vec{v}_g - \vec{q}_g + S_g + a_{gs} h_{c,gs} (T_g - T_s)$$

$$+ (\dot{m}_{sg} h_{sg} - \dot{m}_{gs} h_{gs})$$

$$\frac{\partial(\alpha_s \rho_s h_s)}{\partial t} + \nabla(\alpha_s \rho_s \vec{v}_s h_s) \quad (3.26)$$

$$= \alpha_s \frac{\partial P_s}{\partial t} + \bar{\tau}_s : \nabla \vec{u}_s - \vec{q}_s + S_s + a_{sg} h_{c,sg} A_i (T_s - T_g)$$

$$+ (\dot{m}_{gs} h_{gs} - \dot{m}_{sg} h_{sg})$$

The turbulence model was based on standard k-e turbulence with standard wall function (Launder & Spalding 1972). The drag law is based on the model by Syamlal & O'Brien (1987) for dilute flows. The solid and frictional pressure, radial distribution and bulk viscosity are taken from Lun et al. (1984). The kinetic and collisional viscosity are given based on Syamlal et al. (1993). The frictional viscosity is based on Johnson et al. (1990) with a maximum packing limit of 0.63 and angle of internal friction 30.007. This is implemented using ANSYS Fluent 14.0 and an in-house built pyrolysis model code.

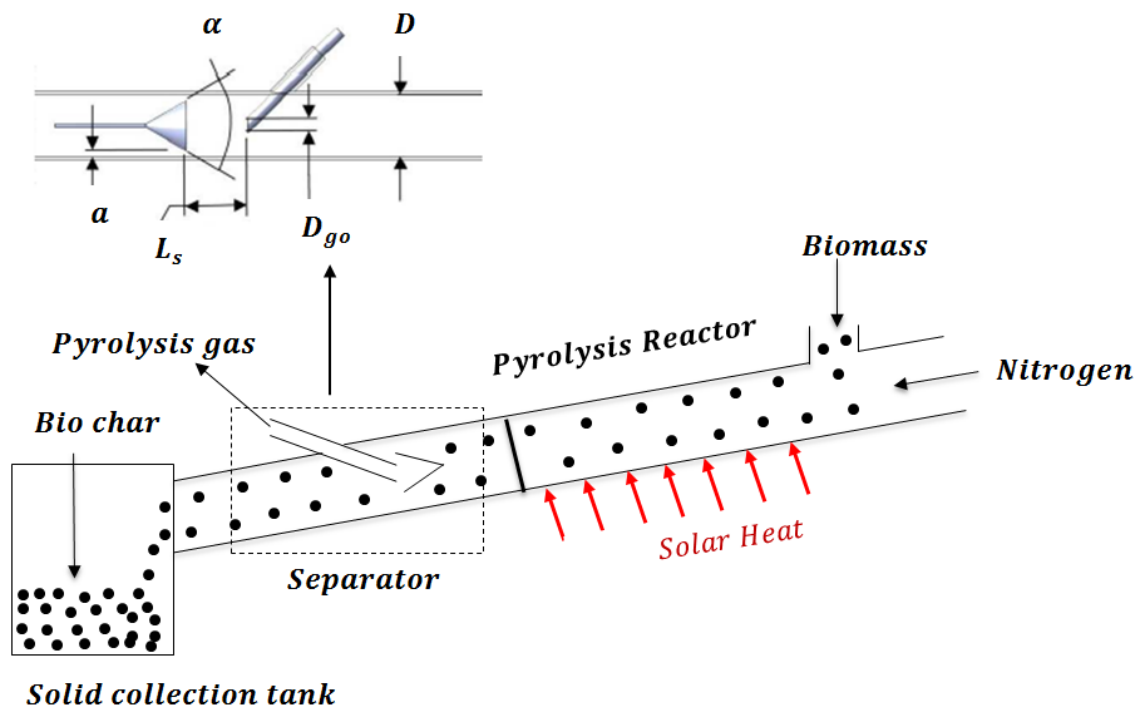


Figure 3.15: Schematic of solar pyrolysis reactor

The receiver model is illustrated in Figure 3.15; the separation mechanism consists of a 60° cone deflector and gas removal stripping pipe. The separator was connected to a solid collection tank of height 0.218m and diameter 20.4cm. The complete dimensions of the separator and reactor are given in Table 3.4.

Table 3.4: Dimensions of simulation domain

Dimensions	Value
Reactor length(m)	3.70
Biomass Inlet D_{in} (m)	0.024
Separator zone length (m)	0.80
a (m)	0.0035
α (°)	60
D_c (m)	0.066
L_s (m)	0
D_{go} (m)	0.015

The geometry of the reaction domain was discretized into small fine elements size to be used for the finite volume method. The 3D mesh contains 162377 cells and 337859 faces

using a tetrahedral mesh. The complex behaviour was captured using a fine mesh of grid size was set to 0.5 and 1cm near the conical deflector and the heated wall. The coarse grid size was set at size of 1 to 5cm for all other domains to reduce computational time. The mesh domain used in this study is shown in Figure 3.16. The minimum grid size was set up to 10 particle diameters and a maximum skewness factor of 0.93 was obtained for the mesh.

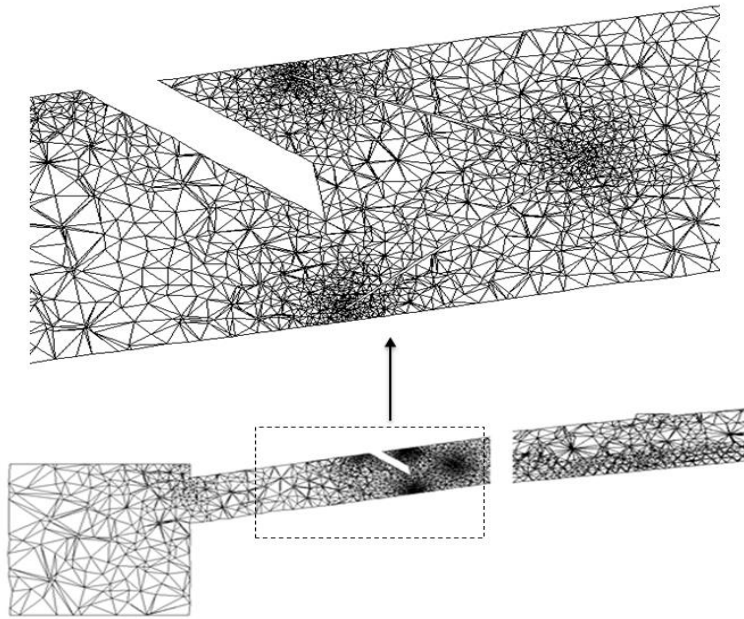
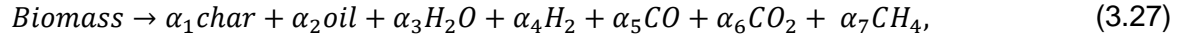


Figure 3.16: Cross-sectional view of mesh and computational domain

The pyrolysis and drying model were implemented as a user-defined function. The drying model was based on the mass transfer of the liquid water to the gas phase with no condensation (Kaushal et al. 2011). In deriving the biomass pyrolysis model a number of assumptions have been made as follows:

- i. The biomass releases a pyrolysis gas mainly consisting of condensable hydrocarbons (bio-oil), non-condensable (permanent gas) consisting of H_2 , CH_4 , CO and CO_2 in addition to H_2O vapour and bio-char.
- ii. The pyrolysis reaction is represented by a single chemical reaction with the reaction rate given by Arrhenius equation.
- iii. The homogenous reaction (gas-gas) (i.e. thermal cracking, reforming, combustion etc.) are negligible due to the low reactor temperature, limited oxygen and short gas residence time.
- iv. The heterogeneous reactions between the pyrolysis gas and bio-char are negligible due to the fast separation of the phases.

The biomass contains a mixture of fixed carbon, volatile matter, ash, and moisture based on the proximate analysis. This is given for switch grass biomass in Table 3.5.



where, $\alpha_1 - \alpha_7$ are the stoichiometric coefficients of the reaction. The stoichiometric coefficients for the switch grass pyrolysis is given as follows 0.138, 0.805, 0.15, 0.003, 0.035, 0.018, and 0.008 for char, bio oil, H₂O, H₂, CO₂, CO, CH₄.

Table 3.5: Proximate and ultimate analysis of switch grass (Boateng et al. 2007)

Analysis	Parameters				
Proximate analysis	Moisture(wt%)	Volatile(wt%)	Ash(wt%)	Fixed carbon (wt%)	HHV (MJ/Kg)
	2.65	81.20	2.54	13.61	19.6
Ultimate analysis	C(wt%)	H(wt%)	O(wt%)	N(wt%)	S(ppm)
	48.80	6.99	43.68	0.53	<120

The pre-exponential factor and Activation energy are $1.063 \times 10^8 \text{ s}^{-1}$ and 103.7 KJ/mol used in for the Arrhenius-rate constant (Pasangulapati 2012). The rate equation r for switch grass pyrolysis used is given from the C_v concentration of volatiles below (Pasangulapati 2012):

$$r = k \times C_v^{0.67} \quad (3.28)$$

3.3.2.1. Boundary/operating conditions

The particles of size 500 μm were introduced at 1g/s from the biomass inlet at the top of the reactor 20cm from the sweeping gas inlet. The particle size was within the appropriate size for fast pyrolysis to achieve optimum liquid production. The sweeping gas which was mainly nitrogen at 350°C is introduced to create an environment for fast pyrolysis and to prevent cracking reactions by decreasing the gas residence time. The biomass particle was assumed to be spherical with sphericity equal to unity. The effect of particle shrinkage and fragmentation was not taken into account. Hence, there was no change in the particle size during or after reaction. This normally over-predicts the mass loss, which may contribute to the high residual. The Eulerian-Eulerian ignores behaviour on a particle scale so heat

transfer is limited to particle surface. These assumptions are fairly accurate for very small biomass particles. The initial conditions of the receiver have the following inlet conditions:

$$\vec{v} = v_{gin}, T_g = T_{gin} = 350^\circ C, \text{ at } L = 0, 0 \leq r \leq D \text{ at gas inlet}, -180^\circ \leq \theta \leq 180^\circ, \quad (3.29)$$

$$\vec{v} = v_{bin}, T_s = T_{bin} = 30^\circ C, \text{ at } L = 0.2, 0 \leq r \leq D \text{ at biomass inlet}, -180^\circ \leq \theta \leq 180^\circ, \quad (3.30)$$

where v_{in} , T_{in} and subscripts g and s are the inlet velocity and the inlet temperature, for corresponding gas and solid phases. The solid phase is assumed to be introduced to the reactor at ambient conditions. The outlet is assumed to be a pressure outlet which is at atmospheric pressure gradient. The flow is assumed to be a fully developed viscous flow leading to a plug flow assumption (tube length \gg hydraulic entry length). The turbulence intensity is calculated from the hydraulic diameter D_h using the relation below at the gas inlets and outlet (Islam et al. 2012):

$$I = 0.16(Re_{D_h})^{-1/8} \times 100\% \quad (D_h = D), \quad (3.31)$$

where I is turbulence Intensity, and Re_{D_h} is Reynolds number based on hydraulic diameter. The hydraulic diameter for a circular pipe is the same as its diameter. The walls are modelled as stationary walls with non-slip wall conditions for the gas phase. The solid phase was modelled with wall shear for particles (Johnson & Jackson 1987). The endothermic pyrolysis reaction heat was supplied by a 3.5m length reactor before entering the gas-solid separating mechanism. The average flux of 12.55KW/m² was used to simulate the concentrated heat flux as a constant heat flux in the model (Morales et al. 2014). The lower part of the absorber has a non-adiabatic heat flux condition and no shell conduction on the walls. The incident solar radiation is modelled as a constant heat flux profile approximated from as follows:

$$Q'' = I_b \times C_R = 12,553 Wm^{-2} \text{ at } D, -180^\circ \leq \theta \leq 0, 0 \leq L \leq 3.7m, \quad (3.32)$$

where Q'' is the heat flux, I_b is beam incident radiation, and C_R is concentration ratio. The upper part of the absorber tube has an adiabatic heat flux condition and no shell conduction on the walls as follows:

$$Q'' = 0 Wm^{-2} \text{ at } D, 0 \leq \theta \leq 180^\circ, 0 \leq L \leq 3.7m \quad (3.33)$$

The reactor was slightly inclined to satisfy the demand of operation conditions in real practise e.g. solar incidence angle, flow and heat distribution. The model implemented only heat transfer by convection and conduction; the heat transfer by radiation was assumed

negligible due to the pyrolysis temperature range. The full operating conditions and physical properties are given in Table 3.6.

Table 3.6. Operating conditions

Parameters	Value	Parameters	Value
Pressure outlet [atm]	1	Biomass inlet temperature [K]	300
Biomass flow rate [g/s]	2	N ₂ inlet temperature [K]	573
Inert gas flow rate [g/s]	0.01	Particle-Particle restitution	0.9
Biomass size [μm]	500	Particle-wall restitution	0.8
N ₂ gas flow rate [g/s]	3.9	Specularity coefficient	0.5

3.3.2.2. Numerical procedure

The governing equations were discretised using the finite volume method. The pressure coupled solver included the pyrolysis model compiled as a user-defined function in FLUENT. The transient formulation for time dependent solution is the first order implicit scheme. The spatial discretisation of the gradient was based on the least squares cell and the other variables were based on first order upwind. The phase coupled SIMPLEC algorithm is used for the pressure-velocity coupling (Patankar 1980). The convergence criterion residuals for energy transport equation were set to 10^{-7} and 10^{-3} for all other transport equations. The under-relaxation factors were set to 0.5 for pressure, 0.7 for momentum, 0.8 for turbulent species, 0.5 for volume fraction, 0.2 for granular temperature, and 1 for rest of the quantities for suitable control of the solution. The courant-Friedrichs-Lewy (CFL) condition for three dimensional domains was implemented to find the optimum time-step. The CFL condition equation is as follows:

$$C = \frac{u_x \Delta t}{\Delta x} + \frac{u_y \Delta t}{\Delta y} + \frac{u_z \Delta t}{\Delta z} \leq C_{max} \quad (C_{max} = \sim 1 - 5) \quad (3.34)$$

A time step of 0.001-0.0025s was found to be suitable for the grid size of the domain. The simulations were performed until quasi-steady state has reached at around 4s implemented with a time-step size of 0.001. The maximum number of iterations was set to 20 until stability of convergence has been achieved. The energy and reactions equations are assumed to be developing until the chemical reactions reach steady state. The processor used for the simulation is a 2.50 GHz 2 Core processor Intel® Xeon® with 32 GB RAM. The total computational time was around 5 days for a real-time of 4s.

3.4. Results and Discussion

3.4.1. Hydrodynamics

The behaviour of the gas and particulate phases have been explored so as to study the hydrodynamic behaviour near the conical deflector separator. At the conical deflector, the behaviour of these fluid phases is dominated by the forces of drag between the particle and the gas and gravitational forces. The pattern of solid-gas disengagement from the core region to the walls of the separator by the conical deflector. This is illustrated in the vector shown in Figure 3.17.

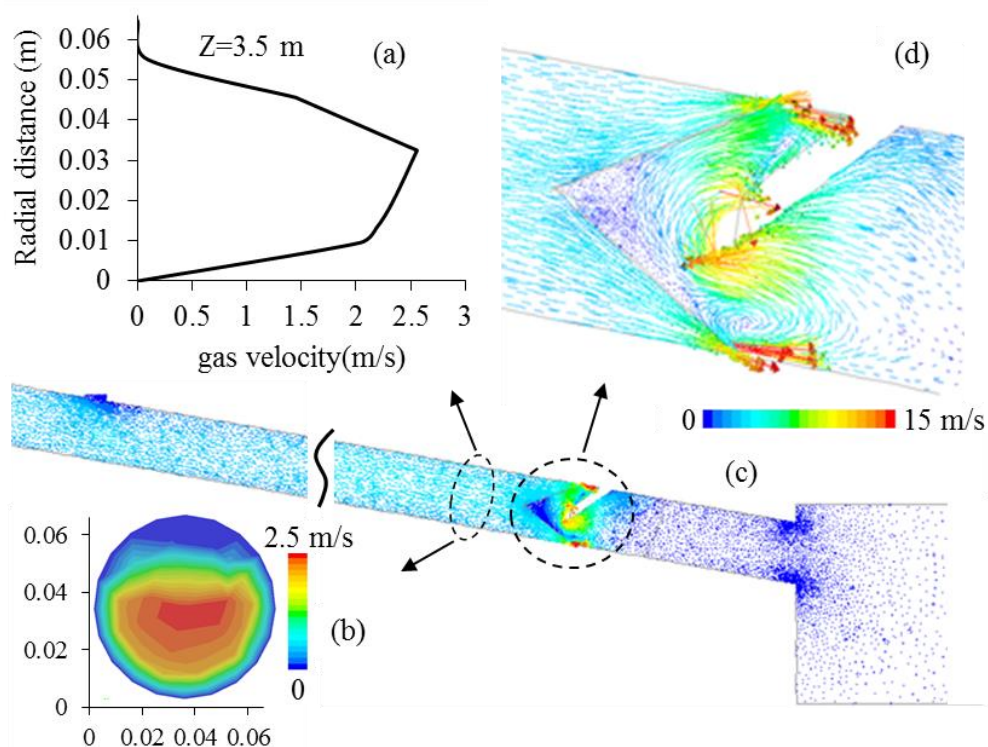


Figure 3.17: Gas velocity distribution (a) Radial velocity profile at 3.5 m from the entrance (b) radial cross-section of velocity contour at 3.5 m from the entrance (c) axial cross-section vectors over the entire simulation domain (d) axial cross-section of velocity vectors around the separator zone.

The gas velocity profiles appear to be reasonably uniform and almost symmetric in most parts. However, in the region beyond the separator, the gas in the upper part of the reactor appears to reverse flow towards the lower wall before being discharge through the exit pipe. The profile along the reactor form a parabolic shape showing a plug flow phenomenon as the flow progresses; this is expected in Eulerian-Eulerian flow predictions. This also agrees fairly with experimental (Tsuji & Morikawa 1982) and numerical literature of horizontal and

inclined flows (Zhu & Wong 2004). The space in between the separator walls and the conical deflector leads to a significant pressure drop, the gas velocity becomes very high creating a swirling motion similar to gas flow around a swirling vane device. The region inside the core below the gas outlet creates a reverse flow of gas where recirculation and extraction occur for the gas phase. The pressure drop at the exit also creates a vacuum where solid particles are entrained by the gases. The gas flowrate and the orientation of the domain lead to the relative ease in the entrainment of particles. The particle concentration has been shown to increase from top to bottom in pneumatic conveying due to the effect of gravity and gas velocity becoming more symmetrical (Lun & Liu 1997). The behaviour near particle-wall has shown that the particles deposit at the bottom of the domain. Therefore, the reverse drag force upward has to be adjusted for maximising separation efficiency and minimising solid entrainment. A parametric analysis for the optimum cone separation and angle was reported by Huard et al. (2010) ,Yu et al. (2014), and Yu & Makkawi (2013) to minimise this phenomenon.

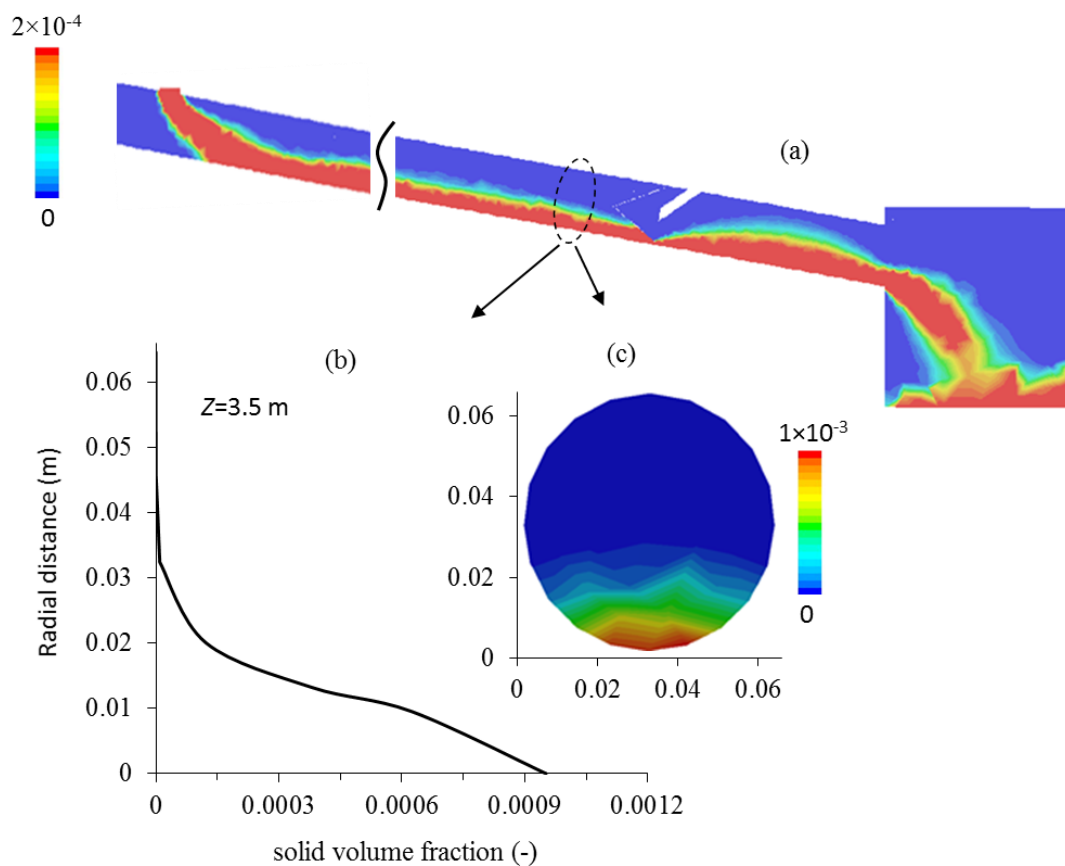


Figure 3.18: Solid (biomass) concentration (a) axial cross-section concentration profile over the entire simulation domain (concentration restricted to 2×10^{-4} to allow better visualization) (b) radial profile at 3.5 m from the entrance (c) radial cross-section contour at 3.5 m from the entrance.

The disengagement of the gas and solid phases happen when the gases are separated sharply through the gas outlet. The concentration profile and velocity profile of the solid phase is needed to determine the behaviour of particles. A timed average concentration profile at different points along the domain is shown in Figure 3.18. The volume fraction of solid initially moves from the inlet top of the reactor to the bottom. The flow is very dilute and the high particle concentration is observed at the bottom. The particles are suspended in between the bottom half of the wall. The lower volume fraction is observed at the top this is due to intensity of pressure effects of the gas and gravity on the particles. The progression is from a homogeneous to an immature dune gas-solid flow behaviour. The flow is dominated near the core region along the reactor, though as earlier stated most of the solids are distributed at the bottom region due to inclination. The gravitational force increases the velocity of the solids; this behaviour is prevalent all through the reactor section. Gravitational settling is present; this is reduced by particles rebounding at the wall. Therefore, increasing the rebound angle reduce gravitational settling at wall. There is weak turbulence near the wall to disperse the particles evenly. The Lagrangian model shows a more even particle distribution as particle-particle level collisions and particle wall collisions are more magnified. The upper part of the reactor is predominantly occupied by the gas phase. This is a classic feature of dilute or intermediate density solid flow in horizontal or slightly inclined pipes and is commonly referred to in pneumatic conveying literature as a strand flow. In the region around the separator, it is evident that the main solid flow is deflected away from the tip of the gas discharge pipe and mainly passes the deflector through the lower gap.

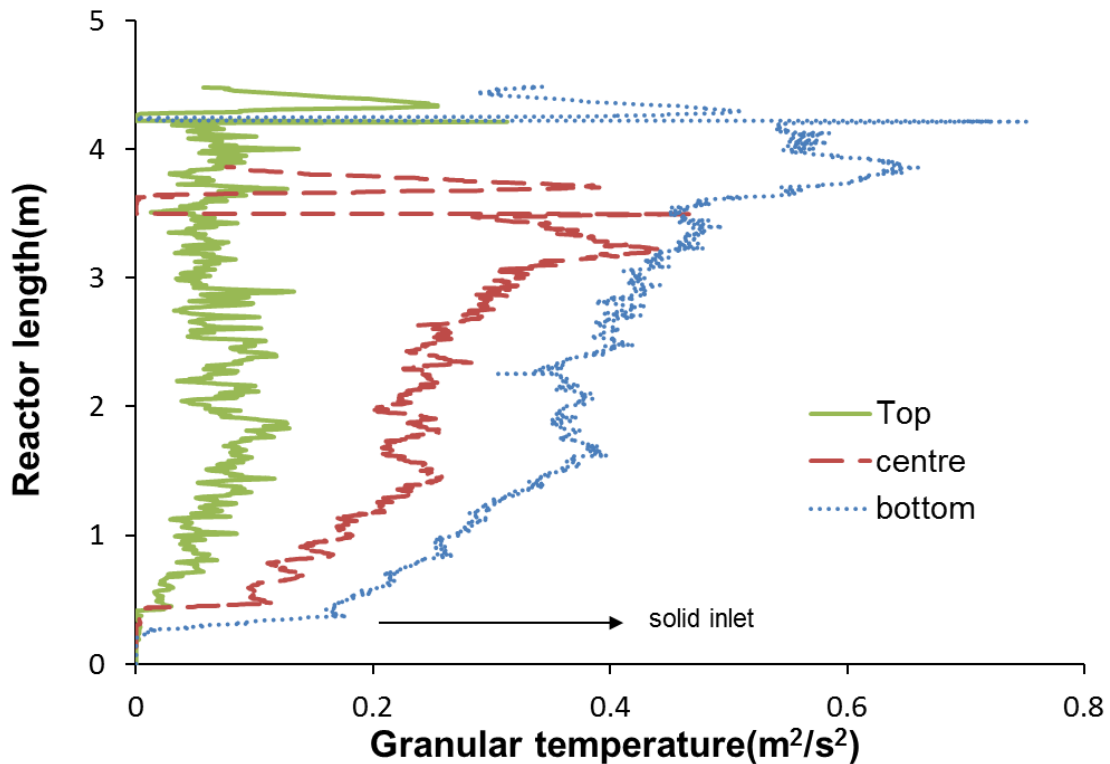


Figure 3.19: Axial granular temperature at points along the domain.

The granular temperature is the measure of average fluctuating kinetic energy of the solid particles (Serero et al. 2008). The granular temperature is an important parameter in gas-solid flow as it indicates the degree of particle velocity fluctuation. According to the kinetic theory of granular flow, these parameters are used in the calculation of solid stress and energy dissipation. In rapid solid flow with the low solid volume fraction, the granular temperature is high as there are more collisions. It decreases with increasing particle concentration after 50% volume fraction reaching the lowest value at enduring contacts (Dartevelle 2003). Figure 3.19 shows the granular temperature at different levels in the domain. The bottom of the reactor has a higher solid fraction than the top, this lead to more collisions and velocity fluctuations.

3.4.2. Residence time distribution

The operating conditions needed to achieve fast pyrolysis have to be adjusted to maximise liquid yield. Huard & Briens (2010) reviewed different gas-solid separators and elaborated their limitation on operating conditions (residence time and gas-solid contact time) for fast pyrolysis. The cyclones and other separators increase additional char contact time. The gas-solid separation mechanism is capable of limiting the effect through achieving optimum residence time. The residence time of the gas is an important parameter used in controlling

secondary reaction that lead to decomposition of liquid to gases. The presence of a near plug flow phenomenon maintains the gas-solid distribution to be fairly linear. This makes the distribution of most of the particles and the gas to be within similar band of residence time distribution. The pathlines in Figure 3.20 shows the time required for the gas phase to exit at the gas outlet.

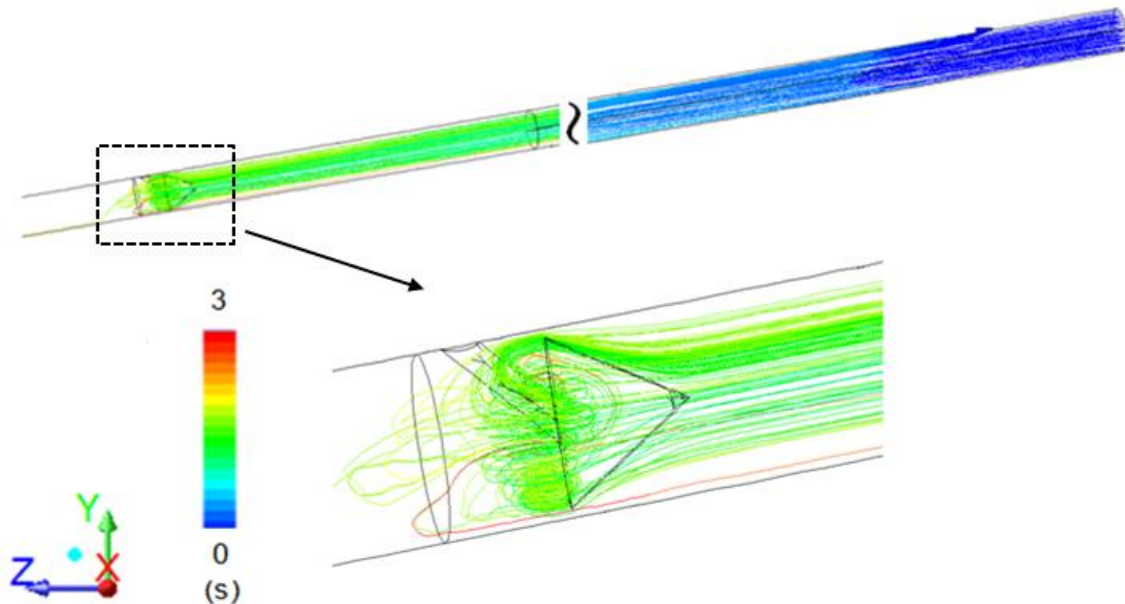


Figure 3.20: Pathlines of gas velocity distribution. This indicates the average residence time of the gas particles

The particle trajectory method from gas velocity pathlines is used to determine the residence time distribution. This is done by releasing 126 massless particles from the inlets to the gas exit. Most of the particles left the reactor with only 10% remaining in the reactor. The residence time distribution (RTD) of the gas phase is represented in Figure 3.21.

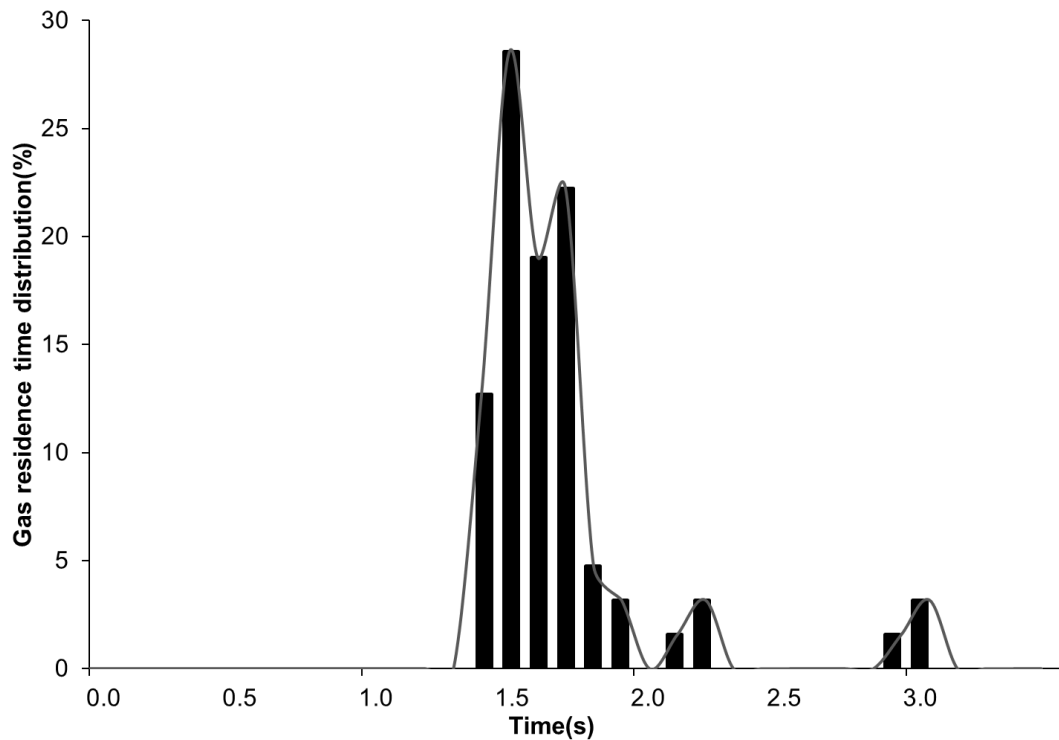


Figure 3.21: Residence time distribution of the gas phase

The majority of the particles were between 1.4-1.9 s with the highest peak at 1.5s. This means that over 80% were within fast pyrolysis range thereby limiting the effect of secondary reactions. The particle residence time is assumed to be greater than the average gas residence time because of possibility of collisions and reverse flow in the reactor and the separator. However, it is essential for the gas residence time to be within the range for fast pyrolysis which should be less than 2s (Bridgwater et al. 1999).

3.4.3. Separation efficiency

The continuous timed averaged separation efficiency of the separator is shown in Figure 3.22. The efficiency was at 100% for the first 2s of the simulation because the solid particles have not reached the gas outlet. The solids reach the gas outlet and the flow is destabilised, the particles are entrained with the gas at the exit. The flow reaches steady state after 3s with separation efficiency of 99.99%. This efficiency is in good agreement with reported experimental literature by Huard et al. (2010). Yu et al. (2014) employed a similar hydrodynamic model for a downer reactor using the novel gas separator. They also achieved separation efficiency of 99.99% using the Eulerian-Eulerian approach.

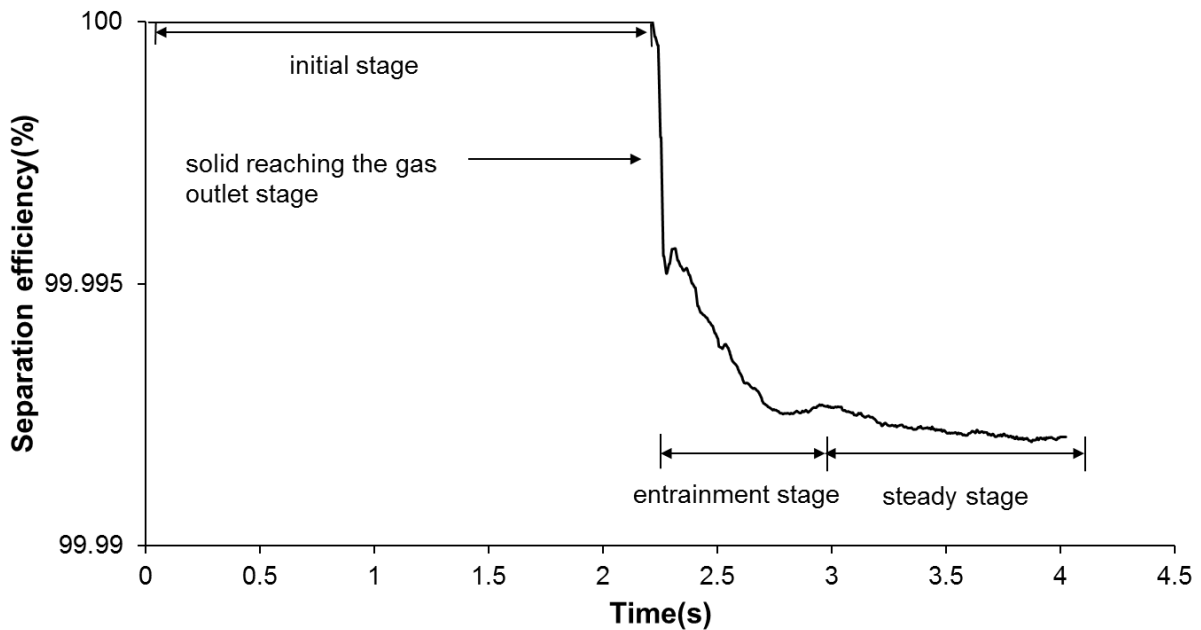


Figure 3.22: Timed evolution of Separation efficiency of the gas-solid conical deflector separation mechanism

The separation efficiency in this separator is greater due to the geometry positively affecting the solid downward velocity, so particles are focused to the wall forming clusters and the gas is separated (Huard et al. 2013). The efficiency achieved by the conical separator is similar to that of a cyclone. This separator is preferred to the cyclone because cyclones affect the solid contact time and gas residence time which increases the tendency for secondary reactions.

3.4.4. Heat distribution and Energy efficiency

In biomass fast pyrolysis, the quality of products is dependent on the process operating conditions such as temperature and heat transfer rate. They mostly affect the conversion efficiencies of the process. The pre-heated inert gas enters the process and sweeps the biomass as the volatilised are being evolved. The heat is transferred from the nitrogen to the biomass concurrently being heated by the solar flux induced as a constant heat flux. This heat transfer process provides the heat for the endothermic pyrolysis reaction. The process of pyrolysis is endothermic therefore enough heat has to be transferred to raise the temperature to optimum required for the process. The temperature distribution of the inert gas and biomass is shown in Figure 3.23. The temperature of the domain was below 500°C; this is well below thermal cracking temperature(600-1280°C) as reported in literature (Wongchang 2013). The equilibrium temperature between the gas and solid phases are

achieved at a height of 1.5m; the temperatures become stable. The final solid temperature near the solid outlet is greater than the gas due to high particle collisions causing increased conduction between them.

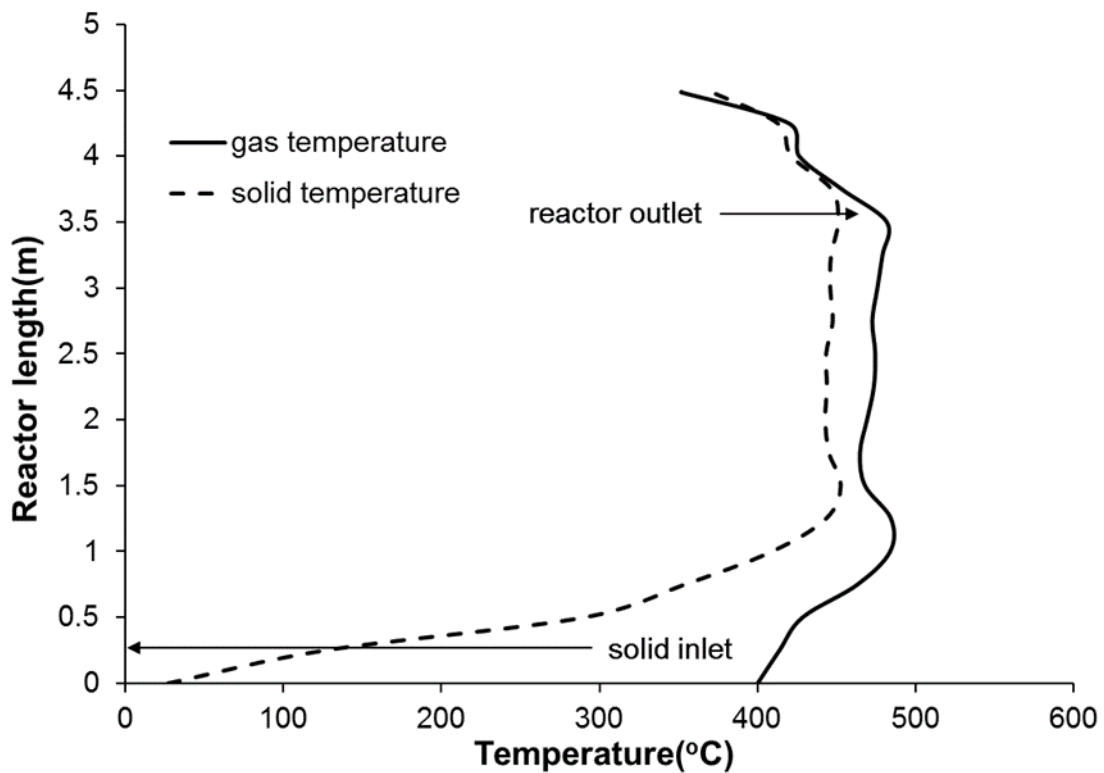


Figure 3.23: Average biomass and gas temperature distribution along the riser

The high heating value (HHV) of char is given as 30MJ/Kg calculated from literature correlations (Sheng & Azevedo 2005). The yield is in good agreement with those reported for switch grass pyrolysis by Sandia National labs (Shaddix & Hardesty 1999). The heat demand for the pyrolysis reaction for the given is 4.18KW. The value is sufficiently supplied through the heat flux induced on the reactor as calculated earlier. The details of thermodynamic performance of the solar trough pyrolysis are given in Table 3.7.

Table 3.7: The thermodynamics and performance of solar parabolic trough pyrolyser

HHV _{biomass} (KJ/Kg)	20.25
HHV _{bio-oil} (KJ/Kg)	20.27
HHV _{product gas} (MJ/Nm ³)	6.96
Q _{solar} (KW)	4.82
Amount of sand needed (g/s)	37.62
Amount of biomass to be combusted (g/s)	0.29
Upgrade factor	1.69
Energy conversion efficiency (%)	41.72
Solar to chemical conversion efficiency (%)	86.85

The biomass to be combusted directly in the process to provide the needed heat was 29% of the total biomass. Solar pyrolysis creates free and clean energy without contamination or pre-processing. The energy supplied by the solar receiver is 4.82KW at the average heat flux.

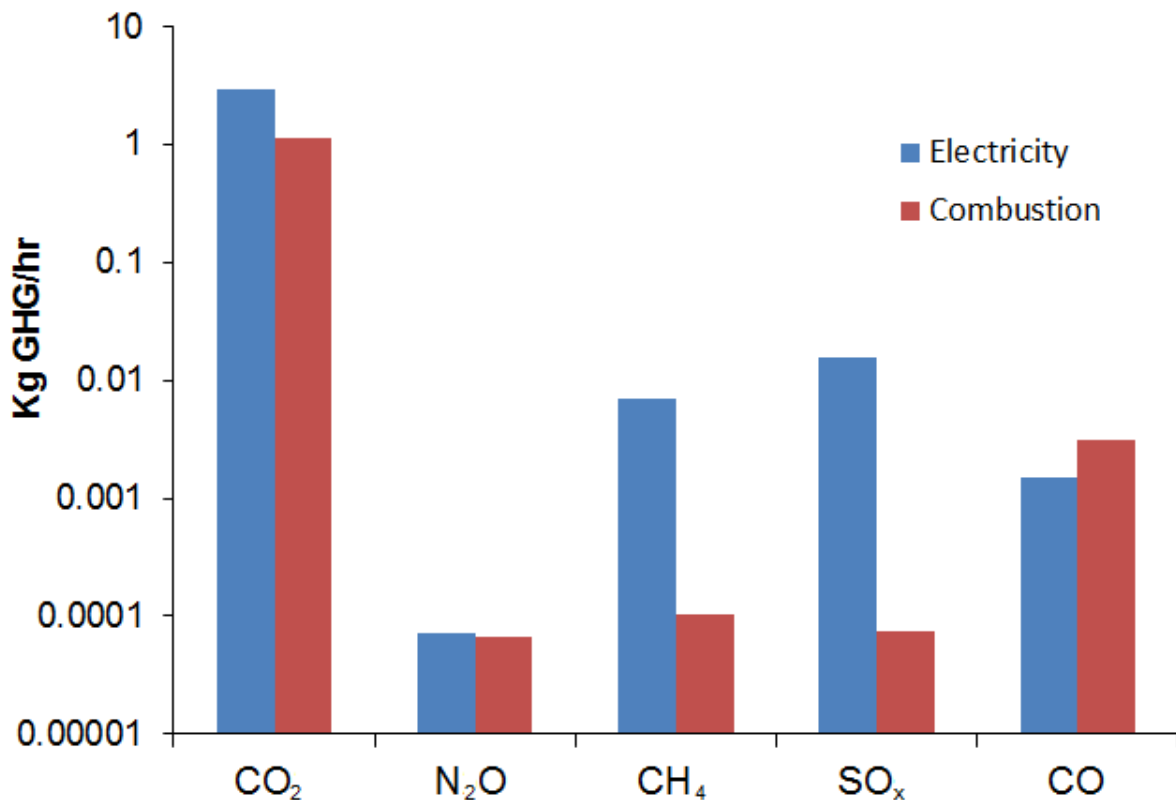


Figure 3.24: Greenhouse gas emissions for heat needed supplied by switch grass combustion and electricity.

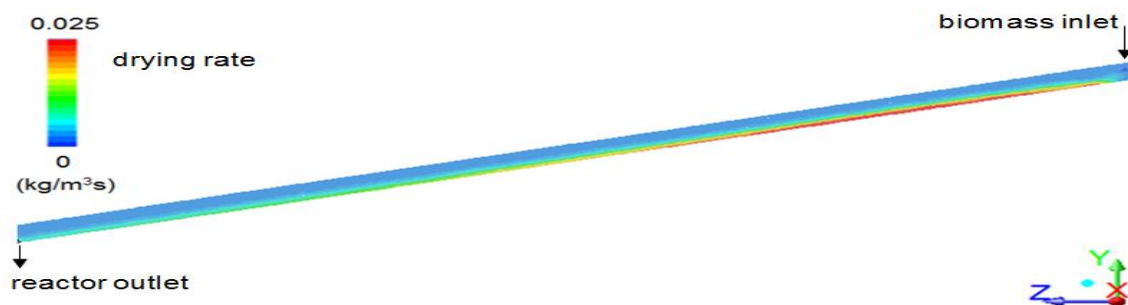
The greenhouse gas (GHG) emission factors are represented in Table 3.8. These factors were used to calculate the different greenhouse emissions avoided when heat is applied indirectly or directly using combustion or electricity. Figure 3.24 shows the greenhouse gas emissions for the different gases. These emissions are avoided by using solar energy as the heat source. The process achieved an efficiency of 42%, this showed considerable heat losses in the process as the remaining energy is mainly used for heating and drying. The solar upgrade factor was 1.69 and solar to chemical energy is 87%. These shows that majority of solar energy has been utilised and the feedstocks heating value has been considerably upgraded.

Table 3.8: GHG emission factors(Deru & Torcellini 2007)(Saidur & Abdelaziz 2011)

Species	CO ₂	N ₂ O	CH ₄	SO _x	CO
Emission factor (kg/kg switch grass)	1.525	9.0 x 10 ⁻⁵	1.4 x 10 ⁻⁴	1.0 x 10 ⁻⁴	4.12 x 10 ⁻³
Emission factor (kg/kwh electricity)	7.0 x 10 ⁻¹	1.69 x 10 ⁻⁵	1.68 x 10 ⁻³	3.79 x 10 ⁻³	3.65 x 10 ⁻⁴

3.4.5. Reaction Rate and devolatilisation efficiency

The devolatilisation rate is dependent on the particle size, heating rate, and residence time. The contours in Figure 3.25 represent the rate of drying and devolatilisation along the reactor length. The drying of biomass is initiated immediately the biomass enters the reactor and reaches maximum.



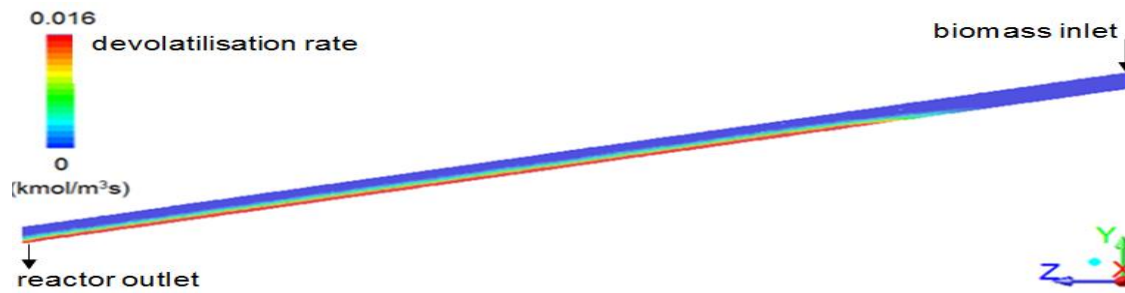


Figure 3.25: The drying and devolatilisation rate for the pyrolysis process along the domain

This maximum is observed up to halfway along the reactor when most of the water content in the biomass has vaporised. The devolatilisation of the volatiles from the biomass progresses. The devolatilisation rate for pyrolysis occurs at the optimum temperatures between 450-500°C. The devolatilisation rate increases due to increase in temperature from the wall heat and most of the energy being utilised for pyrolysis. The biomass is concentrated at the high thermal zone of the reactor. This stimulates the decomposition of the biomass as the temperature increases along the reactor. The devolatilisation rate becomes uniform till it leaves the reactor zone to the separator zone. The remaining bio-char consisting of volatiles, fixed carbon and ash are collected in the solid collection tank. Figure 3.26 shows the devolatilisation efficiency at a localised area along the process domain. The maximum efficiency achieved was 62%, this efficiency remained constant till after the separation zone. The devolatilisation is shown to be dependent on the concentration of biomass and temperature at the given area.

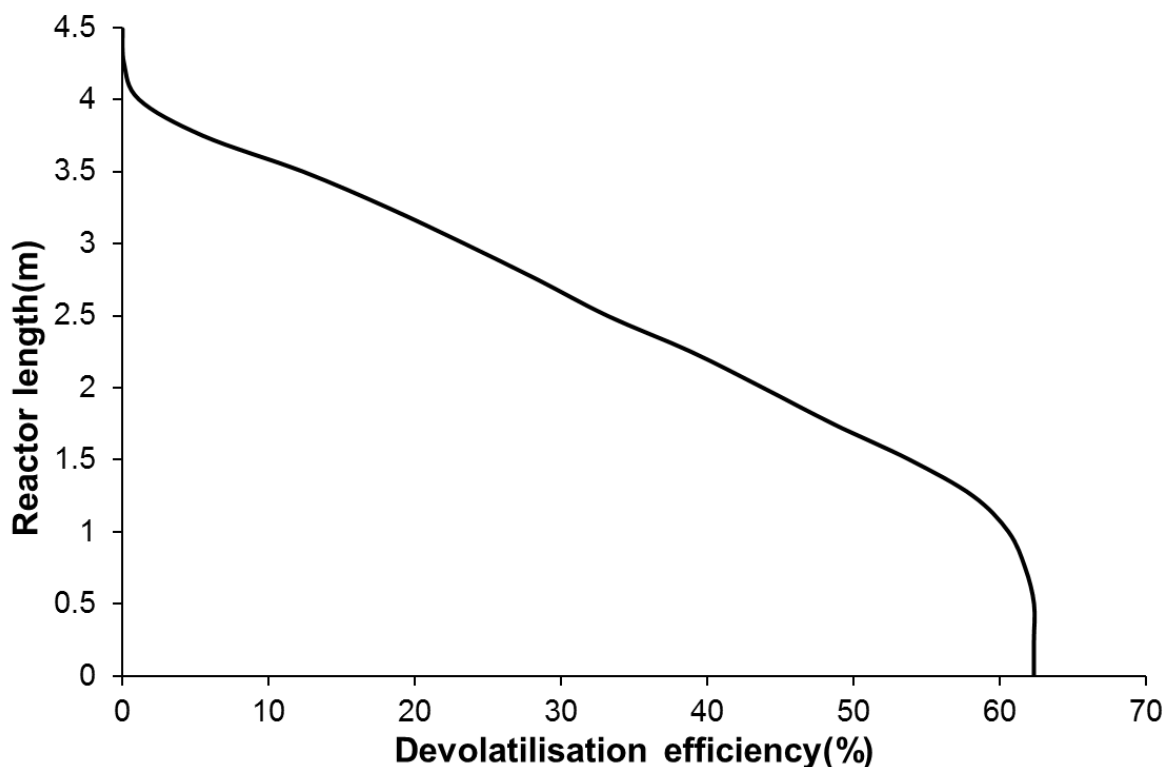


Figure 3.26: The devolatilisation efficiency at localised zones along the reactor

3.4.6. Heterogeneous Reactions and Product gas composition

Biomass fast pyrolysis is an endothermic reaction which energy is required not only for the heterogeneous reaction but drying and heating of the biomass, reactor and inert gas. The timed evolution of the product composition is given in Figure 3.27. The fraction of water vapour reaches equilibrium initially, its fraction decreases as pyrolysis temperature is reached. The pyrolysis products are released until stability is achieved at 1.5s. The pyrolysis phenomenon is explained by initiation of the drying process as water vapour evolves at $<220^{\circ}\text{C}$. This is followed by the decomposition of hemicellulose between $220\text{--}315^{\circ}\text{C}$. The cellulose cracking reactions occur between $315\text{--}400^{\circ}\text{C}$; the weight loss of lignin at temperatures over $>400^{\circ}\text{C}$. Lignin is composed of high density fractions; these fractions at high temperature increase the bio-oil content. The non-condensable gases increase at temperatures $>600^{\circ}\text{C}$, the effect of catalytic and thermal cracking is prevalent at that condition. The product mass fraction of the bio-oil, char and non-condensable gases at the gas outlet is 51.50%, 43.72%, and 4.78%. Since the bio-oil is the main targeted product, it is of first interest to compare the bio-oil yield with literature data obtained in pyrolysis reactors that are partially or fully heated by concentrated solar radiation. Unfortunately, there are no reported studies on the exact type of reactor studied here (horizontal flow reactor), therefore the comparison is made with the available solar fixed bed reactors only. The bio-oil yield was

compared with experimental findings Joardder et al. (2014) and Morales et al. (2014) as in Figure 3.28.

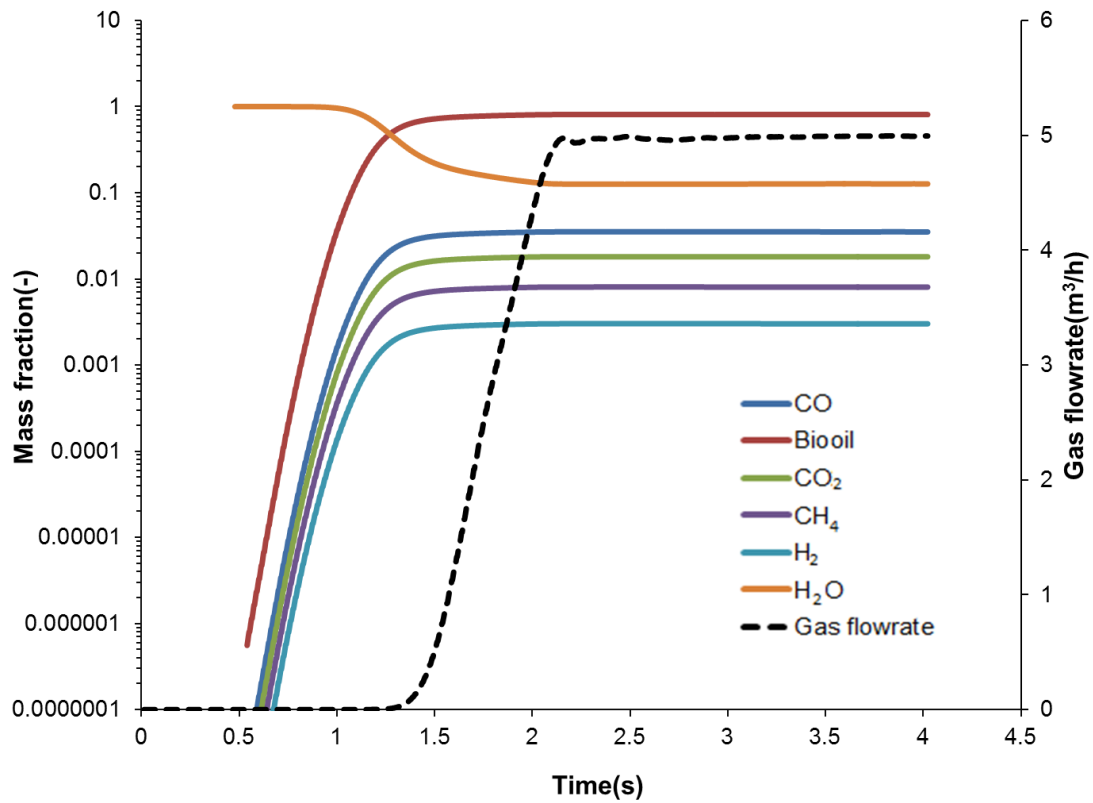


Figure 3.27: Timed evolved product yield composition

Morales et al. (2014) predicted higher bio-oil content because of the presence of photochemical effect caused by radiation penetrating directly onto the biomass and the longer residence time within the reaction section. The particles are of smaller diameter (450 μ m) therefore easily broken down with radiation (Punsuwan & Tangsathitkulchai 2014). The product yields were similar to other pyrolysis reactors for the same biomass sample as shown in Figure 3.29.

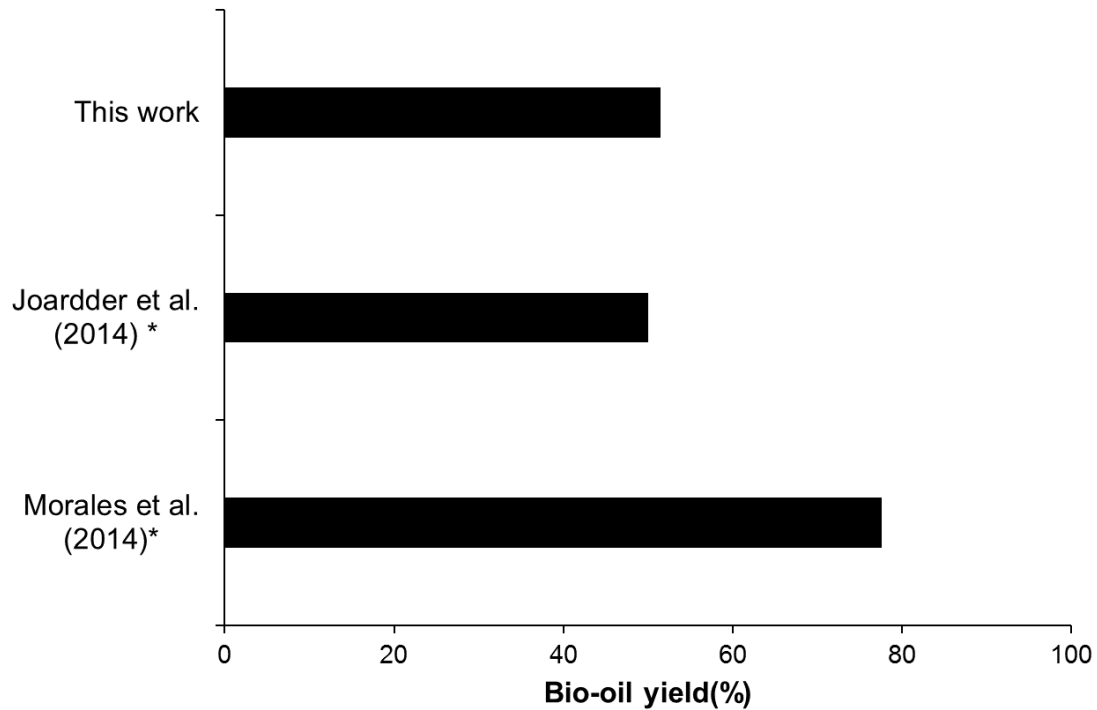


Figure 3.28: Composition of bio oil yields with solar pyrolysers.

*Comments: Joardder et al. (2014); Solar concentrator; rotating tubular reactor; wall heating; date seed biomass; 162-500°C; biomass size volume of 0.11–0.2 cm³; and gas flow rate of 5 L/min
 Morales et al. (2014); Parabolic trough solar concentrator; tubular reactor (borosilicate glass); wall heating; orange peel; 290-465 °C; and biomass size of 20 mm x 20 mm x 3 mm.

Authier et al. (2009) and Boateng et al. (2007) reported low char content; this is due to the presence of secondary reactions. Furthermore, the effect of sand particles on pyrolysis to increase the rate of reaction is seen in Yu et al. (2015) and Boateng et al. (2007).

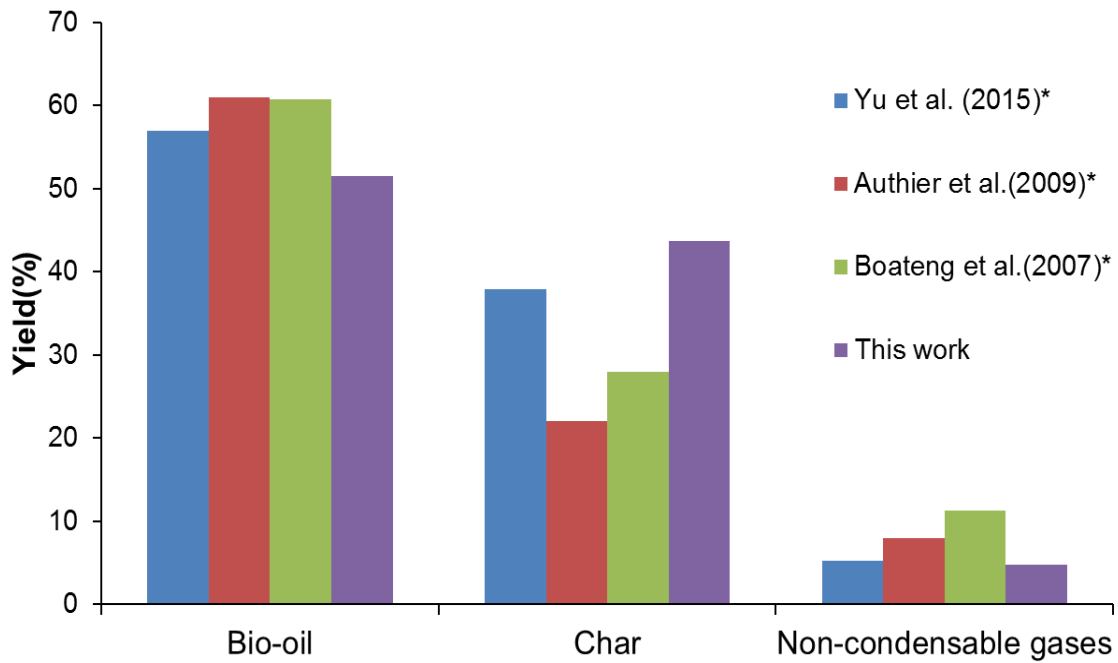


Figure 3.29: Comparison of products yield with other fluid-particle reactors.

*Comments: Authier et al. (2009); Image furnace; quartz reactor; Oakwood; 850oC; biomass size of 5 mm x3mm cylinder; and gas flow rate of 2.2 L/min

Boateng et al. (2007); Indirect heating; fluidised bed; switch grass; 480-550 oC; biomass size of 16mm - 25mm; and gas flow rate of 7 L/min

Yu et al. (2015); Indirect heating; Downer reactor; switch grass; 350-500 oC; biomass size of 500µm

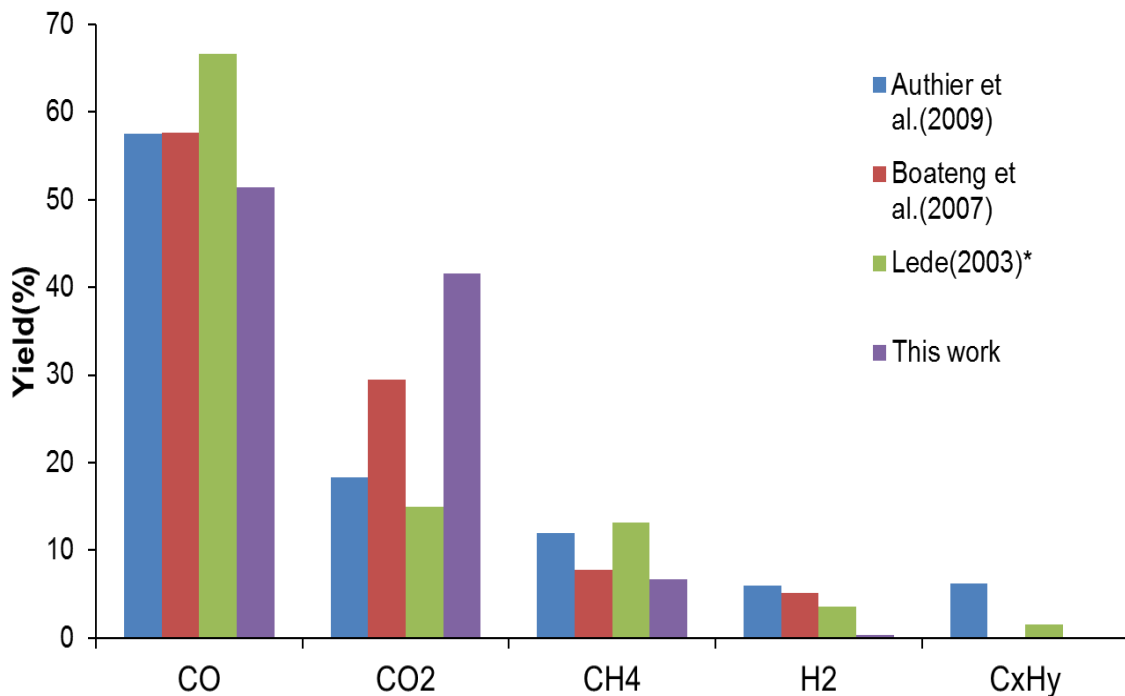


Figure 3.30: Comparison of non-condensable gases compositions.

*Comments: Lédé (2003); Image furnace; rotating tubular reactor; 655 °C; cellulose; biomass area of 2x10⁻⁵ m²

Figure 3.30 illustrates the non-condensable fractions produced compared to similar wall heating reactors. Lédé (2003) compared pyrolysis in a spinning disc and rotating cylinder with wall heating; the reaction occurs at 655 °C. This is relatively a high temperature, which favours high CO yield due to secondary reactions. Boateng et al. (2007) reactor operates within 480-550 °C, hence the higher samples of CO and H₂. The CO₂ yield is attributed to the type of biomass used which is similar to this work. The results showed that the inclined solar pyrolysis reactor has more advantages compared to other pyrolysis reactors discussed due to its ability to produce high quality contamination free and emission free bio-oil with limited tar cracking; the high separation efficiency of the conical separator prevents long contact with char thereby limiting catalytic tar cracking and reforming reactions. The final product composition in pyrolysis is generally dependent on process conditions. When compared to the literature data, this study predicted low CO and H₂ and high CO₂. This discrepancy can be attributed to the effect of excessive contact between the char and the pyrolysis gas in practical experimentation, which lead to catalytic effects through the following reactions:

Boudouard reaction: consuming CO₂ and producing CO ($C+CO_2 \rightarrow 2CO$)

Shift reaction: giving more CO and H₂ ($C+H_2O \rightarrow H_2+CO$)

The study ignores these reactions due to in-situ quick separation of the pyrolysis gas from the char and because of the noticeable phase separation behaviour observed along the reactor length. These factors typically result in increasing CO₂ and lowering CO and H₂, which is consistent with the observation in this study.

3.5. Conclusion

The chapter discussed the several literature of solar thermochemical conversion processes. This was extended for solar pyrolysis of biomass and biomass fast pyrolysis in general. A CFD study was implemented to study a biomass fast pyrolysis process in a solar-thermal reactor. The investigation was implemented using Eulerian-Eulerian model using a robust pyrolysis code to predict the behaviour of switch grass biomass induced with solar flux. This was done in ANSYS Fluent. The behaviour of the separator was analysed based on the flow hydrodynamics and particle entrainment. The greenhouse gas emissions for alternative biomass heating methods were compared to show emissions avoided by using solar energy. The energy efficiency of the process was 42% and the solar utilisation efficiency was 87%. The product yields for bio-oil, char and non-condensable gases were 51.50%, 43.72%, and 4.78%. It has shown that CFD models are capable of predicting separation efficiency and flow dynamics features in a solar reactor augmented with the gas-solid conical separator.

CHAPTER 4 : SENSITIVITY ANALYSIS OF SOLAR PYROLYSIS MODEL

4.1. Literature review

4.1.1. Studies on sensitivity analysis of tubular solar receiver/reactors

Nowadays, CFD models are capable of predicting fluid flow and chemical reactions on all scales of engineering processes. Small-scale experiments can be used for the validation of these models; such an approach allows reducing the cost associated with product development and large-scale experimentation. In recent years, CFD modelling has been used extensively for studying the flow behaviour in solar receiver/reactors and its application in energy conversion.

Cheng et al. (2010) combined monte-carlo ray tracing (MCRT) of the solar flux with CFD to study heat transfer characteristics using Fluent. The MCRT calculates accurately the flux distribution in the outer layer of the absorber tube. The model was in agreement with experimental results. A symmetric characteristics behaviour of the different solar flux is observed in the radial direction. The temperature distribution followed similar characteristics to the solar flux distribution. The model with both conduction and convection had the highest outlet temperature followed by the conduction only model. They showed that radiation losses are the most significant in tubular receivers. The temperature of the outer wall is significantly lower in the conduction only model compared to the other models.

Shuai et al. (2010) reported a thermal and structural analysis of a tubular solar receiver. The model assumes constant heat flux at the top half periphery of the receiver and concentrated heat flux at the bottom half periphery. The heat flux distribution was presented as a fitted polynomial regression to be coupled with the CFD model. The maximal temperature of the uniform heat flux was 21K higher than that of the concentrated heat flux. The temperature variation both in the axial and radial direction was higher for the concentrated heat flux model. The temperature gradient for stainless steel was higher than for copper and aluminium.

Liu et al. (2011) developed a non-isothermal model to analyse the performance of a mid/low temperature solar tubular receiver/reactor and found that temperature increases with tube length, inlet temperature, and feeding rate. They also reported that the temperature of the receiver is affected by the length of the receiver and there is an insignificant effect of receiver thickness on the heat transfer to the fluid.

Wu et al. (2014) studied the heat transfer of a parabolic trough collector using a non-uniform concentrated heat flux. The CFD model was also coupled with a MCRT method ignoring the effect of conduction. The radiation model was based on Surface-to-Surface (S2S) radiation model treated as a grey enclosure. They found that the dominant heat transfers between the heat transfer fluid and absorber tube is conduction and forced convection mainly. They obtained maximum deviation of heat loss of the CFD model, when compared with experiment, of 5.8%. They showed that heat transfer fluid velocity affects the temperature of the absorber or outlet temperature. A high temperature difference between the absorber tube and heat transfer fluid is attributed to low velocity of heat transfer fluid. Hachicha (2013) used radiation model based on discrete ordinate model. Yaghoubi et al. (2013) analysed heat losses in a parabolic trough for a thermal power plant. They also implemented the discrete ordinate (DO) to model the radiation heat exchanges between the receivers. The results showed good agreement with experimental values though the heat loss was higher in the mainly due to operational errors.

Tijani & Roslan (2014) developed a CFD model to study the heat transfer in a tubular receiver. The S2S radiation model was treated as a grey enclosure. They reported the effect of mass flowrate on the heat transfer fluid and absorber. They found out that lower mass flowrate leads to higher absorber and outlet temperature. The lower the flowrate the more heat losses due to convection and radiation; the greatest heat loss is found to be due to convection as is the dominant heat transfer mechanism.

Cheng et al. (2012) in his study used the discrete ordinate radiation model to study the turbulent flow and coupled heat transfer enhancements in an absorber tube. They studied the effect of Reynolds number, fluid inlet temperature, incident radiation and geometric parameters on the absorber wall temperature. They found that increasing the Reynolds number decreases the wall temperature and heat losses. The fluid inlet temperature and incident radiation increase leads to an increase in the absorber temperature and heat losses.

Mwesigye et al. (2015) also used the same radiation model to study the effect of rim angles and concentration ratio. They also concluded that the inlet temperature positively affects the heat losses and absorber temperature. The discrete ordinate model has the ability to model both surface to surface and participating media radiation as S2S is not applicable for Eulerian-granular phases in FLUENT.

Wang et al. (2014) developed a detailed temperature profile of the heat transfer fluid showing a linear relationship between stagnation temperature and time. The temperature changes inversely with velocity in the fluid. Heat flux, temperature, and thermal stress distribution of heat transfer fluid under uniform and concentrated solar flux in a parabolic

trough has been implemented. The temperature distribution of the fluid was varying with circular angle and length (L). A secondary reflector was used for a more homogeneous radial heat flux distribution and consistency in the parabolic trough receiver operation. There was a 4 % loss in efficiency and reduction in temperature difference of the fluid compared to non-homogenous receivers; though there was more uniformity in both temperature and flux of the heat transfer fluid.

4.1.2. Studies on sensitivity analysis of biomass fast pyrolysis

The choice of operating conditions has an effect on the composition of final products; to obtain a high bio-oil yield, a high temperature, high heating rate and very short gas residence time is the requirement. There have been several experimental and numerical studies on the effect of operating conditions on biomass pyrolysis.

Lee et al. (2005) studied the effect of temperature in fast pyrolysis of rice straw and bamboo sawdust which they obtained optimum reaction temperature of around 410-510°C. They concluded that temperature greater than the optimum leads to increase in product gas composition due to vapour cracking reactions.

The influence of particle size on rapeseed pyrolysis of sizes 0.224–1.8 mm has been investigated to study their effect on product yields (Şensöz et al. 2000). They concluded that the effect of particles size positively impacts the gas yields; the bio-oil yield impact is fairly negligible. They found that high particles size has significant effect on the water content, therefore more energy is required to pyrolyse the sample. The temperatures between 450-550 °C is optimum bio-oil production, above which the yield shifts to higher gas yields and lower oil yields.

Furthermore, the different reactions conditions to obtain optimum operating conditions for the feed rate, feed size, fluidizing medium and reaction temperature were investigated in a fluidised bed reactor (Jung et al. 2008). They also attributed the presence of optimum temperature which above that the bio-oil yield starts to decrease and gas yield starts to rise. This behaviour is mainly due to tar cracking reactions attributed to the increase in char content and temperature. Therefore, they all concluded that higher temperatures above the optimum favours gas production. Large feed particle sizes favour the decrease in bio oil yield and increase in char yield. This is due to the limitation of heat transfer to the inner part of the feed sample. The feed rate affects the product distribution by increasing the yield of bio oil, this is because the high flowrate enhances the prevention of secondary cracking reactions. Kalgo (2011) also studied the effect of temperature and particle size for beech, moringa, pine, willow, miscanthus, and *Jatropha*. They obtained the most yield of bio-oil at particle sizes 355-500µm. This proves the fact that small particle sizes favour the production of oil.

Mante & Agblevor (2011) studied the effect of feed and gas flowrate in a fluidised bed reactor for fast pyrolysis of manure and wood shavings. The feed rate affects the heat transfer and the solid residence time of the biomass feed. An increase in the feed rate leads to an increase in bio oil yield up to a temperature of 500 °C. The possibility of decreased heat transfer rate leads to the production of high molecular weight compounds. There are less thermal cracking reactions so less production of non-condensable gas. The liquid yield is rarely affected by increase in the feed rate at higher temperatures.

The gas flowrate is affected by the residence time of the gas and the final pyrolysis product composition. The increase in gas flowrate leads to a high heat transfer rate with short gas residence time; this minimises secondary reactions (thermal cracking, repolymerization and recondensation) thereby increasing the yield of bio-oil. They concluded that higher temperatures and long vapour residence time leads to secondary reactions. The yield of volatile oil reaches a maximum and decreased as temperature increases. The temperature increase promotes the devolatilisation of biomass up to the optimum where gasification of primary tars changes the product composition.

Zeng et al. (2015) reported the influence of temperature, gas flow rate on the solar pyrolysis of beech wood. The temperature drastically affects the product composition. The observed that increase in temperature from 600 to 800 °C, the gas yield increased from 20.9% to 27.8%. This is mainly due char decomposition and other secondary reactions that led to char decrease from 16.8% to 9.4%. The gas composition H₂ and CO yields increase significantly at temperatures higher than 600°C. The found that increasing the heating rate decreases the char and bio oil yield. The enhanced tar and char cracking reaction are initiated due to reduction in the limitation to heat and mass transfer. The studied gas flowrate using argon as the sweep gas from 6 to 12 NL/min. The bio-oil yield decreased from 37.5% to 27.2% with constant char yield. Generally, the increase in gas flowrate decreases bio-oil residence time thereby inhibiting secondary reactions. The volatiles become diluted at higher gas flowrate, which reduce gas-particle reactions.

Ashcraft et al. (2012) used a gas/solid vortex reactor for fast pyrolysis with a multiphase Eulerian model. The effect of flow rate and temperature distribution was investigated on product distribution. They found that high temperatures up to 500°C favour liquid production; the temperature profiles were very similar though they were at different temperatures. The tar yield increased from 74% to 76% between the temperatures of 450 °C-500 °C. The compared simulations for the base case at feed rate of the biomass at 0.0348kg/s and inlet gas 0.0222kg/s with 1.5x and 2x this values. This showed increased biomass fraction and

convective heat transfer coefficient in the reactor. The residence time of the gas becomes shorter as the rates increase; the product distribution remained constant.

Xue et al. (2012) studied the pyrolysis of cellulose and red oak in a fluidized bed using a Eulerian-Eulerian multiphase model. They also studied the effect of operating conditions on the product yield. The model was validated with an experimental procedure for both red oak and cellulose. There was good agreement between the simulation and experiment for different sizes of biomass. They showed that smaller particle size is attributed to high apparent density of the particles; thus the bio-oil yield is likely under-predicted in CFD models. The effective diameter affects the residence time and product yield. They obtained high product yield for larger particles due to their longer residence time. The operating temperature is important in determining the final products. The optimum temperature reached was 500°C, where bio-oil yields were at their peak. An operating temperature above that leads to an increase in the gas composition due to cracking reactions. The yield of char is negligibly affected by temperature. The fluidising gas velocity affects the residence time of the gas and solid phases; this leads to incomplete reaction at high fluidising velocities. They concluded that both the micro particle model and reactor environment model are crucial for predicting pyrolysis processes.

Xiong et al. (2013) also investigated the effect of operating conditions on the product distribution. The temperature of the fast pyrolysis process can be controlled through the temperature of the fluidizing gas. The increase in temperature at constant nitrogen gas flowrate positively affects the velocity of the gas. This abruptly changes the bio-yield and gas yield due to more biomass being devolatilised up to the optimum temperature of 500°C. The variation in the velocity of nitrogen leads to a decrease in gas and char yields. This is due to the very short residence time of the bio-oil which limits secondary reactions. The mass of unreacted biomass increases as well as there is not sufficient time for complete conversion. The presence of two competing phenomena affects the final product yield due to variation in nitrogen velocity. The bio-oil residence time is reduced to avoid secondary reactions and at the same time the biomass residence time is reduced leading to less tar production. Overall high gas velocity has a positive impact on the bio-oil yield. With particle sizes below 900µm there is a positive relationship with the product yield. The percentage of unreacted biomass decreases as the particle size increases up to 1200 µm. This increases the residence time of the particles in the reactor. The variation in particle sizes can lead to high inter-particle temperature gradient. This increases the heating time of the biomass thereby affecting the rate of the pyrolysis reaction. The phenomenon was not considered by the author due to the nature of the Eulerian-Eulerian model.

A 3D Eulerian-Eulerian was also developed to study biomass pyrolysis with emphasis on the product and fluidising gas (Mellin et al. 2013). They studied the effect of temperature and fluidising gas velocity. The increased fluidising velocity raises the temperature as more heat is added to the system. There was low liquid concentration for high gas velocities along the reactor. The effect of fluidising velocity showed increased residence time; they also showed significant liquid yield drop at high temperature similar to the authors stated earlier.

Sharma et al. (2015) also reported the effect of temperature, gas velocity and particle size on product yield and hydrodynamics in a fluidised bed. The effect of temperature variation validated both experiment and CFD models that maximum liquid yield is achieved at 500°C. The bio-oil yield decreased from 77.7% to 6.4% between temperature 500-700 °C for a particle diameter of 400µm. This showed the significant effect of secondary reactions above 500°C. The ratio of mean gas residence time and tar conversion time should be below 0.1 to prevent tar cracking reactions. At high gas velocities this ratio is well below 0.1 therefore there will be simultaneous increase in liquid yield. The gas velocity increase had no effect on the biochar yield. Small particles favour good distribution and mixing in the reactor due to a high drag force from the fluidising gas. They concluded increasing the particle size leads to low heat transfer rate which causes the biomass to char.

Ranganathan & Gu (2016) reported a CFD model for fluidised bed pyrolysis. The model compared different particle types, particle diameter, gas velocity and temperature. They also compared a simple, global and advanced pyrolysis models. The advanced model showed very good prediction compared to experimental results due to a more detailed reaction mechanism of primary, intermediate and secondary reactions. The simple model generally has a higher liquid yield as the condensable gases are produced quickly as an initial step rather than several steps. Also, the secondary reaction produces more condensable gas leading to more liquid yield. The global scheme over predicted the non-condensable gas; the char was under predicted due to the absence of intermediate reactions. They all accurately predict qualitatively the liquid yield similar to experimental results by Kalgo (2011). The advanced model requires high computational cost due to the significantly large number of reactions. They showed that different biomass samples produce different product yield. The increase in particle diameter leads to a decrease in non-condensable gases because in larger particle primary pyrolysis is the major reaction. The operating temperature of the reactor was varied from 400 °C-600 °C. The liquid yield increase from 57% to 60% at 500 °C and dropped at 385 °C with a rise in both char and non-condensable gas yield. They concluded that further study on the residence time of the gas and particle phase should render a complete picture of the analysis.

Lastly, all the authors discussed above concluded that operating conditions and model parameters affect the final product yield in both CFD and experimental techniques. This chapter looks into an earlier research on solar pyrolysis as a benchmark used to produce an optimization of the effect of operating conditions. The base case model in Chapter 3 has been optimised for the different characteristics to be studied in this chapter. Therefore, the hydrodynamic, reaction and heat transfer model remains the same unless otherwise stated. The effect of heat flux and the different heat transfer mechanism attributed to solar receivers were also reported in this study.

4.2. Results and discussion

4.2.1. Heat flux distribution

The heat flux on the receiver wall is dependent mainly on several characteristics: the incidence angle and aperture size. The actual heat flux in a tubular receiver is non-homogenous and changes in both axial and radial directions. The heat flux has been improved to be more homogeneous through including a compound concentrator to the actual trough receiver. This reduces the maximum flux by introducing homogeneity into it.

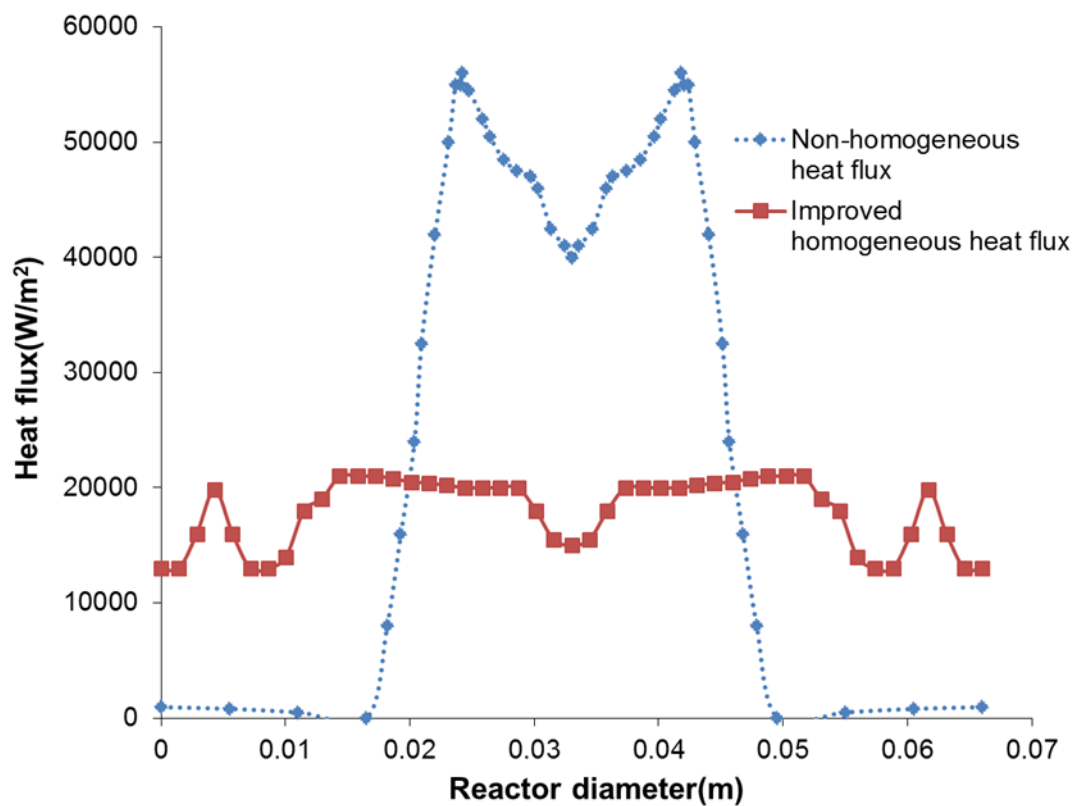


Figure 4.1: Heat flux distribution in the absorber tube of a parabolic trough solar collector (modified from Wang et al. (2014)).

The average circumferential solar heat flux distribution for the non-homogeneous and improved parabolic trough concentrator around the absorber is represented in Figure 4.1. The heat flux was implemented as a User defined function (UDF) in Fluent 14.0 based on polynomial regression parameters as shown in APPENDIX A: UDF codes. The UDF was coupled as a wall boundary condition to use the actual wall heat flux and calculate the temperature of the fluid domain. The regression values for the non-homogeneous flux distribution is given by the functional fit below:

$$\left\{ \begin{array}{l} Q = -5E + 06 x^3 - 462810 x^2 - 7969.7x + 950 \quad x \in (-0.035,0) \text{ top wall}, \\ Q = 5E + 06 x^3 - 462810 x^2 + 7969.7x + 950 \quad x \in (0,0.035) \text{ top wall}, \\ Q = 2E + 11 x^4 + 2E + 10 x^3 + 4E + 08 x^2 + 1E + 06x + 41906 \quad x \in (-0.035,0) \text{ bottom wall}, \\ Q = 2E + 11 x^4 - 2E + 10 x^3 + 4E + 08 x^2 - 1E + 06x + 41906 \quad x \in (0,0.035) \text{ bottom wall} \end{array} \right. \quad (4.1)$$

The regression for the improved homogeneous heat flux are given by the functional fit below:

$$\left\{ \begin{array}{l} Q = 3E + 15x6 + 3E + 14x5 + 1E + 13x4 + 2E + 11x3 + 1E + 09x2 + 2E + 06x + 12926 \quad x \in (-0.035,0) \text{ top wall}, \\ Q = 3E + 15x6 - 3E + 14x5 + 1E + 13x4 - 2E + 11x3 + 1E + 09x2 - 2E + 06x + 12926 \quad x \in (0,0.035) \text{ top wall}, \\ Q = 6E + 14x6 + 7E + 13x5 + 3E + 12x4 + 5E + 10x3 + 4E + 08x2 + 649350x + 14974 \quad x \in (-0.035,0) \text{ bottom wall}, \\ Q = 6E + 14x6 - 7E + 13x5 + 3E + 12x4 - 5E + 10x3 + 4E + 08x2 - 649350x + 14974 \quad x \in (0,0.035) \text{ bottom wall} \end{array} \right. \quad (4.2)$$

The regression values were both obtained from Figure 4.1. The effect of the different circumferential heat flux is likely to affect the average temperature in the reactor. The exit temperatures for the different heat flux distributions is shown in Figure 4.2. The variation of outlet temperature in the two conditions were that the non-homogeneous model has a higher temperature due to the high heat flux concentration compared to the homogeneous case. The outlet temperature achieved was 578 °C compared to 548°C for the homogeneous.

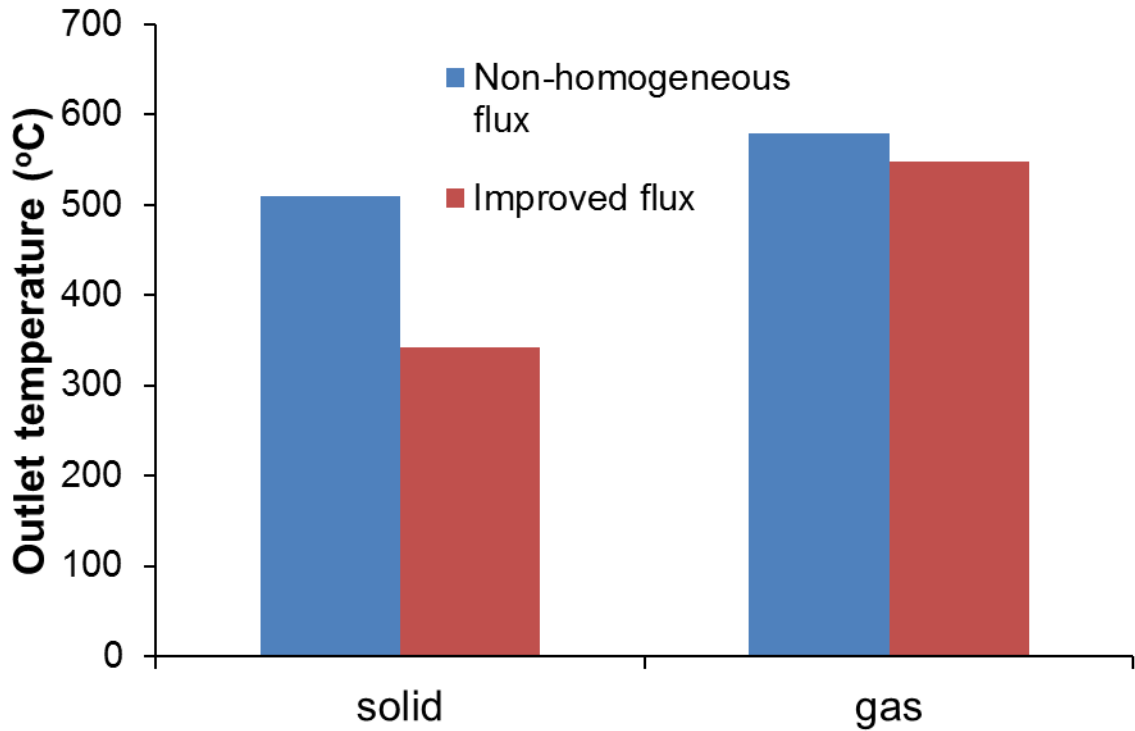


Figure 4.2: Parametric results for non-homogeneous flux and homogeneous flux for exit temperature of the gas and solid phases.

The temperature gradient is high with continuous augmentation of the flux according to Shuai et al. (2010) in non-homogeneous heat flux models. They also obtained higher temperatures overall for the non-homogeneous model. The conclusion is non-homogeneous provides a greater heating rate and temperature compared to the homogeneous flux. The advantages of uniform heating are mainly that the temperature becomes more uniform and mechanical failures such as breakage of glass, deformation, coating degradation and hydrogen formation caused by high temperature variation is limited.

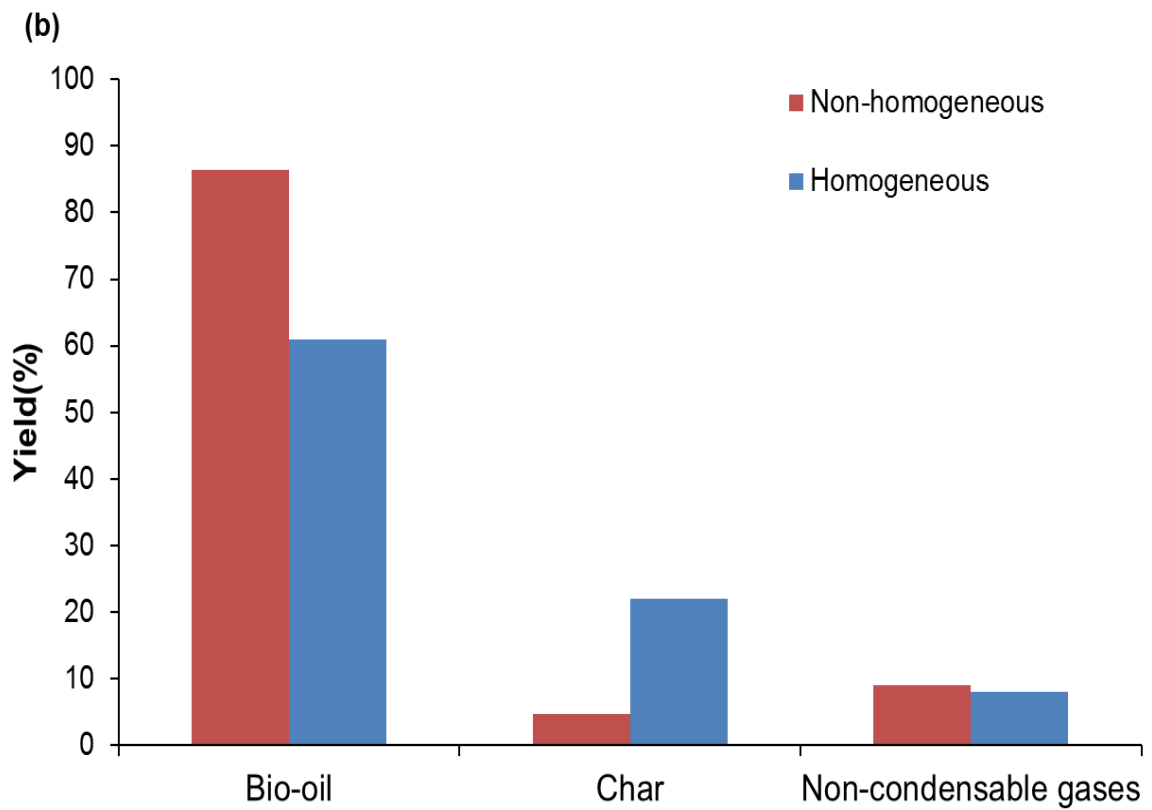
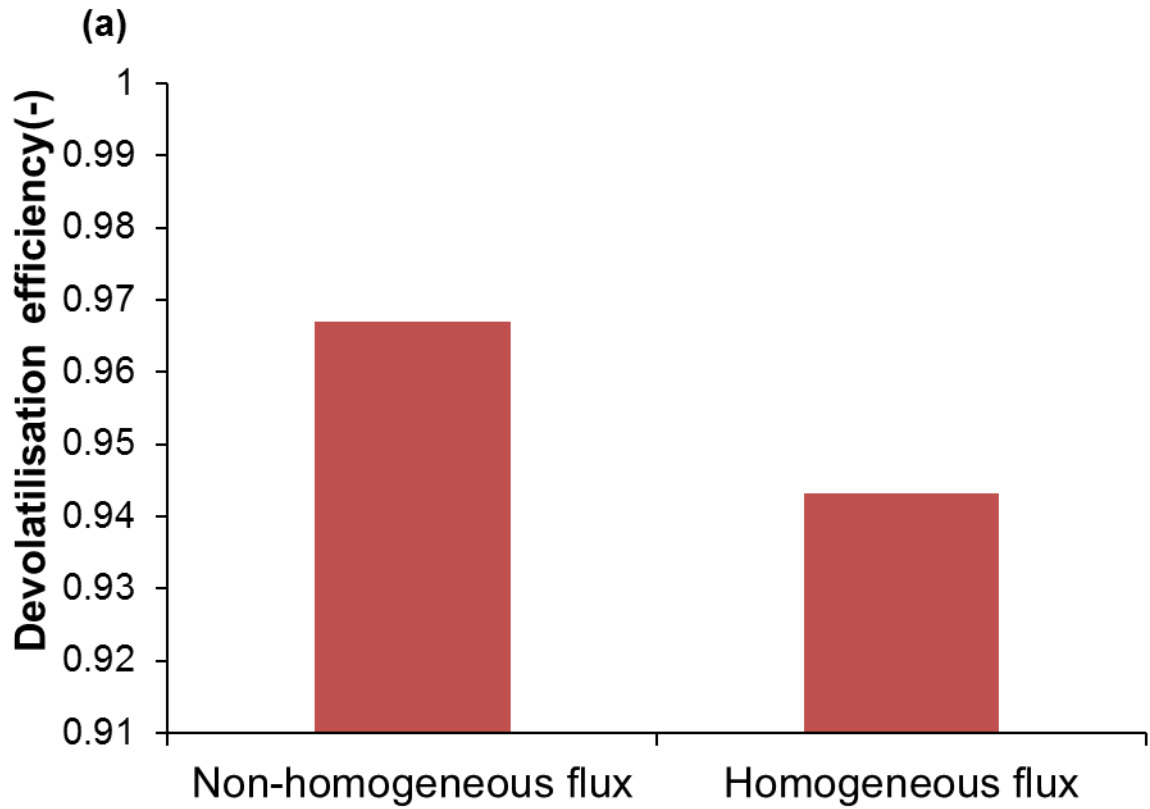


Figure 4.3: Parametric results for non-homogeneous flux and homogeneous flux a) Devolatilisation efficiency b) final product composition

In Figure 4.3, the devolatilisation efficiency for the non-homogeneous model was higher compared to the homogeneous model. Temperature has an important effect on the devolatilisation rate in a pyrolysis process. This makes the non-homogeneous model is more likely to devolatilise a high percentage of the biomass. The bio-oil yield is greater in the non-homogeneous model, this is due to the high flux at the bottom leading to higher biomass temperature and more devolatilisation. The final product yield are qualitatively similar to values obtained for contact and radiant pyrolysis by Lédé (2003). The temperature causes the possibility of cracking reactions. The inclusion of secondary reactions will improve the gas yield very similar to experimental values though this has not been considered in this work.

4.2.2. Heat transfer mechanisms

The main mechanism of heat transfer inside the tubular receiver is through forced convection. The model was adjusted to include a conduction model through the walls of the receiver and radiation model at the surface of the receiver. The conduction wall model attributes both heat transfer through forced convection from the wall of the receiver to the heat transfer fluid and through the wall. The wall was assumed to have a thickness of 0.004m considering heat losses through the wall. The radiation model includes also conduction through the wall and forced convective heat transfer to the heat transfer fluid. The discrete ordinate model is used to model the radiation heat transfer in the process. The absorption coefficient of biomass was assigned a value of 1 (Liu 2014). The gas phase has neither rotational nor vibrational excitement at low temperatures. Therefore, the gas is assumed transparent to thermal radiation as suggested by Lathouwers & Bellan (2001). All other operating conditions have been kept the same as the base case in Chapter 3. The detail on the heat transfer model formulation is given in Chapter 2. The heat transfer mechanisms used have a strong impact on the average temperature of the phases leaving the reactor. The exit temperatures for the conduction and radiation cases are shown in Figure 4.4a at the corresponding exits.

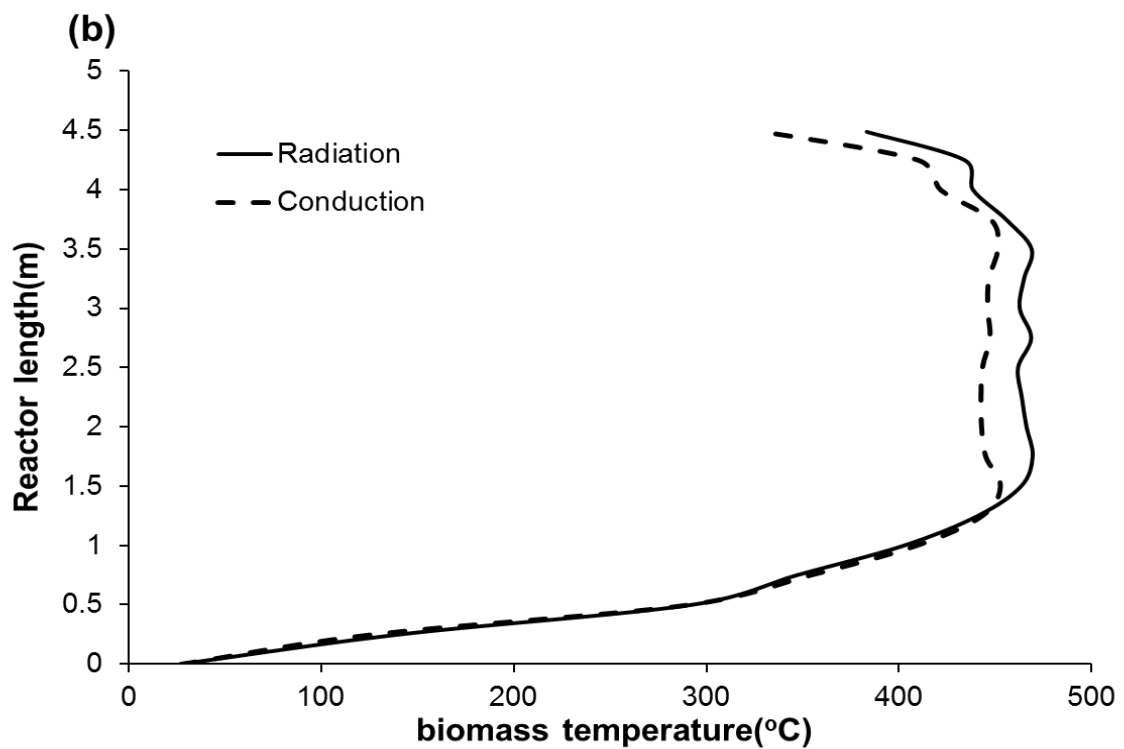
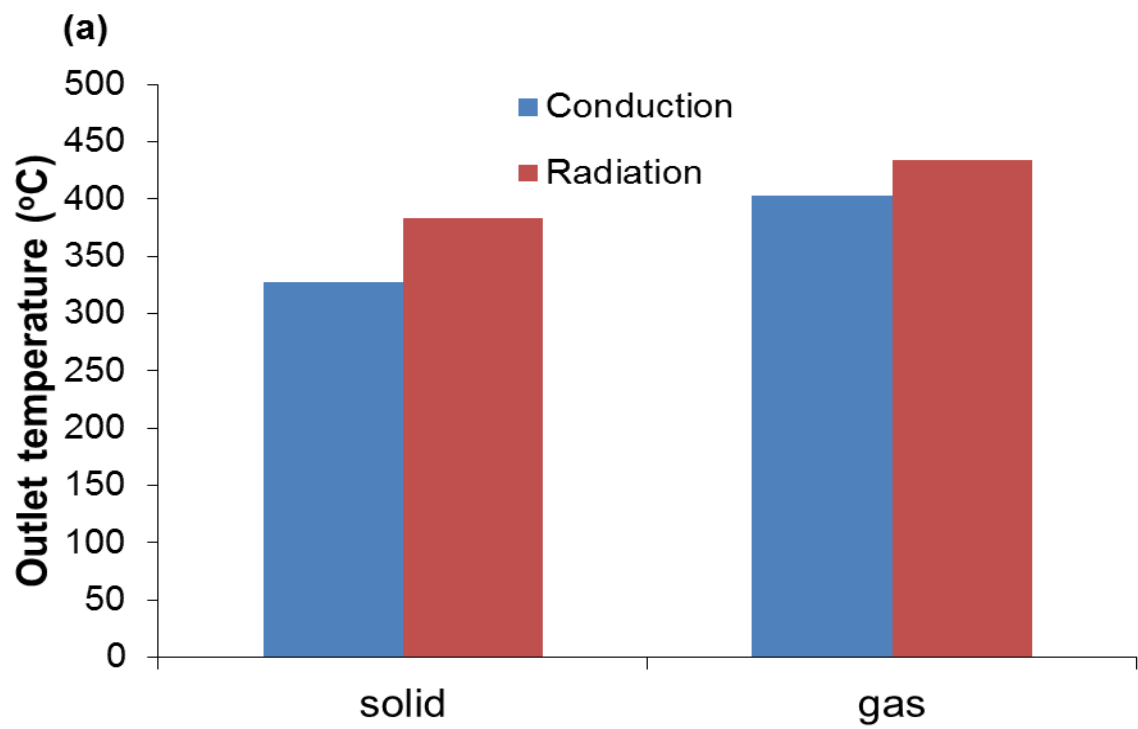


Figure 4.4: Parametric results for (conduction+convection only) and complete model (conduction+convection+radiation) a) exit temperature of the gas and solid phases b) average temperature of the solid phase.

The maximum outlet temperature of the solid increased from around 328 °C to 383 °C. This increase was due to the effect of particle concentration on radiation. The effect of radiation is generally less pronounced in the gas phase. This is due to the fact that gas-phase radiation effect was not considered, as the presence of two temperature effect was assumed in the domain. The average temperature profile in the domain follow a similar trend by which the temperature increases sharply at start, then reaches a peak before thermal equilibrium is achieved (see Figure 4.4b).

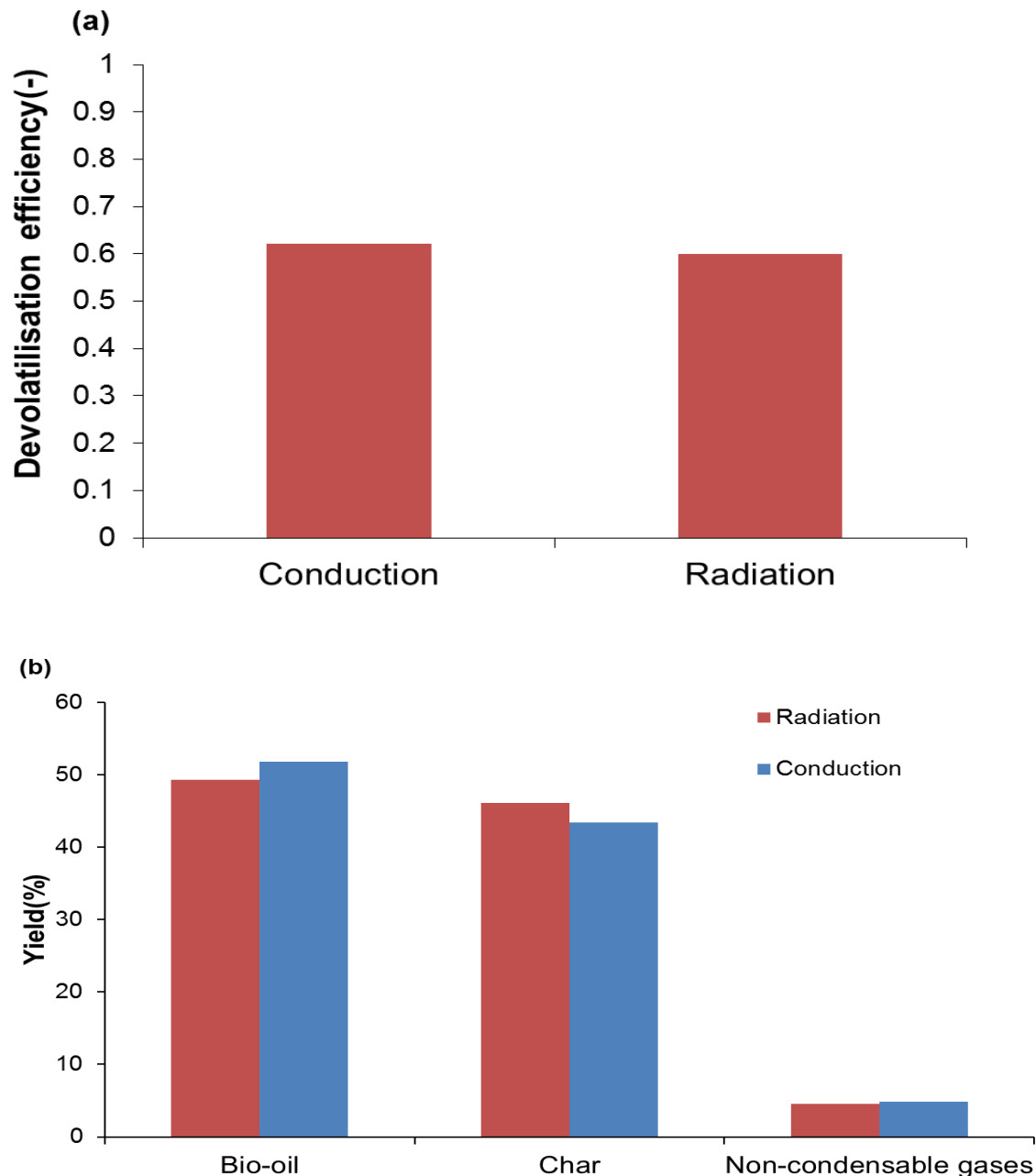


Figure 4.5: Parametric results for cases of wall model (conduction+convection only) and complete model (conduction+convection+radiation) a) devolatilisation efficiency b) final product composition

The devolatilisation efficiency for the conduction and conduction case decreased from 62% to 60% as shown in Figure 4.5a. It shows that the higher temperature in the radiation case produced less devolatilised biomass. It is realised that the majority of the energy is lost to the environment or to heat the biomass. Therefore, to improve efficiency the radiation heat losses need to be kept to the minimal. The final product composition for the two cases were compared in Figure 4.5b. The bio-oil yield and gas yield decreases, when radiation was added to the case. This low devolatilisation rate caused the bio-oil yield to be lower for the radiation case, though qualitative agreement is achieved for both cases. It has been shown that radiation increases the effect of secondary reactions as this effect was not considered in this study (Di Blasi 1996). This led to the low level of non-condensable gases as compared to the conduction model. The biomass becomes more charred; this phenomenon occurs at low radiative heat flux. As char is broken down almost completely in high radiative heat flux processes as reported by Lédé (2003).

4.2.3. Effect of sweeping gas temperature

The temperature of the sweeping/inert gas has a considerable effect on the average temperature of the reactor. It is crucial in determining the overall pyrolysis products and readily affects the kinetic rate of devolatilisation. The sweeping gas inlet temperature for cases of 200°C and 300°C was analysed to see its effect on the product yield. The average biomass temperature distribution and exit temperatures for both phases at sweeping gas temperature of 200°C and 300°C is represented in Figure 4.6.

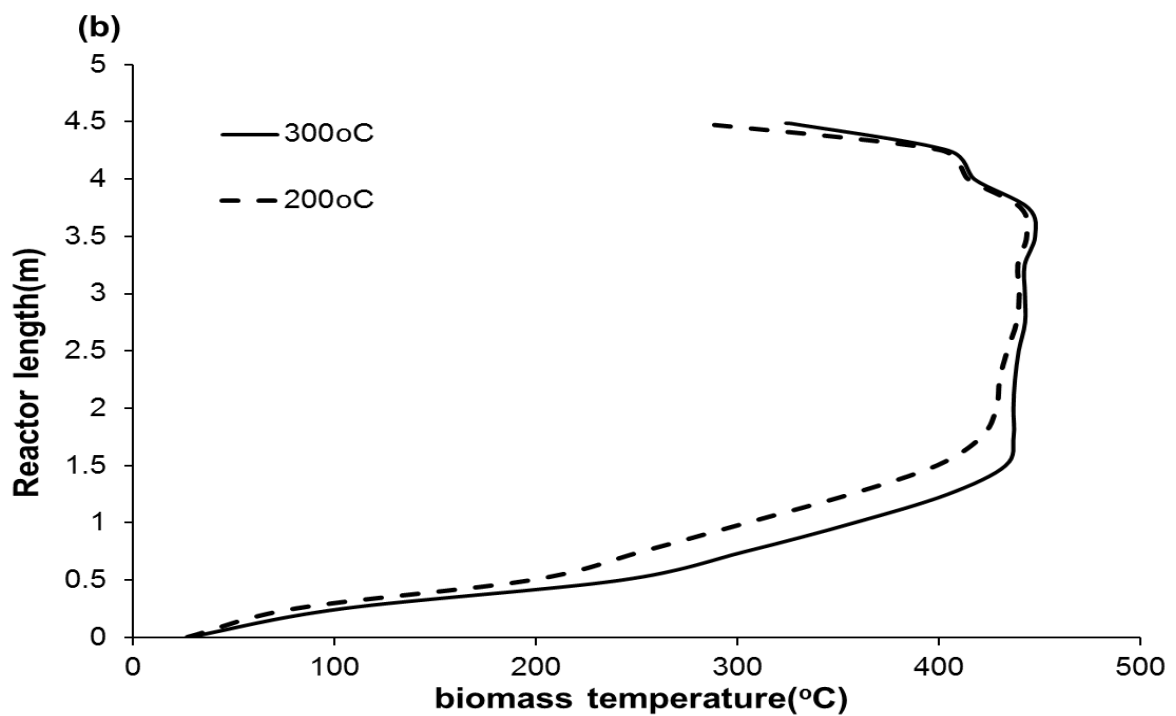
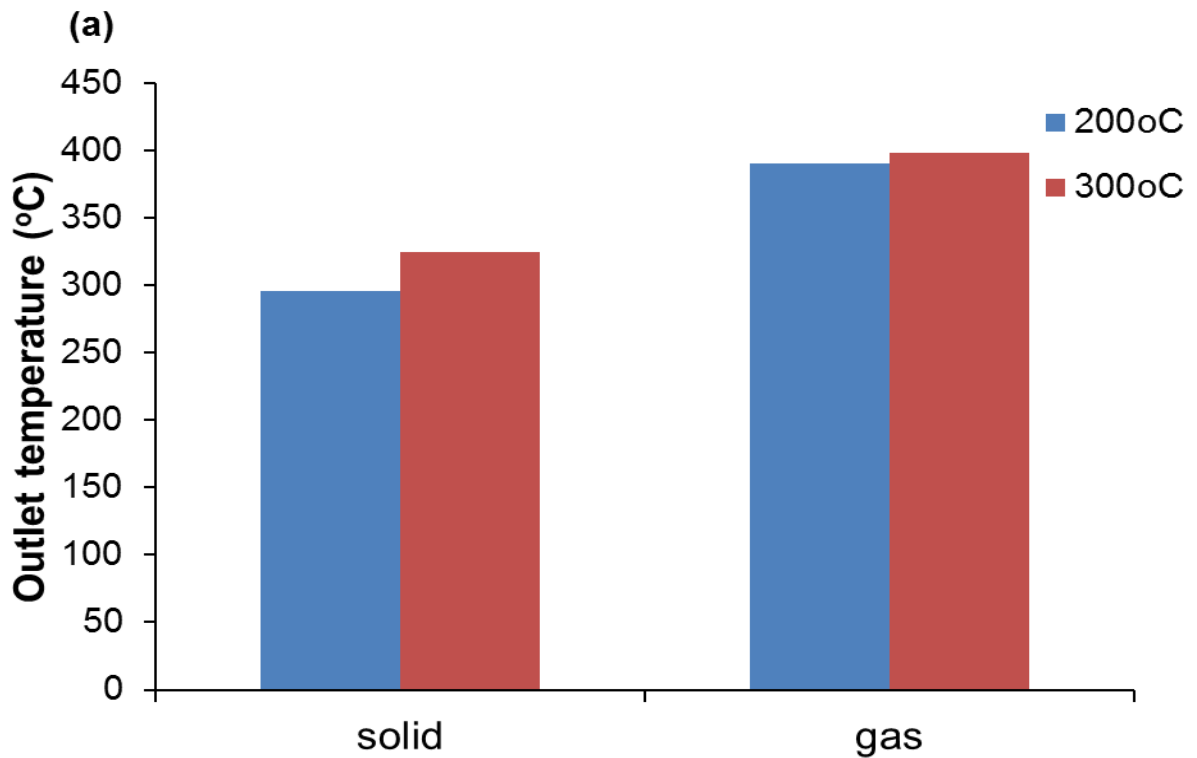


Figure 4.6: Parametric results for cases of 300°C and 200°C sweeping gas temperatures a) outlet temperature at the gas and solid outlet b) average biomass solid temperature

The increase in inlet nitrogen gas temperature leads to an increase in the overall reactor temperature and the final temperature of both phases. The flowrate remains constant therefore the velocity of the gas changes due to change in temperature. The effect of

temperature on the devolatilisation rate is observed in Figure 4.7a; the efficiency is higher for high temperatures. This relationship causes the biomass to decompose and react. There is sufficient heat at high temperatures and hence the level of unreacted biomass drops when temperature rises. We can see that this favours an increase in bio-oil and gas yield, as shown in Figure 4.7b. This is consistent with literature results (Aramideh et al. 2015). The lower temperatures favour char yield decrease as the maximum temperature achieved in all cases is below 550°C. The temperatures are well below operating conditions for secondary reactions to occur. Sharma et al. (2015) also proved that between 400 °C -500 °C increase in temperature causes the char yield to decrease and the bio-oil and gas yields to increase; this validates our results. The experimental findings from literature concluded that temperature is a major parameter that negatively affects the char yield in a pyrolysis process (Mante & Agblevor 2011).

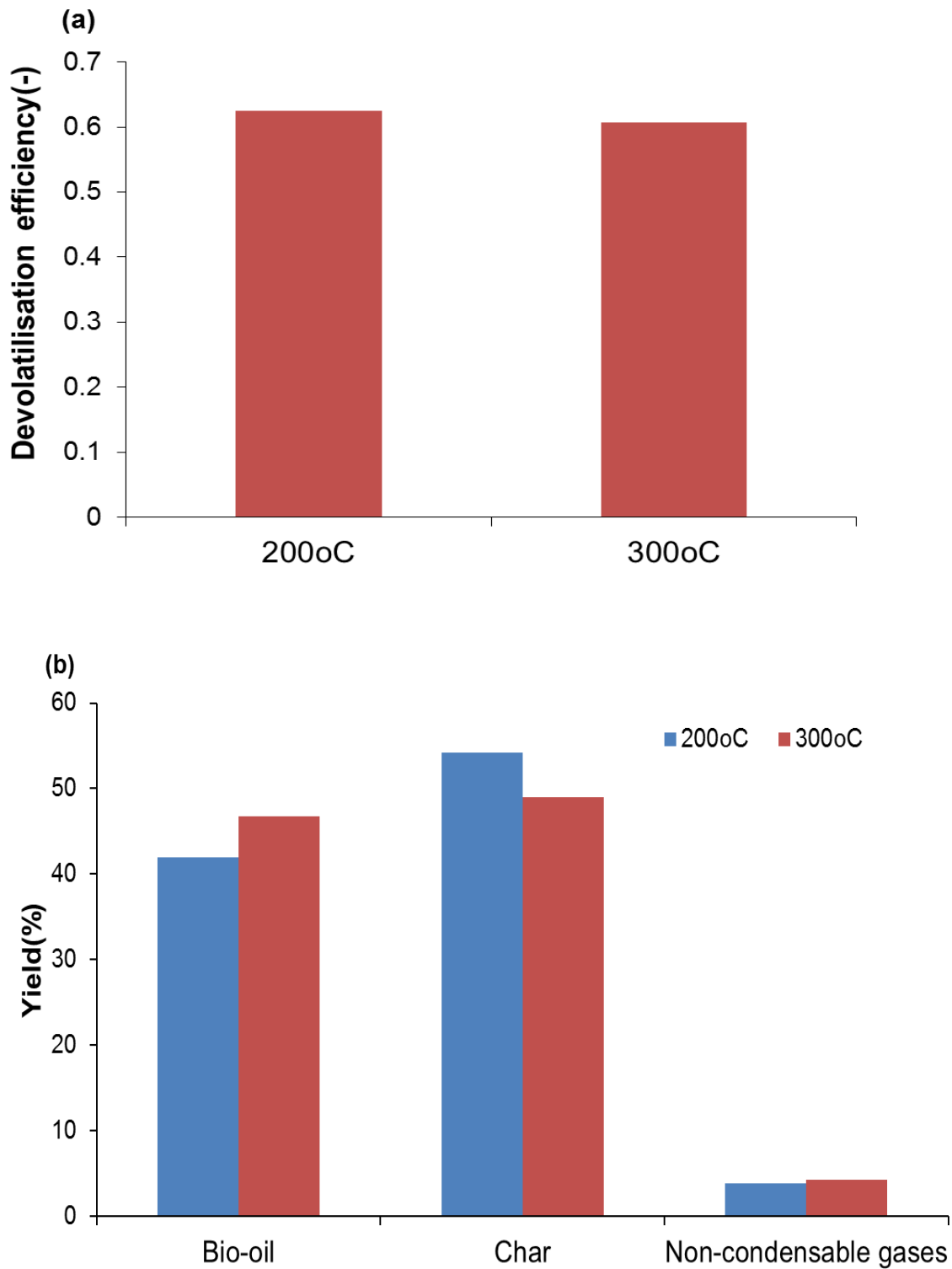


Figure 4.7: Parametric results for cases of 300°C and 200°C sweeping gas temperatures at the gas outlet for a) devolatilisation efficiency b) final product composition.

4.2.4. Effect of particle size

The particle size of the biomass is inherent in determining the reactor type and final product composition. In a kinetically controlled model, the diameter of particle effectively affects the

residence time and heating rate in the reactor. The particle size compared were within appropriate size for liquid production which is between 100-6000 μm . The inter-particle temperature gradient was not considered to affect the reaction kinetics, though larger particles tend to exhibit this phenomenon (Xiong et al. 2013). The time evolved separation efficiency is shown for particle diameters of 250 μm and 1mm in Figure 4.8.

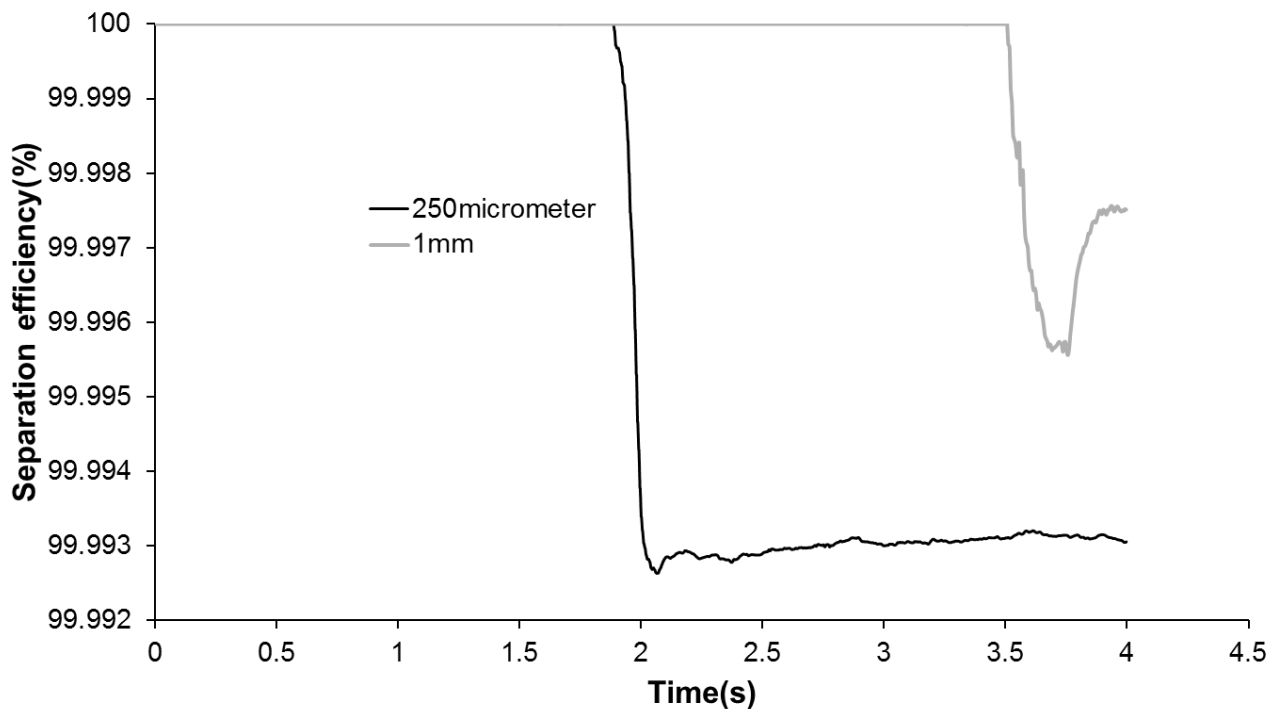


Figure 4.8: A timed variation of separation efficiency with respect to temperature for 250 μm and 1mm biomass particles undergoing fast pyrolysis.

The separation efficiency at steady state for the smaller particle was 99.993%, particle entrainment occurs after 2s. It is observed that smaller particles are easily entrained therefore reduce the separation efficiency. The 1mm particle had an efficiency of 99.997% and entrainment occurs at 3.7s. This behaviour have been reported and has been shown that the separation efficiency is closely linked to the particle size (Yu & Makkawi 2013).

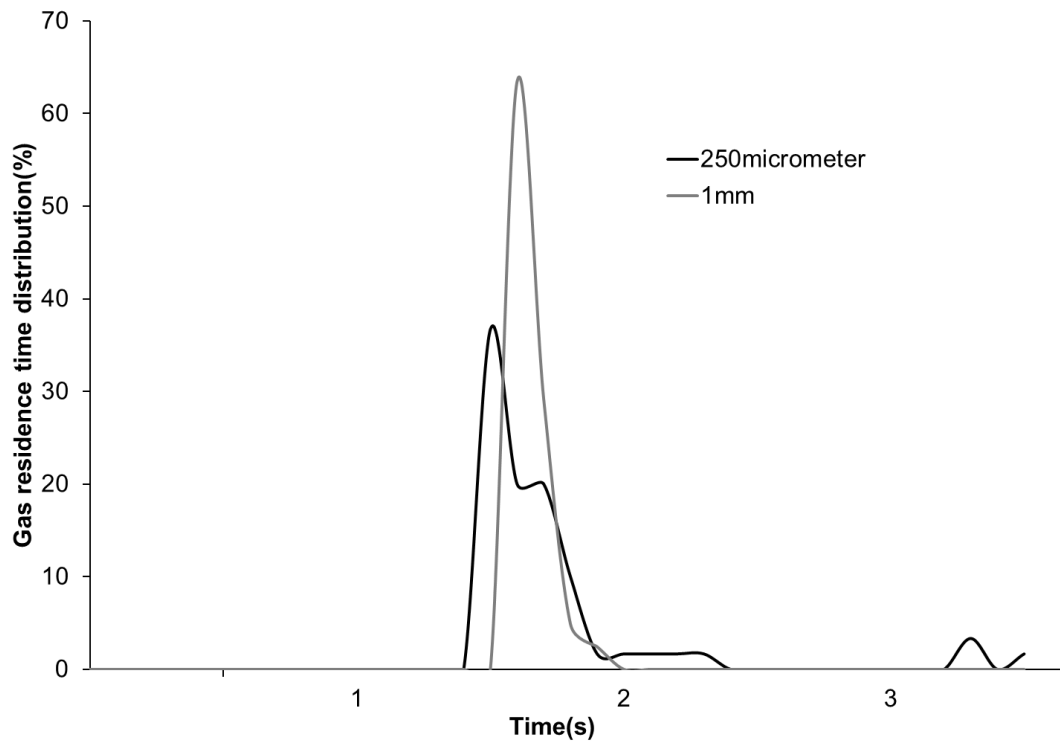


Figure 4.9: Gas phase residence time distribution for 250 μ m and 1mm biomass particles undergoing fast pyrolysis.

The residence time of the particles is longer for larger particle as they have low drag force with the gas phase. The gas residence time is shown in Figure 4.9; the 250 μ m case has its residence time more distributed compared to the 1mm case. The peak distribution for the 250 μ m and 1mm cases were at 1.5s and 2s. The effect of forces of drag in the smaller particles is smaller, while gravitational deposition is very low. This generally increases the velocity of both the gas and particulate phases. The particle residence time would normally be larger than the reaction time as a result the composition and residence time will be influenced mainly by particle size, density and sweeping gas velocity. The devolatilisation efficiency being dependent on temperature and localised biomass concentration. Figure 4.10 represents the maximum devolatilisation achieved for both cases. The 1mm case has more particles concentrated at a localised point and longer residence time this means more biomass is converted to product gas. This means that small particles are rarely heated and they exit the reactor quickly causing high concentration of unreacted biomass. There is a tendency of the percentage of unreacted biomass increasing with increased particle size. The relationship between particle size and final product compositions is shown in Figure 4.11.

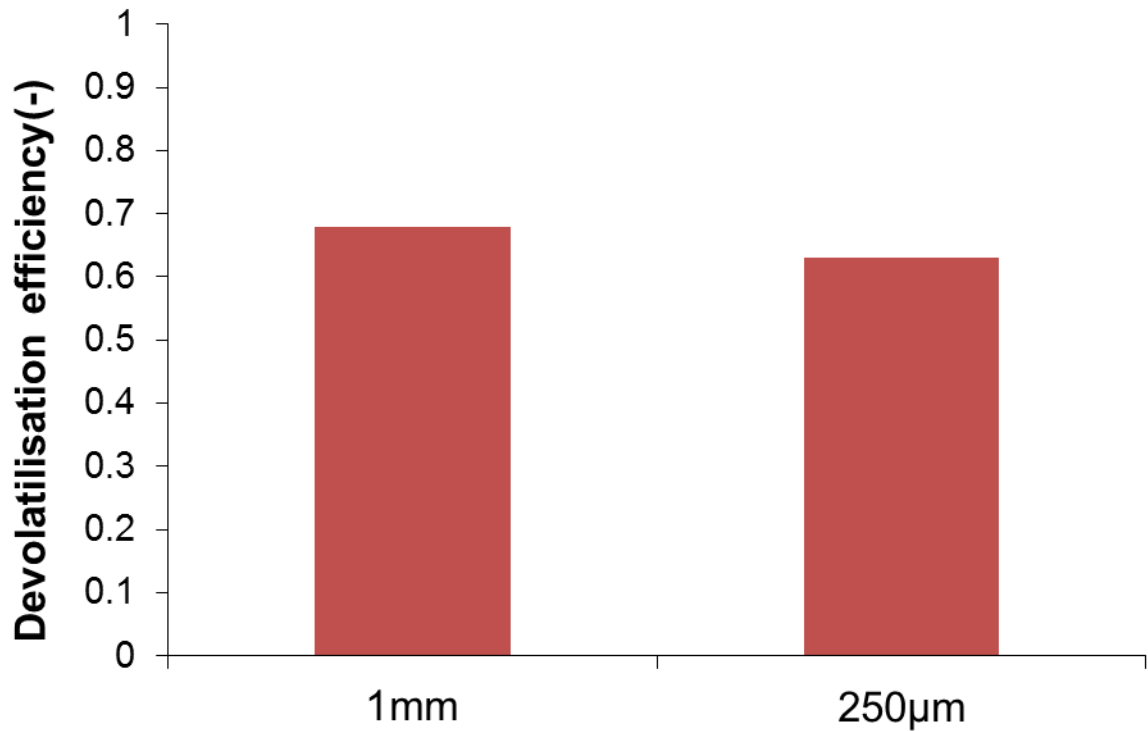


Figure 4.10: Devolatilisation efficiency for 250µm and 1mm biomass particles undergoing fast pyrolysis.

Higher yields are predicted for the larger biomass particle this is presumably because the particles are retained longer in the reactor thus a high degree of decomposition time. The increase in particle size positively affects both the bio-oil and non-condensable gas yield. There was an inverse relationship between char yield and particle size as predicted. This observations diverge from experimental findings though similar CFD models by Ranganathan & Gu (2016) and Xiong et al. (2013) predicted similar results. The reason is large particle diameter leads to high Reynolds number which causes less particles to be entrained out of the reactor. This increases the residence time as stated earlier so high percentage of particles are converted to final products. Şensöz et al. (2000) obtained increase in gas yields with increasing particle size similar to this study. Generally, the reactor type and conditions play a significant role in the final products. A particle size distribution is ideally to be considered for optimal tar yield controlling heating rate and the residence time in the reaction environment (Xue et al. 2012).

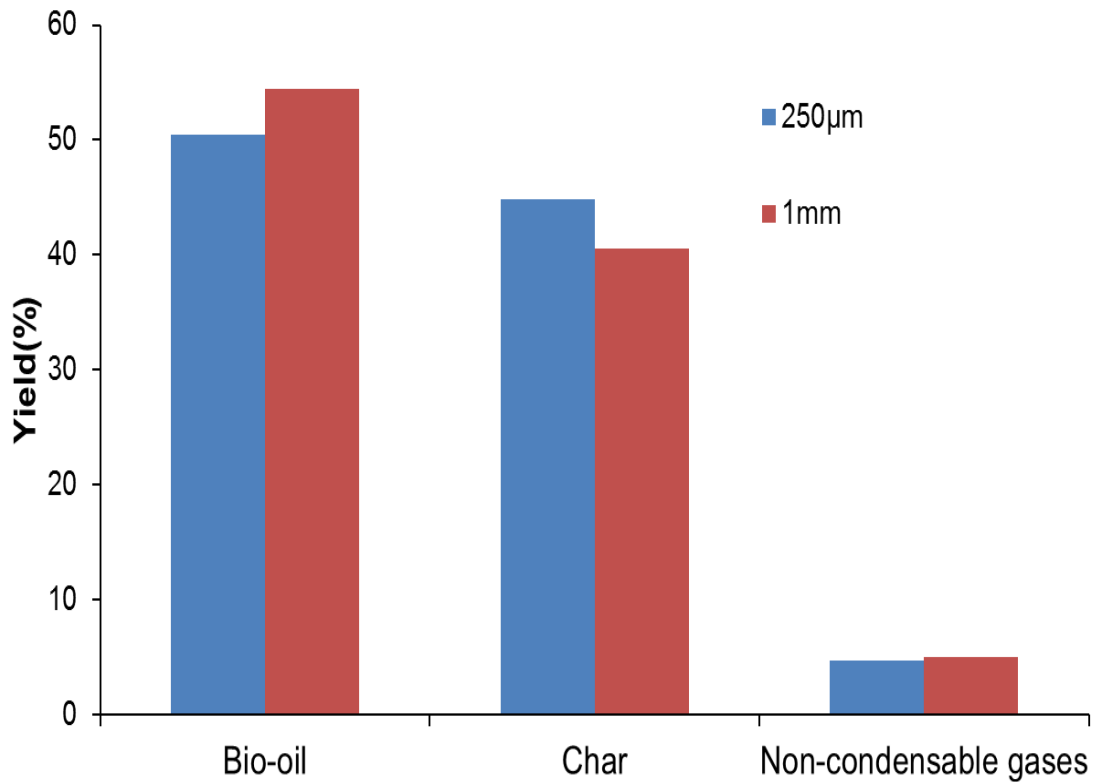


Figure 4.11: Product composition 250µm and 1mm biomass particles undergoing fast pyrolysis.

4.3. Conclusion

This chapter used the base case model in chapter 3 to study the effect of parametric parameters such heat flux, heat transfer model, temperature, flowrate, and particle size. The results were examined and compared with literature findings. The flux distribution in a parabolic trough can be homogeneous or non-homogeneous. The homogeneous heat flux distribution provides the optimum temperature to reduce secondary reactions compared to the non-homogeneous model. The non-homogeneous model produced 85% bio-oil yield, the yield is attributed to the high heat flux situated at a high localised biomass concentration. The high yield was also attributed to the absence of secondary tar reactions due to temperatures above the optimum. The presence of radiation negligibly affects the final product composition; the radiation heats the biomass mainly rather than cause devolatilisation. The larger the biomass diameter the more bio-oil is produced when a uniform particle temperature is assumed. The sensitivity analysis obtained a more detailed behaviour of the solar pyrolysis process in a parabolic trough.

5. : HYDRODYNAMICS OF A CIRCULATING FLUIDISED BED RISER

This chapter discusses the experimental procedure used to study the hydrodynamics of a circulating fluidised bed based on pressure fluctuations. The solid circulation rate was discussed and its effect on the superficial velocity is examined. The pressure experimental values were compared with CFD models to validate the drag laws, wall treatment, turbulence models, and wall shear properties using Fluent 14.0.

5.1. Background theory

Fluidisation is a phenomenon by which particles exhibit fluid like behaviour when suspended under certain operating conditions. It is initiated when a fluid passes through a bed of particles at different velocities. The stationary particles form a packed bed due to low velocities as the fluid passes through the spaces that form the voidages. A sufficient amount of gas passing through it causes the particles to be suspended and behave like a fluid. The velocity is increased significantly to the limit, where particles drag force from the fluid and the gravitational force on the particle are equal. Superficial velocity is the velocity of a fluid from the ratio of its volumetric flowrate to cross-sectional area. The superficial velocity at which this process starts to occur is termed as the minimum fluidization velocity; this point has pressure drop within the bed constant and equal to the gravitational force acting on the particles. The different regimes of fluidisation are shown in Figure 5.1.



Figure 5.1: The transition regimes of fluidization (Almuttahir 2006).

The minimum fluidization velocity is usually determined from Equation (5.1 and (5.2 depending on the minimum fluidisation Reynolds number (Armstrong 2011).

$$u_{mf} = \frac{d_s^2(\rho_s - \rho_g)g}{1650\mu} \quad Re_{mf} < 20 \quad (5.1)$$

$$u_{mf} = \frac{d_s^2(\rho_s - \rho_g)g}{24.5\rho_g} \quad Re_{mf} > 1000 \quad (5.2)$$

The minimum fluidisation Reynolds number Re_{mf} is expressed based on the Archimedes number (ratio of external forces to viscous forces) as follows:

$$Re_{mf} = \sqrt{33.7^2 + 0.00408Ar} - 33.7 \quad (5.3)$$

The increase in velocity causes the bed to expand continuously till it reaches up to a superficial velocity of $3u_{mf}$. The fluid passes through the bed as bubbles leading to the bubbling fluidisation regime. Further increases in the fluid velocity lead to the particles being forced out into the freeboard up to the terminal velocity of the particle at the turbulent

fluidization regime. The terminal velocity of the particle u_t is given as (Balasubramanian et al. 2005):

$$u_t = \frac{d_s^2(\rho_s - \rho_g)g}{18\mu} \quad \text{Re}_s < 0.4 \quad (5.4)$$

$$u_t = d_s \left(\frac{4}{225} \frac{g^2(\rho_s - \rho_g)^2 g}{\mu \rho_g} \right)^{1/3} \quad 0.4 < \text{Re}_s < 500 \quad (5.5)$$

$$u_t = d_s \left(\frac{3.1(\rho_s - \rho_g)g}{\rho_g} \right)^{1/2} \quad 500 < \text{Re}_s \quad (5.6)$$

The particles descend back along the wall until when the superficial velocity exceeds the terminal velocity. This leads to the particles being entrained where they are carried out of the riser. The point at which this occurs is the fast fluidization regime. The particles are generally circulated through a downer and cyclone in circulating fluidised beds. This fluidised beds are characterised by fast movement and good particle mixing. The high rate of heat and mass transfer leads to uniform temperature distribution. The behaviour of particles is dependent on the particle size and density.



Figure 5.2: Geldart classification of powders (Geldart 1973).

Geldart classified powders into four categories depending on mean particle diameter and particle density; this is represented in Figure 5.2. The following classification is given below:

- Group A: These are aeratable particles with mean particle size $<30 \mu\text{m}$ and low density $<1400 \text{ kg/m}^3$. This particle group fluidize very easily at smooth fluidization without bubbles being formed. The minimum bubbling velocity is higher than the minimum fluidization velocity so the bubbling regime initiates at higher velocities. The typical material are fluid catalytic cracking catalysts.
- Group B: These are the bubbling particles with mean particle size $30 \mu\text{m} < d_p < 500 \mu\text{m}$ and a low density of $<1400 \text{ kg/m}^3$. The particles have sand like characteristics, and bubbles start to form once the minimum fluidization velocity has been exceeded. The typical materials with this behaviour are glass beads and sand.
- Group C: These are termed as cohesive particles; they are fine powders which are very difficult to fluidise with mean particle size $<30 \mu\text{m}$. This is due to the nature of the strong inter-particle forces compared to the inertial effect of the gas. They do not form bubbles, but rather they give rise to channelling in small diameter beds. The typical materials with this behaviour are flour and starch.
- Group D: These are termed as spoutable particles, they are usually very large and very dense. They produce deep spouting beds rather than fluidized beds. This behaviour of spouting and channelling is prevalent when the gas distribution is uneven. The typical materials are coffee beans and rice.

This classification gives a detailed type of fluidization behaviour prevalent in the different particle regimes and can be used to predict the properties of the bed.

5.2. Experimental settings and procedure

5.2.1. Experiment setup

The 12 kg/h circulating fluidised bed gasifier used in this experiment was designed and constructed at Aston University. The system is made up of a riser with a diameter of 4cm and 308cm in height. The distributor plate is located above the primary inlet for the fluidising medium to distribute at 5%. The feed inlet has a diameter of 2cm and the solid recirculation inlet diameter of 3cm, the outlet dimensions were width 2cm and height of 8cm leading to the cyclone. The biomass inlet is connected to a screw feeder and hopper with manifold and hopper air delivery systems manufactured by Dwyer; the values of air flowrate range from 0-100L/min. The hopper is connected to a tank, where there is screw feeder for feeding at the biomass inlet. The manifold air on the other hand disallows solid particles from the risers entering into the air probes that are located at different points up the riser to cause

blockages on the probes. The variable rotating screw controls the feed rate of biomass and the maximum mass flowrate of biomass. The biomass inlet is located 20cm above the air distributor plate. The heating element attached to the riser was within the first 70 cm of the riser. This part of the apparatus was not used in this work because only the hydrodynamics of the bed material was studied.

The riser has 4 pressure probes at 40cm, 160cm, 280cm, and 308 cm spread along the riser to provide pressure profiles. The riser has 4 temperature probes to measure the temperature at 40cm, 70cm, 160cm, and 280cm. The probes were attached to IMPRESS IMP-LR sensors to deliver the values to a data logger. The loggers are connected to a data system to record the temperature and pressure at different points in the riser. This can be attached to a laptop and the time averaged data of the two variables can be analysed. At around 10 cm above the air distributor a metal pipe was connected to allow for the circulating solids coming from the receiving tank to enter the riser. The riser outlet was located 5cm below the top and connected by an 8 cm diameter stainless steel pipe to a cyclone.

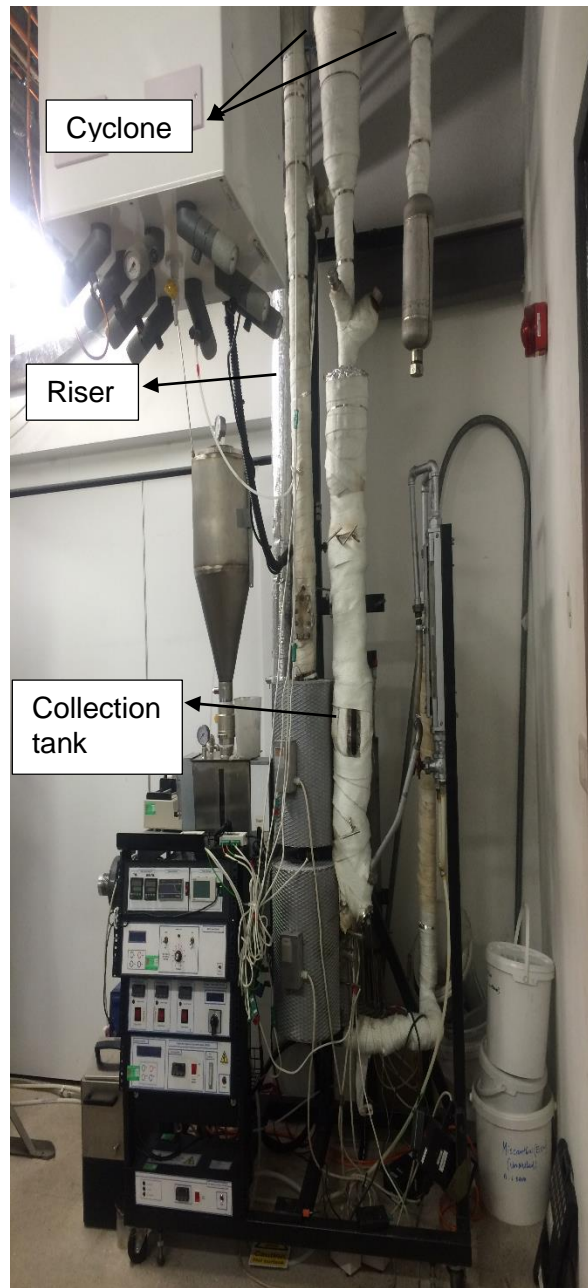
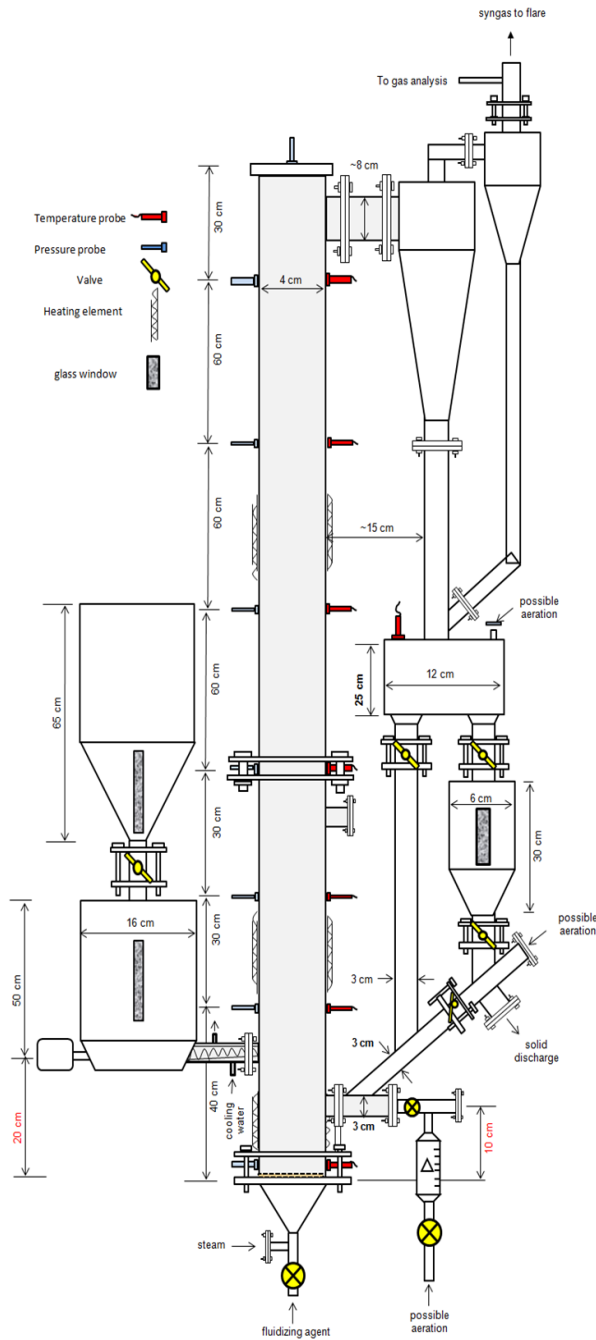


Figure 5.3: Picture and diagram of the Experimental CFB at Aston University's EBRI.

There are two downers leading out of the solid receiving tank that connect to the cyclone. The first downer has a diameter of 3cm and extends to the return leg of the riser. The second downer has a collection tank of diameter 6cm and height of 30cm to measure the solid recirculation rate. Two valves were located above the two downers allowing for control of the solid recirculation rate and diversion of solids. The solid collection tank has two valves to prevent recirculation back to the return leg. The return leg was connected to the secondary inlet pipe. This return leg was designed with two small openings; one for solid feeding and other for discharge of solid from the system during operation. The downer

section has five butterfly valves labelled V-1 to V-5 to adjust the bed material in the solid collection tank.

Cyclone is a device that separates particulate from the gas phase through vortex separation without using filters. Two cyclones were connected in series to the riser to separate solid particles from the gas. The primary cyclone collects the initial solids from the riser, some of these solids are entrained, therefore need to be separated completely. The secondary cyclone generally collects smaller particles. This is connected to the downer to allow recirculation of the solids within the riser. The dimensions and diagram for the primary cyclone is given in Table 5.1 and Figure 5.4.

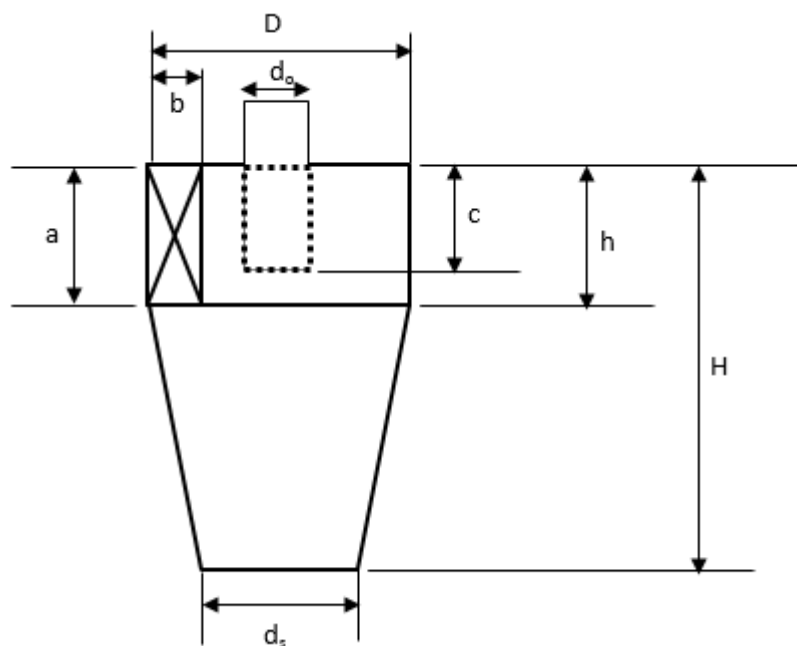


Figure 5.4: Diagram of the primary cyclone.

Table 5.1: Dimensions of the primary cyclone.

Diameter D (cm)	12
Inlet height a (cm)	6
Inlet width b (cm)	2
Outlet diameter d_o (cm)	6
Outlet length c (cm)	6
Cylinder height h (cm)	18
Cyclone height H (cm)	47
solid outlet diameter d_s (cm)	4

The rotameter valves were used to control the amount of primary and secondary air to achieve recirculation. The rotameter for the primary air works in the range 0-500L/min to supply the main fluidising air. The secondary rotameter works in the range of 20-200L/min to push the solids for better recirculation. The rotameters were manufactured by Rotameter Manufacturing Company Croydon; the rotameters used are shown in Figure 5.5



Figure 5.5: Picture of the primary and secondary rotameters used for the experiment.

5.2.2. Operating conditions

The process was a cold flow experimental setup. The experiment was carried out using air as the fluidizing agent at ambient conditions. The materials tested were single phase silica sand of two particle sizes. The solid particles used were weighted and sieved to obtain optimum particles within the experimental range.

Table 5.2: Operating conditions for the CFB gasifier process.

Operating Conditions		
AIR FLOW(l/min)	180,200,220,240,260	
PHASES	Single phase	
SOLID PARTICLE SIZE	0.3MM	0.4MM
SOLIDS AMOUNT	3KG	3KG

The operating conditions for the experiment are given in Table 5.2. The particle terminal velocity was calculated to estimate the minimum air velocity required to achieve circulation in the apparatus. This required taking a range of air flowrates from within the range of 50-300l/min to find the minimum needed to achieve circulation. The Reynolds number was used to specify which equation is applicable for the process. This was within the range for 13-91, therefore the terminal velocity equation from (5.5) was used in the analysis. The minimum terminal velocity obtained for the 0.3mm and 0.4mm size sand particles was 1.69 m/s and 2.25 m/s. The fluidization velocity was obtained from the air flowrate from the rotameters. These values were converted from the unit used by the rotameters to the fluidisation velocity using the cross-sectional area.

5.2.3. Procedure

The measurement of the solids recirculation rate is measured in ambient conditions for 0.3mm and 0.4mm sand particles. The experiment was carried out for the effect of particle size and air flowrate on the solids recirculation rate. The sand is loaded at the loading point above the solid collection tank; the sand is packed in the tank. The butterfly valves in the downer were adjusted to allow settling of the inert solids in the solid receiving vessel in the downer. The sand particles in the receiving vessel were gradually moved into the riser by opening the valve V-5 after setting the air supplies into the reactor to the required air flow rates. For the first run, the hopper and manifold air were maintained at 20L/min, whereas the primary and secondary air supplies were set at 160 L/min and 20L/min respectively. At this time, valves V-1 to V-5 were constantly adjusted, except V-4, until all the solid materials entered into the reactor and solid re-circulation was achieved. The primary air valve was also regulated but not above 20L/min air flow rate at the time solid re-circulation was being sorted. This was immediately maintained at 20 L/min when re-circulation of solids was achieved. The system was allowed to attain a steady state of solid re-circulation for about 5min, after which valve V-3 was closed to collect solids at the cylindrical solid receiving unit, and which was monitored through a glass window in this section of the gasifier. The process

of solid collection involved allowing solids to fill a 5 cm mark (height) made on the receiving vessel. The time taken for the sand particles (solids) to fill this height was recorded with a timer. The process was repeated for three different times in order to ensure accurate measurements. The average time in this case was calculated. The same process was repeated using 200, 220 240, 260, 280 L/min total air flow rates at the same initial experimental conditions. In order to discharge the solids from the system after the measurement, solids were allowed to accumulate in the receiving vessel of the downer, the air supplies were turned off, and sand particles were then gradually discharged into an iron bucket by opening the butterfly valve BTV 04 at the lower section of the downer. The solid re-circulation rate for each experimental runs were calculated using equations below from the solid collection tank.

$$V = \pi r^2 h , \quad (5.7)$$

$$V/t = \dot{Q} , \quad (5.8)$$

$$\rho \dot{V} = \dot{m} , \quad (5.9)$$

where V , \dot{Q} , h , r is the volume of tank, volumetric flowrate, height of tank, and radius. The same procedure is also repeated but the V-3 valve is not closed and the probes measure the pressure values in the riser. The probes are attached to a sensor which convert the pressure values and store them in the data logger system. The raw pressure values at the different points were sent to the HOBOPRO software for a time-series analysis of the pressure difference in the system. The process was repeated for 0.4 mm sand particles at 180 200, 220 240, 260, 280 L/min total air flow rates.

5.3. Proposed CFD Model

The model presents the hydrodynamics model for the 12 kg/h circulating fluidised bed riser designed at EBRI Aston University. The riser section was modelled similar to the experimental reactor based on the Eulerian- Eulerian model. The governing equations were described in Chapter 2. The turbulence models used were the Standard, RNG and Realisable k-e models and the large eddy simulation (LES) model. The near wall treatment considered the standard and enhanced wall treatments. Standard wall treatment and standard k-e models were implemented in the base case.

The drag models considered were Wen Yu drag model (Wen & Yu 1966), Gibilaro (Gibilaro et al. 1985), Gidaspow drag model(Gidaspow 1994), and Syamlal & O'Brien(Syamlal & O'Brien 1987). The drag law is based on the model by Syamlal & O'Brien model for the base

case. The solid and frictional pressure, radial distribution and bulk viscosity are taken from Lun et al. (1984). The kinetic and collisional viscosity are given based on Syamlal et al. (1993). A detailed literature about the different hydrodynamics models above was explained in Chapter 2.

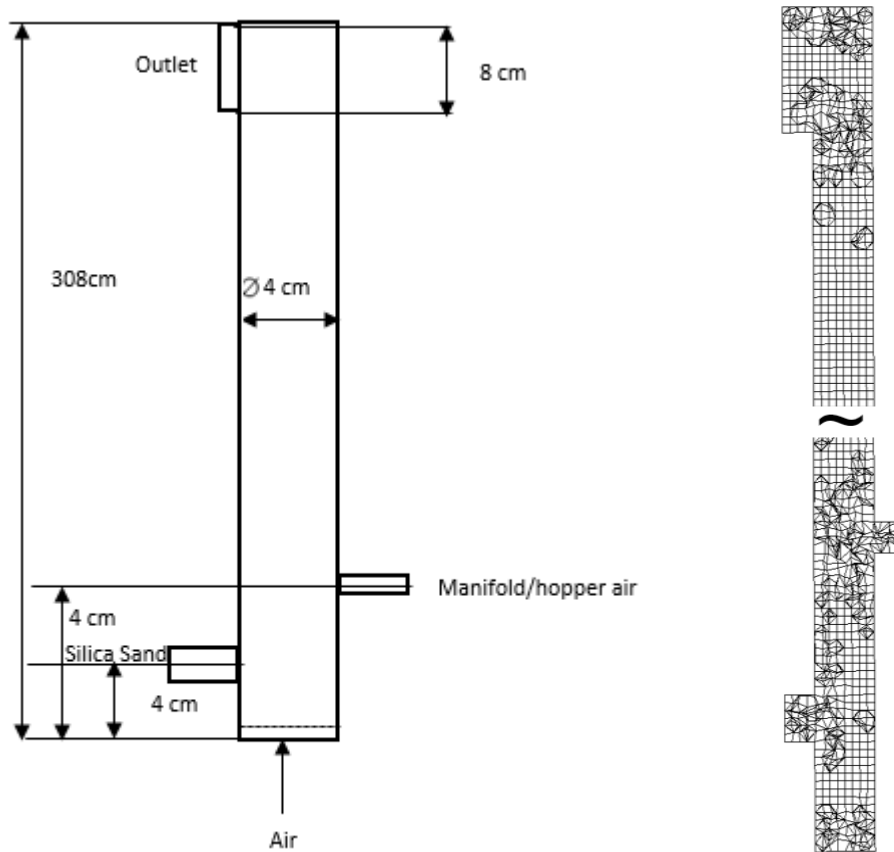


Figure 5.6: Geometry and mesh of the CFB gasifier.

The riser geometry and mesh domain is illustrated in Figure 5.6. The geometry of the reaction domain was discretized into small fine elements size to be used for the finite volume method. The 3D mesh contains 70327 cells, 230018 faces using a polyhedral mesh. The minimum grid size was set up to 10x particle diameters and a maximum skewness factor of 0.89 was obtained for the mesh. The particles size of 400 μ m was introduced at the solid recirculation rate from experimental values. The fluidising gas which was mainly air was introduced at 240L/min. The effect of particle fragmentation was not taken into account; thus the absence of particle-particle mass transfer. The initial conditions of the riser had the following inlet conditions:

$$\vec{v} = v_{air}, T_g = T_{air} = 30^{\circ}C, \text{ at } L = 0, 0 \leq r \leq D \text{ at air inlet, } -180^{\circ} \leq \theta \leq 180^{\circ} \quad (5.10)$$

$$\vec{v} = v_s, T_s = 30^{\circ}C, \text{ at } L = 2\text{cm}, 0 \leq r \leq D \text{ at biomass inlet, } -180^{\circ} \leq \theta \leq 180^{\circ} \quad (5.11)$$

$$\vec{v} = v_{manifold air}, T_g = 30^{\circ}C, \text{ at } L = 4\text{cm}, 0 \leq r \leq D \text{ at air inlet, } -180^{\circ} \leq \theta \leq 180^{\circ} \quad (5.12)$$

The solid phase is assumed to be introduced to the reactor at ambient conditions. The outlet is assumed to be a pressure outlet which is at atmospheric pressure gradient. The flow is assumed to be a fully developed viscous flow leading to a plug flow assumption (tube length \gg hydraulic entry length). The walls are modelled as stationary walls with non-slip wall conditions for gas phase. The solid phase was modelled with wall shear for particles (Johnson & Jackson 1987). The full operating conditions and physical properties are given in Table 5.3:

Table 5.3: Operating conditions of CFD model.

Parameters	Value	Parameters	Value
Pressure outlet [atm]	1	Density [kg/m ³]	1540
Sand mass flux rate [kg/m ² s]	22.5	Operation temperature [K]	ambient
Manifold air flow rate [L/min]	20	Particle-Particle restitution	0.9
Particle size [μ m]	400	Particle-wall restitution	0.5,0.9,0.95,0.99
Superficial velocity [m/s]	3.2	Specularity coefficient	0,0.1,0.5,1

The governing equations were discretised using the finite volume method and the pressure coupled solver. The transient formulation for time dependent solution is the first order implicit scheme. The spatial discretisation of the gradient used the least squares cell based and the other variables were based on first order upwind. The phase coupled SIMPLEC algorithm is used for the pressure-velocity coupling (Patankar 1980). The convergence criterion residuals for transport equations were set to 10^{-5} . The under-relaxation factors were set to 0.1 for pressure, 0.7 for momentum, 0.8 for turbulent species, 0.5 for volume fraction, 0.2 for granular temperature, and 1 for rest of the quantities for suitable control of the solution. A time step of 0.001 was found to be suitable for the grid size used in the domain. The maximum number of iterations was set to 30 until stability of convergence has been achieved. The simulation was for 60s in real-time for each case. The processor used for the simulation is a 2.70 GHz 2 Core processor Intel® Xeon® with 32 GB RAM.

5.4. Results and Discussion

5.4.1. Experimental results

5.4.1.1. Solid circulation rate

The solid circulation rate was estimated from the procedure above using the solid collection tank. The particle size affects the recirculation rate, this is investigated for sizes of 0.3mm and 0.4mm. Figure 5.7 shows the recirculation rate at different superficial gas velocity for a 0.3mm particle size compared with a 0.4mm particle. The solid circulation rate increases steadily at superficial gas velocities between 2-3 m/s; after which higher velocities are needed to achieve the same effect. This is caused by the effect of drag on the particles as the velocity is increased at higher fluidising gas flowrate. At lower gas velocities, the recirculation rate for both the two particle sizes were very close; they start to deviate at higher velocities. There is generally more drag and gravitational forces acting on larger particles. The profiles exhibits a flow regime of a fully developed fluidised bed similar to experiment reported in Namkung et al. (1999). The lower solid recirculation rate leads to uniform flow in the riser; it becomes very dilute and particles are easily entrained in this case.

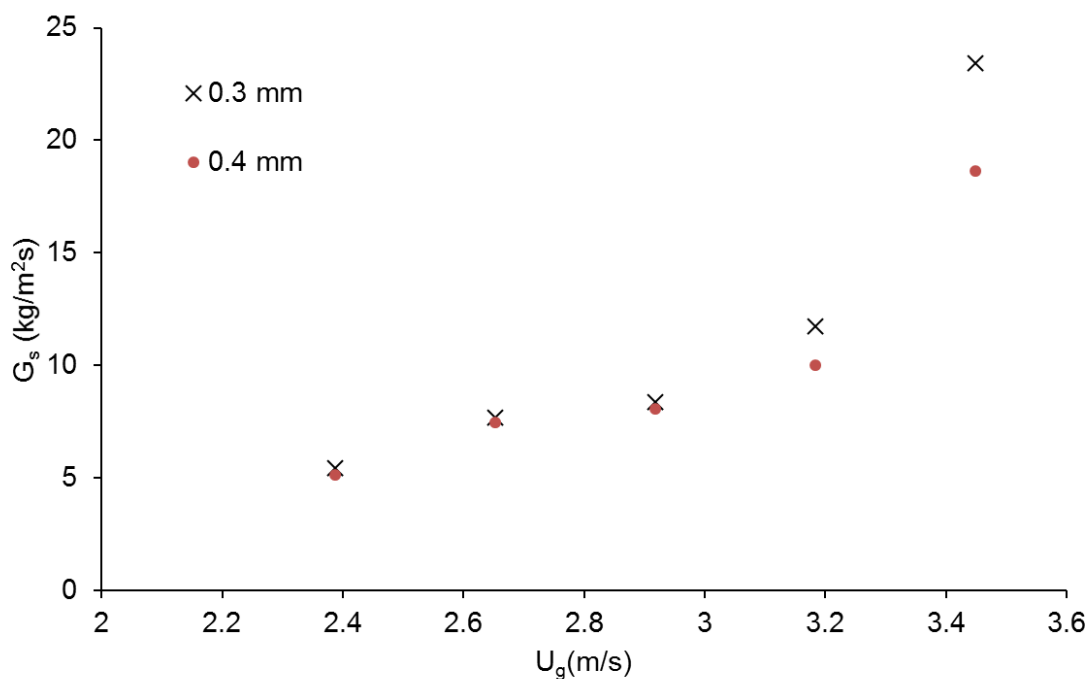


Figure 5.7: A graph showing the effect of particle size on the solid circulation rate for 0.3mm and 0.4mm particle diameters.

5.4.1.2. Pressure Profiles

The pressure probes measured the pressure at the different points in the riser. This raw values are analysed in the HOBOPRO software. The timed-series analysis of a sample of pressure data from the experimental data for the two particle diameters (0.3mm and 0.4mm) is shown in Figure 5.8.

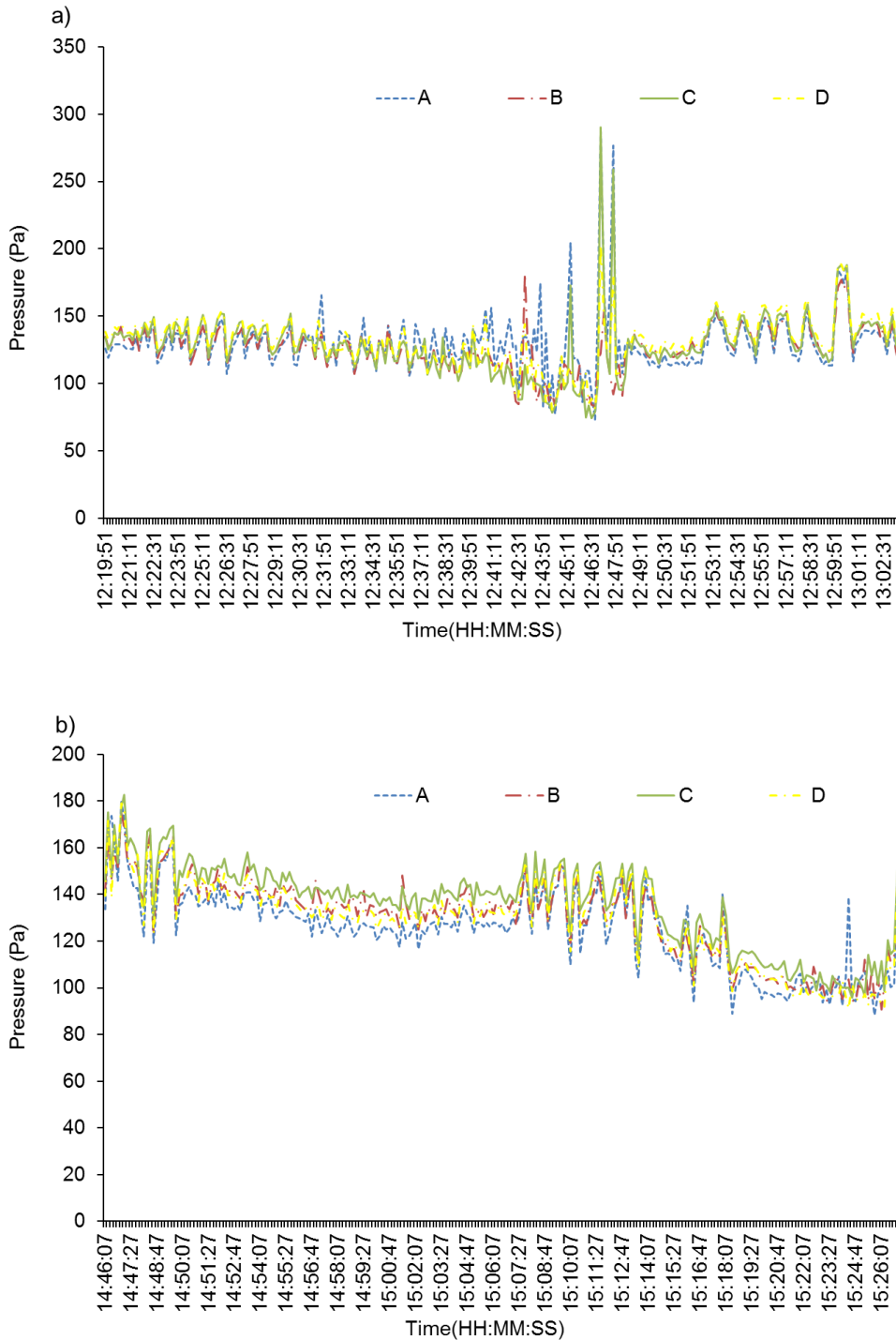


Figure 5.8: Time series raw experimental values from pressure measurement a) 0.3mm sand particle diameter b) 0.4mm sand particle diameter.

The areas of instability are the initial stages of the experiment needed to achieve the recirculation of sand particles. The pressure profiles for most of the flowrate follow a similar trend as shown in Figure 5.9 . The pressure gradient is smaller at the top and larger at the bottom near the solid entrance. This is caused by the turbulence mixing before equilibrium is reached between the two phases. In a CFB, generally the bottom bed is denser and bubbling behaviour is likely especially at low gas velocities as was seen for the 180L/min flowrate.

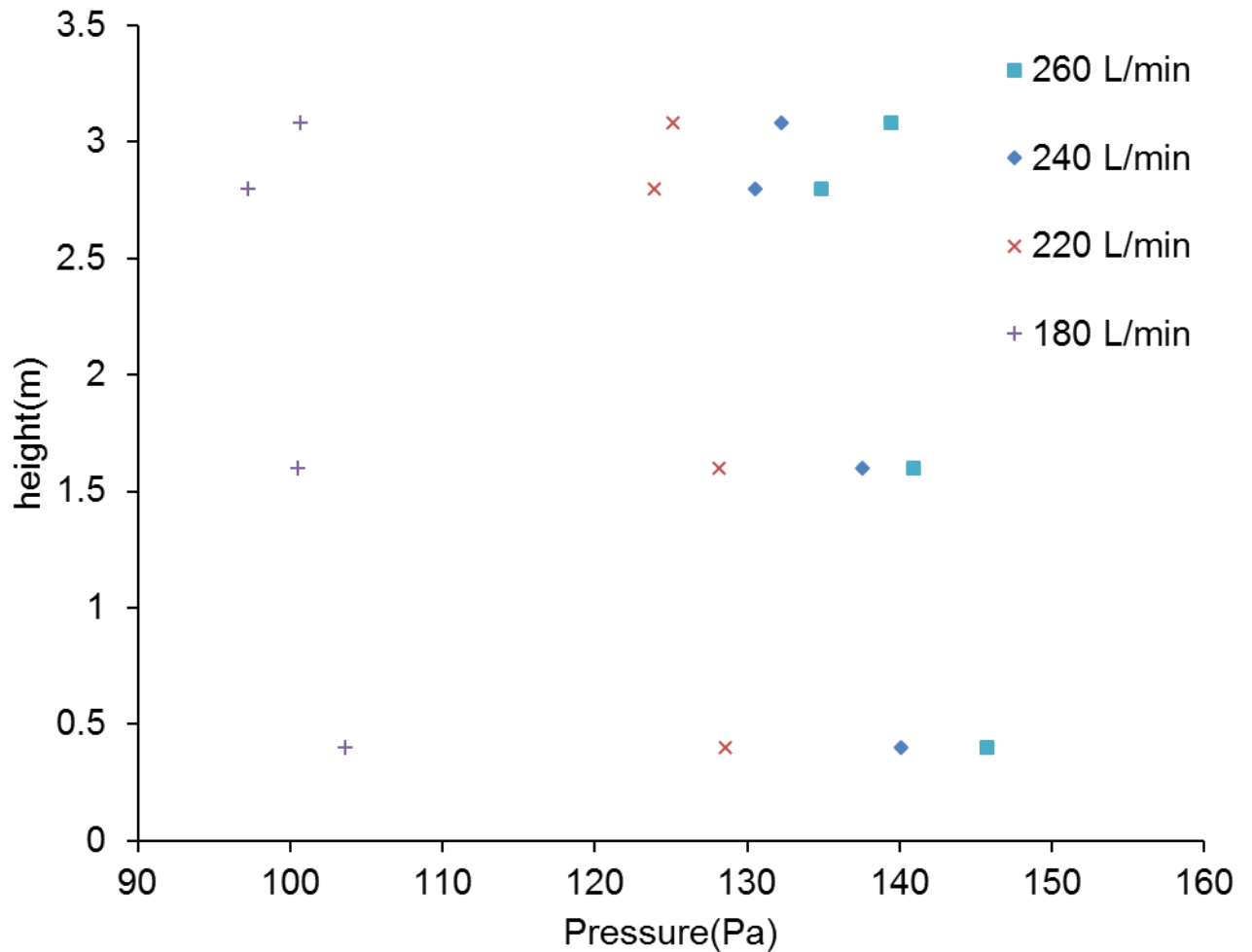


Figure 5.9: Pressure values at different air flowrate in the riser for 0.3mm particle size.

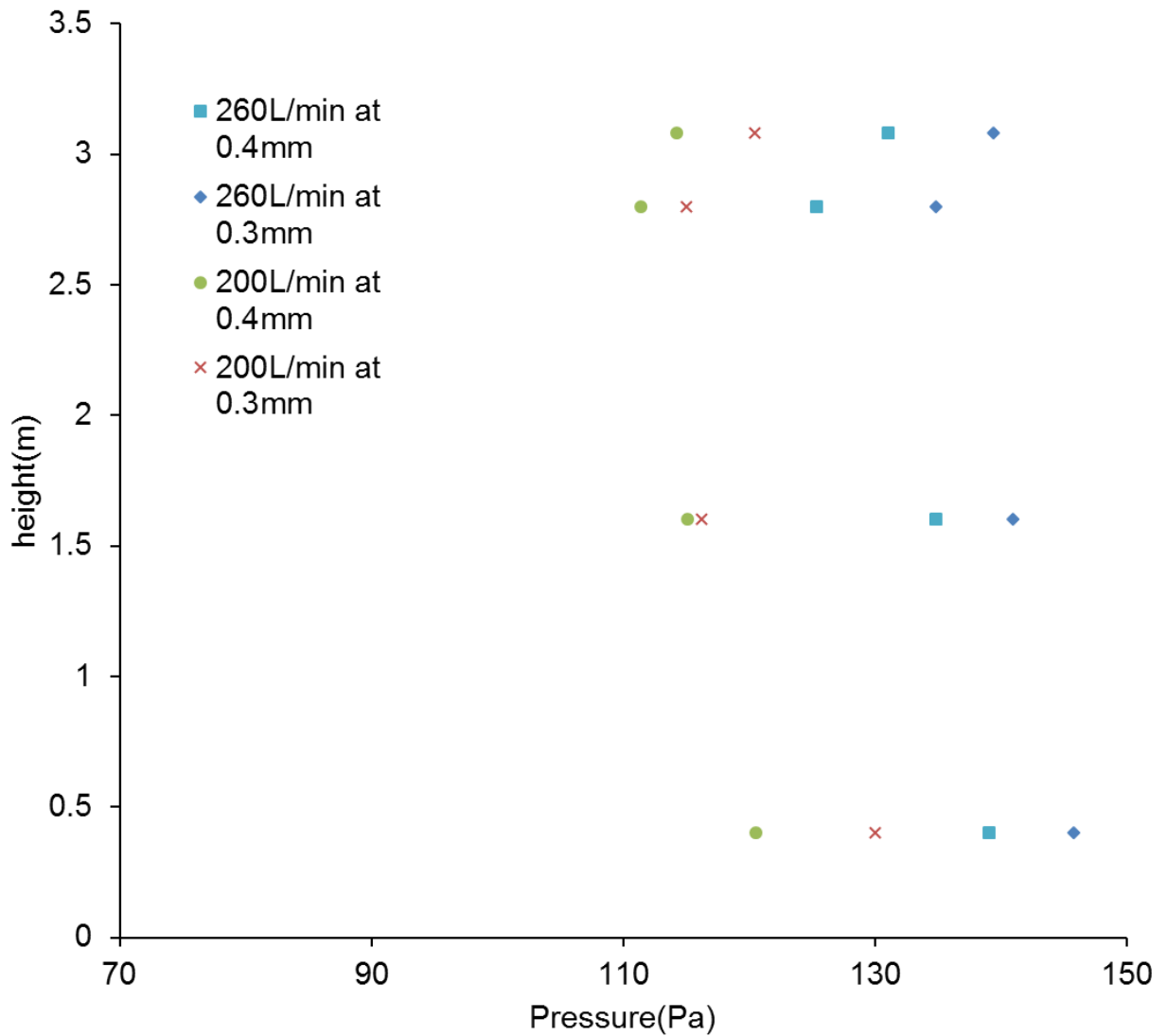


Figure 5.10: A comparison of pressure values at 260L/min and 200L/min along the riser for 0.3mm and 0.4mm particle sizes.

Figure 5.10 shows a comparison between two particle sizes of 0.3mm and 0.4mm at similar fluidising gas flowrate of 200L/min and 260L/min. The trend of pressure profiles agree with one another. It is observed that small particles tend to show higher pressure profiles in the riser with increasing gas flowrate. The superficial gas velocity becomes high leading to the high pressure. The terminal velocity for small particles is low therefore they are entrained easily at low superficial gas velocity than large particles. As stated earlier the gravitational force and drag force between the solid and the gas is dependent on the size of the particle and the superficial gas velocity. The pressure gradient in the riser was significantly low compared to high flux CFB. They proved that circulation was achieved and a significant amount of solids were entrained leading to a uniform flow in the riser.

5.4.2. Modelling results

5.4.2.1. Effect of Grid size

A grid study was implemented to find the effect of the grid cells on the results. The base case originally contains 70327 cells. The grid size was investigated further for 24480 cells. The different grid size was compared with experiment as shown in Figure 5.11.

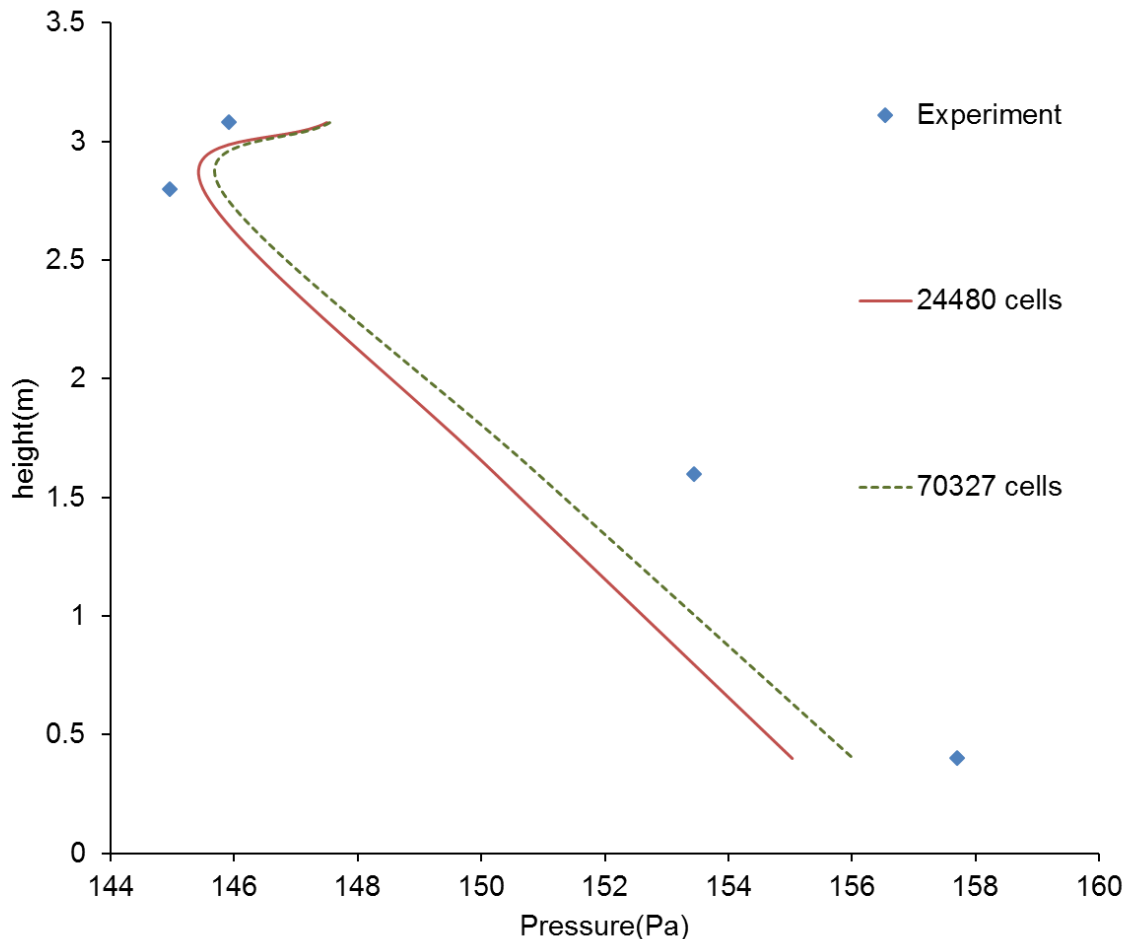


Figure 5.11: Pressure profiles for experiment and simulation of different grid sizes.

There is clearly an effect of the grid size on the pressure profile in the riser. The similarity between the different grid sizes is observed with great accuracy; on a qualitative perspective the grid size effect is within a margin of error. Its effect is normally more observed in the hydrodynamics and less or negligible effect on the temperature and product composition Liu (2014). This effect has been studied extensively and similar observations were predicted by Ibsen et al. (2001), Armstrong (2011), and Hassan (2013). The coarser the grid size the less computational time required to run cases, therefore the grid size need to be optimised for accuracy and computational time especially in finer meshes.

5.4.2.2. Effect of drag laws

The solid-gas momentum exchange coefficient is validated in a single solid phase model. The experiment was compared with Wen Yu, Gidaspow, Gibilaro, and Syamlal & O'Brien drag models shown in Figure 5.12.

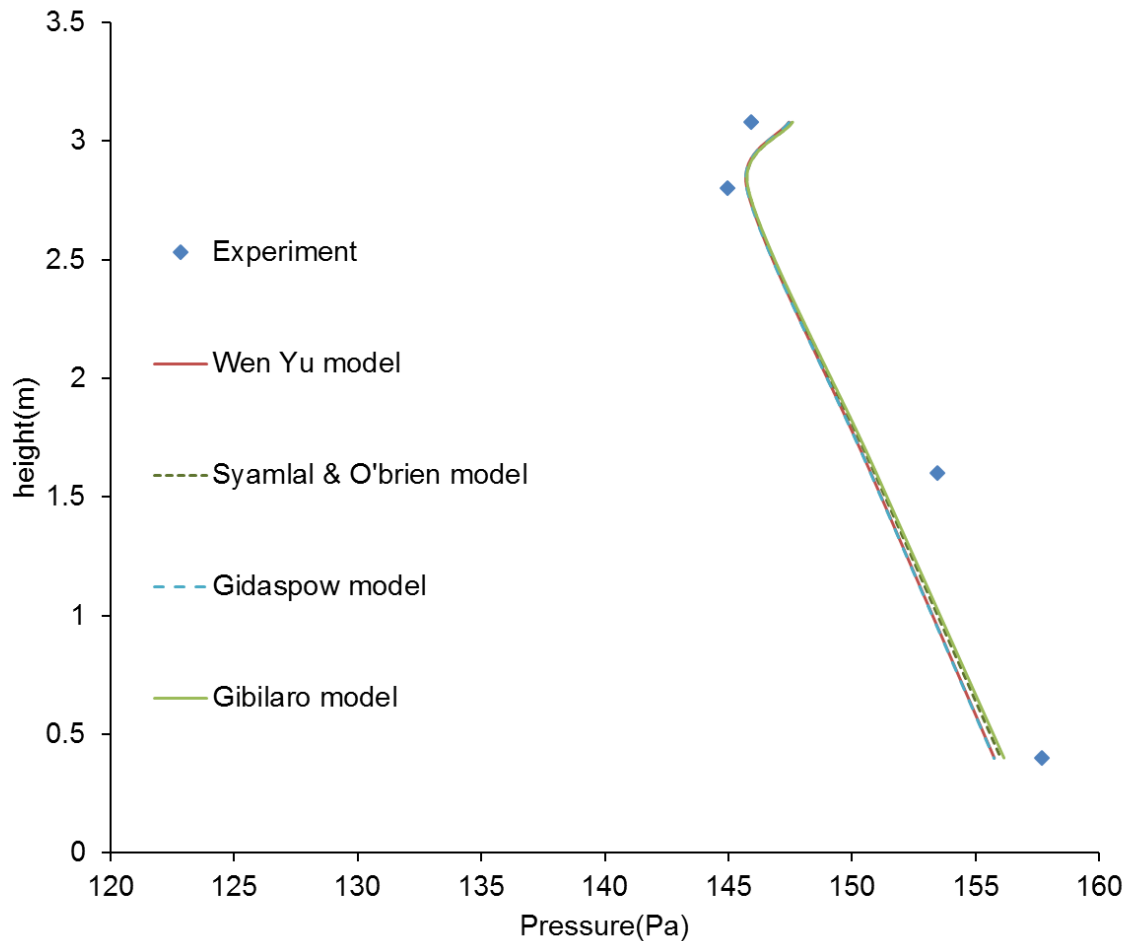


Figure 5.12: Pressure profiles for experiment and simulation of different drag laws.

The drag laws agree well with experimental findings and are mostly sufficient to model the hydrodynamics of a CFB. The Gidaspow model switches to Wen Yu model at gas volume fraction greater than 0.8, therefore the similarity in the pressure profiles. The Syamlal O'Brien model and Gibilaro model have been used in CFB by Gujjula & Mangadoddy (2015) and have shown good prediction at high solid concentration areas compared to Syamlal O'Brien model and Gidaspow model. The Syamlal O'Brien predicts the solid distribution and velocity profile by showing more of the clustering effect of particles in a CFB. The impact of drag laws are more pronounced in the radial direction of velocity and volume fraction.

5.4.2.3. Effect of turbulence model

Fluidised beds are turbulent in nature; this turbulent behaviour has to be accounted for especially in the fast fluidisation regime. Laminar and turbulent flow models were compared with experimental values as shown in Figure 5.13. The turbulence models agree qualitatively with the experimental findings; the difference in the pressure gradient in all cases is relatively small.

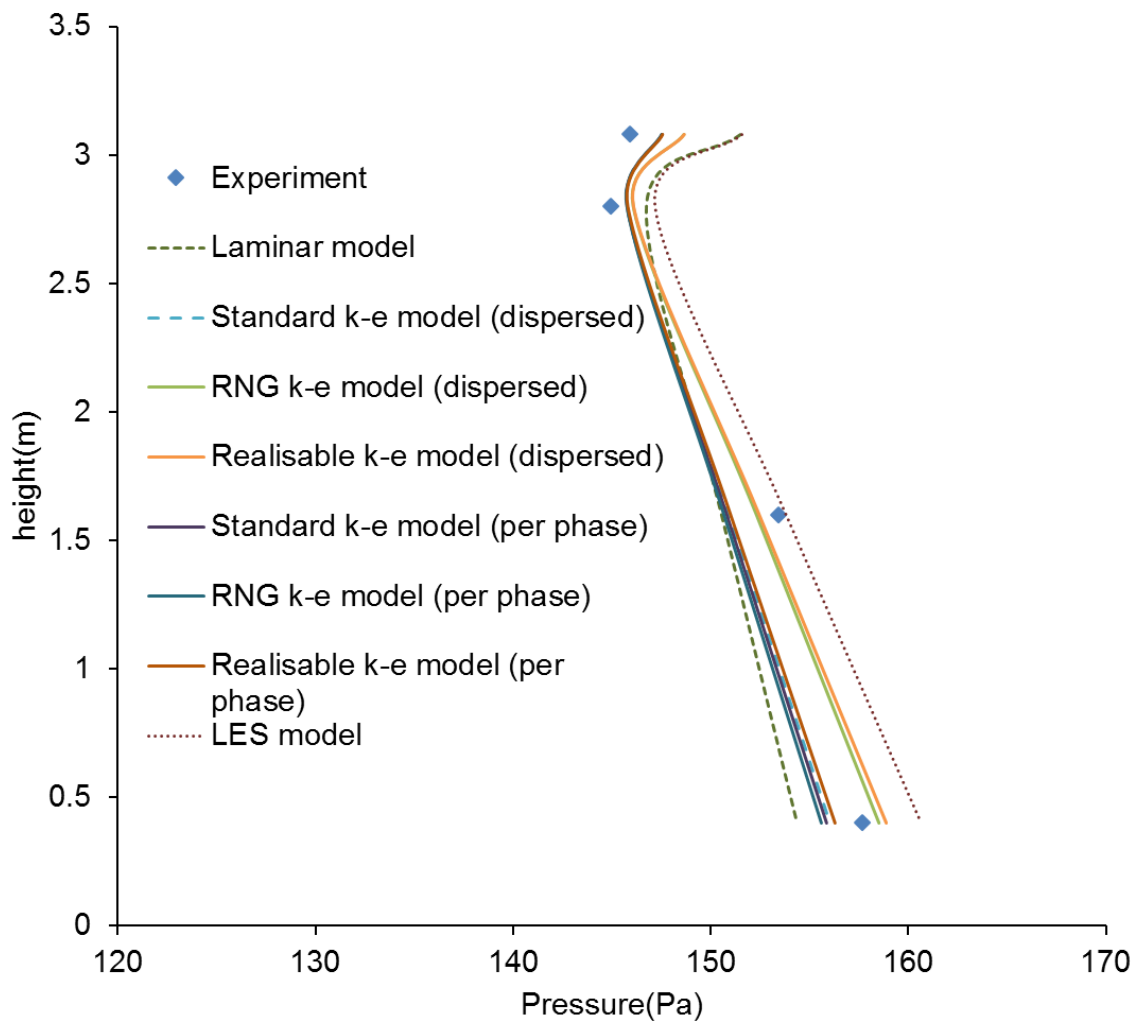


Figure 5.13: Pressure profiles for experiment and simulation of different turbulence models.

There is a small difference in the exit region as a steeper change is observed compared to the experiment and the dispersed k-e model. This is due to a high localised mass concentration of particle at the top and different models augment the pressure gradient at this area differently. It also shows that the exit structure is slightly different; the exit effect is stronger in the CFD models compared to experiment. As stated earlier the standard k-e model and RNG models are semi-empirical correlations, though Hartge et al. (2009)

concluded that the realisable k-e under predicts the volume fraction at the bottom of the riser.

According to the results, the RNG and realisable k-e models provided a much better fit than the remaining turbulence model. RNG k-e model has been used to model circulating fluidised bed; Hartge et al. (2009) and Liu et al. (2013) obtained similar trend with experimental findings. Other authors suggested time averaged turbulent behaviour and interaction between phases are likely to make predictions more realistic (Almuttahir & Taghipour 2008b). The different empirical constants and closures available in literature have to be modified to achieve better consistency with experimental findings.

5.4.2.4. Effect of wall treatment

The velocity distribution in the near wall-region is an important aspect of turbulence modelling as velocity fluctuations are significant at this region, which they affect the mean velocity of the flow. The comparison between experiment and wall treatment models (standard and enhanced wall functions) is shown in Figure 5.14.

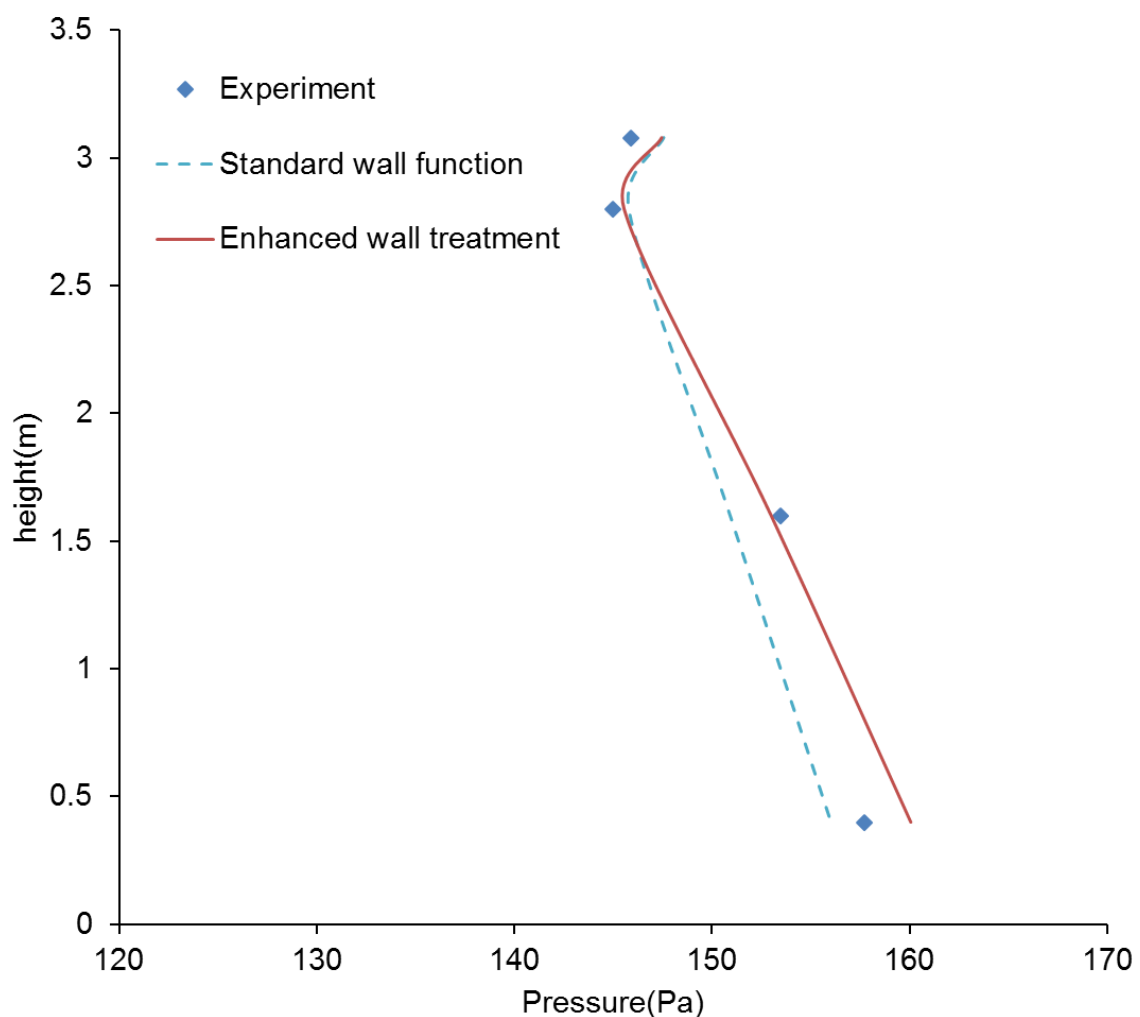


Figure 5.14: Pressure profiles for experiment and simulation of different near-wall treatment models

According to the diagram above the standard wall function, though followed a similar trend with the enhanced wall model and experiment a greater pressure gradient was observed. The reason being standard wall functions simplify the velocity fluctuations and this affects the pressure gradient. Liu et al. (2013) reported that the standard wall function is grid dependent and are important in the near-wall region. This means in non-equilibrium and non-ideal ideal conditions the standard wall function is insufficient. The standard wall function does not predict better when the viscous boundary layer equation is used. Therefore, an enhanced wall treatment should be ideal to show the near- wall effect in a CFB as suggested by Liu (2014).

5.4.2.5. Effect of particle-wall restitution coefficient

The restitution coefficient measures the turbulent kinetic energy dissipated due to collisions with the wall. Figure 5.15 shows the pressure profiles at different particle-wall restitution of 0.4,0.9 and 1; the trend for pressure in the riser was very similar to experimental values. Hassan (2013) confirmed that different particle-wall restitution coefficient has less effect on the pressure gradient. Jin et al. (2010) also confirmed this with regards to solid concentration, solid velocity and gas velocity for Geldart B particles in a CFB.

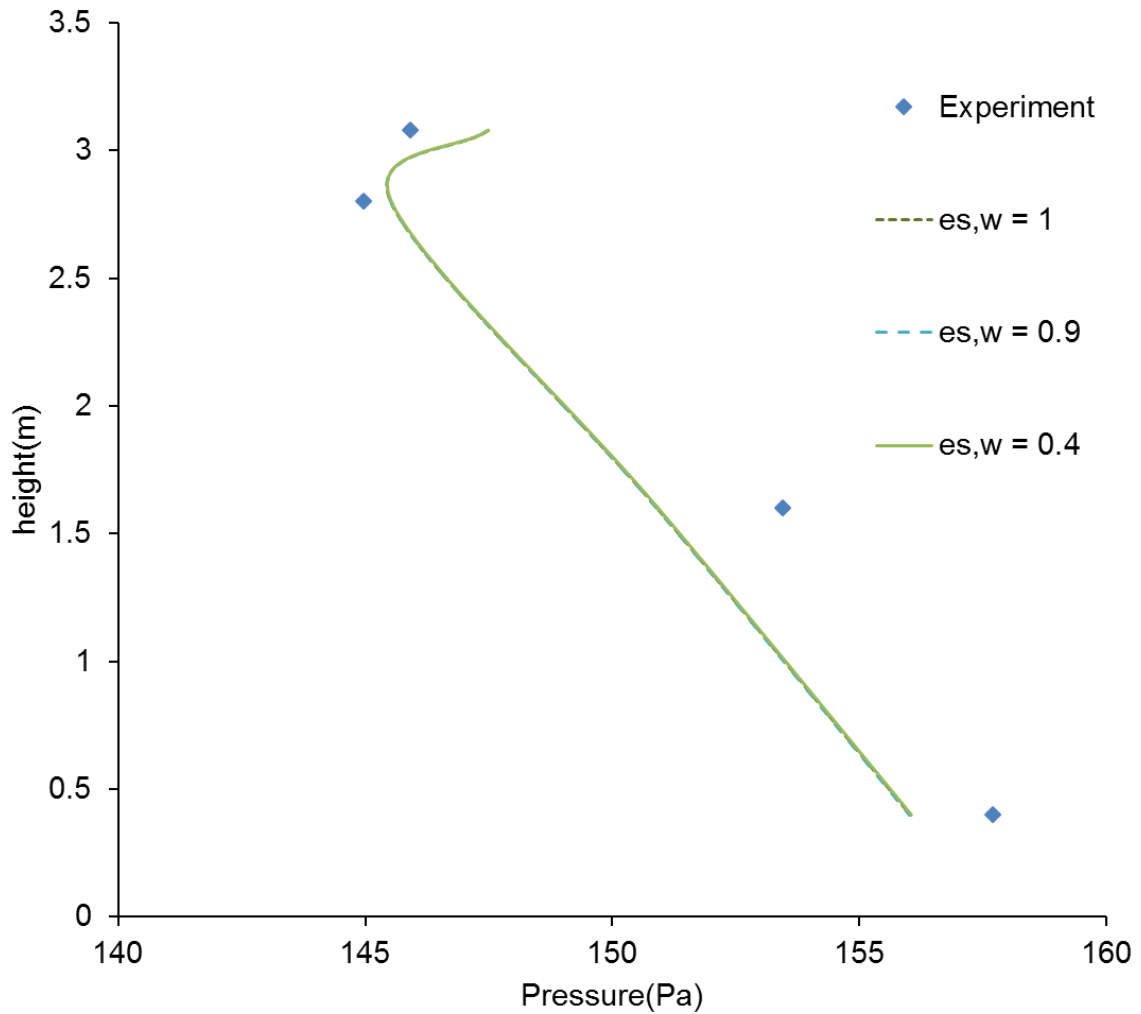


Figure 5.15: Pressure profiles for experiment and simulation for particle-wall restitution of 0.4, 0.9, and 1

5.4.2.6. Effect of specular coefficient

The specular coefficient is a measure of collisions which transfer momentum to the wall based on shear and no shear as stated earlier in Chapter 2. Figure 5.16 shows the pressure profiles from smooth wall condition ($\varphi = 0$) to rough wall conditions ($\varphi = 1$). There is free-slip for solid velocity at wall boundary in smooth walls and significant momentum transfer in rough walls (Almuttahir & Taghipour 2008b).

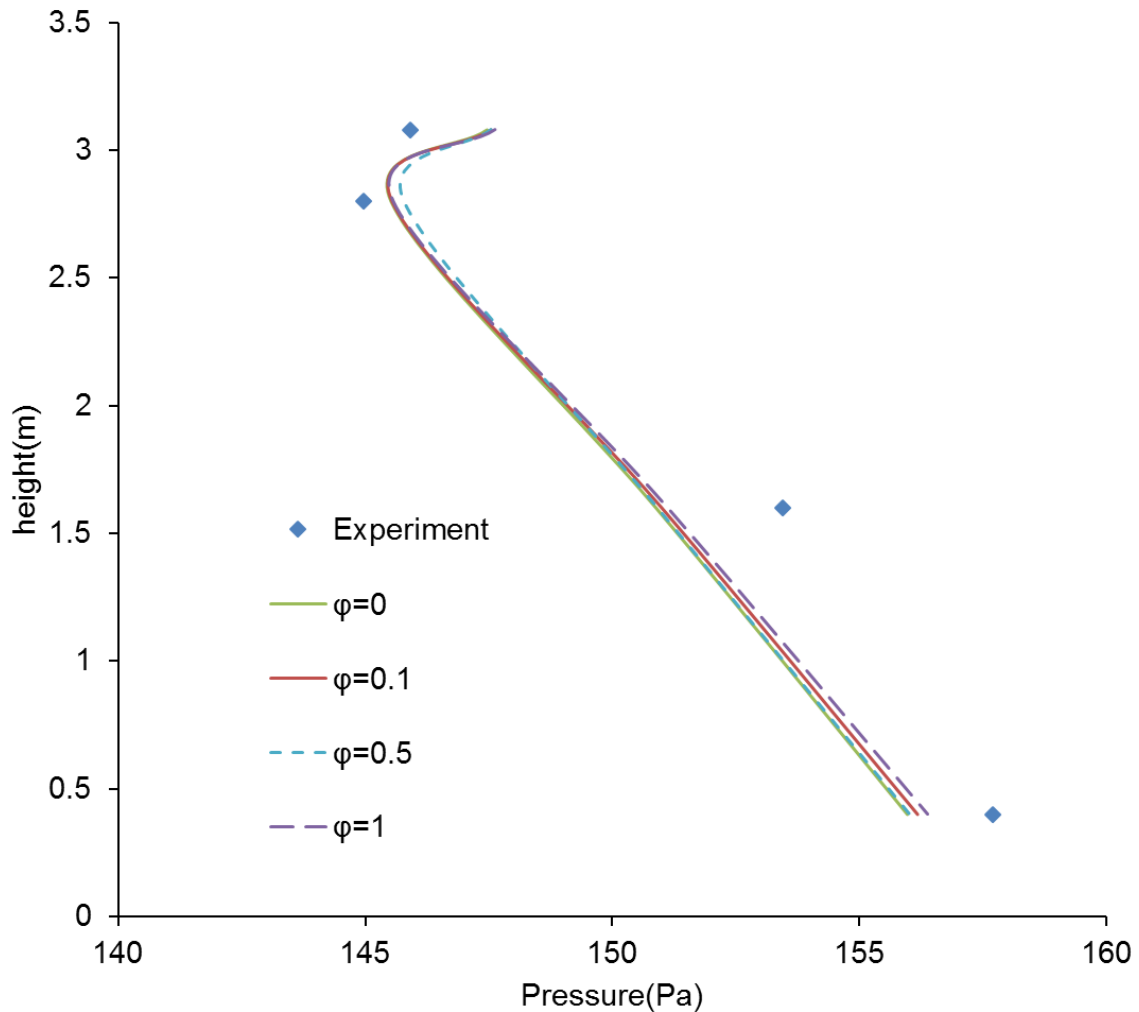


Figure 5.16: Pressure profiles for experiment and simulation of different turbulence models

The pressure profile at specular coefficient of 0, 0.1, 0.5, and 1 was similar to the profile observed in experiment. The effect of specular coefficient is observed in more detail for solid concentration in the radial direction. The usage of a lower specular coefficient predicts high concentration at the near-wall region which is similar to the behaviour observed in circulating fluidised beds.

5.5. Conclusion

In this Chapter, the experimental technique to validate the CFD model used for the hydrodynamics in a CFB was described. The solid circulation rate showed a behaviour similar to literature for a fast fluidisation regime. The pressure profiles were tested to validate the hydrodynamics model to be used for char gasification in a CFB. The different drag laws showed qualitative agreement with the experimental results for pressure profiles. The RNG and realisable turbulence model were more similar to the experimental results. The enhanced wall model proved to be more accurate in terms of simulating the near-wall

boundary regime. The effect of wall shear properties (specularity coefficient and restitution coefficient) was also compared with the experiment. The restitution coefficient showed no effect on the pressure gradient across the riser. It has shown significant agreement with experimental literature. The specularity coefficient exhibited a similar trend with minimal effect on the pressure gradient. The results established that pressure profiles rarely show the effect of wall shear on the CFD model though reasonable for representing the flow dynamics in a CFB. It has shown that using the Eulerian-Granular model the hydrodynamics in a CFB are predicted well.

CHAPTER 6 : MODELLING OF CIRCULATING FLUIDISED BED GASIFICATION OF CHAR

The chapter initially comprises of the background knowledge on biomass gasification and the different reactors used for the process. A literature review on the experimental and numerical investigations were reported especially with regards to catalytic biomass gasification. The possibility of using char as a catalyst on tar was reported and compared with other natural sources. A Eulerian-Eulerian model for char gasification was implemented in a Circulating fluidised bed. A sensitivity analysis was introduced to study the different species rate models. Also, the effect of char on tar was studied to analyse its catalytic activity.

6.1. Background theory

6.1.1. Gasification

The conversion of biomass fuels to non-condensable gases usually for chemical feedstock or as fuel. Most of the progresses in gasification were done using coal or natural gas as raw material. It converts the fuel to gaseous fuels with the purpose of either increasing the heating value, removal of gases that produce pollutant when burnt or increasing the hydrogen-carbon ratio. It requires a gasifying medium unlike pyrolysis. A summary of the gasification process conditions is shown in Table 6.1.

Table 6.1: Summary of Gasification (Shinya & Yukihiro 2008).

Operating Condition Type	Conditions
Pressure	Normal Pressure (0.1-0.12MPa) ,High Pressure (0.5-2.5MPa)
Temperature	Low Temperature (below 700°C), High temperature (above 700°C)
Gasifying agent	Air, oxygen, steam, CO ₂ or a mixture
Mode of Heating	Indirect, and Direct
Reactors	Fixed bed, bubbling bed, circulating bed, entrained bed, rotary kiln, twin tower, molten furnace

The gasifying agent affects the heating value of the product, the reaction pathways and the final product gases. In Figure 6.1, the gasification products are mainly CO and CO₂ when the gasifying agent is oxygen. When the proportion keeps increasing it reaches a point where the amount is sufficient to produce only combustion products; these products have no significant heating value. Steam as a gasifying agent shift the reaction upwards towards the

hydrogen corner producing high hydrogen-carbon ratios. Air as a gasifying agent dilutes the final product and produces other contaminants from nitrogen.



Figure 6.1: C-H-O diagram of the gasification process (Basu 2010).

6.1.1.1. *Gasification process*

The process of gasification is divided into different stages by which biomass is converted to mainly non-condensable gases for fuel, chemical or energy needs. This stages are as follows pre-processing, drying, devolatilisation, and char gasification.

Pre-processing

This is the stage where the biomass feedstock is prepared for conversion. It includes size reduction of biomass, drying feedstock and densification due to low density of the material. This is vital for increasing surface area for the process and contact points within the biomass particles. The feed properties of the biomass and their condition greatly affect thermochemical conversion processes and product.

Drying

This depends on the mode of heating usually the part of the carbonaceous feedstock is heated to provide energy for the endothermic reaction or heating of an external source provides the heat. The moisture content of the organic matter is removed before the beginning of the process. This moisture content can be from 10- 90% depending on the type of feedstock, this takes away a minimum of 2260KJ of energy to vaporize a kilogram of moisture (Basu 2010).

Pyrolysis

In the pyrolysis zone large hydrocarbon molecules are broken down into smaller molecules in a zero oxygen environment. The process produces primary liquid tars and char for the gasification reaction. These primary tars are converted into secondary and tertiary tars that create a huge problem during the gasification process i.e catalyst deactivation, fouling of equipment. The process of devolatilisation/pyrolysis is discussed in more detail in Chapter 3.

Char gasification

These reactions proceed after pyrolysis; the pyrolysis products and the gasifying medium which includes char, hydrocarbons, and gases react in several reactions. The reactions are shown in Table 6.2.

Table 6.2: Summary of Gasification Reactions (Basu 2010).

Reactions	Chemical Reactions	Enthalpy of Reaction(KJ/mol)
Water –gas shift	$CO + H_2O \leftrightarrow CO_2 + H_2$	-41.1
Water gas	$C + H_2O \leftrightarrow H_2 + CO$	131.3
Hydrogasification	$C + 2H_2 \leftrightarrow CH_4$	-74.8
Boudouard Reaction	$CO_2 + C \leftrightarrow 2CO$	172.8
Partial Char oxidation reaction	$C + 0.5O_2 \leftrightarrow CO$	-111
Oxidation reaction	$C + O_2 \leftrightarrow CO_2$	-394
Carbon Monoxide Oxidation	$CO + 0.5O_2 \leftrightarrow CO_2$	-284
Methane Oxidation	$CH_4 + 2O_2 \leftrightarrow CO_2 + 2H_2O$	-803
Hydrogen Oxidation	$H_2 + 0.5O_2 \leftrightarrow H_2O$	-242
Carbon monoxide methanation	$2CO + 2H_2 \leftrightarrow CH_4 + CO_2$	-247
Carbon monoxide methanation	$CO + 3H_2 \leftrightarrow CH_4 + H_2O$	-206
Carbon monoxide methanation	$CO_2 + 4H_2 \leftrightarrow CH_4 + 2H_2O$	-165
Steam Reforming	$CH_4 + H_2O \leftrightarrow CO_2 + 2H_2$	206
Methane oxidation	$CH_4 + 0.5O_2 \leftrightarrow CO + 2H_2$	-36

The rate of gasification of char material is dependent on the biomass and the gasifying medium used for the process. Oxidation reactions are relatively very quick; these reactions usually follow the water gas reaction. The boudouard reaction is 2-5 times slower than the water gas reaction. The slowest is the methanation reactions, which occurs mainly over 1273K without the need of a heterogeneous catalyst. It is estimated that the relative rates of

the reactions excluding the shift reactions at 1073K, 10KPa was $10^5, 10^3, 10^1$, and 3×10^{-3} (Basu 2010).

6.1.1.2. Tars

The major problem of gasification is the amount of tar produced during the process. Tars are generally compounds with molecular weight greater than benzene; they are produced from low temperature and low oxidant concentration (Duc et al. 2013). The quantity and composition of this tars are dependent on the biomass type, gasifier type, and operating conditions. It is a mixture of complex aromatic compounds derived from cellulose or lignin. Tar has been generally classified into classes due to its complex nature as shown in Table 6.3.

Table 6.3: Classification of biomass tars (Paasen & Kiel 2004).

Classification of tars	Description	Examples
Class 1: GC undetectable	These tars are normally undetected using GC-FID or GC-MS.	Undetectable
Class 2: Heterocyclic components	These are highly soluble compounds and are a representative of tars at $< 800 \text{ }^\circ\text{C}$.	phenol, Pyridine, cresols, and dibenzophenol
Class 3: Aromatic hydrocarbons (LAH)	These are pathways for tar formation and do not present solubility and condensation problems.	1-ring compounds i.e. benzene, ethylbenzene, styrene, xylenes, and toluene
Class 4: Light polyaromatic hydrocarbons (LPAH's)	Condensation problems at low temperature. They form a major part at temperatures $> 800 \text{ }^\circ\text{C}$	2-3 rings compounds i.e. naphthalene, methylnaphthalene, fluorine, Indene, and anthracene
Class 5: Heavy polyaromatic hydrocarbons (HPAH's)	They condense at high temperatures and are mainly complex tertiary tars.	4-7 rings compounds i.e. pyrene, perylene, coronene, and chrysene

Class 1 tars are generally undetectable and do not present any problems as part of tars. The LAH class of tars are not problematic and represent mainly benzene and toluene. Benzene is a more stable compound and is formed at extremely high temperatures. HPAH are present at very low concentration in tars, though favoured by high temperature. LPAH are

considered the most difficult tars as they easily condense and cause fouling of process equipment.

Researchers mostly model these tars based on the major constituent of the different classes (i.e. benzene, toluene, phenol, naphthalene, heptane, cyclohexane, pyrene etc.). LPAH and heterocyclic tars as they are the classes that represent Naphthalene and phenols as the major tar compounds. Phenol is mostly decomposed at high temperatures and corresponds to tars broken down through thermal cracking. Naphthalene are considered a problem, they require extremely high temperatures to break down and condenses at low temperatures. Therefore, it is used extensively in literature to model the behaviour of tars.

Tar cracking/reforming Catalysts

Tars can be removed by physical, catalytic, and non-catalytic processes. Tar is difficult to remove by thermal processing only due to the high activation energy $>250\text{KJ/mol}$ required to break down these complex compounds (Guan et al. 2014). The presence of catalyst reduces the activation energy $<123\text{kJ/mol}$ of this endothermic reactions and increase the possibility of low temperature gasification between $650\text{-}850\text{ }^{\circ}\text{C}$ (Coll et al. 2001). The catalytic processing of tar has been implemented both downstream and in-processing. The catalysts used for tar cracking are divided into natural and synthetic catalyst. The synthetic metallic catalysts are based on K, Fe, Co, Ni, Mn, and Cu. They deactivate rapidly due to toxic substances like sulphur, chlorine, and alkaline metals in the product gas and coke formation. These catalysts have been doped with catalyst from natural sources olivine, dolomite, calcite and magnetite to increase activity and prevent coking. Natural catalysts are relatively cheap compared to synthetic catalyst. Synthetic non-metallic catalyst include ash, char and charcoal which are low cost and generally produced from thermal conversion processes. Char is a major product of biomass pyrolysis; a solid residue containing mainly up to 90% carbon, ash and metal impurities. The properties and composition of the char produced is dependent on gasifier type and process conditions. The catalytic activity of char is dependent on the pore size, surface area, ash, mineral impurities (El-Rub 2008). Char is consumed through gasification reactions and hence continuous supply is required for catalytic activity to be achieved.

6.1.2. Gasification reactors

6.1.2.1. *Fixed bed Reactors*

Downdraft

It is the most popular gasifier used for biomass gasification occupying 75% of usage (Maniatis 2008). This reactor has a co-current flow of gases and solids down to the combustion zone from the top (see Figure 6.2). The biomass and the gasifying agent enter through the top of the gasifier slightly passing through preheating and pyrolysis zone producing char and pyrolysis gases. The pyrolysis products pass through the combustion zone; this in essence decomposes most of the tars about $1\text{g}/\text{Nm}^3$ produced during the process (Milne et al. 1998). This zone is at a throat constriction for an imbert downdraft gasifier; it creates a bridging that causes the concentrating of the biomass leading to high tar accumulation. The final products leave at the bottom of the reactor after gasification of the char.



Figure 6.2: Imbert downdraft gasifier (Warnecke 2000).

However, it produces a very high temperature gas (800°C) which needs energy recovery to improve overall process efficiency (Kumar et al. 2009). Also, the biomass feedstock needs to be densified. It has to have very low moisture content (20%), low ash content (5%), and low

finer, which limits the flexibility on the type of material. Low Fines reduce the pressure drop in the reactor, while low moisture and ash makes it possible for high temperatures to be achieved.

Updraft

This reactor has a counter-current flow between the gasifying agent and biomass solids. It is the simplest form of fixed bed gasifiers and has the ability to withstand high ash (15%) and moisture (50%) than the downdraft gasifier (Chopra & Jain 2007). It does not have specificity problem with regards to biomass size and quality.



Figure 6.3: Updraft Gasifier (Warnecke 2000).

In Figure 6.3, the biomass feedstock enters at the top of the reactor flowing down slowly into the drying zone. Drying occurs with the help of the upward flowing high temperature product gas; the dried biomass goes into devolatilisation and the char produced moves downward to be gasified. The vapours produced moves upward with the product gas; while the tars either vaporize with producer gas or condense on the char produced. The producer gas leaves the reactor at a low temperature and dust content with very high tar content ($100\text{g}/\text{Nm}^3$) because drying and pyrolysis products leave the reactor without decomposition (Milne et al. 1998).

The char and the condensed tar are further reduced and cracked to gas and char particles in the gasification zone. The final products leave the reactor at the top.

Side draft

This are mostly used for high quality charcoal based feedstock; the fuel is feed at the top while the gasifying agent mostly air is injected through the side of the reactor. High velocity air or oxygen is injected through the side just above the grate; this creates a small area combustion zone due to high concentration of oxygen (Chopra & Jain, 2007). The next zone gasifies the char produced in the pyrolysis zone from the hearth zone. Gases leave the gasifier through the side opposite to that of the air entrance.

6.1.2.2. Fluidised bed

Bubbling Fluidised Reactors

Fluidization is a process by which solids are transformed into fluid like state through contact with liquid or gas (Basu 2006). Bubbling fluidised reactors operate at bubbling regime. The heat transfer medium is mainly through flue gas or product gas. The high superficial gas velocity is greater than the minimum fluidization velocity, therefore bubble and emulsion phases are created. A schematic of a fluidised bed reactor is shown in Figure 6.4.



Figure 6.4: Bubbling fluidised bed (Geldart 1986).

Bubbling fluidised beds are normally used for gasification of biomass as shown in Figure 6.4. The mode of operation is similar to that used for the pyrolysis process rather it operates at a higher temperature. The oxidizing agents serve as the fluidising gases. The biomass feed is near the bottom with the conversion occurring mostly within the bed. The bed temperature is in the range of 700°C-900°C (Bridgwater, Beenackers, et al. 1999).

Circulating and transported beds

This type of reactor operates along the fast fluidization regime. The particles sizes are between 1-2mm to achieve extremely high heating rates (Bridgwater & Peacocke 2000). The fluidizing media circulates continuously around and into the reactor with the residence times of all products being similar due to high velocity gas mixing.



Figure 6.5. Circulating Fluidised bed (Bridgwater 1984).

The circulating fluidised bed velocity is capable of easily entraining the particles. Therefore, it has the bed material circulated around the cyclone and reactor; this removes the ash and recycles the char particles. This reactor has a wide range of acceptability of feedstock with high conversion rates though produces a high tar content.

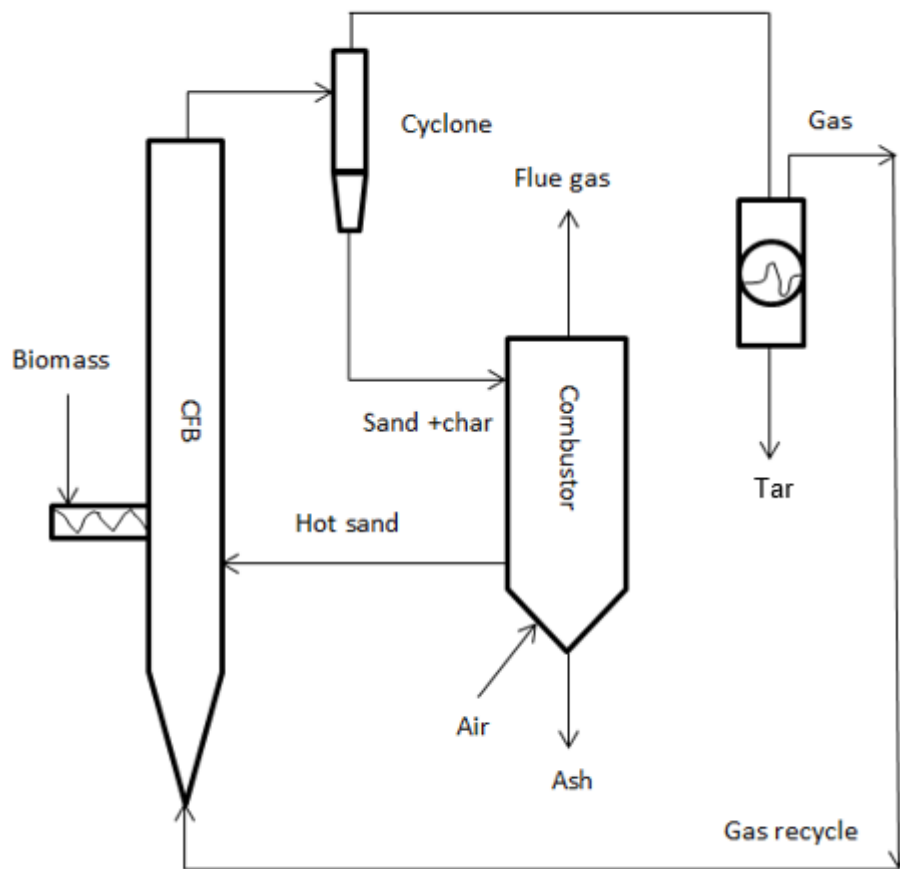


Figure 6.6: Dual circulating fluidised bed (modified from Bridgwater & Peacocke (2000))

A configuration by which the media is heated in a combustor is termed as the dual or twin fluidized bed (see Figure 6.6). The combustor can be either a bubbling type or fast bed. The temperature and flux from the combustor has to be controlled to meet requirements for gasification. The scale-up of fluidised beds are easier therefore very favourable for commercialisation. The advantages and disadvantages of these technologies are given in Table 6.4. Though the reactors are vital for gasification the product gas has to be cleaned to set standard for use in different applications.

Table 6.4: Advantages and Disadvantages of Reactors in a gasification process (Warnecke 2000).

Reactors	Advantages	Disadvantages
Downdraft	<p>Tar consumed due to high exit temperature</p> <p>Produces very clean product gas</p> <p>Multiple fuels processing capabilities</p>	<p>Limitations in biomass particle size and diameter</p> <p>High particulates in the product gas</p> <p>Low efficiency due to high amount of energy used in tar cracking</p>
Updraft	<p>It can handle high moisture and ash content biomass feedstock</p> <p>Low dust content in gas due to low velocities</p> <p>Higher efficiency process than the downdraft</p>	<p>Large amounts of tar in product gas</p> <p>Possible clinkering</p>
Bubbling bed	<p>Very high carbon conversion efficiencies almost 100%</p> <p>In bed Catalyst integration possible</p> <p>Easily scalable and good temperature control</p>	<p>Bed agglomeration and sintering</p> <p>Uneconomical for small scale operation</p> <p>High particulate product gas</p>
Circulating and transported bed	<p>High throughput</p> <p>Very high reaction rates and biomass conversion</p> <p>Greater biomass particle size range than other reactors</p> <p>Lower particulate product gas than fluid beds</p> <p>Twin beds have easy catalyst integration</p> <p>Greater quality gas overall</p>	<p>Bed slugging</p> <p>Corrosion and Attrition</p> <p>High pressure drop</p> <p>Twin beds have complex design so scale up is difficult</p> <p>Twin beds produce higher heating value gas than individual fluidised reactors.</p> <p>Tar loading from first reactor</p>
Entrained bed	<p>Low tar producer gas due to extremely high temperatures(1200°C)</p> <p>High conversion efficiency</p> <p>Easy scale up</p>	<p>Low calorific value gas</p> <p>Ash melting</p> <p>Feed specificity and Material of construction selection due very high temperature</p>

6.2. Literature review

6.2.1. Experimental studies on biomass gasification

The gasification of biomass in a circulating fluidised bed has been reported rarely in literature. The majority of the experiments are for bubbling fluidised beds especially with respect to catalytic gasification. The gasification of biomass in a bubbling bed has been reported for different biomass samples (Herguido et al. 1992). They suggested that temperature is important in determining the final product and gas composition. There is generally high gas yield with high temperature processes. They found it to be due to the favourable effect of temperature on the cracking of volatile matter, gasification of char, cracking and reforming of tars. The Tar yield decreases with temperature and steam/biomass ratio and was 2.8-5% at gasification temperature between 750 °C-800 °C.

The effect of gasifying medium was considered by Gil et al. (1999) for biomass gasification in a fluidised bed. The gasifying medium reported was steam, air and steam-O₂ gasification. In Air gasification the nitrogen dilutes the product gas and favours CO₂ and CO yield. The gasification using steam leads to significant increase in hydrogen as stated that steam/biomass ratio increase favours shift reaction that produces H₂ and CO₂ at the expense of CO. They observed tar content decreases according to the following gasifying agents (steam > steam- O₂ > Air). They reported that tar is a major problem in gasification and is dependent on the gasifying medium used for gasification.

Lv et al. (2004) studied the characteristics of steam-air gasification in a fluidised bed. They reported a parametric analysis on the effect of ER, temperature, Steam-to-biomass ratio, and particle size. The reported increase in gas yield with steam-to biomass ratio up to 1.35. They also found out that high steam content lowers the temperature of the process which can make it susceptible to high tar product gas. They concluded that the ER required for optimal yield is 0.23 and steam improves gas quality in a gasification process.

Narvaez et al. (1996) also reported gasification of biomass in a bubbling bed and considered the effect of temperature on tar and product composition. Air was used as a gasifying agent to analyse other conditions such as Equivalence ratio, secondary air feeding, H/C ratio, calcined dolomite. ER values vary from 0.20-0.40 for gasification; values greater than 0.45 produce gas with insignificant calorific value. They suggested for temperatures below 850 °C, the ER values should be between 0.3-0.4 due to high tar yield. An increase in ER value showed a decrease in the gas composition of the valuable product gases leading to high CO₂ arising from combustion reactions; though the total gas yield is increased. The H/C ratio increase leads to an increase in shift reactions that favour reforming of tar therefore the tar yield falls. The presence of calcined dolomite showed 40% reduction in the tar yield.

Arena et al. (2009) used calcined olivine in-bed for tar removal from the gasification of plastic waste. At temperatures between 794 °C-910 °C they observed 85% tar yield decrease. The carbon conversion increased from 59% to 65% and up to 84% at high ER values. The hydrogen content increased from 10% to 32%. The Cold gas efficiency was 56% for sand and up to 84% with olivine bed; the Carbon conversion efficiency was raised from a peak of 68% to 82%.

Miccio et al. (2009) compared different catalyst (quartzite, dolomite, olivine, and Ni-alumina) in-bed for gasification of biomass in a fluidised bed. The quartzite showed the minimal increase in H₂ concentration; the effect of olivine was shown to improve better. Ni-alumina generally showed better catalytic activity compared to the natural sources. Metal based catalyst K, Fe, Co, Ni, Mn, and Cu have higher reactivity but they are expensive. These catalysts deactivate rapidly due to catalyst poisoning caused by sulphur, chlorine and alkaline metals in the producer gas. Coke formation is prevalent at high tar levels on catalyst surface blocking pores. These catalysts can be doped with catalyst from non-metallic sources like olivine, dolomite, char, calcite and magnetite. Pfeifer et al. (2004) showed that dual fluidised beds have the ability to regenerate this doped metal catalyst in the combustor. The catalyst showed increases in the H₂ and CO yield consequently the CO₂ and CH₄ decreased due to reforming reactions.

van der Drift et al. (2001) used a 5kW circulating fluidised bed to study gasification of different biomass samples not limited to sewage sludge, wood, railroad ties, and cacao shells. The experimental analysis reported that water content has a major effect on the HHV, cold gas efficiency (CGE) and carbon conversion efficiency (CCE). The average values for the CCE, CGE and tar concentration were 92%, 61%, 270mg/Nm³. They showed that hydrocarbon concentration has a tendency to increase the heating value of the product gas due to high energy density. These hydrocarbons depend on the amount of oxygen in the process, which is determined by the Equivalence ratio (ER). The concentration of tars hugely depend on the following variables: ER, temperature, H-C-ratio and fuel size (van der Drift et al. 2001).

Yin et al. (2002) designed a circulating fluidised bed for risk husk gasification with the producer gas used for power generation. They found out that a lower temperature positively affects the gasification efficiency. This condition leads to high tar content though very high temperature leads to fusion of the char and ash, which causes bed agglomeration. The heating value of the product gas was between 4.7-6.2 MJ/Nm³. The yield of CO increases with increasing temperature though reaches a peak at about 750°C. He concluded that temperature is regulated in a circulating fluidised by altering the gas flowrate and feed rates.

A 300KW circulating fluidised bed was tested using olive oil waste for air gasification (García-Ibañez et al. 2004). The increase in the equivalence ratio (ER) causes the carbon conversion efficiency to increase slightly. They observed an increase from 81%- 87% in CCE for ER values from 0.41-0.76. They also found out that high ER leads to low heating value. Higher ER values generally increase the yield of the gas and favour tar cracking.

The elimination of tar can also be improved by integrated processes with pyrolysis and gasification occurring as a continuous process or separated within the system. Kersten et al. (2003) reported biomass gasification in a multi-stage novel circulating fluidised bed. The reactor is made up of several segments with opposite cone welded together in the riser. The advantage of the novel reactor is its ability to prevent gas back mixing and improve solid-gas residence time ratio. The novel reactor when compared with a general CFB predicted higher yield for CO and CH₄ at similar temperatures. The primary tars are converted completely due to the larger residence time. The H₂ yield was the same for both types of reactor configuration. Overall the CCE is higher at lower equivalence ratio of 0.3 for the novel CFB multistage reactor. The CCE increased from 87-96% and the gasification efficiency from 60-70%. They concluded that the separation zones created by the multistage cones leads to an oxidation zone where complete carbon efficiency and gasification efficiency >80% is attainable in a scale-up version of the reactor.

Zhou et al. (2009) implemented sawdust and rice husk gasification in a clapboard-type internal circulating fluidized bed gasifier. The ER values between 0.25-0.30 reached maximum heating value for rice husk and sawdust gasification. The gasification efficiency obtained was within 77%-81% at ER 0.25-28. They confirmed that increasing ER raises the overall temperature of the gasification process.

Chen et al. (2004) integrated biomass pyrolysis with gasification in a circulating fluidised bed to improve producer gas quality. It combines the processes of partial oxidation, fast pyrolysis, gasification, and tar cracking. The processes occur at different levels in the circulating fluidised bed so only char is gasified at the gasification zone. They obtained tar yields of 0.75g/Nm³; the CO₂ yield was 42%, which is relatively higher than CO concentration. This is prevalent in air gasification especially at the ER value of 0.30 used in the reactor. The heating value was about 3.6 MJ/ Nm³ which is very low though acceptable for air gasification processes.

The Viking gasification concept is a two-stage gasifier that pyrolysis and gasification takes place in two reactors (Henriksen et al. 2006). This gasifier produced minimal amount of tars as compared to other gasification processes. Brandt et al. (2000) compared the process with and without passing the product gas through activated char. Naphthalene was reduced by a

factor of 65. They showed that activated char is capable of reforming tars to a minimal level in the gasifier.

Borson et al. (1989) reported the effect of passing tars through activated char bed. The conversion was from 0% at 400 °C to 30% at 600 °C. El-Rub et al. (2002) carried out a tar cracking in an entrained flow cracker using cheap catalyst (FCC catalyst, char and ash). These catalysts were compared with situations where the catalytic material was silica sand and nickel catalyst. At 40 g/Nm³ of tar compound model as naphthalene, they obtained 2%, 55%, 61%, 100% in order of sand < olivine < dolomite < nickel. The conversion obtained for FCC, ash, biomass char, and commercial char are 60.3%, 73.7%, 94.4%, 99.6% for 90 g/Nm³ naphthalene tar.

Kuhn et al. (2008) simultaneously reformed toluene, methane and naphthalene as model tar compounds. The naphthalene conversion of 88.3% at 850 °C was achieved using Ni/olivine mixture. They found that methane conversion (0.7%) was negligible throughout the process and the reforming of tars is temperature dependent.

El-Rub et al. (2008) also reported a comparison of different catalyst including biomass char, calcined dolomite, olivine and nickel using phenol and naphthalene as a model tar compound. The phenol conversion at 700 °C showed that silica sand, olivine, commercial biomass char, FCC, dolomite, nickel achieved the following conversions 34.5 %, 42.7 %, 81.6%, 87.1%, 90%, and 91%. The naphthalene conversion was similar to results obtained by El-Rub et al. (2002). They concluded that naphthalene, toluene, and phenols are the main problematic tars.

Gilbert et al. (2009) passed pyrolysis tars through a bed of char in a tubular reactor at different conditions of temperature, bed length, and particle size in a nitrogen environment. They showed steam and CO₂ environment are needed for tar conversion as char conversion of tar is through steam or dry reforming reactions.

Fuentes-Cano et al. (2013) also studied catalytic decomposition of coconut char, coal char, and DSS char using naphthalene and toluene as model tar compound. The kinetics of naphthalene and toluene over char was determined, which included the char deactivation rate with time. They concluded that for efficient tar conversion the carbon consumption rate should be greater than deactivation rate; higher temperature and steam concentration prevents the chances of char deactivation.

Klinghoffer (2013) studied utilising the catalytic effect of char to breakdown toluene (tar model compound). The test results showed that char has the ability to crack and reform toluene present in tars thereby increasing the hydrogen concentration of the product gas.

Char does it by decomposing the C-C and C-H bonds in the hydrocarbon. They also found out that metals in the char increase its catalytic activity.

Tars have also been tested using biomass char in a fluidised bed (Nitsch et al. 2014). Phenol was used to represent the tars present in biomass pyrolysis and gasification. They found out that H₂ inhibits gasification as compared to nitrogen and steam; the presence of 20% led to increased formation of methane. The cracking of tars over char produced 20% decrease in CO concentration. The presence of steam caused all the hydrocarbons to be eliminated excluding methane and benzene; this catalytic activity is considered very high. The issue was the need to separate products of gasification and reforming of tars. Char is more efficient at higher H₂O concentrations than olivine at reforming tars. The catalytic activity of char should not be excluded from gasification models.

6.2.2. Numerical studies on biomass gasification

There have been several models describing the gasification of biomass in bubbling fluidised bed and circulating fluidised beds. These models have been described as Computational fluid-dynamics models (CFDM), fluidization models (FM) and black-box models (BBM) (Gómez-Barea & Leckner 2010). The Fluidisation models have been reported extensively in literature and provide a linkage between the other two models. Fiaschi & Michelini (2001) developed a one dimensional two phase model of biomass gasification in a bubbling fluidised bed. The model considered the reaction kinetics and mass transfer model to study the one-dimensionality of fluidised beds and other diffusion phenomena. A sensitivity analysis was reported for the ER, pressure and surface gas velocity. The model was validated with experiment and had very good agreement with the results. The model showed that mass transfer dominates the gasification initial and reaction kinetics take over after equilibrium has been reached. The biomass gasification of beech wood using a two-phase model was also reported in literature (Radmanesh et al. 2006). The model included the hydrodynamics of both phases and reaction kinetics in the fluidised bed and freeboard regions. A two-phase model was used to describe the gas phase in the bed, whereas a counter-current back-mixing model was used for the char mixing. The model was in good agreement with experimental results. The model has been suggested not to be very good for CFBs (Johansson 2005).

Jennen et al. (1999) reported a one-dimensional mathematical model for circulating fluidised bed gasification of wood. The model included the hydrodynamics, kinetics and heat models in the CFB. The pressure and temperature profiles agree with pilot plant results and there was qualitative agreement with the product gas composition as well. Liu & Gibbs (2003) also

used a simple hydrodynamic model coupled with reaction kinetics. The model predicted the effect of ER, temperature, moisture content, tar, NO, NH₃, and HCN emissions. The model qualitatively agreed with experimental results and the catalytic effect of bed was observed for oxidation and reduction of NH₃ and NO. Petersen & Werther (2005) used a similar mathematical model to describe the validating with experimental findings. The model described both the fluid dynamics and gasification model using sewage sludge as a feedstock. They found out that gasification process is dominated by the kinetics which affects the product composition. They extended the earlier model to a 3D to account local effects in scaling up 2D and 1D models. The model gives a good description of combustion zone at riser bottom and can be used for fluidised bed with different geometries. Miao et al. (2013) developed a more comprehensive model which includes the hydrodynamics, chemical kinetics, mass and energy balance to predict the performance of a CFB. Rice husk was used as the feedstock to obtain concentration and temperature profiles. The combustion zone saw increase in temperature at the dense region and a gradual decrease is observed at the dilute region due to endothermic reactions of gasification. It shows that steam reaction and partial reforming occurs at the bed region showing improvements in hydrogen and carbon monoxide.

The BB models are mainly equilibrium, thermodynamic and heat/mass balance models. Mansaray et al. (2000) implemented the model in ASPEN PLUS with the hydrodynamics and concluded that the model could be used for different feedstocks. Nikoo & Mahinpey (2008) also used ASPEN PLUS simulator coupled with hydrodynamics and reaction kinetics in a fluidised bed. The model was used for parametric study of the effect of temperature, ER, SBR, and particle size on the product composition and the conversion efficiency. The results predicted increase of conversion and CO concentration with increased temperature; this temperature also increases at higher ER values.

Doherty et al. (2009) reported a model using ASPEN PLUS for a circulating fluidised bed. This model studied the effect of ER, temperature, moisture and other operating conditions on the gas composition and conversion efficiencies. The model is based on the Gibbs free energy minimisation and broken down into the different stages occurring in a gasification process. The model was in agreement with experiment from Li et al. (2004) though it over predicted the CH₄ leading to high CGE and LHV of product gas. Li et al. (2004) used a similar non-stoichiometric equilibrium model to describe biomass gasification in a CFB based on Gibbs free energy.

Loha et al. (2011) used an equilibrium model to study the effect of using different biomasses (sugarcane bagasse, rice husk, rice straw, and groundnut shells). They proposed a

correlation to calculate hydrogen gas yield at different temperatures and steam-to-biomass ratio.

Ardila et al. (2012) modelled the gasification of sugarcane bagasse in a circulating fluidised bed using ASPEN PLUS. The model also used the Gibbs free energy minimisation method to investigate the effect of operating conditions which has been coupled with hydrodynamics and reaction kinetics models. The tar was represented as naphthalene and the process is divided into stages. The product gas compositions of CO, CO₂, and H₂ were in agreement with experiment. The CO₂ was negligibly affected by the shift in temperature and steam-to-biomass ratio. Ngo et al. (2011) used a quasi-equilibrium model for a dual circulating fluidised bed. The model considered investigated the gasification temperature and steam to biomass ratio. They concluded the model needs to include the tar cracking for a complete picture of the process.

Some BB models do not describe the dynamics of the fluidised bed while the ASPEN PLUS models had FORTRAN codes describing these characteristics. The CFD models provides a superior description of the process in a fluidised bed though they are rare in literature due to computational time and expense. Oevermann et al. (2009) used a 2D Eulerian-Lagrange model for bubbling fluidised bed gasification using Large Eddy simulation model based on the Smagorinsky sub-grid model. They acknowledged the computational demand required for the Eulerian-Lagrange model due its consideration of particle scale interactions. Pasangulapati (2012) used the Eulerian-Lagrangian model with a BFB for switchgrass biomass. The finite rate/eddy dissipation and realisable k-e model was used to describe the chemistry model and turbulence. The non-uniform characteristics of the temperature showed the different reaction zones in the fluidised bed. Xie et al. (2012) also used the developed model for a 3D gasification of forest residues in a bubbling fluidised bed. The gasification performance was studied by adjusting the different parameters of temperature, equivalence ratio and steam to biomass ratio. They produced an increase in Hydrogen and a decrease in methane yield with increasing temperature. This was attributed to temperature favouring methane steam reforming and tar cracking reactions. The ER values favour the increase in temperature and rate of reactions up to a certain limit; though the total fraction of combustible products decrease with higher ER. The optimum carbon conversion efficiency was obtained at ER value of 0.23. The increase in SBR can cause low temperatures, this favours the production of CO₂ and H₂. The relative error obtained from experimental results by Lv et al. (2004) was about 7% for all cases. Cadile et al. (2013) also applied the same model to a shallow dense fluidised bed for wood gasification and obtained similar agreement with experiments. Thapa & Pfeifer (2014) used Barracuda® VR15 to develop a Eulerian-Lagrangian model for a bubbling fluidised bed. The model predicted high concentration of

hydrogen peculiar to steam gasification and the characteristics of the freeboard and dense bed with regards to product composition and reactions. CH₄ and CO are produced in the dense region where they react to form higher concentrations of H₂ and CO₂ in the freeboard. Ku et al. (2015) also used the Eulerian-Lagrangian and predicted that higher temperature was favourable to endothermic reactions. The carbon conversion decreases and product composition behaviour was similar to the Barracuda@VR15 model.

Gerber et al. (2010) reported Eulerian-Eulerian model of a bubbling fluidised bed using char as a bed material. The model considered two secondary tar reactions and the char material was considered as a reactive bed. There was good agreement between the experimental results for temperature, product gas, and tar concentration with the CFD model. The concentration of CO₂ was higher than the results predicted from experimental findings. The effect of the different tar secondary models showed significant variations in the gas composition. The Euler-Lagrange model from Oevermann et al. (2009) produced higher CO value than CO₂ which corresponds to the experiment. This might be due to the temperature difference at different zones along the riser for the different cases. They reported the possibility of using char as a bed material though its effect was not considered in the model.

Xue & Fox (2014) accounted for variable density of particle due to devolatilisation and chemical reactions in a polydisperse fluidised bed. The volatiles and char are generated immediately in the injection point. The results provided a detail of the particle behaviour in which the particle density variation affected the hydrodynamics and char elutriation. The small particles segregate and elutriate while larger particle become difficult to fluidise. The particle density decreases as the devolatilisation and char gasification proceeds. The effect of moisture content on the reaction temperature was evident and this will favour WGS reaction and char gasification.

Thankachan et al. (2014) also reported gasification with the Eulerian-Eulerian model. The rate of chemical species was determined by eddy dissipation and finite rate. The results of gas velocities, flow patterns, and gas compositions were predicted similar to experiment results. Patra (2014) incorporated the eddy dissipation and laminar finite rate to a model for rice husk gasification in a fluidised bed. The model used standard k-e to describe the turbulence and included homogeneous and heterogeneous reaction kinetics. The showed that high temperature leads to more heterogeneous reaction which gives higher conversion of char. At a gasification temperature of 800°C, they achieved 100% carbon conversion and similar product compositions to experiment.

Shi et al. (2015) studied the effect of Steam to Biomass ratio and temperature for steam gasification of biomass in a fluidised bed. The model considered biomass to be ash free and

contain only volatile and char. The H₂ concentration increases at high SBR values and CO decreases, which they both reach an optimum yield. The experiment contained tar cracking at high temperature which was not considered in the model, therefore there was a lower concentration of CO. Other studies of fluidised bed gasification using Eulerian-Eulerian multiphase model were studied by the following authors. They showed that gasification can be implemented using Eulerian-Eulerian model in a fluidised bed and results were in good agreement with experiment.

CFD models for a CFB gasification of biomass are very sparse to the best of my knowledge. The reported authors are Liu et al. (2013), (Liu et al. 2014), and Hassan (2013). The gasification of reported a 3D air gasification model in a circulating fluidised bed using the Eulerian-Eulerian model (Hui Liu et al. 2013). The model included the hydrodynamics, energy and reaction kinetics to describe concentrations, velocity and temperature. The finite rate/eddy dissipation for the species model. The effect of grid, turbulence model, radiation, equivalence ratio, and water gas shift reaction was investigated for the product distribution and gasification temperature. The devolatilisation was a single-step process and tar cracking was not considered. They showed that number of grid cells and the different k-e turbulence models have negligible effect on the composition and temperature of gasifier. The effect of radiation on the temperature was radiation decreases the predicted temperature in the riser and produced temperature trend similar to experimental data. The impact of water gas shift reaction was noticed on the H₂ and CO₂ yield increase in the product gas compared to the base case.

Liu et al. (2014) also investigated the effect of char combustion product distribution coefficient (0.5, 0.75, and 1) for biomass gasification in a CFB. The multiphase model used the RNG k-e turbulence model coupled with enhanced wall treatment to describe the turbulence in the riser. The results were validated with experiment from García-Ibañez et al. (2004) and was in good agreement.

Hassan (2013) also reported Eulerian-Eulerian 3D model for biomass gasification in a CFB. The work was comprehensive which included a sensitivity and parametric analysis of the process. They also studied the effect of radiation and combustion reactions on the product distribution. The effect of radiation was different from results from Liu et al. (2013) due to the lower temperature and low concentration of solid particles. They showed that H₂ and CH₄ combustion has minimal effect at low air or oxygen flowrates. They concluded a strong influence between temperature with tar and product yields.

The literature above has shown that char can be used both as a feed material and bed material according to Gerber et al. (2010). The possibility of char cracking reactions was

considered in the model, which was mostly reported in experimental findings. The literature of CFB has shown both laminar finite rate and eddy dissipation have been used to describe the rate of the chemical species. They also considered the way tar is modelled as (naphthalene, toluene, benzene and phenol) and their effect on the final product composition. Naphthalene has shown to be the main problematic tar component in the product gas, therefore can represent the complex material. The effect of bed material on the product composition is observed; as catalytic reforming does affect the product quality. It also concluded that the optimum operating conditions have to be considered in modelling gasifiers. This chapter looks into the gasification of char in a CFB considering the effect of char as a catalyst and reactant. The tar model compound used was naphthalene for the tar catalytic reactions with char.

6.3. Proposed CFD Model

A three phase Eulerian-Eulerian model for char gasification was implemented in a circulating fluidised bed. The model included the continuity, momentum, energy and species equations incorporated with chemical reaction kinetics. The gas phase was assumed as a Eulerian phase, while the two solid phases were modelled based on the kinetic theory of granular flow (KTGF). The turbulence was described using the dispersed RNG k- ϵ model and the near wall region was described using the enhanced wall treatment. The drag law is based on the model by Syamlal & O'Brien (1987), which is suitable for dilute flows for both the solid-solid and solid-gas momentum exchange coefficient. The solid and frictional pressure, radial distribution and bulk viscosity are taken from Lun et al. (1984). The kinetic and collisional viscosity are given based on Syamlal et al. (1993). The frictional viscosity was not considered due to the nature of circulating fluidised beds. The heat transfer coefficient between the gas and particulate phase was given from Gunn (1978). This is implemented with a C- subroutine UDF gasification model code using ANSYS Fluent 14.0. A detailed literature about the hydrodynamics are given in chapter 2.

6.3.1. Species rate model and reaction kinetics

The species model compared both laminar finite rate and the finite rate/eddy dissipation rate to study the difference in product composition. The rate of the pyrolysis and tar reactions are given in Table 6.6. The process produces the char provided for the heterogeneous gasification reactions. The volatiles are released from the biomass to evolve to tars (bio-oil) and non-condensable gases; the carbon particles are transformed to char which is mainly carbon. The proximate and ultimate analysis is given in Table 6.5.

Table 6.5: Proximate analysis of switch grass char

Analysis	Parameters				
	Moisture(wt%)	Volatile(wt%)	ash(wt%)	Fixed carbon (wt%)	HHV(MJ/Kg)
Proximate analysis	0.3	37.5	16.4	46.10	18.34

The pyrolysis reaction model is a two-step model including the primary and secondary reactions. The thermal cracking of tars are important only at temperatures above 500°C to improve yield but has no effect on the gas composition (Fagbemi et al. 2001). The simple equation for the thermal cracking of tar is given below (Boroson et al. 1989b):

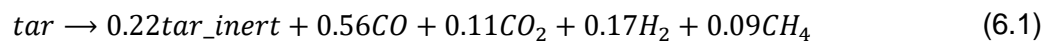


Table 6.6: Kinetic rate equations of Primary and secondary reactions

Reaction	Rate Equation	A	E	References
Primary Pyrolysis	$r_{pyrolysis} = kC_{volatiles}^{0.67}$	3.88×10^{10}	103.7	Pasangulapati (2012)
Thermal tar cracking	$r_{tar-cracking} = kC_{tar}$	1.55×10^5	87.6	Diebold (1985)
Catalytic Tar reforming (char)	$r_{tar-reforming} = kC_{tar}$	1.0×10^4	61	EI-Rub et al. (2004)

The catalytic steam reforming of tar was considered as a particle surface reaction model in ANSYS Fluent 14.0. The reforming reaction is given as follows:



The tar model compound used is naphthalene similar to an experimental literature to study tar reforming using biomass char. The Arrhenius rate constant for the catalytic reactions is given in Table 6.7.

The carbon containing char produced from the pyrolysis reaction is consumed in gasification and combustion reactions. The reactions are dependent on the rate of the pyrolysis and gas composition in the process. A summary of the heterogeneous reactions considered are shown in Table 6.6. The combustion and hydrogasification reactions are exothermic in nature; they provide heat for endothermic reactions. The reaction kinetics were modelled as a UDF using C-subroutine coupled with the hydrodynamics.

Table 6.7: Rate of reaction equations for heterogeneous reactions (Pasangulapati 2012).

Reactions	Rate	A(1/s)	E(KJ/mol)
Boudouard Reaction	$\frac{dC_C}{dt} = -kC_{CO_2}$	3.62×10	77
Carbon combustion reaction	$\frac{dC_C}{dt} = \frac{-fP_{O_2}}{\frac{1}{k_1} + \frac{1}{k_2}}$ $k_1 = \frac{0.292(1-\varepsilon) D_g}{2d_p T_g}$ $D = 4.26 \left(\frac{T_g}{1800} \right)^{1.75}$ $k_2 = k_1 \varepsilon^{2.5} \frac{d_c}{1-d_c}$	—	—
Hydrogasification	$\frac{dC_C}{dt} = -kC_{H_2}$	4.20×10^3	19
Water –gas reaction	$\frac{dC_C}{dt} = -kC_{H_2O}$	1.52×10^4	122

The reactions are normally influenced by diffusive and kinetic factors. The carbon combustion reaction considers mainly the diffusive effect using the equation from Syamlal & Bissett (1992) as shown in Table 6.6 . The Sherwood number correlation for fluidised bed is given by Froessling equation (Scala 2011).The remaining heterogeneous reactions are based as kinetic controlled only reactions. The breaking up of char is not modelled as Eulerian-Eulerian models assume a constant particle diameter.

The rates of homogeneous reactions are generally kinetic controlled reaction. The reactions are exothermic in nature and occur at the dilute region of the riser. The reforming and oxidation reactions of the gas species are considered due to the presence of air/steam mixture and pyrolysis non-condensable gases supplied into the reactor. The rates of the homogeneous reactions are given in Table 6.8.

Table 6.8: Kinetic rate equations for homogeneous gasification reactions (Miao et al. 2013).

Reactions	Rate	A(1/s)	E(KJ/mol)
Water –gas shift reaction	$\frac{dC_{CO}}{dt} = -kC_{CO}C_{H_2O} + \frac{C_{CO}C_{H_2O}}{K_p T}$	2.65×10^{-2}	66
Carbon–monoxide Oxidation	$\frac{dC_{CO}}{dt} = -kC_{CO}C_{O_2}^{0.25}C_{H_2O}^{0.5}$	8.83×10^{11}	100
Methane Oxidation	$\frac{dC_{CH_4}}{dt} = -kC_{CH_4}^{0.7}C_{O_2}^{0.8}$	1.58×10^8	202
Hydrogen Oxidation	$\frac{dC_{H_2}}{dt} = -kC_{CO}C_{H_2}$	3.09×10^{11}	100
Steam Reforming reaction	$\frac{dC_{CH_4}}{dt} = -kC_{CH_4}C_{H_2O}$	3.02×10^6	125

6.3.2. Boundary/Operating conditions

A 3D transient model is built for the base case comparable to circulating fluidised bed gasifier in Aston University's EBRI. The size of the riser is of the same size based on diameter and height as the one used in Chapter 5 to study its hydrodynamics. The model setup for the circulating fluidised bed is shown in Figure 6.7.

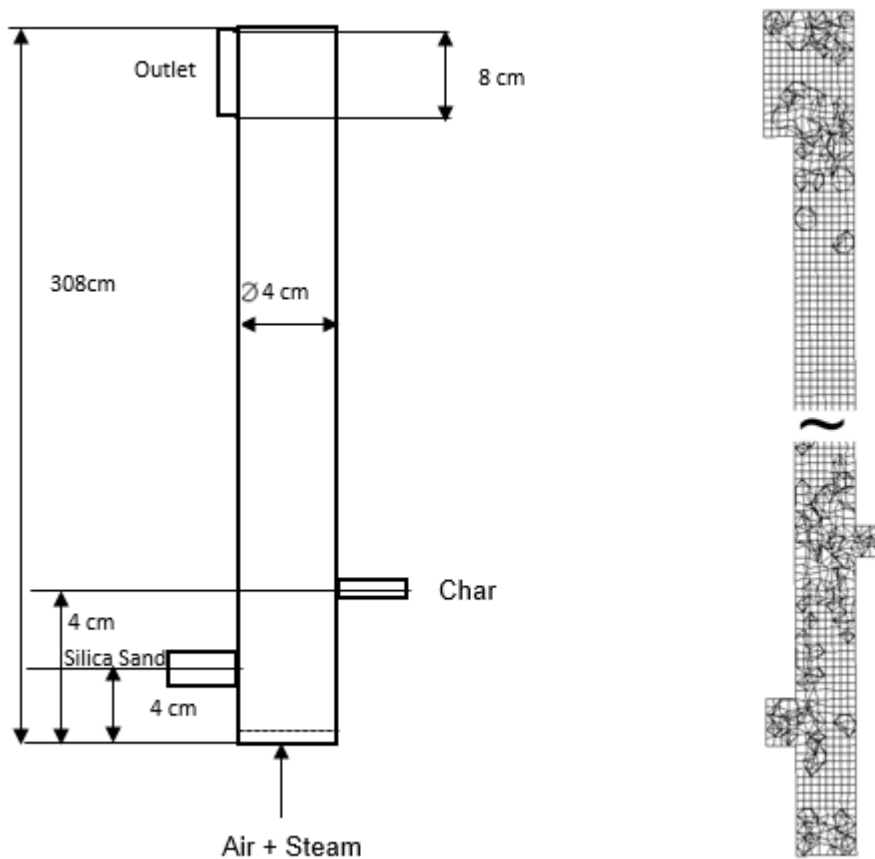


Figure 6.7: Model setup for the circulating fluidised bed gasifier (diagram and computational mesh domain).

The equivalence ratio (ER) is the amount of oxygen supplied in relation to the stoichiometric oxygen amount needed for complete combustion. The value of ER ranges from 0-1, which values less than 1, signifies gasification (partial combustion). The ER has an impact on the gasification reactions and process; ER have an effect on the overall gasification temperature and quality of producer gas as the energy needed for the process is partly or mainly supplied by oxidation reaction (Gungor 2009). The ER value of 0.40 was used for this process. The steam to biomass ratio is a relation between the steam feed rate to the feed rate of biomass. Steam to biomass ratio used was 0.15; this greatly influences the quality of the product gas. It determines the rate of reforming reactions; the reactions increase the concentration of hydrogen in the product gas. The final product gas produced from the gasifier defines the

criteria for measuring the performance of the process. The LHV of the product gas is given from the following equation below (Lv et al. 2004):

$$LHV = (30 \times X_{CO}\% + 25.7 \times X_{H_2}\% + 85.5 \times X_{CH_4}\% + 151.3 \times X_{C_nH_m}) \times 4.2(KJ/Nm^3), \quad (6.3)$$

where X_{CO} , X_{H_2} , and X_{CH_4} are the mole fraction of the product species. The carbon conversion efficiency signifies the percentage of total sum of carbon converted from the biomass to product gases containing carbon in the gasifier. The carbon conversion efficiency (CCE) is given as:

$$CCE = \left(\frac{V_g \times 1000 \times (X_{CO_2} + X_{CO} + X_{CH_4}) \times (12/22.4)}{\dot{m}_{in,feed}(1 - X_{ash}) \times X_{carbon}} \right), \quad (6.4)$$

where V_g is the product gas flowrate (Nm^3/h), X_{ash} is the ash content, X_{carbon} is the carbon content, and $\dot{m}_{in,feed}$ is the char flowrate (kg/h). The efficiency of a gasifier is calculated as the cold gas efficiency. The cold gas efficiency (CGE) is measured based on the equation below:

$$CGE = \frac{\dot{m}_{out}(X_{CO}HHV_{CO} + X_{H_2}HHV_{H_2} + X_{CH_4}HHV_{CH_4})}{\dot{m}_{in,feed}HHV_{feed}} \quad (6.5)$$

The flow rates of fluidising gas, char, and sand are specified at the fluidising gas and solid inlets respectively. The pressure at the outlet is at atmospheric pressure. The densities of the gases are assumed as an incompressible ideal gas law. The fluidising gas inlet was at a superficial gas velocity of 3.8m/s with a mixture of air and steam. The char inlet contains char and pyrolysis gas from the solar pyrolysis process in Chapter 4. The small fraction of pyrolysis gas at ambient condition is used to force the solid into the riser. The char has been prescribed a flowrate of 7 kg/h and the secondary gas at a volumetric flowrate of 8 L/min. The mass flux of the solid (sand) at 700°C is presumed as 26 kg/m²s with secondary air of 20L/min. The fluidising gas was predicted with a superficial velocity of 3.8m/s. The wall boundary condition assumed for all phases is a no-slip boundary wall condition. The summary for the properties of biomass samples and the operating conditions are listed in Table 6.9.

Table 6.9: Properties and operating conditions of the domain

Material Properties	Values
Mean particle diameter d_{char} (mm)	0.4
Mean particle diameter d_{sand} (mm)	0.3
Sand density ρ_{sand} (kg/m ³)	2600
Specific heat capacity of char $c_{p,char}$ (J/kg K)	1600
Specific heat capacity $c_{p,sand}$ (J/kg K)	860
Thermal conductivity λ_{char} (W/m K)	0.107
Thermal conductivity λ_{sand} (W/m K)	1.75
Boundary/Operating conditions	Values /Conditions
char flow rate (kg/h)	6.9
Solid mass flux (kg/m ² s)	26
Fluidising gas flowrate	8.38
Superficial velocity (m/s)	3.8
Fluidising gas temperature (°C)	400
Char temperature (°C)	350
Sand temperature (°C)	600
Steam-biomass ratio	0.15
Equivalence ratio	0.40
Outlet condition	Atmospheric Pressure outlet
Wall condition	No slip

The discretized model is solved using finite volume method in FLUENT 14.0. The first-order upwind is used for spatial discretization and transient formulation. The SIMPLEC scheme is applied for pressure- velocity coupling. The criteria for convergence is set based on residuals for energy equation as 1.0×10^{-12} and the rest of the equations was set to 1.0×10^{-6} . The time step is fixed to 5×10^{-5} until hydrodynamic stability is achieved with only gas-solid flows. The energy and chemical reactions is set in at a time step of 1×10^{-5} due to temperature effect attributed to the combustion reaction after flow is established. The simulation is run until quasi-steady state solution is achieved. The computational time for each case is about 17 days using 2.50 GHz 2Core processors Intel® Xeon® with 32 GB RAM.

6.4. Results and Discussion

6.4.1. Hydrodynamics

The distribution of the solid fraction in the riser was considered to describe the behaviour of the particles. The distribution of the solid volume fraction is shown in Figure 6.8. The concentration in the riser is divided into the bottom dense section, mid transition section, dilute section and the exit section. The behaviour of the sand and char particles shows higher concentration at the bottom regions of the riser. There was a non-uniform concentration throughout the riser. The exit region has a high concentration of particles at the top of the riser. The reason being the solids move upward until they reach the top of the

riser, they collide with the top wall near the exit and rebound back. The decelerated particles moving down and accelerated particles moving up collide forming clusters at near the exit region. This behaviour was depicted by Zhang et al. (2013) as the collision and cavity effect at the exit regions of CFB.

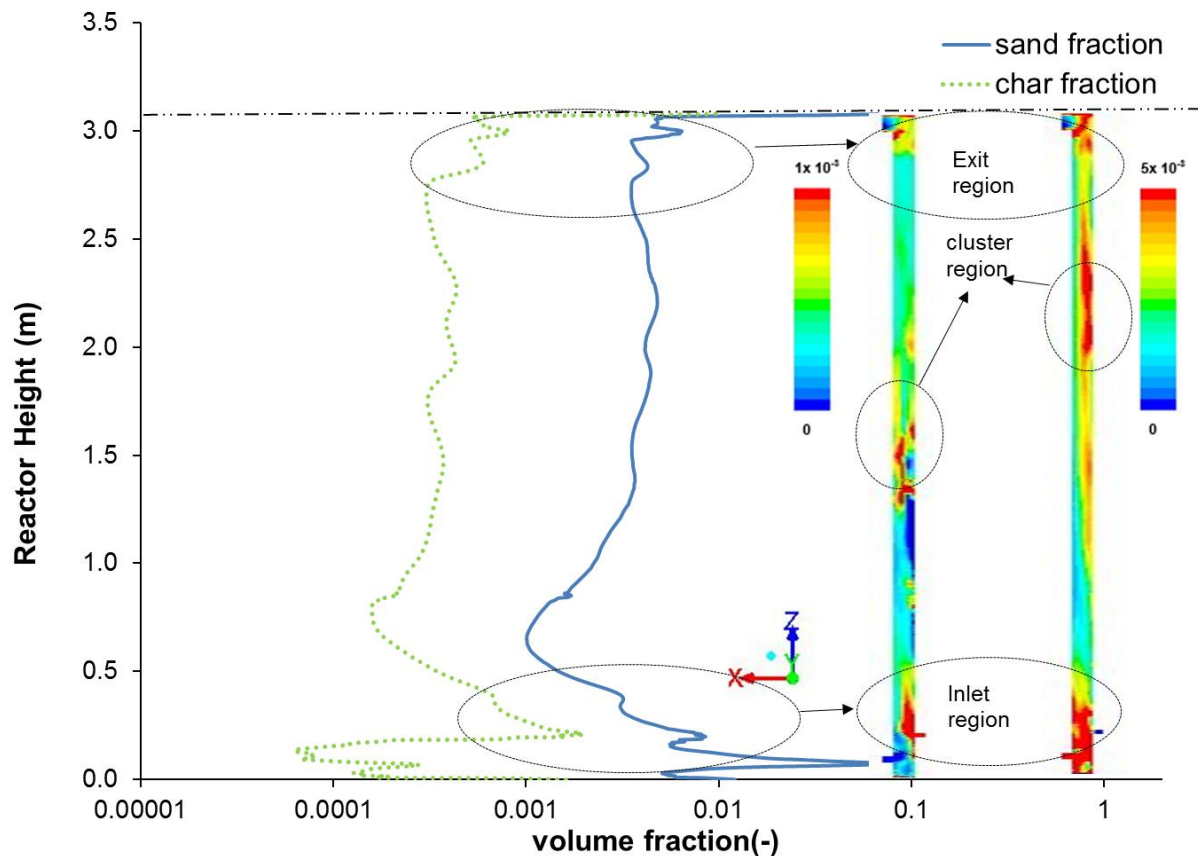


Figure 6.8: Solid volume fraction distribution in the riser.

Figure 6.9 shows the axial velocity distribution of all three phases along the full length of the reactor. There is significant turbulence near the entrance region due to the inlet boundary effect. The mixing of the phases occurs at this region where the phases are trying to reach dynamic equilibrium. The velocity behaviour in the axial direction is acceleration at the initial stage then fully developed and deceleration towards the exit (excluding inlet and exit boundary effect zones). The char and sand velocities are very similar because they are of similar sizes the only differing characteristics is their inherent properties. The velocity of the gas phase is significantly higher than the solid phases; the reason being it is more sensitive to changes in temperature and pressure along the riser height. The vector of solid distribution in Figure 6.10 showed this behaviour and the behaviour at entrance and exit regions with regards to velocity. The behaviour of the phases shows near constant velocity at the developed zone of the riser. The inlet boundary zone showed recirculation of the solid,

this lead to negative velocities at that region. The sand has a higher density than the other phases this phenomenon leads to settling at the bottom of the reactor. The decrease in velocity at the exit boundary zone is caused by the collision effect of the solid particles with the top of the wall. The clusters formed at those regions also contribute to this low velocity compared to the developed zone. The maximum velocity achieved was at the acceleration zone though this zone is at different length for the solid and gas phases. The exit effect is more pronounced in the gas phase as sudden rise and fall in velocity is achieved at the exit region; this is attributed to the high turbulence occurring at that region.

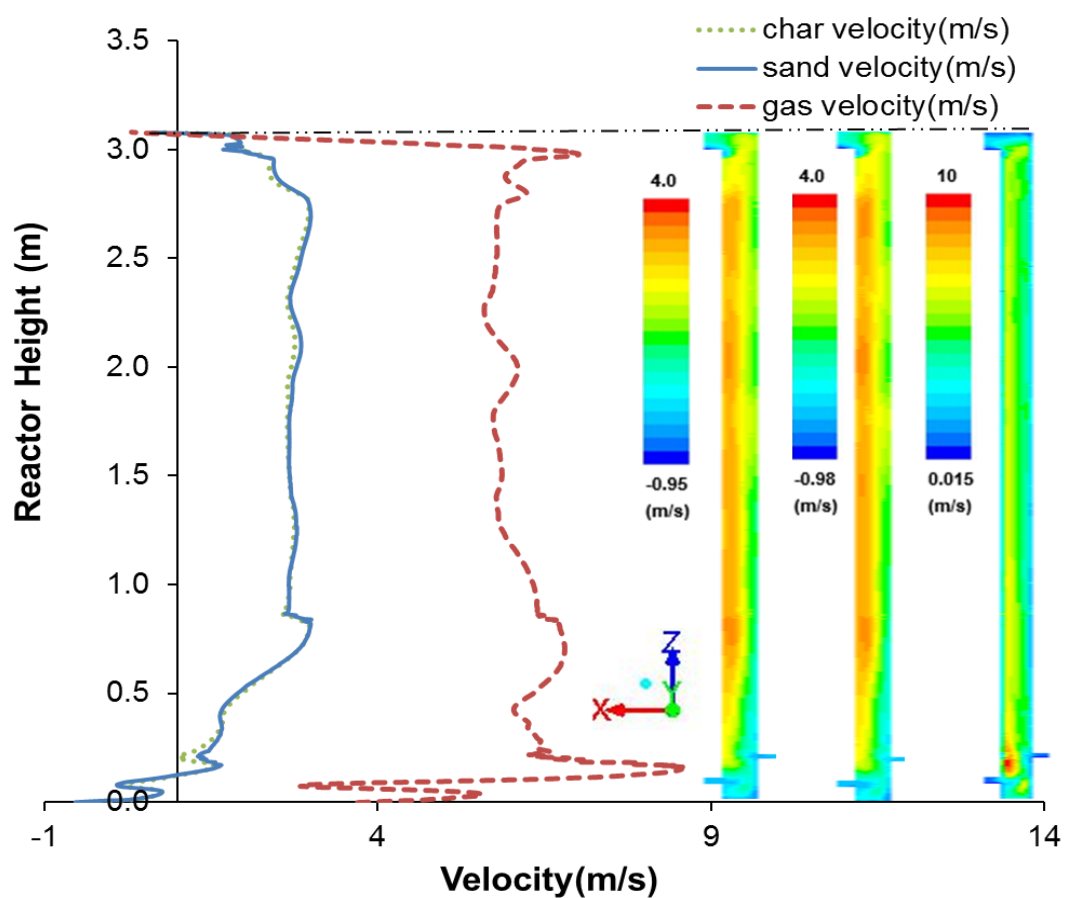


Figure 6.9: Axial velocity distribution of char, sand and gas phases.

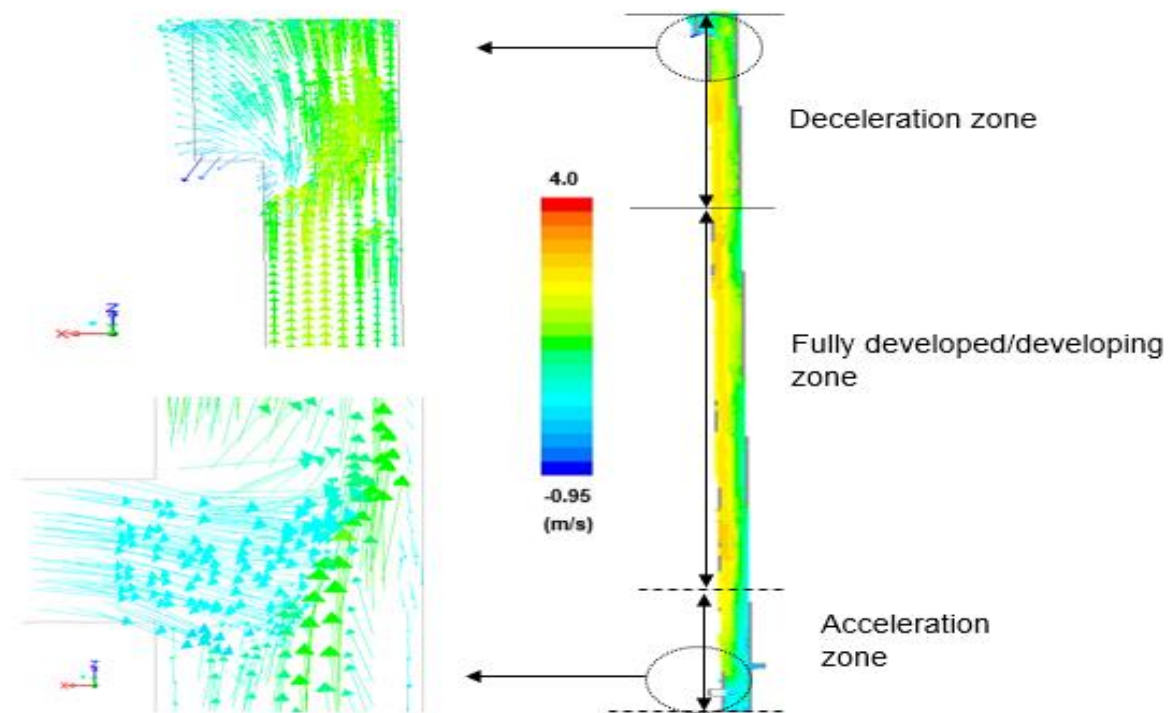


Figure 6.10: Entrance and exit regions for the solid velocity (sand).

6.4.2. Heat distribution and rate of reactions

The amount of heat transfer and average temperature distribution are major factors that affect the progress of biomass gasification. The temperature distribution determines the rate of the homogeneous and heterogeneous reaction therefore the final product composition. The temperature profile in the riser is shown in Figure 6.11. It predicted that pyrolysis, combustion, and gasification zones occur at the different length along the reactor; this zones are mainly where the major characteristics of those reactions are observed. The pyrolysis zone occurs between 0 and 0.2m, the combustion zone within 0.2m to 1.5m and the gasification zone from 1.5m to the top of the reactor. The behaviour of temperature shows increase in the pyrolysis and combustion zones. This is primarily due to the energy released from combustion. The temperature decreases slowly as the energy released from exothermic reactions are absorbed by the gasification reactions. The sand temperature reaches thermal equilibrium slower compared to the char particles.

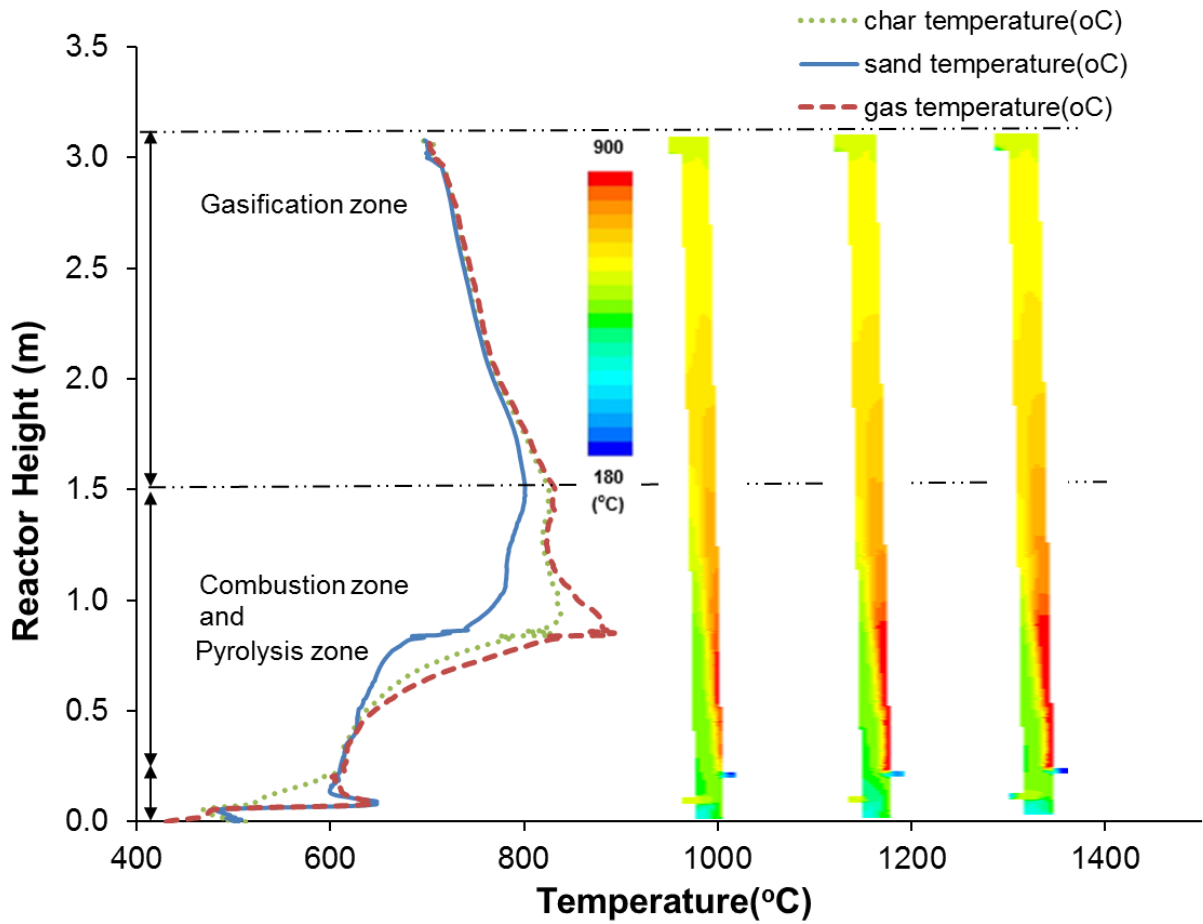


Figure 6.11: Axial Temperature profile along the riser height.

The following reactions considered are labelled based on R1 (devolatilisation), R2 (Boudouard), R3 (water-gas), R4 (hydrogasification), and R5 (Combustion). The rate of the heterogeneous reactions is shown in Figure 6.12. The rate of the devolatilisation reaction R1 is the most prevalent reaction produces the initial primary tar and non-condensable gases. The reaction normally has a lower activation energy and its endothermic nature makes it utilise the high temperature in the riser. Higher rate of reaction is observed at the pyrolysis and combustion zone due to the high temperature attributed from combustion reaction R5. The reaction is fast and consumes the available oxygen in the riser. The water-gas reaction R3 increases the concentration of hydrogen in the riser, therefore the rate of reaction has to be utilised for gasification processes to favour hydrogen production. The boudouard and hydrogasification have higher rates at the dense bottom bed of the riser. These reactions are the slowest reaction; thus they require a longer residence time. The order of reactivity based on rate was $R1 > R5 > R3 > R2 > R4$.

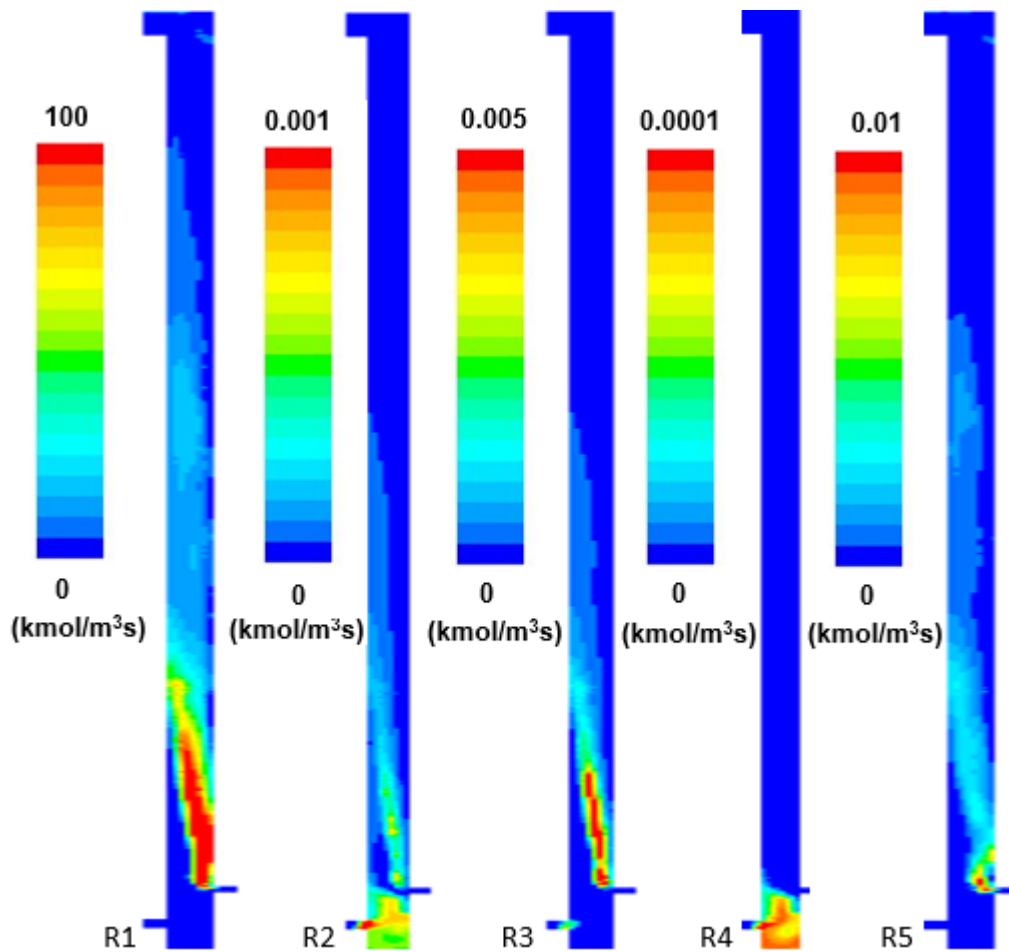


Figure 6.12: Axial profile contour of rate of reaction for heterogeneous reactions.

The rates of homogeneous reactions are shown in Figure 6.13 . The following homogeneous reactions considered are labelled based on R-1 (carbon monoxide oxidation), R-2 (tar cracking), R-3 (hydrogen oxidation), R-4 (methane oxidation), R-5 (Shift), and R-6 (methane steam reforming). The rate of reaction was higher in the combustion reaction in the following order of carbon monoxide, hydrogen, and methane. The thermal tar cracking reaction R-2 showed higher rate at areas with high temperature. It occurs at temperatures above 500°C. This reaction has high activation energy and therefore is favoured by high temperature zones in the riser. The shift reaction R-5 showed both increases in the backward and forward reaction. The rate of reaction showed the exothermic nature of the reaction where areas of high combustion reaction (temperature) shift the equilibrium backward.

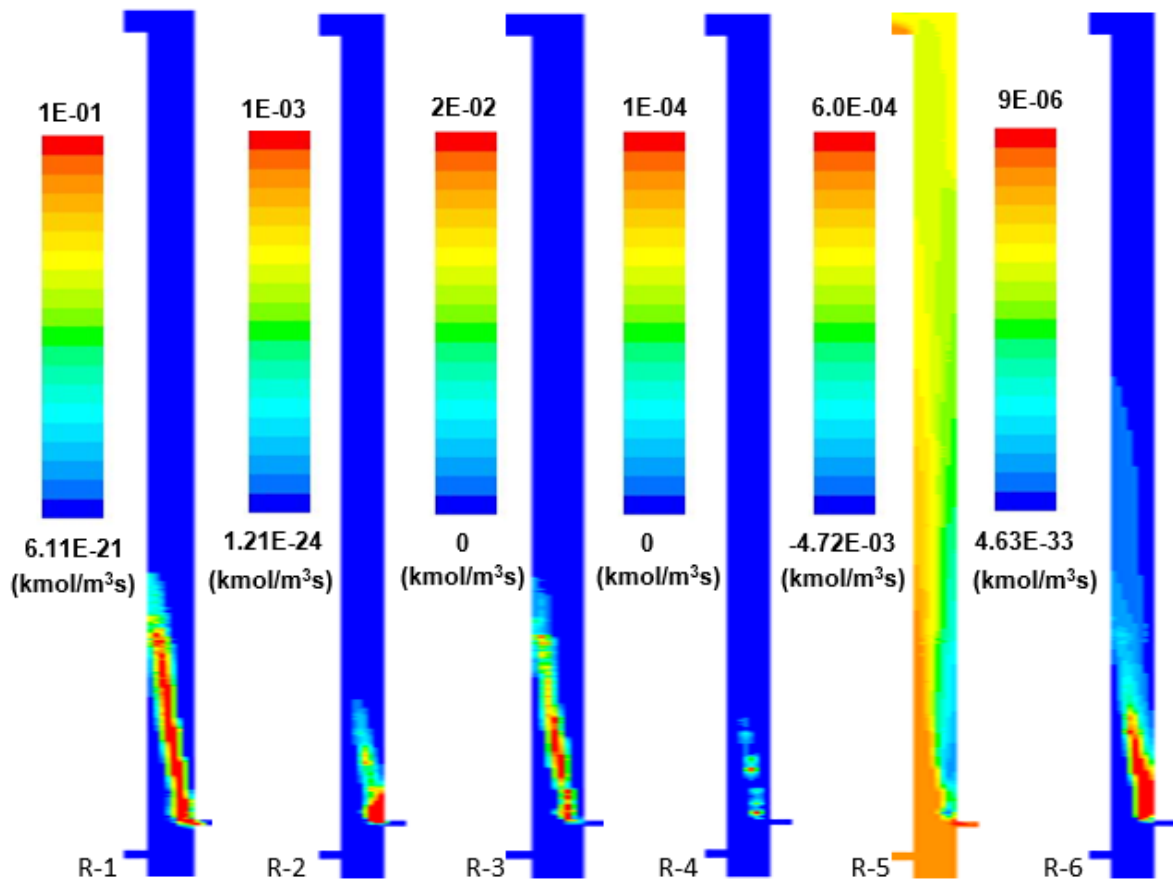


Figure 6.13: Axial profile contour of rate of reaction for homogeneous reactions.

6.4.3. Product composition and Efficiencies

The distribution of the composition of the products in a gasification process is influenced mainly by reactor design and operating conditions. The distribution of gases in the gasifier is shown in Figure 6.14. The O_2 and H_2O mole fraction decreases quickly up to 0.7m of the gasifier, this is followed by a gradual decrease; the behaviour is due to char combustion, water-gas and shift reaction. The trends of CO and H_2 were opposite to those of the O_2 and H_2O . The CH_4 mole fraction increases due to production from the devolatilisation reaction. There is a small decrease in the gasification and combustion zone due to methane steam reforming and combustion. The following compositions were obtained for CO (12%), CO_2 (19%), H_2 (6%), CH_4 (0.7%), and N_2 (63%) at the exit of the gasifier.

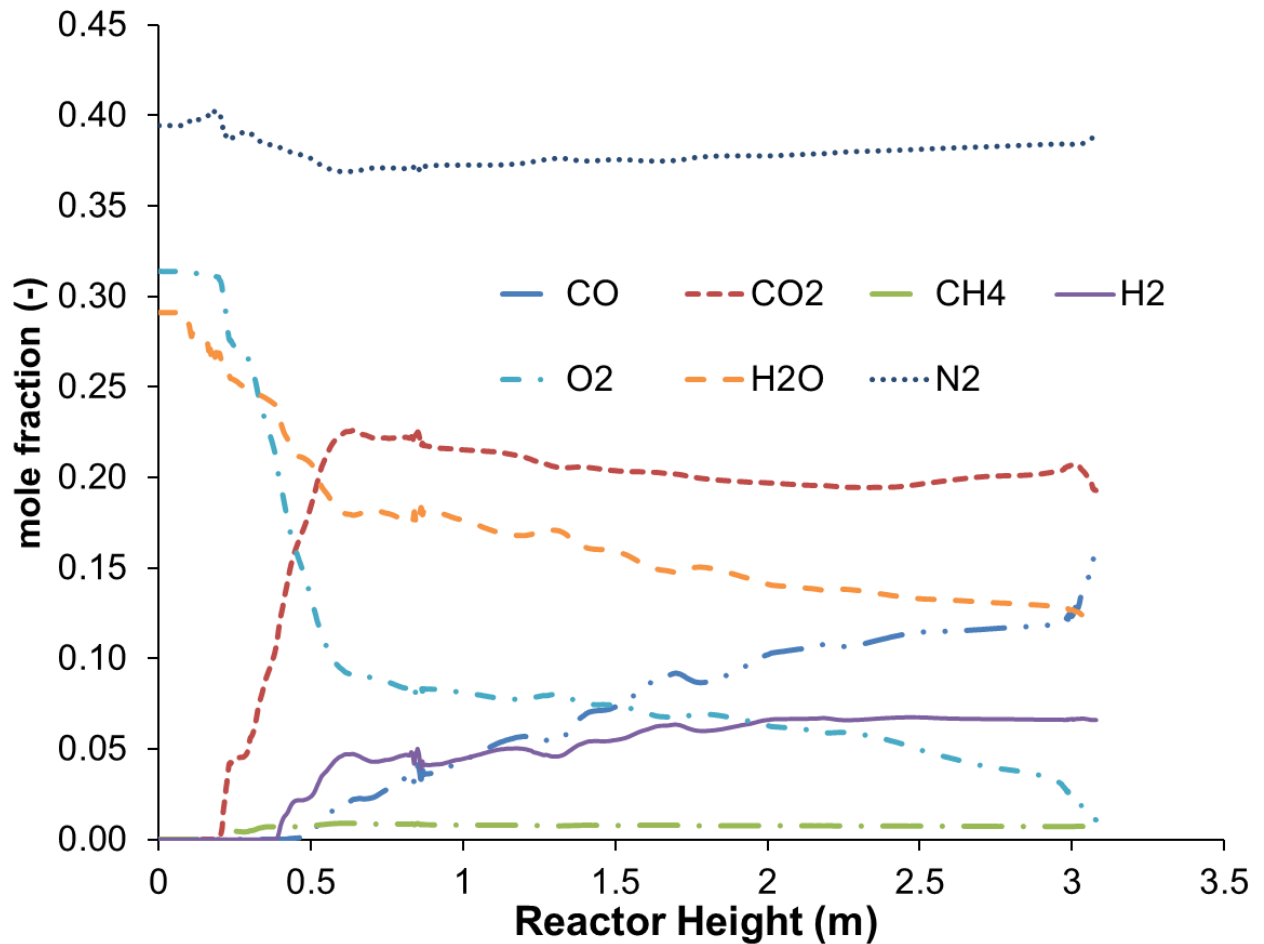


Figure 6.14: Outlet gas composition along the riser height for CO, CO₂, CH₄, H₂, O₂, H₂O, and N₂.

The tar content for the base case was 17 g/Nm³, this is within limit for air/steam gasification at maximum of 20 g/Nm³ (Cao et al. 2006). Figure 6.15 presented the comparison of the base case with the inclusion of tar reforming with char case (Case 3). The tar content was reduced to 15 g/Nm³ with the reforming reaction. The low conversion of tar is attributed to char being consumed during gasification; this can be improved through using char as bed material or with inert mixture similar to Gerber et al. (2010) and continuous feeding of char. The HHV of product gas was 6.89MJ/Nm³ (base case) which is similar to literature values reported by Lv et al. (2004). The CCE and CGE were 76.67% and 54% for the base case and 74.35% and 67.74% for the tar reforming reaction with char.

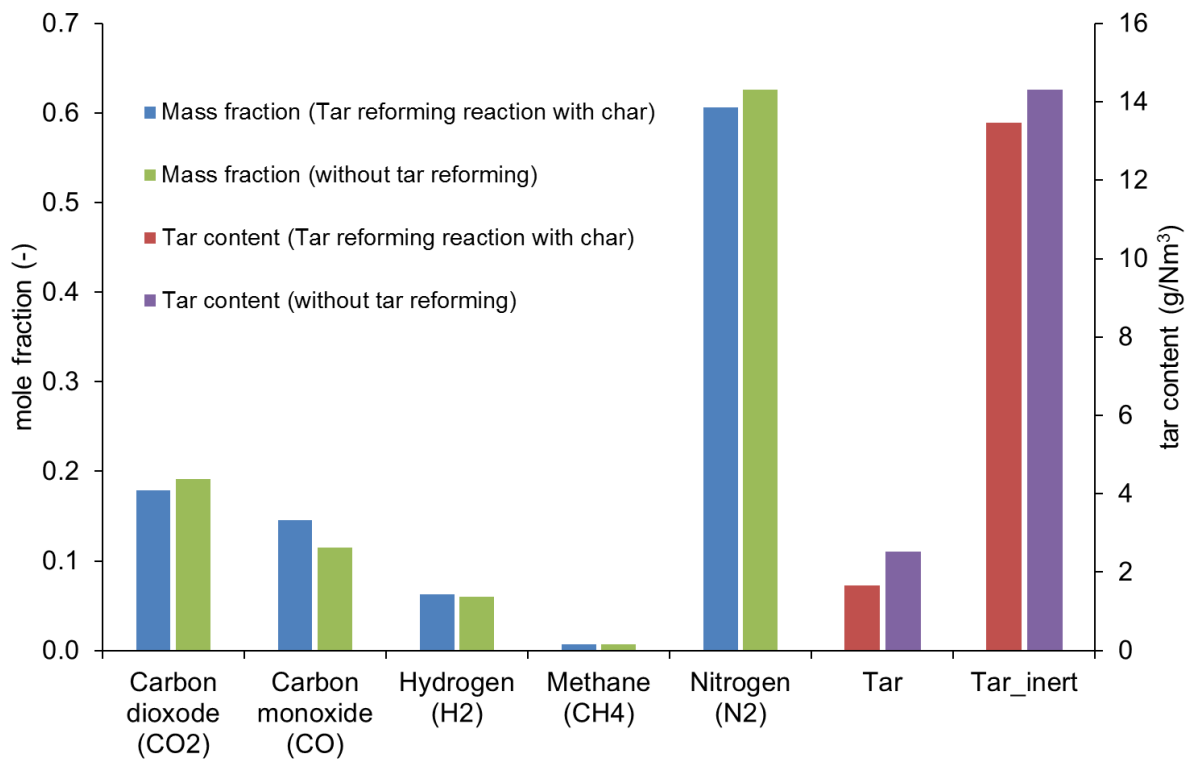


Figure 6.15: Outlet gas composition compared with char cracking reactions.

Table 6.10 shows a comparison between the tar reforming case and recently published modelling and experimental findings. The operating conditions reported in the literature studies are different from the current work. The comparison demonstrates the validity of the modelling approach and its capability as a predicting tool. The comparison showed good agreement with regards to the composition of gases and tar yield with experiment and models. As stated earlier, the average tar content for air-steam gasification is 20 g/Nm³ and tar content decreases according to the following gasifying agents (steam > steam- O₂> Air).

The results also proved that high CCE does not correspond to high CGE; the CCE in air-steam is lower than experimental values due to increase in reactions with steam on C, CH₄, CO₂, and CO. The low methane concentration observed was due to a higher intensity of methane combustion and steam reforming reactions. A similar behaviour was reported by Pasangulapati (2012) showing good agreement with experimental values. Bingyan et al. (1994) also found decreasing trend in CH₄ concentration with increasing ER values.

Table 6.10: Outlet gas composition of reported literature values for gasification in a CFB compared with the tar reforming case (Case 3).

Author	Li et al. (2004) ¹	Petersen & Werther (2005a) ²	Miao et al. (2013) ³	Liu (2014) ⁴	[This study with tar reforming]
	Experiment	Experiment	Model	Model	Model
CGE (%)	63.3	58.0	67.12	-	67.74
CCE (%)	81.60	87.00	98.47	-	74.35
LHV (MJ/Nm ³)	6.13	4.00	6.57	4.0	7.02
Gas composition (%)					
CO ₂	31.89	29.44	37.98	52.63	45.41
CO	46.42	30.00	29.20	24.56	36.86
H ₂	11.71	15.88	15.70	14.04	15.90
CH ₄	9.99	15.88	17.12	8.77	1.83
Tar (g/Nm ³)	15.13	-	-	-	15.12
Comments	(1) CFB: Spruce/pine; temperature of 700-850 °C; Air ratio is 0.22. (2) CFB: Sewage sludge; temperature of 750-850 °C; Air ratio is 0.30. (3) CFB: Rice husk; temperature of 750-830 °C; ER of 0.26. (4) CFB: Eulerian-Eulerian (two-fluid) CFD model without tar cracking reaction; temperature of 400-1100 °C; ER of 0.41.				

6.5. Conclusion

A 3D CFD model was used to describe the gasification of char in a circulating fluidised bed in ANSYS FLUENT. A multiphase model was implemented from a validated experimental hydrodynamic model using kinetic theory of granular flow. The RNG k-ε model was coupled with enhanced wall treatment. The governing equations were integrated with the devolatilisation and gasification reactions (homogeneous and heterogeneous). The concentration, velocity and temperature distribution in the riser was analysed and the effect of combustion reaction showed temperature increase up to 900° C at the combustion zone. The gasification of char reported product gas compositions of CO (12%), CO₂ (19%), H₂ (6%), CH₄ (0.7%), and N₂ (63%) for the base case. The tar yield was about 17g/Nm³; the

CCE and CGE were 76.67% and 54% for the base case, which are in agreement with literature values. The catalytic effect of char was reported with the inclusion of tar reforming reaction of tar in the base case. There was an improvement in the tar yield and CGE to 15.12g/Nm³ and 67.74% for the tar reforming reaction with char. The simulation results were compared with experimental and model values in literature; there was qualitative agreement with the results. The model proved the capability of CFD model to describe reactive processes in complex reactors.

CHAPTER 7 : CONCLUSION

The final chapter summarises the conclusion drawn and the novel breakthroughs achieved in this work. The process of integrating solar energy with a pyrolysis and gasification process was designed using CFD. The CFD modelling of solar pyrolysis in a parabolic trough has not been realised and solar pyrolysis are rare in literature especially with regards to CFD modelling. This work implemented this process in Eulerian-Eulerian multiphase model. The hydrodynamics of a CFB gasifier was investigated and compared with experimental results. The hydrodynamic model was used to describe gasification of char in a Circulating fluidised bed. The results provided a conclusion to the above process discussed in this work. Finally, there were recommendations for future work to provide an extension further in the fields of renewable energy process integration and CFD modelling of thermochemical conversion process using solar energy.

7.1. Conclusions

The research is focused on modelling solar thermochemical conversion processes of biomass pyrolysis and gasification. The concept of computational fluid modelling was used to achieve the project objectives to model solar pyrolysis and circulating fluidised bed gasification of char.

The review of different literatures led to the improvement from the initial problem of using solar heated particles to be integrated with circulating fluidised bed gasification to an integrated solar pyrolysis and circulating fluidised bed gasification concept. This has the capability to produce cleaner wide range of fuels, higher throughput, and reduce tars in the thermochemical process.

The methodology of modelling the hydrodynamics, heat transfer, reaction and numerical model using computational fluid dynamics approach was reviewed. The Eulerian-Eulerian model showed to be capable of modelling complex systems with reasonable computational expense compared to the Eulerian-Lagrangian model. The heat transfers due to convection, conduction and radiation were described. The different chemical kinetics for pyrolysis and gasification was explored and the species rate model. The process of discretisation of the governing equations and the different solver used for the numerical process were also reviewed based on finite volume method. The numerical solver is based on pressure based coupled solver for the iterative method of the governing equations. The discretisation was based on first order upwind for all the cases.

The CFD modelling was twofold; solar pyrolysis in a trough and circulating fluidised bed of char from the pyrolysis process. Therefore, the two process were modelled separately as

part of an integrated system. The models were based on the Eulerian-Eulerian multiphase and the solid were modelled based on kinetic theory of granular flow (KTGF). The momentum exchange coefficient was based on Syamlal & O'Brien (1987) due to its ability to model drag in dilute gas-solid flow. This was incorporated with a convective heat transfer model by Gunn (Gunn 1978). The species model rate was based on the laminar finite rate for the base case.

7.1.1. Solar trough biomass fast pyrolysis

A novel approach was implemented in a CFD model to study the behaviour of biomass particles undergoing fast pyrolysis in a parabolic trough arrangement. The turbulence was based on standard turbulence model. The reactor was augmented with a novel conical separating mechanism and a UDF pyrolysis code. The model validated an experimental finding showing high efficiency similar to cyclones for gas-solid separation. It concluded that the separator is capable of limiting char cracking reactions in pyrolysis processes thereby leading to higher oil yield. The efficiency of the process and green emissions compared to heat from combustion or electricity was explored. The level of greenhouse emissions avoided using solar energy was predicted. The final product composition was in agreement with experimental findings. The above concluded model is proposed to model biomass fast pyrolysis in a simulated solar flux environment. A sensitivity analysis of the developed model was conducted for the effect of the following variables on the product yield:

- Effect of heat flux distribution
- Effect of heat transfer mechanism
- Effect of sweeping gas temperature
- Effect of biomass particle size

The heat flux was shown to affect the final product yield and the non-homogeneous and homogeneous showed increased devolatilisation compared to constant heat flux conditions in the base case. Radiation effect was shown to be negligible with regards to the final product yield. Temperature was shown to be an important parameter affecting the devolatilisation efficiency therefore the bio-oil yield. The increase in biomass size leads to higher devolatilisation efficiency in constant particle size models. The analysis provided a detailed behaviour of the process which can help with the design, optimisation, and scale up of the reactor.

7.1.2. Circulating fluidised bed gasification of char

The experimental pressure measurement technique was used to study the hydrodynamic behaviour of a single phase sand particles in a riser. The effect of particle size on the solid circulation rate and pressure was observed in the riser. The larger the particles the smaller

the recirculation rate as higher velocity is required to circulate them. Therefore, small particles are easily entrained at high gas velocities. The pressure profile along the riser showed that turbulent mixing occurs at the dense bottom section of riser with higher pressure drop observed compared to the dilute top section. The inlet and exit effects attributed to CFB risers was also observed from the pressure distribution. The effect of the modelling approach considered were compared with experiments. The gas-solid momentum exchange coefficient was investigated for the optimum model. The drag laws in literature from Wen Yu, Gidaspow, Gibilaro, and Syamlal & O'Brien proved sufficient to describe the hydrodynamics. The Syamlal & O'Brien proved more suitable as it is capable to show the clusters formed in a CFB. The following turbulence models laminar, k-e (standard, RNG, and realisable), and large eddy simulation models were investigated; the k-e models proved to be in sync with the experimental values. The enhanced wall treatment showed better correlation with experimental values than the standard wall function.

Table 7.1: Summary of hydrodynamic model for a CFB riser

Turbulence	RNG k-e model (dispersed)
Drag law	Syamlal & O'Brien model
Wall treatment	Enhanced wall treatment
Particle-particle Restitution coefficient	0.9
Granular model	Algebraic model
Boundary Condition	No-slip

The effect of wall shear was investigated based on the particle-wall restitution coefficient and the specular coefficient. There was negligible variation of the restitution coefficient values when compared with the experimental values. A summary of the hydrodynamic model is shown in .

Table 7.1.

The gasification of char in a CFB was investigated using the product from solar pyrolysis as feed for this model. The chemical reaction included both heterogeneous and homogeneous reactions. The heterogeneous reactions were as a UDF to describe the gas-solid reactions. The presence of thermal cracking of tar and char reforming of tars was considered in the model. The species rate model was compared between the laminar finite rate and finite rate/eddy dissipation. The catalytic effect of char was reported with the inclusion of tar reforming reaction of tar in the base case. The catalytic effect showed decreased tar compared to were this is not considered and the tar content is similar to experimental

findings. The effect of combustion was observed in the temperature distribution in the riser. The simulation results were in qualitative agreement with experimental results of similar cases. The complete overall concept of the integrated pyrolysis-gasification process is shown in Figure 7.1.

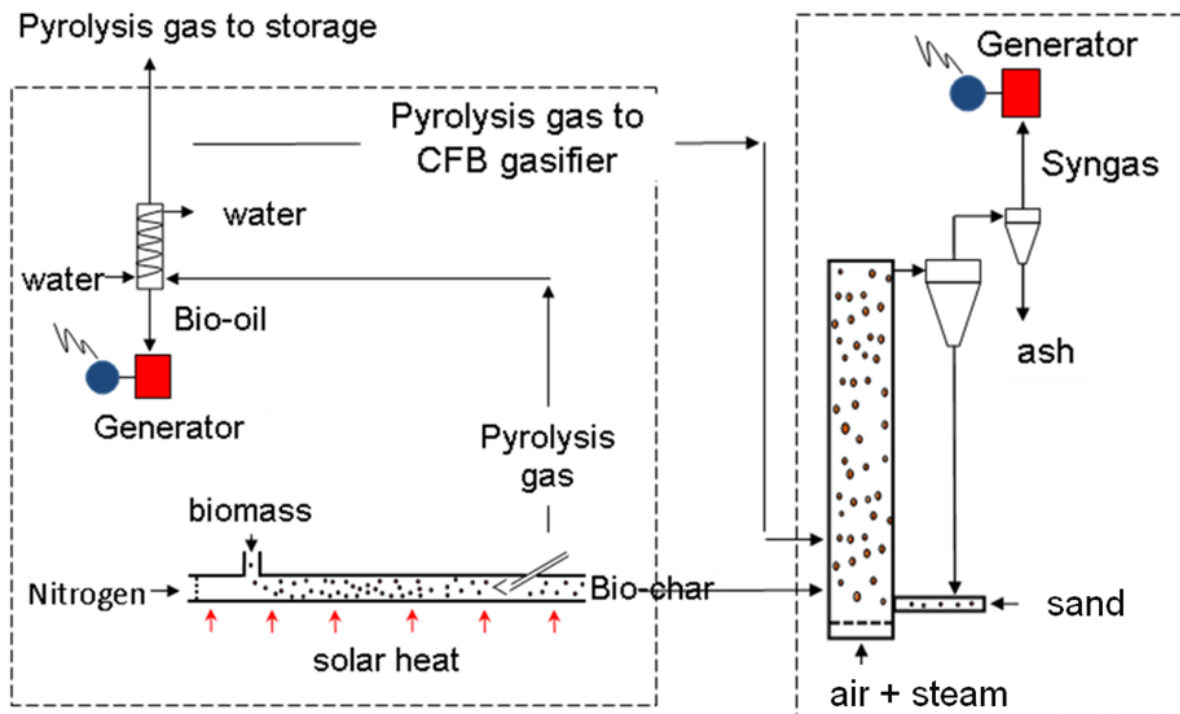


Figure 7.1: Integrated solar biomass thermochemical conversion process

7.2. Summary of contributions

The following contributions were achieved using computational fluid dynamics to model integrating solar energy with biomass thermochemical conversion:

- Computational fluid dynamics was developed to model an integrated solar-biomass thermochemical conversion coupled with a User Defined Function to describe the fluid hydrodynamics and chemical reactions. A novel technique was used to model solar fast pyrolysis of switchgrass in a parabolic trough receiver has been developed. The model showed sufficient qualitative agreement when compared to experimental results for the final product composition. The bio-oil yield produced was similar to yield from auto thermal processes with the added benefit of heat supplied from solar energy. An optimization of the model through a sensitivity analysis showed consistent improvement in yield especially in cases where radiation was considered and heat

flux was coupled from Monte-Carlo ray tracing (MCRT). It also showed the effect of operating and boundary conditions for scale-up and design purposes.

- The pressure measurement technique was used to validate the hydrodynamic model for a circulating fluidised bed riser. The model looked into the different drag laws, turbulence models, and wall models; the optimum model for the hydrodynamics of a circulating fluidised bed was predicted. The hydrodynamic model was extended to a model for gasification of char in a circulating fluidised bed. A model was implemented for the gasification reactions of char. The model has proven that for smaller particle diameters the species reactions are mainly kinetic controlled. It also validated that char affects the tar content through catalytic reforming reactions.
- The potential of integrating the proposed solar reactor with a conventional gasifier to create a highly efficient and sustainable closed loop thermo-solar process was achieved. This validated the use of computational fluid dynamics for design and optimisation of processes at all stages of development. The closed loop system allows for recovering and using the char as well as the permanent gas from the pyrolysis in the gasification process to achieve maximum throughput in one single novel energy system.

7.3. Future work

This work is not exhaustive as there is room for improvement with regards to the modelling and experimental observations.

- The parametric analysis showed that radiative effects have an impact on the reactor and pyrolysis process. The design of the receiver/reactor can be reconfigured in a nonconventional design to be mainly of glass material to investigate the radiative aspect of solar pyrolysis using CFD. The pyrolysis will be driven using radiative heat transfer as opposed to mainly convection in this work. This will require a more comprehensive discrete ordinate (DO) radiation model for the primary and secondary phase. The wall boundary condition will be based on a semi-transparent medium as opposed to opaque medium used in this work to account for the transfer of solar rays.
- The hydrodynamics model was proven based on axial changes of the pressure gradient along the riser. This method of validation has been proven to give accurate behaviour of the risers in literature. The hydrodynamics also changes radially across the riser diameter. A more detailed hydrodynamic experiment including accurate void

fraction and velocity calculations to show a complete change in the radial direction of the riser is an important aspect to describe fluidised bed behaviour. The experiment can be extended to include char and account for energy and chemical reactions so as provide a full detailed validation of gasification results.

- The User Defined Functions developed for the gasification can be applied to Eulerian-Eulerian multiphase models in other types of gasifiers. The advantages of the Eulerian-Eulerian offers good results at coarser grids. This means the simulation of catalytic large-scale circulating fluidised bed reactors at small computational expense is possible. The tar reforming model can be extended to other catalysts using CFD to model this processes. The variation of biomass compositions and operating conditions affect the final composition of products as observed in this work. The models in literature are mostly not biomass specific and more detailed advanced reaction models are required to describe the pyrolysis and gasification reactions especially with regards to large scale reactor. Finally, this will help achieve optimal designs that are energy efficient; further improvements in the process through simulations will reduce the frequency and cost of modifications in design and optimisation

REFERENCES

- Abanades, S., Charvin, P. & Flamant, G., 2007. Design and simulation of a solar chemical reactor for the thermal reduction of metal oxides: Case study of zinc oxide dissociation. *Chemical Engineering Science*, 62(22), pp.6323–6333. Available at: <http://www.sciencedirect.com/science/article/pii/S0009250907005878> [Accessed February 18, 2016].
- Abanades, S. & Flamant, G., 2007. Experimental study and modeling of a high-temperature solar chemical reactor for hydrogen production from methane cracking. *International Journal of Hydrogen Energy*, 32(10-11), pp.1508–1515. Available at: <http://www.sciencedirect.com/science/article/pii/S0360319906005118> [Accessed March 30, 2016].
- Adinberg, R., Epstein, M. & Karni, J., 2004. Solar Gasification of Biomass: A Molten Salt Pyrolysis Study. *Journal of Solar Energy Engineering*, 126(3), p.850. Available at: <http://solarenergyengineering.asmedigitalcollection.asme.org/article.aspx?articleid=1457062> [Accessed March 14, 2016].
- Agarwal, A., 2005. Theory and Design of Dilute Phase Pneumatic Conveying Systems. *Powder Handling & Processing*. Available at: https://scholar.google.co.uk/scholar?hl=en&q=Theory+and+Design+of+Dilute+Phase+Pneumatic+Conveying+Systems&btnG=&as_sdt=1%2C5&as_sdtp=#0 [Accessed April 18, 2016].
- Agrawal, K. et al., 2001. The role of meso-scale structures in rapid gas–solid flows. *Journal of Fluid Mechanics*, 445, pp.151–185. Available at: http://journals.cambridge.org/abstract_S0022112001005663 [Accessed January 6, 2016].
- Almುತ್ತahar, A. & Taghipour, F., 2008a. Computational fluid dynamics of a circulating fluidized bed under various fluidization conditions. *Chemical Engineering Science*, 63(6), pp.1696–1709. Available at: <http://www.sciencedirect.com/science/article/pii/S0009250907008524> [Accessed March 1, 2016].
- Almುತ್ತahar, A. & Taghipour, F., 2008b. Computational fluid dynamics of high density circulating fluidized bed riser: Study of modeling parameters. *Powder Technology*, 185(1), pp.11–23. Available at: <http://www.sciencedirect.com/science/article/pii/S0032591007004895> [Accessed May 7, 2015].
- Almುತ್ತahar, A.M., 2006. CFD modeling of the hydrodynamics of circulating fluidized bed riser. Available at: <https://circle.ubc.ca/handle/2429/17912> [Accessed July 8, 2015].
- Alves, J.J.N., Martignoni, W.P. & Mori, M., 2001. Fluid dynamic modelling and simulation of circulating fluidized bed reactors: importance of the interface turbulence transfer. *Journal of the Brazilian Society of Mechanical Sciences*, 23(1), pp.91–104. Available at: http://www.scielo.br/scielo.php?script=sci_arttext&pid=S0100-73862001000100008&lng=en&nrm=iso&tlng=en [Accessed March 16, 2016].
- Anderson, J.R. et al., 2011. A Slow Pyrolysis Reactor Utilizing Concentrated Solar Radiation to Drive a Thermo-Chemical Conversion of Carbonaceous Material. In *13th Annual Texas National McNair Scholars Research Conference*. Denton, TX.
- Ansart, R. et al., 2013. 3D numerical simulation of Circulating Fluidized Bed: comparison between theoretical results and experimental measurements of hydrodynamic. Available at: http://oatao.univ-toulouse.fr/9231/1/Ansart_9231.pdf [Accessed March 19,

2016].

- ANSYS, 2014. ANSYS fluent features. Available at: <http://www.ansys.com/Products/Simulation+Technology/Fluid+Dynamics/Fluid+Dynamics+Products/ANSYS+Fluent/Features> [Accessed March 23, 2014].
- ANSYS, 2009. Fluent 12.0 Documentation: Theory Guide. Available at: https://www.sharcnet.ca/Software/Ansys/16.0/en-us/help/flu_th/flu_th.html [Accessed March 28, 2016].
- Antal, M. & Varhegyi, G., 1995. Cellulose pyrolysis kinetics: the current state of knowledge. *Industrial & Engineering Chemistry*. Available at: <http://pubs.acs.org/doi/abs/10.1021/ie00042a001> [Accessed July 29, 2016].
- Aramideh, S. et al., 2015. Numerical simulation of biomass fast pyrolysis in an auger reactor. *Fuel*, 156, pp.234–242. Available at: <http://linkinghub.elsevier.com/retrieve/pii/S0016236115004366> [Accessed June 15, 2016].
- Arastoopour, H., Pakdel, P. & Adewumi, M., 1990. Hydrodynamic analysis of dilute gas—solids flow in a vertical pipe. *Powder technology*. Available at: <http://www.sciencedirect.com/science/article/pii/003259109080080I> [Accessed March 5, 2016].
- Ardila, Y., Figueroa, J. & Lunelli, B., 2012. Syngas production from sugar cane bagasse in a circulating fluidized bed gasifier using Aspen Plus TM: Modelling and Simulation. *on Computer Aided ...*. Available at: <http://www.academia.edu/download/38897130/1-s2.0-B9780444595201500774-main.pdf> [Accessed July 21, 2016].
- Arena, U., Zaccariello, L. & Mastellone, M.L., 2009. Tar removal during the fluidized bed gasification of plastic waste. *Waste Management*, 29(2), pp.783–791.
- Armstrong, L., 2011. CFD modelling of the gas-solid flow dynamics and thermal conversion processes in fluidised beds. Available at: http://eprints.soton.ac.uk/192155/1/Final_corrected_thesis.pdf [Accessed February 9, 2016].
- Ashcraft, R.W., Heynderickx, G.J. & Marin, G.B., 2012. Modeling fast biomass pyrolysis in a gas—solid vortex reactor. *Chemical Engineering Journal*, 207-208, pp.195–208. Available at: <http://www.sciencedirect.com/science/article/pii/S1385894712007693> [Accessed May 18, 2016].
- Authier, O., Ferrer, M. & Mauviel, G., 2009. Wood fast pyrolysis: comparison of Lagrangian and Eulerian modeling approaches with experimental measurements. *Industrial & engineering ...*, 48(10), pp.4796–4809. Available at: <http://pubs.acs.org/doi/abs/10.1021/ie801854c> [Accessed July 14, 2015].
- Babu, B. & Sheth, P., 2006. Modeling and simulation of reduction zone of downdraft biomass gasifier: effect of char reactivity factor. *Energy Conversion and Management*. Available at: <http://www.sciencedirect.com/science/article/pii/S0196890405002840> [Accessed July 30, 2016].
- Badarayani, P., 2015. Flash Pyrolysis of Biomass due to Concentrated Solar Radiation. Available at: <http://www.sersc.org/journals/IJAST/vol77/5.pdf> [Accessed March 14, 2016].
- Balasubramanian, N., Srinivasakannan, C. & Basha, C.A., 2005. Transition velocities in the riser of a circulating fluidized bed. *Advanced Powder Technology*, 16(3), pp.247–260. Available at:

<http://booksandjournals.brillonline.com/content/journals/10.1163/1568552053750198>
[Accessed July 31, 2016].

Bamford, C.H. et al., 1946. The combustion of wood. Part I. *Mathematical Proceedings of the Cambridge Philosophical Society*, 42(02), p.166. Available at: http://journals.cambridge.org/abstract_S030500410002288X [Accessed April 8, 2016].

Barrio, M. et al., 2001. Steam gasification of wood char and the effect of hydrogen inhibition on the chemical kinetics. *on Progress in ...*. Available at: http://orbit.dtu.dk/fedora/objects/orbit:54508/datastreams/file_3378884/content [Accessed July 30, 2016].

Barrio, M. & Hustad, J., 2008. CO₂ gasification of birch char and the effect of CO inhibition on the calculation of chemical kinetics. *Progress in thermochemical biomass*. Available at: https://books.google.co.uk/books?hl=en&lr=&id=6QD69PvV0foC&oi=fnd&pg=PA47&dq=CO2+Gasification+of+Birch+Char+and+the+Effect+of+CO+Inhibition+on+the+Calculation+of+Chemical+Kinetics&ots=to2MO95fI9&sig=o9EZUAvTv1rGwAiWLAakwY3Vm_g [Accessed July 30, 2016].

Basu, P., 2010. Biomass Gasification and Pyrolysis: practical design and theory. In Burlington, MA: Academic Press, p. 364. Available at: <https://books.google.co.uk/books?hl=en&lr=&id=QSypbUSdkikC&oi=fnd&pg=PP2&dq=Biomass+Gasification+and+Pyrolysis&ots=Vf-v52Ksj9&sig=fcSiE7KiBH8M1tExum4Uq4H4rzU> [Accessed July 27, 2016].

Basu, P., 2006. Combustion and gasification in fluidized beds. , pp.1 – 467. Available at: https://books.google.co.uk/books?hl=en&lr=&id=2F3LBQAAQBAJ&oi=fnd&pg=PP1&dq=Combustion+and+Gasification+in+fluidised+bed&ots=nShaj71o3o&sig=8vXKuTyQNGU70FP_uWhVm7JnuHw [Accessed July 28, 2016].

Bhat, A., Ram Bheemarasetti, J.V. & Rajeswara Rao, T., 2001. Kinetics of rice husk char gasification. *Energy Conversion and Management*, 42(18), pp.2061–2069.

Bilbao, R. et al., 1996. Modelling of the pyrolysis of wet wood. *Journal of analytical and*. Available at: <http://www.sciencedirect.com/science/article/pii/0165237095009183> [Accessed July 29, 2016].

Bilgen, E. et al., 1977. Use of solar energy for direct and two-step water decomposition cycles☆. *International Journal of Hydrogen Energy*, 2(3), pp.251–257. Available at: <http://www.sciencedirect.com/science/article/pii/0360319977900210> [Accessed January 9, 2016].

Bingyan, X. et al., 1994. Circulating fluidized bed gasifier for biomass. Available at: <http://agris.fao.org/agris-search/search.do?recordID=XF9545799> [Accessed August 29, 2016].

Birchenough, A. & Mason, J., 1976. Local particle velocity measurements with a laser anemometer in an upward flowing gas—solid suspension. *Powder technology*. Available at: <http://www.sciencedirect.com/science/article/pii/0032591076800162> [Accessed January 28, 2016].

Blasi, C. Di, 2009. Combustion and gasification rates of lignocellulosic chars. *Progress in energy and combustion science*. Available at: <http://www.sciencedirect.com/science/article/pii/S0360128508000440> [Accessed July 30, 2016].

Di Blasi, C., 1996. Heat, momentum and mass transport through a shrinking biomass particle exposed to thermal radiation. *Chemical Engineering Science*, 51(7), pp.1121–

1132. Available at: <http://www.sciencedirect.com/science/article/pii/S000925099680011X> [Accessed November 30, 2015].
- Blasi, C. Di, 2004. Modeling wood gasification in a countercurrent fixed-bed reactor. *AIChE journal*. Available at: <http://onlinelibrary.wiley.com/doi/10.1002/aic.10189/pdf> [Accessed July 14, 2015].
- Boateng, A.A. et al., 2007. Bench-Scale Fluidized-Bed Pyrolysis of Switchgrass for Bio-Oil Production †. *Industrial & Engineering Chemistry Research*, 46(7), pp.1891–1897. Available at: <http://dx.doi.org/10.1021/ie0614529> [Accessed April 25, 2016].
- Boateng, A.A. & Mtui, P.L., 2012. CFD modeling of space-time evolution of fast pyrolysis products in a bench-scale fluidized-bed reactor. *Applied Thermal Engineering*, 33-34(1), pp.190–198. Available at: <http://dx.doi.org/10.1016/j.applthermaleng.2011.09.034>.
- Boroson, M.L. et al., 1989a. Heterogeneous cracking of wood pyrolysis tars over fresh wood char surfaces. *Energy & Fuels*, 3(6), pp.735–740. Available at: <http://dx.doi.org/10.1021/ef00018a014> [Accessed August 5, 2015].
- Boroson, M.L. et al., 1989b. Product yields and kinetics from the vapor phase cracking of wood pyrolysis tars. *AIChE Journal*, 35(1), pp.120–128. Available at: <http://doi.wiley.com/10.1002/aic.690350113> [Accessed June 25, 2015].
- Boutin, O., Ferrer, M. & Lédé, J., 2002. Flash pyrolysis of cellulose pellets submitted to a concentrated radiation: experiments and modelling. *Chemical Engineering Science*, 57(1), pp.15–25. Available at: <http://www.sciencedirect.com/science/article/pii/S0009250901003608> [Accessed July 14, 2015].
- Brandt, P., Larson, E. & Henriksen, U., 2000. High Tar Reduction in a Two Stage Gasifier Brant. *Energy & Fuels*, 14, pp.816–819.
- Bridgwater, A., Beenackers, A., et al., 1999. *An assessment of the possibilities for transfer of European biomass gasification technology to China*, Available at: http://www.ieatask33.org/app/webroot/files/file/publications/IEA_EU_China.pdf [Accessed July 28, 2016].
- Bridgwater, A., 1984. Thermochemical processing of biomass. Available at: <http://agris.fao.org/agris-search/search.do?recordID=XF2015015395> [Accessed July 28, 2016].
- Bridgwater, A., Meier, D. & Radlein, D., 1999. An overview of fast pyrolysis of biomass. *Organic Geochemistry*, 30(12), pp.1479–1493. Available at: <http://www.sciencedirect.com/science/article/pii/S0146638099001205> [Accessed July 14, 2015].
- Bridgwater, A. & Peacocke, G., 2000. Fast pyrolysis processes for biomass. *Renewable and sustainable energy* Available at: <http://www.sciencedirect.com/science/article/pii/S1364032199000076> [Accessed March 4, 2016].
- Bridgwater, A. V., 2012. Upgrading biomass fast pyrolysis liquids. *Environmental Progress & Sustainable Energy*, 31(2), pp.261–268. Available at: <http://doi.wiley.com/10.1002/ep.11635> [Accessed March 9, 2016].
- Bridgwater, A.V., 1999. Principles and practice of biomass fast pyrolysis processes for liquids. *Journal of Analytical and Applied Pyrolysis*, 51(1-2), pp.3–22. Available at: <http://www.sciencedirect.com/science/article/pii/S0165237099000054> [Accessed April

8, 2015].

- Bryden, K., Ragland, K. & Rutland, C., 2002. Modeling thermally thick pyrolysis of wood. *Biomass and Bioenergy*, 22(1), pp.41–53. Available at: <http://www.sciencedirect.com/science/article/pii/S0961953401000605> [Accessed July 14, 2016].
- Buck, R., Muir, J.F. & Hogan, R.E., 1991. Carbon dioxide reforming of methane in a solar volumetric receiver/reactor: the CAESAR project. *Solar Energy Materials*, 24(1-4), pp.449–463. Available at: <http://www.sciencedirect.com/science/article/pii/016516339190082V> [Accessed January 13, 2016].
- Burkholder, F. & Kutscher, C., 2009. *Heat loss testing of Schott's 2008 PTR70 parabolic trough receiver*, Available at: <http://www.nrel.gov/docs/fy09osti/45633.pdf> [Accessed April 16, 2016].
- Cadile, C., Topin, F. & Tadrist, L., 2013. Euler-Lagrange/DEM Simulation of Shallow Dense Fluidized Bed Dynamic and Application to Wood Gasification. Available at: http://dc.engconfintl.org/cgi/viewcontent.cgi?article=1052&context=fluidization_xiv [Accessed July 23, 2016].
- Cao, Y. et al., 2006. A novel biomass air gasification process for producing tar-free higher heating value fuel gas. *Fuel Processing Technology*, 87(4), pp.343–353.
- Cetin, E. et al., 2005. Biomass gasification kinetics: Influences of pressure and chars structure. *Combustion Science and Technology*, 177(4), pp.765–791. Available at: <http://www.tandfonline.com/doi/abs/10.1080/00102200590917266> [Accessed July 29, 2016].
- CFD Direct, 2014. OpenFOAM Features. Available at: <http://www.openfoam.org/features/index.php> [Accessed March 23, 2014].
- Chan, C.W. et al., 2009. Particle motion in the CFB riser with special emphasis on PEPT-imaging of the bottom section. *Powder Technology*, 196(3), pp.318–325. Available at: <http://www.sciencedirect.com/science/article/pii/S0032591009004690> [Accessed February 16, 2016].
- Chan, W., Kelbon, M. & Krieger, B., 1985. Modelling and experimental verification of physical and chemical processes during pyrolysis of a large biomass particle. *Fuel*. Available at: <http://www.sciencedirect.com/science/article/pii/0016236185903643> [Accessed April 6, 2016].
- Chen, G. et al., 2004. Biomass gasification integrated with pyrolysis in a circulating fluidised bed. *Solar Energy*, 76(1), pp.345–349.
- Chen, X. & Wang, J., 2014. A comparison of two-fluid model, dense discrete particle model and CFD-DEM method for modeling impinging gas–solid flows. *Powder Technology*, 254, pp.94–102. Available at: <http://www.sciencedirect.com/science/article/pii/S0032591014000096> [Accessed February 25, 2016].
- Cheng, Z.D. et al., 2010. Three-dimensional numerical study of heat transfer characteristics in the receiver tube of parabolic trough solar collector. *International Communications in Heat and Mass Transfer*, 37(7), pp.782–787.
- Cheng, Z.D., He, Y.L. & Cui, F.Q., 2012. Numerical study of heat transfer enhancement by unilateral longitudinal vortex generators inside parabolic trough solar receivers. *International Journal of Heat and Mass Transfer*, 55(21-22), pp.5631–5641. Available

- at: <http://www.sciencedirect.com/science/article/pii/S001793101200378X> [Accessed April 21, 2016].
- Chopra, S. & Jain, A., 2007. A review of fixed bed gasification systems for biomass. Available at: <https://ecommons.cornell.edu/handle/1813/10671> [Accessed July 28, 2016].
- Coll, R. et al., 2001. Steam reforming model compounds of biomass gasification tars: conversion at different operating conditions and tendency towards coke formation. *Fuel Processing Technology*, 74(1), pp.19–31. Available at: <http://www.sciencedirect.com/science/article/pii/S0378382001002144> [Accessed July 23, 2015].
- Cozzani, V., 2000. Reactivity in oxygen and carbon dioxide of char formed in the pyrolysis of refuse-derived fuel. *Industrial & engineering chemistry research*. Available at: <http://pubs.acs.org/doi/abs/10.1021/ie990534c> [Accessed July 30, 2016].
- CPFD, 2014. CPFD baracuda fluidised bed gasifier modelling. Available at: <http://cpfd-software.com/resources/videos/cfd-simulation-in-cpfd-barracuda-of-a-fluidized-bed-gasifier> [Accessed March 23, 2014].
- Dartevelle, S., 2003. Numerical and granulometric approaches to geophysical granular flows. Available at: <http://digitalcommons.mtu.edu/etds/316/> [Accessed June 10, 2016].
- Demirbas, A., 2005. Pyrolysis of ground beech wood in irregular heating rate conditions. *Journal of Analytical and Applied Pyrolysis*, 73(1), pp.39–43. Available at: <http://www.sciencedirect.com/science/article/pii/S0165237004000889> [Accessed August 22, 2015].
- Deru, M. & Torcellini, P., 2007. *Source energy and emission factors for energy use in buildings*, Golden, CO. Available at: https://scholar.google.com/scholar?q=Source+energy+and+emission+factors+for+energy+use+in+buildings&btnG=&hl=en&as_sdt=0%2C5#0 [Accessed July 14, 2015].
- Diebold, J.P., 1985. *The Cracking Kinetics of Depolymerized Biomass Vapors in a Continuous, Tubular Reactor*, Colorado School of Mines. Available at: https://books.google.co.uk/books/about/The_Cracking_Kinetics_of_Depolymerized_B.html?id=pDy6NwAACAAJ&pgis=1 [Accessed June 25, 2015].
- Ding, J. & Gidaspow, D., 1990. A bubbling fluidization model using kinetic theory of granular flow. *AIChE Journal*. Available at: <http://onlinelibrary.wiley.com/doi/10.1002/aic.690360404/full> [Accessed March 21, 2016].
- Doherty, W., Reynolds, A. & Kennedy, D., 2009. The effect of air preheating in a biomass CFB gasifier using ASPEN Plus simulation. *Biomass and Bioenergy*, 33(9), pp.1158–1167.
- van der Drift, A., van Doorn, J. & Vermeulen, J., 2001. Ten residual biomass fuels for circulating fluidized-bed gasification. *Biomass and Bioenergy*, 20(1), pp.45–56.
- Duc, L., Morishita, K. & Takar, T., 2013. Catalytic Decomposition of Biomass Tars at Low-Temperature. In *Biomass Now - Sustainable Growth and Use*. InTech. Available at: <http://www.intechopen.com/books/biomass-now-sustainable-growth-and-use/catalytic-decomposition-of-biomass-tars-at-low-temperature> [Accessed July 27, 2016].
- EI-Rub, A., 2008. *Biomass char as an in-situ catalyst for tar removal in gasification systems*. Available at: http://doc.utwente.nl/58713/1/thesis_Abu_EI_Rub.pdf [Accessed July 27, 2016].

- El-Rub, Z., Bramer, E. & Brem, G., 2002. Tar removal in an Entrained Flow Cracker (EFC) with application to biomass gasification. *Pyrolysis and gasification of*. Available at: [https://www.researchgate.net/profile/Ziad_Abu_El-Rub/publication/269808821_Tar_Removal_in_an_Entrained_Flow_Cracker_\(EFC\)_with_Application_to_Biomass_Gasification/links/5496b56f0cf20f487d30d7cd.pdf](https://www.researchgate.net/profile/Ziad_Abu_El-Rub/publication/269808821_Tar_Removal_in_an_Entrained_Flow_Cracker_(EFC)_with_Application_to_Biomass_Gasification/links/5496b56f0cf20f487d30d7cd.pdf) [Accessed July 18, 2016].
- El-Rub, Z., Bramer, E.A. & Brem, G., 2008. Experimental comparison of biomass chars with other catalysts for tar reduction. *Fuel*, 87(10-11), pp.2243–2252. Available at: <http://www.sciencedirect.com/science/article/pii/S0016236108000082> [Accessed January 13, 2015].
- El-Rub, Z.A., Bramer, E.A. & Brem, G., 2004. Tar Reduction in Biomass Gasification Using Biomass Char as a Catalyst.
- Ergun, S. & Orning, A., 1949. Fluid flow through randomly packed columns and fluidized beds. *Industrial & Engineering Chemistry*. Available at: <http://pubs.acs.org/doi/abs/10.1021/ie50474a011> [Accessed March 13, 2016].
- Ersoy, L. et al., 2004. Circulating fluidized bed hydrodynamics with air staging: an experimental study. *Powder Technology*, 145(1), pp.25–33. Available at: <http://www.sciencedirect.com/science/article/pii/S0032591004002281> [Accessed February 16, 2016].
- Fagbemi, L., Khezami, L. & Capart, R., 2001. Pyrolysis products from different biomasses. *Applied Energy*, 69(4), pp.293–306. Available at: <http://www.sciencedirect.com/science/article/pii/S0306261901000137> [Accessed April 8, 2015].
- Fend, T., 2010. High porosity materials as volumetric receivers for solar energetics. *Opt. Appl.* Available at: <http://www.dbc.wroc.pl/Content/11222#page=7> [Accessed March 4, 2016].
- Fiaschi, D. & Michelini, M., 2001. A two-phase one-dimensional biomass gasification kinetics model. *Biomass and Bioenergy*, 21, pp.121–132.
- Fletcher, E., 2001. Solarthermal processing: a review. *Journal of Solar Energy* Available at: http://solarenergyengineering.asmedigitalcollection.asme.org/data/Journals/JSEEDO/28300/63_1.pdf [Accessed July 14, 2015].
- Forristall, R., 2003. *Heat transfer analysis and modeling of a parabolic trough solar receiver implemented in engineering equation solver*, Available at: <http://large.stanford.edu/publications/coal/references/troughnet/solarfield/docs/34169.pdf> [Accessed March 4, 2016].
- Fuentes-Cano, D. et al., 2013. Decomposition kinetics of model tar compounds over chars with different internal structure to model hot tar removal in biomass gasification. *Chemical Engineering Journal*, 228, pp.1223–1233.
- García-Ibañez, P., Cabanillas, A. & Sánchez, J.M., 2004. Gasification of leached orujillo (olive oil waste) in a pilot plant circulating fluidised bed reactor. Preliminary results. *Biomass and Bioenergy*, 27(2), pp.183–194.
- Geldart, D., 1986. *Gas fluidization technology*, Wiley.
- Geldart, D., 1973. Types of gas fluidization. *Powder technology*. Available at: <http://www.sciencedirect.com/science/article/pii/0032591073800373> [Accessed April 17, 2016].

- Gerber, S., Behrendt, F. & Oevermann, M., 2010. An Eulerian modeling approach of wood gasification in a bubbling fluidized bed reactor using char as bed material. *Fuel*, 89(10), pp.2903–2917. Available at: <http://www.sciencedirect.com/science/article/pii/S0016236110001377> [Accessed April 27, 2015].
- Gibilaro, L.G. et al., 1985. Generalized friction factor and drag coefficient correlations for fluid-particle interactions. *Chemical Engineering Science*, 40(10), pp.1817–1823. Available at: <http://linkinghub.elsevier.com/retrieve/pii/0009250985801160> [Accessed July 14, 2016].
- Gidaspow, D., 1994. *Multiphase flow and fluidization: continuum and kinetic theory descriptions*, Available at: <http://books.google.com/books?hl=en&lr=&id=DTAFZ9rIfQwC&oi=fnd&pg=PP2&dq=gidaspow+1994+&ots=cruyq63did&sig=c7XBI3iOU518lz2TfqrurRMBLCg> [Accessed January 20, 2016].
- Gidaspow, D., Bezburuah, R. & Ding, J., 1991. Hydrodynamics of circulating fluidized beds: Kinetic theory approach. Available at: <http://www.osti.gov/scitech/biblio/5896246> [Accessed February 26, 2016].
- Gil, J. et al., 1999. Biomass gasification in atmospheric and bubbling fluidized bed: Effect of the type of gasifying agent on the product distribution. *Biomass and Bioenergy*, 17(5), pp.389–403.
- Gilbert, P. et al., 2009. Tar reduction in pyrolysis vapours from biomass over a hot char bed. *Bioresource Technology*, 100(23), pp.6045–6051.
- Gómez-Barea, A. & Leckner, B., 2010. Modeling of biomass gasification in fluidized bed. *Progress in Energy and Combustion Science*, 36(4), pp.444–509. Available at: <http://www.sciencedirect.com/science/article/pii/S0360128509000707> [Accessed July 22, 2014].
- Gong, G. et al., 2010. An optimized model and test of the China's first high temperature parabolic trough solar receiver. *Solar Energy*, 84(12), pp.2230–2245. Available at: <http://www.sciencedirect.com/science/article/pii/S0038092X10002628> [Accessed March 4, 2016].
- González, J., Ramiro, A. & Sabio, E., 2002. Hydrogasification of almond shell chars. Influence of operating variables and kinetic study. *Industrial & Engineering Chemistry Research*, 41(10), pp.3115–3124. Available at: <http://pubs.acs.org/doi/abs/10.1021/ie010625l> [Accessed July 30, 2016].
- Grassmann, H. & Boaro, M., 2015. Solar Biomass Pyrolysis with the Linear Mirror II. *Smart Grid and Renewable Energy*, 6(1), pp.1–10. Available at: <http://search.proquest.com/openview/4a55bbabd411640d4f5c1e223d0b86c5/1?pq-origsite=gscholar> [Accessed March 23, 2016].
- Graven, W. & Long, F., 1954. Kinetics and Mechanisms of the Two Opposing Reactions of the Equilibrium $\text{CO} + \text{H}_2\text{O} = \text{CO}_2 + \text{H}_2$. *Journal of the American Chemical Society*, 76(1), pp.1–10. Available at: <http://pubs.acs.org/doi/abs/10.1021/ja01639a002> [Accessed July 30, 2016].
- Grønli, M.G., 1996. A theoretical and experimental study of the thermal degradation of biomass. *Journal of Analytical and Applied Pyrolysis*, 10(3), pp.275–282.
- Guan, G., Hao, X. & Abudula, A., 2014. Heterogeneous Catalysts from Natural Sources for Tar Removal: A Mini Review. *Journal of Advanced Catalysis*, 2014(1), pp.1–10. Available at: <http://www.cosmoscholars.com/phms/index.php/jacst/article/view/78> [Accessed July 23, 2015].

- Gujjula, R. & Mangadoddy, N., 2015. Hydrodynamic Study of Gas–Solid Internally Circulating Fluidized Bed Using Multiphase CFD Model. <http://dx.doi.org/10.1080/02726351.2015.1013590>.
- Gungor, A., 2009. Simulation of the effects of the equivalence ratio on hydrogen production in fluidized bed biomass gasifiers. In *13th International Research/Expert Conference Trends Hammamet, Tunisia*, pp. 16–21. Available at: <http://tmt.unze.ba/zbornik/TMT2009/117-TMT09-053.pdf> [Accessed June 15, 2015].
- Gunn, D., 1978. Transfer of heat or mass to particles in fixed and fluidised beds. *International Journal of Heat and Mass Transfer*, 21(4), pp.467–476. Available at: <http://www.sciencedirect.com/science/article/pii/0017931078900807> [Accessed July 14, 2015].
- Gupta, S. et al., 2006. Investigations into the Factors Influencing the Fluidized Motion Conveying of Flyash.
- Hachicha, A., 2013. Numerical modelling of a parabolic trough solar collector. Available at: <http://www.tdx.cat/bitstream/handle/10803/129729/TAAH1de1.pdf?sequence=1> [Accessed April 19, 2016].
- Hartge, E.-U. et al., 2009. CFD-simulation of a circulating fluidized bed riser. *Particuology*, 7(4), pp.283–296. Available at: <http://www.sciencedirect.com/science/article/pii/S167420010900073X> [Accessed March 5, 2016].
- Hassan, M., 2013. *Modelling and simulation of biomass gasification in a circulating fluidized bed reactor*. Aston University.
- Hathaway, B.J., Kittelson, D.B. & Davidson, J.H., 2014. Development of a Molten Salt Reactor for Solar Gasification of Biomass. *Energy Procedia*, 49, pp.1950–1959. Available at: <http://www.sciencedirect.com/science/article/pii/S1876610214006614> [Accessed March 12, 2016].
- Hawley, M. et al., 1983. Gasification of wood char and effects of intraparticle transport. *Fuel*. Available at: <http://www.sciencedirect.com/science/article/pii/0016236183902016> [Accessed July 30, 2016].
- Helland, E., Occelli, R. & Tadriss, L., 2000. Numerical study of cluster formation in a gas–particle circulating fluidized bed. *Powder Technology*, 110(3), pp.210–221. Available at: <http://www.sciencedirect.com/science/article/pii/S0032591099002600> [Accessed February 24, 2016].
- Henriksen, U. et al., 2006. The design, construction and operation of a 75kW two-stage gasifier. *Energy*, 31(10), pp.1542–1553.
- Herguido, J., Corella, J. & Gonzalez-Saiz, J., 1992. Steam gasification of lignocellulosic residues in a fluidized bed at a small pilot scale. Effect of the type of feedstock. *Industrial & Engineering Chemistry Research*, 31(5), pp.1274–1282. Available at: <http://pubs.acs.org/doi/abs/10.1021/ie00005a006> [Accessed July 10, 2016].
- Hinze, J.O., 1975. *Turbulence*, McGraw-Hill.
- Hirota, M. et al., 2002. Effect of mechanical properties of powder on pneumatic conveying in inclined pipe. *Powder Technology*, 122(2-3), pp.150–155. Available at: <http://www.sciencedirect.com/science/article/pii/S0032591001004119> [Accessed February 26, 2016].
- Hoffschmidt, B. et al., 1999. A new closed/open volumetric receiver concept for parabolic trough collectors (test results). *Le Journal de Physique IV*, 09(PR3), pp.Pr3–557–Pr3–

562. Available at: <http://dx.doi.org/10.1051/jp4:1999388> [Accessed March 3, 2016].
- Hofmann, L. & Antal, M., 1984. Numerical simulations of the performance of solar fired flash pyrolysis reactors. *Solar energy*. Available at: <http://www.sciencedirect.com/science/article/pii/0038092X84901956> [Accessed March 30, 2016].
- Hong, H., Liu, Q. & Jin, H., 2009. Solar Hydrogen Production Integrating Low-Grade Solar Thermal Energy and Methanol Steam Reforming. *Journal of Energy Resources Technology*, 131(1), p.012601. Available at: <http://energyresources.asmedigitalcollection.asme.org/article.aspx?articleid=1414877> [Accessed March 8, 2016].
- Hong, J. & Zhu, J.-X., 1997. Effect of pipe orientation on dense-phase transport I. Critical angle in inclined upflow. *Powder Technology*, 91(2), pp.115–122. Available at: <http://www.sciencedirect.com/science/article/pii/S003259109603241X> [Accessed February 24, 2016].
- Hoomans, B.P. et al., 2001. Experimental validation of granular dynamics simulations of gas-fluidised beds with homogenous in-flow conditions using Positron Emission Particle Tracking. *Powder Technology*, 116(2-3), pp.166–177. Available at: <http://www.sciencedirect.com/science/article/pii/S0032591000003910> [Accessed February 24, 2016].
- Huard, M., Berruti, F. & Briens, C., 2010. Experimental Study of a Novel Fast Gas-Solid Separator for Pyrolysis Reactors. *International Journal of Chemical Engineering*, 8(1), pp.1–22. Available at: <http://www.degruyter.com/view/j/ijcre.2010.8.1/ijcre.2010.8.1.1969/ijcre.2010.8.1.1969.xml> [Accessed July 14, 2015].
- Huard, M., Berruti, F. & Briens, C., 2013. Gas Backmixing Study in a CFB Downer Gassolids Separator. Available at: http://dc.engconfintl.org/cgi/viewcontent.cgi?article=1102&context=fluidization_xiv [Accessed July 14, 2015].
- Huard, M. & Briens, C., 2010. A Review of Rapid Gas-Solid Separation Techniques. *International Journal of Chemical Engineering*, 8(1), pp.1–22. Available at: <http://www.degruyter.com/view/j/ijcre.2010.8.1/ijcre.2010.8.1.2069/ijcre.2010.8.1.2069.xml> [Accessed July 15, 2015].
- Huber, N. & Sommerfeld, M., 1998. Modelling and numerical calculation of dilute-phase pneumatic conveying in pipe systems. *Powder Technology*, 99(1), pp.90–101. Available at: <http://www.sciencedirect.com/science/article/pii/S0032591098000655> [Accessed January 29, 2016].
- Ibsen, C., Solberg, T. & Hjertager, B., 2001. Evaluation of a three-dimensional numerical model of a scaled circulating fluidized bed. *Industrial & Engineering Chemistry Research*, 40(23), pp.5081–5086. Available at: <http://pubs.acs.org/doi/abs/10.1021/ie0010060> [Accessed July 8, 2015].
- Ibsen, C.H. et al., 2004. Comparison of multifluid and discrete particle modelling in numerical predictions of gas particle flow in circulating fluidised beds. *Powder Technology*, 149(1), pp.29–41. Available at: <http://www.sciencedirect.com/science/article/pii/S0032591004004127> [Accessed March 13, 2016].
- Ibsen, C.H., Solberg, T. & Hjertager, B.H., 2001. Evaluation of a Three-Dimensional Numerical Model of a Scaled Circulating Fluidized Bed. *Industrial & Engineering Chemistry Research*, 40(23), pp.5081–5086. Available at: <http://dx.doi.org/10.1021/ie0010060> [Accessed March 13, 2016].

- Iqbal, M., 1983. *An Introduction to Solar Radiation*, Elsevier. Available at: <http://www.sciencedirect.com/science/article/pii/B9780123737502500161> [Accessed February 18, 2016].
- Islam, M. et al., 2012. Three Dimensional Simulation of A Parabolic Trough Concentrator Thermal Collector. *The 50th Annual Conference, Australian Solar Council, Melbourne, Australia*, (December).
- Janajreh, I. & Syed, S., 2010. Solar assisted gasification: Systematic analysis and numerical simulation. *Int. J. of Thermal & ...* Available at: https://www.researchgate.net/profile/Isam_Janajreh/publication/265119553_Solar_Assisted_Gasification_Systematic_Analysis_and_Numerical_Simulation/links/544df24a0cf2bca5ce8eb116.pdf [Accessed March 31, 2016].
- Jaworski, A. & Dyakowski, T., 2001. Application of electrical capacitance tomography for measurement of gas-solids flow characteristics in a pneumatic conveying system. *Measurement Science and ...* Available at: <http://iopscience.iop.org/article/10.1088/0957-0233/12/8/317/meta> [Accessed February 9, 2016].
- Jennen, T. et al., 1999. Modeling of gasification of wood in a circulating fluidized bed. *Chemical Engineering and Technology*, 22(10), pp.822–826. Available at: <http://doi.wiley.com/10.1002/%28SICI%291521-4125%28199910%2922%3A10%3C822%3A%3AAID-CEAT822%3E3.0.CO%3B2-G> [Accessed July 21, 2016].
- Jin, B. et al., 2010. Modeling on High-Flux Circulating Fluidized Bed with Geldart Group B Particles by Kinetic Theory of Granular Flow. *Energy & Fuels*, 24(5), pp.3159–3172. Available at: <http://dx.doi.org/10.1021/ef100096c> [Accessed March 8, 2016].
- Jin, H. et al., 2009. Fundamental study of novel mid-and low-temperature solar thermochemical energy conversion. *Science in China Series E: Technological ...* Available at: <http://link.springer.com/article/10.1007/s11431-009-0097-1> [Accessed March 8, 2016].
- Jin, H., Sui, J. & Hong, H., 2007. Prototype of middle-temperature solar receiver/reactor with parabolic trough concentrator. *Journal of ...*, 129(4), pp.378–381. Available at: <http://biomechanical.asmedigitalcollection.asme.org/article.aspx?articleid=1457952> [Accessed July 14, 2015].
- Joardder, M. et al., 2014. Solar assisted fast pyrolysis: a novel approach of renewable energy production. *Journal of Engineering*, 2014, pp.1–4. Available at: <http://www.hindawi.com/journals/je/2014/252848/abs/> [Accessed July 14, 2015].
- Johansson, A., 2005. *Solids flow pattern in circulating fluidized-bed boilers*, Available at: <http://publications.lib.chalmers.se/publication/7428-solids-flow-pattern-in-circulating-fluidized-bed-boilers> [Accessed July 21, 2016].
- Johnson, P. & Jackson, R., 1987. Frictional–collisional constitutive relations for granular materials, with application to plane shearing. *Journal of Fluid Mechanics*, 176, pp.67–93. Available at: http://journals.cambridge.org/abstract_S0022112087000570 [Accessed July 14, 2015].
- Johnson, P., Nott, P. & Jackson, R., 1990. Frictional–collisional equations of motion for particulate flows and their application to chutes. *Journal of fluid mechanics*. Available at: http://journals.cambridge.org/abstract_S0022112090001380 [Accessed March 25, 2016].
- Johansson, F. et al., 2000. Characterization of fluidization regimes by time-series analysis of

- pressure fluctuations. *International Journal of Multiphase Flow*, 26(4), pp.663–715. Available at: <http://www.sciencedirect.com/science/article/pii/S0301932299000282> [Accessed December 27, 2015].
- Joshi, A.S., Dincer, I. & Reddy, B. V., 2011. Solar hydrogen production: A comparative performance assessment. *International Journal of Hydrogen Energy*, 36(17), pp.11246–11257. Available at: <http://www.sciencedirect.com/science/article/pii/S0360319910023372> [Accessed December 29, 2015].
- Jung, S.-H., Kang, B.-S. & Kim, J.-S., 2008. Production of bio-oil from rice straw and bamboo sawdust under various reaction conditions in a fast pyrolysis plant equipped with a fluidized bed and a char separation system. *Journal of Analytical and Applied Pyrolysis*, 82(2), pp.240–247. Available at: <http://www.sciencedirect.com/science/article/pii/S0165237008000417> [Accessed May 4, 2015].
- Jurena, T., Recman, M. & Hájek, J., 2009. Simulation of biomass drying in fixed bed of experimental grate combustion reactor. *Chemical Engineering Transactions*. Available at: https://scholar.google.co.uk/scholar?q=simulation+of+biomass+drying+in+fixed+bed+of+experimental+grate&btnG=&hl=en&as_sdt=0%2C5#0 [Accessed April 6, 2016].
- Kader, B., 1981. Temperature and concentration profiles in fully turbulent boundary layers. *International Journal of Heat and Mass Transfer*. Available at: <http://www.sciencedirect.com/science/article/pii/0017931081902209> [Accessed March 30, 2016].
- Kalgo, A.S., 2011. The development and optimisation of a fast pyrolysis process for bio-oil production. Available at: http://eprints.aston.ac.uk/15808/1/Kalgo%2C_Abba_Sani_2011.pdf [Accessed April 26, 2016].
- Kartushinsky, A.I. et al., 2011. Numerical simulation of three-dimensional gas-solid particle flow in a horizontal pipe. *AIChE Journal*, 57(11), pp.2977–2988. Available at: <http://doi.wiley.com/10.1002/aic.12528> [Accessed January 19, 2016].
- Kaushal, P., Proell, T. & Hofbauer, H., 2011. Application of a detailed mathematical model to the gasifier unit of the dual fluidized bed gasification plant. *biomass and bioenergy*, 35(7), pp.2491–2498. Available at: <http://www.sciencedirect.com/science/article/pii/S0961953411000262> [Accessed July 14, 2015].
- Kersten, S.R.A. et al., 2003. Principles of a novel multistage circulating fluidized bed reactor for biomass gasification. *Chemical Engineering Science*, 58(3), pp.725–731.
- Klinghoffer, N., 2013. Utilization of char from biomass gasification in catalytic applications. Available at: <http://academiccommons.columbia.edu/catalog/ac:178955> [Accessed August 12, 2015].
- Kostrin, H.M., 1980. Direct Formation of Pyrolysis Oil from Biomass. In *Specialists workshop on Fast Pyrolysis of Biomass Proceedings*. pp. 105–121. Available at: <http://www.osti.gov/scitech/servlets/purl/6478794#page=104> [Accessed July 28, 2016].
- Ku, X., Li, T. & Løvås, T., 2015. CFD-DEM simulation of biomass gasification with steam in a fluidized bed reactor. *Chemical Engineering Science*, 122, pp.270–283.
- Kuang, S.B. et al., 2012. Gas–Solid Flow and Energy Dissipation in Inclined Pneumatic Conveying. *Industrial & Engineering Chemistry Research*, 51(43), pp.14289–14302.

- Available at: https://www.researchgate.net/publication/255822866_Gas-Solid_Flow_and_Energy_Dissipation_in_Inclined_Pneumatic_Conveying [Accessed January 15, 2016].
- Kuhn, J.N. et al., 2008. Olivine catalysts for methane- and tar-steam reforming. *Applied Catalysis B: Environmental*, 81(1-2), pp.14–26. Available at: <http://linkinghub.elsevier.com/retrieve/pii/S0926337307004444> [Accessed July 19, 2016].
- Kulick, J.D., Fessler, J.R. & Eaton, J.K., 2006. Particle response and turbulence modification in fully developed channel flow. *Journal of Fluid Mechanics*, 277(-1), p.109. Available at: http://journals.cambridge.org/abstract_S0022112094002703 [Accessed January 28, 2016].
- Kumar, A., Jones, D.D. & Hanna, M.A., 2009. Thermochemical Biomass Gasification: A Review of the Current Status of the Technology. *Energies*, 2(3), pp.556–581. Available at: <http://www.mdpi.com/1996-1073/2/3/556/> [Accessed June 10, 2016].
- Láin, S. & Sommerfeld, M., 2012. Numerical calculation of pneumatic conveying in horizontal channels and pipes: Detailed analysis of conveying behaviour. *International Journal of Multiphase Flow*, 39, pp.105–120. Available at: <http://www.sciencedirect.com/science/article/pii/S0301932211002060> [Accessed November 12, 2015].
- Larfeldt, J., Leckner, B. & Chr, M., 2000. 00/03573 Modelling and measurements of heat transfer in charcoal from pyrolysis of large wood particles. *Fuel and Energy Abstracts*, 41(6), p.400.
- Lathouwers, D. & Bellan, J., 2001. Yield optimization and scaling of fluidized beds for tar production from biomass. *Energy and Fuels*, 15(5), pp.1247–1262.
- Lauder, B. & Spalding, D., 1972. Lectures in mathematical models of turbulence. Available at: <http://www.citeulike.org/group/13900/article/11884113> [Accessed July 14, 2015].
- Lauder, B. & Spalding, D., 1974. The numerical computation of turbulent flows. *Computer methods in applied mechanics and ...* Available at: <http://www.sciencedirect.com/science/article/pii/0045782574900292> [Accessed January 20, 2016].
- Lédé, J., 2003. Comparison of contact and radiant ablative pyrolysis of biomass. *Journal of analytical and applied pyrolysis*, 70(2), pp.601–618. Available at: <http://www.sciencedirect.com/science/article/pii/S0165237003000433> [Accessed July 14, 2015].
- Lédé, J., 1999. Solar thermochemical conversion of biomass. *Solar Energy*, 65(1), pp.3–13. Available at: <http://www.sciencedirect.com/science/article/pii/S0038092X98001091> [Accessed July 14, 2015].
- Lee, K.-H. et al., 2005. Influence of Reaction Temperature, Pretreatment, and a Char Removal System on the Production of Bio-oil from Rice Straw by Fast Pyrolysis, Using a Fluidized Bed. *Energy & Fuels*, 19(5), pp.2179–2184. Available at: <http://dx.doi.org/10.1021/ef050015o> [Accessed June 15, 2015].
- Levy, A. et al., 1997. A comparison of analytical and numerical models with experimental data for gas-solid flow through a straight pipe at different inclinations. *Powder Technology*, 93(3), pp.253–260. Available at: <http://www.sciencedirect.com/science/article/pii/S0032591097032804> [Accessed January 19, 2016].

- Levy, A., 2000. Two-fluid approach for plug flow simulations in horizontal pneumatic conveying. *Powder Technology*, 112(3), pp.263–272. Available at: <http://www.sciencedirect.com/science/article/pii/S0032591000003016> [Accessed January 19, 2016].
- Li, J. et al., 1993. Particle–fluid contacting in circulating fluidized beds. *Preprint Volume for CFB-IV; Avidan, AA, Ed.;* Available at: https://scholar.google.co.uk/scholar?q=+Particle%E2%80%93fluid+contacting+in+circulating+fluidized+beds&btnG=&hl=en&as_sdt=0%2C5#0 [Accessed March 6, 2016].
- Li, X.T. et al., 2004. Biomass gasification in a circulating fluidized bed. *Biomass and Bioenergy*, 26(2), pp.171–193. Available at: <http://www.sciencedirect.com/science/article/pii/S0961953403000849> [Accessed June 9, 2015].
- Liden, A.G., Berruti, F. & Scott, D.S., 1988. A kinetic model for the production of liquids from the flash pyrolysis of biomass. *Chemical Engineering Communications*, 65(1), pp.207–221. Available at: <http://www.tandfonline.com/doi/abs/10.1080/00986448808940254> [Accessed June 25, 2015].
- Lincoln, K., 1980. High radiative heat flux pyrolysis of thin biomass. *Proc. Specialist's Workshop on Fast Pyrolysis of* Available at: <http://www.osti.gov/scitech/servlets/purl/6478794#page=149> [Accessed March 9, 2016].
- Liu, H., 2014. *CFD Modeling of Biomass Gasification Using a Circulating Fluidized Bed Reactor*. University of Waterloo.
- Liu, H. et al., 2013. Computational Fluid Dynamics Modeling of Biomass Gasification in Circulating Fluidized-Bed Reactor Using the Eulerian–Eulerian Approach. *Industrial & Engineering Chemistry* ..., pp.18162–18174. Available at: <http://pubs.acs.org/doi/abs/10.1021/ie4024148>.
- Liu, H. et al., 2014. Effect of char combustion product distribution coefficient on the CFD modeling of biomass gasification in a circulating fluidized bed. *Industrial and Engineering Chemistry Research*, 53(13), pp.5554–5563.
- Liu, H. et al., 2013. The impacts of standard wall function and drag model on the turbulent modelling of gas-particle flow in a circulating fluidised bed riser. *Canadian Journal of Chemical Engineering*, 91(4), pp.704–717. Available at: <http://doi.wiley.com/10.1002/cjce.21782> [Accessed July 13, 2016].
- Liu, H. & Gibbs, B.M., 2003. Modeling NH₃ and HCN emissions from biomass circulating fluidized bed gasifiers☆. *Fuel*, 82(13), pp.1591–1604.
- Liu, H. & Lu, H., 2009. Numerical study on the cluster flow behavior in the riser of circulating fluidized beds. *Chemical Engineering Journal*, 150(2-3), pp.374–384. Available at: <http://www.sciencedirect.com/science/article/pii/S1385894709000175> [Accessed February 24, 2016].
- Liu, Q. et al., 2011. Performance analysis of a mid-and low-temperature solar receiver/reactor for hydrogen production with methanol steam reforming. *International Journal of* Available at: <http://onlinelibrary.wiley.com/doi/10.1002/er.1738/full> [Accessed July 14, 2015].
- Liu, S. et al., 2005. Electrical capacitance tomography for gas–solids flow measurement for circulating fluidized beds. *Flow Measurement and Instrumentation*, 16(2-3), pp.135–144. Available at: <http://www.sciencedirect.com/science/article/pii/S0955598605000208> [Accessed February 16, 2016].

- Loha, C., Chatterjee, P.K. & Chattopadhyay, H., 2011. Performance of fluidized bed steam gasification of biomass – Modeling and experiment. *Energy Conversion and Management*, 52(3), pp.1583–1588.
- Lun, C. & Liu, H., 1997. Numerical simulation of dilute turbulent gas-solid flows in horizontal channels. *International Journal of Multiphase Flow*. Available at: <http://www.sciencedirect.com/science/article/pii/S0301932296000870> [Accessed January 20, 2016].
- Lun, C.K.K. et al., 1984. Kinetic theories for granular flow: inelastic particles in Couette flow and slightly inelastic particles in a general flowfield. *Journal of Fluid Mechanics*, 140(1), pp.223–256. Available at: http://journals.cambridge.org/abstract_S0022112084000586 [Accessed March 25, 2016].
- Luo, K. et al., 2013. LES–DEM investigation of an internally circulating fluidized bed: effects of gas and solid properties. *Chemical engineering journal*. Available at: <http://www.sciencedirect.com/science/article/pii/S1385894713006505> [Accessed March 29, 2016].
- Luzzi, A. & Lovegrove, K., 2004. *Encyclopedia of Energy*, Elsevier. Available at: <http://www.sciencedirect.com/science/article/pii/B012176480X005313> [Accessed July 14, 2015].
- Lv, P.M. et al., 2004. An experimental study on biomass air-steam gasification in a fluidized bed. *Bioresource Technology*, 95(1), pp.95–101.
- Magnaterra, M., Fusco, J. & Ochoa, J., 1993. Kinetic study of the reaction of different hardwood sawdust chars with oxygen. Chemical and structural characterization of the samples. *Advances in*. Available at: http://link.springer.com/chapter/10.1007/978-94-011-1336-6_10 [Accessed July 30, 2016].
- Makkawi, Y. & Ocone, R., 2006. A model for gas–solid flow in a horizontal duct with a smooth merge of rapid–intermediate–dense flows. *Chemical Engineering Science*, 61(13), pp.4271–4281. Available at: <http://www.sciencedirect.com/science/article/pii/S0009250906000364> [Accessed January 19, 2016].
- Maniatis, K., 2008. Progress in biomass gasification: an overview. *Progress in thermochemical biomass conversion*. Available at: <https://books.google.co.uk/books?hl=en&lr=&id=6QD69PvV0foC&oi=fnd&pg=PA1&dq=Progress+in+biomass+gasification-an+overview&ots=to2MM54ePc&sig=8aKeKk-gIbBIONCjgIHQMsl5io> [Accessed July 28, 2016].
- Mansaray, K. et al., 2000. Mathematical modeling of a fluidized bed rice husk gasifier: part I – model development. <http://dx.doi.org/10.1080/00908310050014243>, p. Energy Sources ;22:167–85.
- Mante, O.D. & Agblevor, F.A., 2011. Parametric study on the pyrolysis of manure and wood shavings. *Biomass and Bioenergy*, 35(10), pp.4417–4425. Available at: <http://www.sciencedirect.com/science/article/pii/S0961953411004478> [Accessed June 3, 2015].
- Manya, J., Velo, E. & Puigjaner, L., 2003. Kinetics of biomass pyrolysis: a reformulated three-parallel-reactions model. *Industrial & engineering chemistry*. Available at: <http://pubs.acs.org/doi/abs/10.1021/ie020218p> [Accessed July 29, 2016].
- Mason, D. & Li, J., 2000. A novel experimental technique for the investigation of gas–solids flow in pipes. *Powder technology*. Available at: <http://www.sciencedirect.com/science/article/pii/S0032591000002941> [Accessed

February 24, 2016].

- Mathiesen, V., Solberg, T. & Hjertager, B.H., 2000. An experimental and computational study of multiphase flow behavior in a circulating fluidized bed. *International Journal of Multiphase Flow*, 26(3), pp.387–419. Available at: <http://www.sciencedirect.com/science/article/pii/S0301932299000270> [Accessed July 7, 2015].
- McGlinchey, D. & Cowell, A., 2007. Bend pressure drop predictions using the Euler-Euler model in dense phase pneumatic conveying. *Particulate Science* Available at: <http://www.tandfonline.com/doi/abs/10.1080/02726350701492827> [Accessed February 21, 2016].
- McKee, S., Dyakowski, T. & Williams, R., 1995. Solids flow imaging and attrition studies in a pneumatic conveyor. *Powder Technology*. Available at: <http://www.sciencedirect.com/science/article/pii/003259109402894T> [Accessed February 8, 2016].
- Mellin, P. et al., 2013. An Euler–Euler approach to modeling biomass fast pyrolysis in fluidized-bed reactors – Focusing on the gas phase. *Applied Thermal Engineering*, 58(1-2), pp.344–353. Available at: <http://www.sciencedirect.com/science/article/pii/S1359431113003256> [Accessed April 11, 2016].
- Mellin, P., Kantarelis, E. & Yang, W., 2014. Computational fluid dynamics modeling of biomass fast pyrolysis in a fluidized bed reactor, using a comprehensive chemistry scheme. *Fuel*, 117(A), pp.704–715. Available at: <http://www.sciencedirect.com/science/article/pii/S0016236113008387> [Accessed July 14, 2015].
- Miao, Q. et al., 2013. Modeling biomass gasification in circulating fluidized beds. *Renewable Energy*, 50, pp.655–661.
- Miccio, F. et al., 2009. Biomass gasification in a catalytic fluidized reactor with beds of different materials. *Chemical Engineering Journal*, 154(1-3), pp.369–374.
- Milne, T., Abatzoglou, N. & Evans, R., 1998. *Biomass gasifier" tars": Their nature, formation, and conversion*, Available at: http://www.ps-survival.com/PS/Gasifiers/Biomass_Gasifier_Tars_Their_Nature_Formation_And_Conversion_1998.pdf [Accessed July 27, 2016].
- Miltner, M. et al., 2008. Computational fluid dynamic simulation of a solid biomass combustor: modelling approaches. *Clean Technologies and Environmental Policy*, 10(2), pp.165–174. Available at: <http://link.springer.com/10.1007/s10098-007-0137-0> [Accessed April 6, 2016].
- Mitsuoka, K. et al., 2011. Gasification of woody biomass char with CO₂: the catalytic effects of K and Ca species on char gasification reactivity. *Fuel Processing*. Available at: <http://www.sciencedirect.com/science/article/pii/S0378382010002791> [Accessed July 29, 2016].
- Morales, S. et al., 2014. Solar biomass pyrolysis for the production of bio-fuels and chemical commodities. *Journal of Analytical and Applied Pyrolysis*, 109, pp.65–78. Available at: <http://linkinghub.elsevier.com/retrieve/pii/S0165237014001715>.
- Mtui, P.L., 2013. Computational Fluid Dynamics Modeling of Palm Fruit Pyrolysis in a Fast Fluidized Bed Reactor. *Advanced Materials Research*, 699, pp.822–828. Available at: <http://www.scientific.net/AMR.699.822> [Accessed April 7, 2016].

- Mwesigye, A., Huan, Z. & Meyer, J., 2015. Thermal Performance of a Receiver Tube for a High Concentration Ratio Parabolic Trough System and Potential for Improved Performance With Syltherm800-CuO. *ASME 2015* Available at: <http://proceedings.asmedigitalcollection.asme.org/proceeding.aspx?articleid=2501073> [Accessed April 21, 2016].
- Namkung, W., Kim, S.W. & Kim, S.D., 1999. Flow regimes and axial pressure profiles in a circulating fluidized bed. *Chemical Engineering Journal*, 72(3), pp.245–252.
- Narvaez, I. et al., 1996. Biomass Gasification with Air in an Atmospheric Bubbling Fluidized Bed . Effect of Six Operational Variables on the Quality of. *Ind. Eng. Chem. Res.*, 35(95), pp.2110–2120.
- Neri, A. & Gidaspow, D., 2000. Riser hydrodynamics: simulation using kinetic theory. *AIChE Journal*. Available at: <http://onlinelibrary.wiley.com/doi/10.1002/aic.690460108/full> [Accessed March 14, 2016].
- NETL, 2014. MFIX results. Available at: <https://www.mfix.org/results.php> [Accessed March 23, 2014].
- Ngo, S.I. et al., 2011. Performance evaluation for dual circulating fluidized-bed steam gasifier of biomass using quasi-equilibrium three-stage gasification model. *Applied Energy*, 88(12), pp.5208–5220. Available at: <http://www.sciencedirect.com/science/article/pii/S0306261911004910> [Accessed June 2, 2015].
- Nikoo, M.B. & Mahinpey, N., 2008. Simulation of biomass gasification in fluidized bed reactor using ASPEN PLUS. *Biomass and Bioenergy*, 32(12), pp.1245–1254.
- Nitsch, X. et al., 2014. Conversion of Phenol-Based Tars over Biomass Char under H₂ and H₂ O Atmospheres. *Energy & Fuels*, 28(11), pp.6936–6940. Available at: <http://dx.doi.org/10.1021/ef500980g> [Accessed March 21, 2016].
- Norinaga, K. et al., 2013. Detailed chemical kinetic modelling of vapour-phase cracking of multi-component molecular mixtures derived from the fast pyrolysis of cellulose. *Fuel*, 103, pp.141–150. Available at: <http://www.sciencedirect.com/science/article/pii/S0016236111004819> [Accessed April 11, 2016].
- Ocone, R., Sundaresan, S. & Jackson, R., 1993. Gas-particle flow in a duct of arbitrary inclination with particle-particle interactions. *AIChE journal*. Available at: <http://www.princeton.edu/cbe/people/faculty/sundaresan/group/publications/pdf/51.pdf> [Accessed July 2, 2015].
- Oelfke, J.B. et al., 2006. *Circulating fluidized bed hydrodynamics experiments for the multiphase fluid dynamics research consortium (MFDRC)*., Albuquerque, NM, and Livermore, CA. Available at: https://www.researchgate.net/publication/241980536_Circulating_fluidized_bed_hydrodynamics_experiments_for_the_multiphase_fluid_dynamics_research_consorium_MFDRC [Accessed February 16, 2016].
- Oesterle, B. & Petitjean, A., 1993. Simulation of particle-to-particle interactions in gas solid flows. *International Journal of Multiphase Flow*, 19(1), pp.199–211. Available at: <http://www.sciencedirect.com/science/article/pii/030193229390033Q> [Accessed January 26, 2016].
- Oevermann, M., Gerber, S. & Behrendt, F., 2009. Euler-Lagrange/DEM simulation of wood gasification in a bubbling fluidized bed reactor. *Particuology*, 7(4), pp.307–316.

- Ollero, P. et al., 2003. The CO₂ gasification kinetics of olive residue. *Biomass and Bioenergy*. Available at: <http://www.sciencedirect.com/science/article/pii/S0961953402000910> [Accessed July 30, 2016].
- Paasen, S. Van & Kiel, J., 2004. Tar formation in a fluidised bed gasifier. *Impact of fuel properties*. Available at: <ftp://130.112.2.101/pub/www/library/report/2004/c04013.pdf> [Accessed July 27, 2016].
- Papadakis, K., Bridgwater, A. & Gu, S., 2008. CFD modelling of the fast pyrolysis of biomass in fluidised bed reactors, Part A: Eulerian computation of momentum transport in bubbling fluidised beds. *Chemical Engineering Science*. Available at: <http://www.sciencedirect.com/science/article/pii/S0009250908003138> [Accessed July 14, 2015].
- Papadakis, K. & Gu, S., 2009. Application of CFD to model fast pyrolysis of biomass. *Fuel Processing* Available at: <http://www.sciencedirect.com/science/article/pii/S0378382009000162> [Accessed July 14, 2015].
- Papadakis, K., Gu, S. & Bridgwater, A., 2009. CFD modelling of the fast pyrolysis of biomass in fluidised bed reactors. Part B: heat, momentum and mass transport in bubbling fluidised beds. *Chemical Engineering Science*. Available at: <http://www.sciencedirect.com/science/article/pii/S0009250908006222> [Accessed July 14, 2015].
- Pasangulapati, V., 2012. *Devolatilization characteristics of cellulose, hemicellulose, lignin and the selected biomass during thermochemical gasification: experiment and modeling studies*. Available at: <https://shareok.org/handle/11244/7960> [Accessed June 25, 2015].
- Patankar, S., 1980. *Numerical heat transfer and fluid flow*, Boca Raton, FL: CRC. Available at: <https://books.google.com/books?hl=en&lr=&id=5JMYZMX3OVcC&oi=fnd&pg=PR11&dq=A.+Patankar,+Numerical+heat+transfer+and+fluid+flow,+Minnesota&ots=D8msjUcMsf&sig=l22Tz63EqV0MrVhtcryXy773kN4> [Accessed July 14, 2015].
- Patra, C., 2014. *Cfd simulations of fluidized bed Biomass gasification*. Available at: <http://ethesis.nitrkl.ac.in/6563/> [Accessed July 24, 2016].
- Patro, P. & Dash, S.K., 2013. Numerical Simulation for Hydrodynamic Analysis and Pressure Drop Prediction in Horizontal Gas-Solid Flows. *Particulate Science and Technology*, 32(1), pp.94–103. Available at: <http://www.tandfonline.com/doi/abs/10.1080/02726351.2013.829543> [Accessed January 19, 2016].
- Pepiot, P., Dibble, C. & Foust, T., 2010. Computational fluid dynamics modeling of biomass gasification and pyrolysis. *Computational modeling in* Available at: http://pepiot.mae.cornell.edu/pdf/Pepiot_ACS_2010.pdf.
- Perkins, C., Woodruff, B. & Andrews, L., 2008. Synthesis gas production by rapid solar thermal gasification of corn stover. *14th Biennial CSP* Available at: <http://www.nrel.gov/docs/fy08osti/42878.pdf> [Accessed March 14, 2016].
- Peters, B. et al., 2002. Measurements and particle resolved modelling of heat-up and drying of a packed bed. *Biomass and Bioenergy*, 23(4), pp.291–306. Available at: <http://www.sciencedirect.com/science/article/pii/S0961953402000521> [Accessed April 6, 2016].
- Petersen, I. & Werther, J., 2005. Experimental investigation and modeling of gasification of

- sewage sludge in the circulating fluidized bed. *Chemical Engineering and Processing: Process Intensification*, 44(7), pp.717–736. Available at: <http://www.sciencedirect.com/science/article/pii/S0255270104001916> [Accessed June 23, 2015].
- Pfeifer, C., Rauch, R. & Hofbauer, H., 2004. In-Bed Catalytic Tar Reduction in a Dual Fluidized Bed Biomass Steam Gasifier. *Industrial & Engineering Chemistry Research*, 43(7), pp.1634–1640. Available at: <http://pubs.acs.org/doi/abs/10.1021/ie030742b> [Accessed July 10, 2016].
- Picou, J. et al., 2008. Kinetics of noncatalytic water gas shift reaction in a supercritical water medium. Available at: http://scholarsmine.mst.edu/faculty_work/8942/ [Accessed July 30, 2016].
- Prakash, N. & Karunanithi, T., 2009. Advances in modeling and simulation of biomass pyrolysis. *Asian J. Sci. Res.*, 2(Copyright (C) 2011 American Chemical Society (ACS). All Rights Reserved.), pp.1–27. Available at: <http://docsdrive.com/pdfs/ansinet/ajsr/2009/1-27.pdf> [Accessed July 29, 2016].
- Punsuwan, N. & Tangsathitkulchai, C., 2014. Product characterization and kinetics of biomass pyrolysis in a three-zone free-fall reactor. *International Journal of Chemical ...* Available at: <http://www.hindawi.com/journals/ijce/2014/986719/abs/> [Accessed July 14, 2015].
- Radmanesh, R., Chaouki, J. & Guy, C., 2006. Biomass Gasification in a Bubbling Fluidized Bed Reactor: Experiments and Modeling. *J.*, 52(12), pp.4258–4272. Available at: <http://doi.wiley.com/10.1002/aic.11020> [Accessed July 21, 2016].
- Raja, A.K., Shriwastava, A.P. & Dwivedi, M., 2006. *Power Plant Engineering*, Digital Designs. Available at: <https://books.google.com/books?id=7uchHBgAAQBAJ&pgis=1> [Accessed February 18, 2016].
- Ranganathan, P. & Gu, S., 2016. Computational fluid dynamics modelling of biomass fast pyrolysis in fluidised bed reactors, focusing different kinetic schemes. *Bioresource technology*. Available at: <http://www.sciencedirect.com/science/article/pii/S0960852416301687> [Accessed March 28, 2016].
- Ranzi, E. et al., 2008. Chemical Kinetics of Biomass Pyrolysis. *Energy & Fuels*, 22(6), pp.4292–4300. Available at: <http://dx.doi.org/10.1021/ef800551t> [Accessed December 14, 2015].
- Rao, S.M. et al., 2001. Electrical Capacitance Tomography Measurements on the Pneumatic Conveying of Solids. *Industrial & Engineering Chemistry Research*, 40(20), pp.4216–4226. Available at: <http://dx.doi.org/10.1021/ie0100028> [Accessed February 8, 2016].
- Rath, J. et al., 2002. Tar cracking from fast pyrolysis of large beech wood particles. *Journal of Analytical and Applied Pyrolysis*, 62(1), pp.83–92. Available at: <http://www.sciencedirect.com/science/article/pii/S0165237000002151> [Accessed June 25, 2015].
- Rath, J. & Staudinger, G., 2001. Cracking reactions of tar from pyrolysis of spruce wood. *Fuel*, 80(10), pp.1379–1389. Available at: <http://www.sciencedirect.com/science/article/pii/S0016236101000163> [Accessed June 20, 2015].
- Saidur, R. & Abdelaziz, E., 2011. A review on biomass as a fuel for boilers. *Renewable and Sustainable Energy Reviews*, 15(5), pp.2262–2289. Available at: <http://www.sciencedirect.com/science/article/pii/S1364032111000578> [Accessed July

14, 2015].

- Samuelsberg, A. & Hjertager, B., 1996a. An experimental and numerical study of flow patterns in a circulating fluidized bed reactor. *International Journal of Multiphase Flow*. Available at: <http://www.sciencedirect.com/science/article/pii/0301932295000801> [Accessed July 2, 2015].
- Samuelsberg, A. & Hjertager, B., 1996b. Computational modeling of gas/particle flow in a riser. *AIChE journal*. Available at: <http://onlinelibrary.wiley.com/doi/10.1002/aic.690420605/full> [Accessed March 14, 2016].
- Sato, T. et al., 2004. Water gas shift reaction kinetics under noncatalytic conditions in supercritical water. *The Journal of*. Available at: <http://www.sciencedirect.com/science/article/pii/S0896844603000494> [Accessed July 30, 2016].
- Scala, F., 2011. *Mass Transfer around Active Particles in Fluidized Beds*, Available at: <http://cdn.intechweb.org/pdfs/13550.pdf> [Accessed August 21, 2015].
- Şensöz, S., Angın, D. & Yorgun, S., 2000. Influence of particle size on the pyrolysis of rapeseed (*Brassica napus* L.): fuel properties of bio-oil. *Biomass and Bioenergy*, 19(4), pp.271–279. Available at: <http://www.sciencedirect.com/science/article/pii/S0961953400000416> [Accessed May 13, 2016].
- Shaddix, C. & Hardesty, D., 1999. Combustion properties of biomass flash pyrolysis oils: final project report. Available at: <http://www.osti.gov/scitech/biblio/5983> [Accessed July 14, 2015].
- Shakya, B.D., 2007. Pyrolysis of Waste Plastics To Generate Useful Fuel Containing Hydrogen Using a Solar Thermochemical Process. , p.148.
- Sharma, A. et al., 2015. Multi-fluid reactive modeling of fluidized bed pyrolysis process. *Chemical Engineering Science*, 123, pp.311–321. Available at: <http://www.sciencedirect.com/science/article/pii/S0009250914006435> [Accessed May 11, 2016].
- Sheng, C. & Azevedo, J.L.T., 2005. Estimating the higher heating value of biomass fuels from basic analysis data. *Biomass and Bioenergy*, 28(5), pp.499–507. Available at: <http://www.sciencedirect.com/science/article/pii/S0961953404002107> [Accessed June 18, 2015].
- Shi, A. et al., 2015. Numerical Simulation of Biomass Gasification in a Fluidized Bed. , (Asei), pp.1585–1591. Available at: http://www.atlantispress.com/php/download_paper.php?id=25836723 [Accessed July 20, 2016].
- Shinya, Y. & Yukihiro, M., 2008. *The Asian biomass handbook-a guide for biomass production and utilization*,
- Shuai, Y. et al., 2010. *Ray-thermal-structural coupled analysis of parabolic trough solar collector system*, Available at: <http://cdn.intechopen.com/pdfs-wm/12232.pdf> [Accessed July 14, 2015].
- Silva, G., Jiménez, N. & Salazar, O., 2012. *Fluid Dynamics of Gas-Solid Fluidized Beds*, Available at: <http://cdn.intechopen.com/pdfs-wm/31571.pdf> [Accessed February 16, 2016].
- Simanungkalit, S. & Rinaldi, N., 2013. CFD analysis of the fast pyrolysis for empty fruit bunches in fluidized-bed reactor. *JEAS-Journal of Engineering &* Available at:

- <http://www.cabdirect.org/abstracts/20143200448.html> [Accessed April 7, 2016].
- Sinha, S. et al., 2000. Modelling of pyrolysis in wood: a review. *SESI Journal*. Available at: <http://citeseerx.ist.psu.edu/viewdoc/download?doi=10.1.1.457.1318&rep=rep1&type=pdf> [Accessed July 29, 2016].
- Sommerfeld, M. & Huber, N., 1999. Experimental analysis and modelling of particle-wall collisions. *International Journal of Multiphase Flow*, 25(6-7), pp.1457–1489. Available at: <http://www.sciencedirect.com/science/article/pii/S0301932299000476> [Accessed January 29, 2016].
- Steinfeld, A., 2005. Solar thermochemical production of hydrogen—a review. *Solar energy*, 123(2), pp.63–74. Available at: <http://www.sciencedirect.com/science/article/pii/S0038092X03004663> [Accessed March 8, 2016].
- Stine, W., 2001. Power from the sun.
- Sui, J. et al., 2011. Experimental investigation of methanol decomposition with mid- and low-temperature solar thermal energy. *International Journal of Energy Research*, 35(1), pp.61–67. Available at: <http://doi.wiley.com/10.1002/er.1729> [Accessed March 8, 2016].
- Syamlal, M., 1987. The particle-particle drag term in a multiparticle model of fluidization. Available at: <http://www.osti.gov/scitech/biblio/6355923> [Accessed March 28, 2016].
- Syamlal, M. & Bissett, L. a, 1992. METC gasifier advanced simulation (MGAS) model. Available at: <http://www.osti.gov/scitech/biblio/5745174> [Accessed August 24, 2015].
- Syamlal, M. & O'Brien, T., 1987. The derivation of a drag coefficient formula from velocity-voidage correlations. *unpublished report*. Available at: <http://citeseerx.ist.psu.edu/viewdoc/download?doi=10.1.1.627.8743&rep=rep1&type=pdf> [Accessed March 5, 2016].
- Syamlal, M., Rogers, W. & O'Brien, T., 1993. MFIX documentation: Theory guide. ... *Note DOE/METC-95/1013 and* Available at: http://www.researchgate.net/profile/Madhava_Syamlal/publication/252563656_MFIX_documentation_theory_guide/links/00b7d52fa5451d3321000000.pdf [Accessed July 14, 2015].
- Tabatabaie-Raissi, A., 1989. Cellulose pyrolysis kinetics in a simulated solar environment. *Industrial & Engineering Chemistry* Available at: <http://pubs.acs.org/doi/abs/10.1021/ie00090a031> [Accessed July 14, 2015].
- Taylor, R.W., Berjoan, R. & Coutures, J.P., 1983. Solar gasification of carbonaceous materials. *Solar Energy*, 30(6), pp.513–525. Available at: <http://www.sciencedirect.com/science/article/pii/0038092X83900634> [Accessed March 14, 2016].
- Thankachan, I., Rupesh, S. & Muraleedharan, C., 2014. CFD Modelling of Biomass Gasification in Fluidized-Bed Reactor Using the Eulerian-Eulerian Approach. *Applied Mechanics and Materials*, 594, pp.1903–1908. Available at: <http://www.scientific.net/AMM.592-594.1903> [Accessed July 22, 2016].
- Thapa, R. & Pfeifer, C., 2014. Modeling of reaction kinetics in bubbling fluidized bed biomass gasification reactor. *Internal Journal of Energy*. Available at: http://ijee.ieefoundation.org/vol5/issue1/IJEE_03_v5n1.pdf [Accessed July 23, 2016].
- Turner, F. & Mann, U., 1981. Kinetic investigation of wood pyrolysis. *Industrial & Engineering Chemistry Process*. Available at: <http://pubs.acs.org/doi/abs/10.1021/i200014a015> [Accessed July 29, 2016].

- Tijani, A.S. & Roslan, A.M.S. Bin, 2014. Simulation Analysis of Thermal Losses of Parabolic trough Solar Collector in Malaysia Using Computational Fluid Dynamics. *Procedia Technology*, 15, pp.841–848. Available at: <http://www.sciencedirect.com/science/article/pii/S221201731400173X> [Accessed April 19, 2016].
- Tinaut, F. et al., 2008. Effect of biomass particle size and air superficial velocity on the gasification process in a downdraft fixed bed gasifier. An experimental and modelling study. *Fuel Processing Technology*. Available at: <http://www.sciencedirect.com/science/article/pii/S037838200800101X> [Accessed July 14, 2015].
- Tinney, E., 1965. The combustion of wooden dowels in heated air. *Symposium (International) on Combustion*. Available at: <http://www.sciencedirect.com/science/article/pii/S0082078465802351> [Accessed July 29, 2016].
- Tomita, Y. et al., 2008. Low-velocity pneumatic conveying in horizontal pipe for coarse particles and fine powders. *Particuology*, 6(5), pp.316–321. Available at: <http://www.sciencedirect.com/science/article/pii/S1674200108000783> [Accessed February 24, 2016].
- Tsuji, Y. & Morikawa, Y., 1982. LDV measurements of an air–solid two-phase flow in a horizontal pipe. *Journal of Fluid Mechanics*. Available at: http://journals.cambridge.org/abstract_S002211208200281X [Accessed January 21, 2016].
- Tsuji, Y., Shen, N.Y. & Morikawa, Y., 1991. Lagrangian simulation of dilute gas-solid flows in a horizontal pipe. *Advanced Powder Technology*, 2(1), pp.63–81. Available at: <http://booksandjournals.brillonline.com/content/journals/10.1163/156855291x00143> [Accessed February 2, 2016].
- Tsuji, Y., Tanaka, T. & Yonemura, S., 1998. Cluster patterns in circulating fluidized beds predicted by numerical simulation (discrete particle model versus two-fluid model). *Powder Technology*, 95(3), pp.254–264. Available at: <http://www.sciencedirect.com/science/article/pii/S0032591097033494> [Accessed February 24, 2016].
- UNFCCC, 2005. *Annex 8, Clarifications of definition of biomass and consideration of changes in carbon pools due to a CDM project activity, Annex 8*, Available at: <https://cdm.unfccc.int/EB/020/eb20repan08.pdf>.
- Várhegyi, G., Mészáros, E. & Antal, M., 2006. Combustion kinetics of corncob charcoal and partially demineralized corncob charcoal in the kinetic regime. *Industrial & Environmental Engineering Research*. Available at: <http://pubs.acs.org/doi/abs/10.1021/ie0602411> [Accessed July 30, 2016].
- Van de Velden, M., Baeyens, J. & Smolders, K., 2007. Solids mixing in the riser of a circulating fluidized bed. *Chemical Engineering Science*, 62(8), pp.2139–2153. Available at: <http://www.sciencedirect.com/science/article/pii/S0009250907000395> [Accessed February 16, 2016].
- Volker Quaschnig, 2003. Technology Fundamentals: Solar thermal power plants. *Renewable Energy World*, pp.109–113. Available at: http://www.volker-quaschnig.de/articles/fundamentals2/index_e.php [Accessed March 4, 2016].
- Wang, F. et al., 2014. Thermal and chemical reaction performance analyses of steam methane reforming in porous media solar thermochemical reactor. *International Journal of Hydrogen Energy*, 39(2), pp.718–730. Available at: <http://www.sciencedirect.com/science/article/pii/S0360319913026475> [Accessed March 19, 2016].

30, 2016].

- Wang, K., He, Y. & Cheng, Z., 2014. A design method and numerical study for a new type parabolic trough solar collector with uniform solar flux distribution. *Science China Technological Sciences*. Available at: <http://link.springer.com/article/10.1007/s11431-013-5452-6> [Accessed July 14, 2015].
- Warnecke, R., 2000. Gasification of biomass: comparison of fixed bed and fluidized bed gasifier. *Biomass and Bioenergy*, 18(6), pp.489–497. Available at: <http://www.sciencedirect.com/science/article/pii/S096195340000009X> [Accessed April 7, 2015].
- Wen, C. & Yu, Y., 1966. Mechanics of fluidization. *Chem. Eng. Prog. Symp. Ser.* Available at: <http://www.citeulike.org/group/13900/article/11887970> [Accessed March 6, 2016].
- Wongchang, T., 2013. An Analysis of Wood Pyrolysis Tar from High Temperature Thermal Cracking Process. *Energy Sources, Part A:* Available at: <http://www.tandfonline.com/doi/abs/10.1080/15567036.2012.707748> [Accessed July 14, 2015].
- Wu, Z. et al., 2014. Three-dimensional numerical study of heat transfer characteristics of parabolic trough receiver. *Applied Energy*, 113, pp.902–911. Available at: <http://dx.doi.org/10.1016/j.apenergy.2013.07.050>.
- Xie, J. et al., 2012. Simulation on gasification of forestry residues in fluidized beds by Eulerian–Lagrangian approach. *Bioresource Technology*, 121, pp.36–46.
- Xiong, Q., Aramideh, S. & Kong, S., 2013. Modeling effects of operating conditions on biomass fast pyrolysis in bubbling fluidized bed reactors. *Energy & Fuels*. Available at: <http://pubs.acs.org/doi/abs/10.1021/ef4012966> [Accessed April 8, 2016].
- Xue, Q. et al., 2012. Experimental validation and CFD modeling study of biomass fast pyrolysis in fluidized-bed reactors. *Fuel*, 97, pp.757–769. Available at: <http://www.sciencedirect.com/science/article/pii/S0016236112002037> [Accessed July 14, 2015].
- Xue, Q. & Fox, R.O., 2014. Multi-fluid CFD modeling of biomass gasification in polydisperse fluidized-bed gasifiers. *Powder Technology*, 254, pp.187–198. Available at: <http://www.sciencedirect.com/science/article/pii/S0032591014000345> [Accessed March 30, 2015].
- Xue, Q., Heindel, T.J. & Fox, R.O., 2011. A CFD model for biomass fast pyrolysis in fluidized-bed reactors. *Chemical Engineering Science*, 66(11), pp.2440–2452. Available at: <http://www.sciencedirect.com/science/article/pii/S000925091100176X> [Accessed April 7, 2016].
- Yaghoubi, M., Ahmadi, F. & Bandehee, M., 2013. Analysis of heat losses of absorber tubes of parabolic through collector of Shiraz (Iran) solar power plant. *Journal of Clean Energy* Available at: <http://www.jocet.org/papers/008-J024.pdf> [Accessed April 21, 2016].
- Yang, N. et al., 2003. CFD simulation of concurrent-up gas–solid flow in circulating fluidized beds with structure-dependent drag coefficient. *Chemical Engineering Journal*, 96(1-3), pp.71–80. Available at: <http://www.sciencedirect.com/science/article/pii/S1385894703002316> [Accessed November 17, 2015].
- Yin, X.L. et al., 2002. Design and operation of a CFB gasification and power generation system for rice husk. *Biomass and Bioenergy*, 23(3), pp.181–187.

- Yu, X. et al., 2014. A CFD study of biomass pyrolysis in a downer reactor equipped with a novel gas-solid separator - I: Hydrodynamic performance. *Fuel Processing Technology*, 126, pp.366–382.
- Yu, X. et al., 2015. A CFD study of biomass pyrolysis in a downer reactor equipped with a novel gas–solid separator-II thermochemical performance and products. *Fuel Processing Technology*, 133, pp.51–63. Available at: <http://www.sciencedirect.com/science/article/pii/S037838201500017X> [Accessed July 14, 2015].
- Yu, X. & Makkawi, Y., 2013. A CFD study of gas-solid separation in a downer pyrolysis reactor: An eulerian-eulerian approach. *BioEnergy IV: Innovations in Biomass Conversion for Heat, Power, Fuels and Chemicals*. Available at: http://dc.engconfintl.org/bioenergy_iv/9 [Accessed April 27, 2016].
- Z'Graggen, A. & Steinfeld, A., 2008. A two-phase reactor model for the steam-gasification of carbonaceous materials under concentrated thermal radiation. *Chemical Engineering and Processing: Process Intensification*, 47(4), pp.655–662. Available at: <http://www.sciencedirect.com/science/article/pii/S0255270106003163> [Accessed February 11, 2016].
- Zarza, E., 2009. Medium Temperature Solar Concentrators (Parabolic-Troughs Collectors). *Solar Energy Conversion And Photoenergy System-* Available at: http://books.google.co.uk/books?hl=en&lr=&id=XTBUCwAAQBAJ&oi=fnd&pg=PA170&dq=Medium+Temperature+Solar+Concentrators-Parabolic+Trough+Technology+E+zarza&ots=ASJ9nWD9Et&sig=mPPbksVp2ucMG7Gj8BY4A_iMgjI [Accessed March 4, 2016].
- Zeng, K. et al., 2015. Solar pyrolysis of beech wood: Effects of pyrolysis parameters on the product distribution and gas product composition. *Energy*, 93, pp.1648–1657. Available at: <http://www.sciencedirect.com/science/article/pii/S0360544215013705> [Accessed December 31, 2015].
- Zeng, K. et al., 2015. Solar Pyrolysis of Wood in a Lab-scale Solar Reactor: Influence of Temperature and Sweep Gas Flow Rate on Products Distribution. *Energy Procedia*. Available at: <http://www.sciencedirect.com/science/article/pii/S1876610215004695> [Accessed March 23, 2016].
- Zhang, D. & VanderHeyden, W., 2001. High-resolution three-dimensional numerical simulation of a circulating fluidized bed. *Powder Technology*, 116(2-3), pp.133–141. Available at: <http://www.sciencedirect.com/science/article/pii/S0032591000003879> [Accessed July 8, 2015].
- Zhang, R. et al., 2013. Experimental study of exit effect on gas–solid flow and heat transfer inside CFB risers. *Experimental Thermal and Fluid Science*, 51, pp.291–296. Available at: <http://linkinghub.elsevier.com/retrieve/pii/S0894177713001866> [Accessed August 9, 2016].
- Zhou, H. et al., 2002. Lagrangian approach for simulating the gas-particle flow structure in a circulating fluidized bed riser. *International Journal of Multiphase Flow*, 28(11), pp.1801–1821. Available at: <http://www.sciencedirect.com/science/article/pii/S0301932202000496> [Accessed February 24, 2016].
- Zhou, Z. et al., 2009. Study on biomass circulation and gasification performance in a clapboard-type internal circulating fluidized bed gasifier. *Biotechnology Advances*, 27(5), pp.612–615.
- Zhu, K. et al., 2003. Electrical capacitance tomography measurements on vertical and

inclined pneumatic conveying of granular solids. *Chemical Engineering Science*, 58(18), pp.4225–4245. Available at: <http://www.sciencedirect.com/science/article/pii/S0009250903003063> [Accessed February 8, 2016].

Zhu, K. et al., 2004. Pneumatic conveying of granular solids in horizontal and inclined pipes. *AIChE Journal*, 50(8), pp.1729–1745. Available at: <http://doi.wiley.com/10.1002/aic.10172> [Accessed January 20, 2016].

Zhu, K. & Wong, C., 2004. Pneumatic conveying of granular solids in horizontal and inclined pipes. *AIChE* Available at: <http://onlinelibrary.wiley.com/doi/10.1002/aic.10172/pdf> [Accessed February 4, 2016].

Zolin, A. et al., 2001. The influence of inorganic materials on the thermal deactivation of fuel chars. *Energy* &. Available at: <http://pubs.acs.org/doi/abs/10.1021/ef000288d> [Accessed July 30, 2016].

APPENDIX

APPENDIX A: UDF codes

Gasification code

```
/****** Biomass Combustion/Gasification Model *****/
/*
          Version: 3.0

Programmer(s): Muktar Bashir
          Date:

Reviewer(s): Dr. Yassir Makkawi
          Date :

*/

/* ----- */

#include "udf.h"
#include "stdio.h"
#include "math.h"
#include "time.h"

#define SMALL_S 1.e-29
#define eps_g_small 0.99999
#define spe_small 1.e-8
#define TMAX 5000.

static const real Arrhenius_devolatilization = 3.88e+10;
static const real E_Activation_devolatilization = 1.2223e+8;
static const real Arrhenius_steamr = 1.52e+4; /* From P / Fuel 89 (2010) 2903?917 for
C +H2O => CO + H2 */
static const real E_Activation_steamr = -1.22e+8; /* P / Fuel 89 (2010) 2903?917 for
C +H2O => CO + H2 */
static const real Arrhenius_dryr1 = 3.62e+1; /* From P / Fuel 89 (2010) 2903?917 for
C +CO2 => 2CO*/
static const real E_Activation_dryr1 = -7.7e+7; /* P / Fuel 89 (2010) 2903?917 for C
+CO2 => 2CO */
static const real Arrhenius_hydrogasr2 = 4.20e-3; /* From P / Fuel 89 (2010) 2903?917
for C +2H2 => CH4 */
static const real E_Activation_hydrogasr2 = -1.9e+7; /* P / Fuel 89 (2010) 2903?917
for C +2H2 => CH4*/

static const real c_devol_pre = 1., c_devol_exp = 1.;
static const real c_char_comb = 1; /* control the char combustion rate */

static cxboolean init_flag = TRUE;

/* Search the index for each species */
static real mw[MAX_PHASES][MAX_SPE_EQNS];
static int INDEX_PHASE_CH4 = 0, INDEX_SPECIES_CH4 = 0, INDEX_PHASE_CO = 0,
INDEX_SPECIES_CO = 0,
```

```

INDEX_PHASE_CO2 = 0, INDEX_SPECIES_CO2 = 0, INDEX_PHASE_H2 = 0, INDEX_SPECIES_H2 =
0,
INDEX_PHASE_H2O = 0, INDEX_SPECIES_H2O = 0, INDEX_PHASE_O2 = 0, INDEX_SPECIES_O2 =
0,
INDEX_PHASE_H2S = 0, INDEX_SPECIES_H2S = 0, INDEX_PHASE_CL2 = 0, INDEX_SPECIES_CL2
= 0,
INDEX_PHASE_NH3 = 0, INDEX_SPECIES_NH3 = 0, INDEX_PHASE_N2 = 0, INDEX_SPECIES_N2 =
0,
INDEX_PHASE_TAR = 0, INDEX_SPECIES_TAR = 0, INDEX_PHASE_C = 0, INDEX_SPECIES_C =
0,
INDEX_PHASE_VOL = 0, INDEX_SPECIES_VOL = 0, INDEX_PHASE_TARINERT = 0,
INDEX_SPECIES_TARINERT = 0,
INDEX_PHASE_MOISTURE = 0, INDEX_SPECIES_MOISTURE = 0,
INDEX_PHASE_ASH = 0, INDEX_SPECIES_ASH = 0;

```

```

DEFINE_ADJUST(gasification, domain)
{

```

```

    int n, ns;
    Domain *subdomain;

```

```

    /*int n_phases = DOMAIN_N_DOMAINS(domain);*/

```

```

    if(init_flag)
    {

```

```

#ifdef !RP_HOST

```

```

    /* search all the species and saved the Molecular Weight */

```

```

    sub_domain_loop(subdomain, domain, n)

```

```

    {

```

```

        Material *m_mat, *s_mat;

```

```

        if (DOMAIN_NSPE(subdomain) > 0)

```

```

        {

```

```

            m_mat = Pick_Material(DOMAIN_MATERIAL_NAME(subdomain), NULL);

```

```

            mixture_species_loop(m_mat, s_mat, ns)

```

```

            {

```

```

                if (0 == strcmp(MIXTURE_SPECIE_NAME(m_mat, ns), "ch4"))

```

```

                {

```

```

                    INDEX_PHASE_CH4 = n;

```

```

                    INDEX_SPECIES_CH4 = ns;

```

```

                }

```

```

                else if (0 ==

```

```

strcmp(MIXTURE_SPECIE_NAME(m_mat, ns), "co"))

```

```

                {

```

```

                    INDEX_PHASE_CO = n;

```

```

                    INDEX_SPECIES_CO = ns;

```

```

                }

```

```

                else if (0 ==

```

```

strcmp(MIXTURE_SPECIE_NAME(m_mat, ns), "co2"))

```

```

                {

```

```

                    INDEX_PHASE_CO2 = n;

```

```

                    INDEX_SPECIES_CO2 = ns;

```

```

                }

```

```

                else if (0 ==

```

```

strcmp(MIXTURE_SPECIE_NAME(m_mat, ns), "h2"))

```

```

                {

```

```

                    INDEX_PHASE_H2 = n;

```

```

                    INDEX_SPECIES_H2 = ns;

```

```

    }
    else if (0 ==
strcmp(MIXTURE_SPECIE_NAME(m_mat,ns), "h2o"))
    {
        INDEX_PHASE_H2O = n;
        INDEX_SPECIES_H2O = ns;
    }
    else if (0 ==
strcmp(MIXTURE_SPECIE_NAME(m_mat,ns), "o2"))
    {
        INDEX_PHASE_O2 = n;
        INDEX_SPECIES_O2 = ns;
    }
    else if (0 ==
strcmp(MIXTURE_SPECIE_NAME(m_mat,ns), "h2s"))
    {
        INDEX_PHASE_H2S = n;
        INDEX_SPECIES_H2S = ns;
    }
    else if (0 ==
strcmp(MIXTURE_SPECIE_NAME(m_mat,ns), "cl2"))
    {
        INDEX_PHASE_CL2 = n;
        INDEX_SPECIES_CL2 = ns;
    }
    else if (0 ==
strcmp(MIXTURE_SPECIE_NAME(m_mat,ns), "nh3"))
    {
        INDEX_PHASE_NH3 = n;
        INDEX_SPECIES_NH3 = ns;
    }
    else if (0 ==
strcmp(MIXTURE_SPECIE_NAME(m_mat,ns), "n2"))
    {
        INDEX_PHASE_N2 = n;
        INDEX_SPECIES_N2 = ns;
    }
    else if (0 ==
strcmp(MIXTURE_SPECIE_NAME(m_mat,ns), "tar"))
    {
        INDEX_PHASE_TAR = n;
        INDEX_SPECIES_TAR = ns;
    }
    else if (0 == strcmp(MIXTURE_SPECIE_NAME(m_mat,ns), "c"))
    {
        INDEX_PHASE_C = n;
        INDEX_SPECIES_C = ns;
    }
    else if (0 ==
strcmp(MIXTURE_SPECIE_NAME(m_mat,ns), "volatile"))
    {
        INDEX_PHASE_VOL = n;
        INDEX_SPECIES_VOL = ns;
    }
    else if (0 ==
strcmp(MIXTURE_SPECIE_NAME(m_mat,ns), "h2o<1>"))
    {
        INDEX_PHASE_MOISTURE = n;
        INDEX_SPECIES_MOISTURE = ns;
    }
    else if (0 == strcmp(MIXTURE_SPECIE_NAME(m_mat,ns), "ash-
coal"))

```

```

        {
            INDEX_PHASE_ASH = n;
            INDEX_SPECIES_ASH = ns;
        }
        else if (0 ==
strcmp(MIXTURE_SPECIE_NAME(m_mat,ns), "TARINERT"))
        {
            INDEX_PHASE_TARINERT = n;
            INDEX_SPECIES_TARINERT = ns;
        }

        CX_Message ("\n --- %d %d, %d %d, %d %d, %d %d,%d %d,
%d %d, %d %d, %d %d, %d %d, %d %d, %d %d, %d %d \n",
            INDEX_PHASE_CO2, INDEX_SPECIES_CO2, INDEX_PHASE_H2,
INDEX_SPECIES_H2,
            INDEX_PHASE_CH4, INDEX_SPECIES_CH4, INDEX_PHASE_CO,
INDEX_SPECIES_CO,
            INDEX_PHASE_H2O, INDEX_SPECIES_H2O, INDEX_PHASE_O2,
INDEX_SPECIES_O2,
            INDEX_PHASE_H2S, INDEX_SPECIES_H2S,
INDEX_PHASE_CL2, INDEX_SPECIES_CL2,
            INDEX_PHASE_NH3, INDEX_SPECIES_NH3, INDEX_PHASE_N2,
INDEX_SPECIES_N2,
            INDEX_PHASE_TAR, INDEX_SPECIES_TAR, INDEX_PHASE_C,
INDEX_SPECIES_C,
            INDEX_PHASE_VOL, INDEX_SPECIES_VOL,
INDEX_PHASE_TARINERT, INDEX_SPECIES_TARINERT,
            INDEX_PHASE_MOISTURE, INDEX_SPECIES_MOISTURE,
            INDEX_PHASE_ASH, INDEX_SPECIES_ASH);

        mw[n][ns] = MATERIAL_PROP(s_mat,PROP_mwi);
    }
    else
    {
        s_mat = Pick_Material(DOMAIN_MATERIAL_NAME(subdomain),NULL);
        mw[n][0] = MATERIAL_PROP(s_mat,PROP_mwi);
    }
}

#endif

    init_flag = FALSE;
    /* to calculate some commonly used values here in order to save the CPU time */

}

}

DEFINE_HET_RXN_RATE(devolatilization,c,t,hr,mw,yi,rr,rr_t)
{
    Thread **pt = THREAD_SUB_THREADS(t);
    Thread *tp = pt[0]; /* gas phase */
    Thread *ts = pt[1]; /* solid phase */

    real prod;
    real x0_star = 0., x_star =0.;
    real T = MAX(273.,C_T(c,ts));
    real T_SAT = 373.15;

```

```

*rr = 0;
prod = 0.;
if(T>TMAX) T = TMAX;
if(T > T_SAT)
{
  if(C_VOF(c, tp) < eps_g_small && yi[INDEX_PHASE_VOL][INDEX_SPECIES_VOL] >
spe_small)
  {
    prod = (yi[INDEX_PHASE_VOL][INDEX_SPECIES_VOL]-
x_star)*C_R(c,ts)/mw[INDEX_PHASE_VOL][INDEX_SPECIES_VOL];

    *rr = c_devol_pre * Arrhenius_devolatilization *
exp(- c_devol_exp *
E_Activation_devolatilization/(UNIVERSAL_GAS_CONSTANT*T))
* pow(prod*C_VOF(c, ts), 0.67); /* kmol/(m3.s) */
  }
}
}

```

```

DEFINE_HET_RXN_RATE(char_combustion,c,t,hr,mw,yi,rr,rr_t)

```

```

{
  Thread **pt = THREAD_SUB_THREADS(t);
  Thread *tp = pt[0]; /* gas phase */
  Thread *ts = pt[1]; /* solid phase */

  real T = MAX(273.,C_T(c,tp));
  real T_s = MAX(273.,C_T(c,ts));
  real T_f;
  real Rgas = 82.06; /* atm.cm^3/mol.K */ /*UNIVERSAL_GAS_CONSTANT;*/

  real p_o2 = 0.;
  real k_f, k_a, k_r, diff, Sc1o3;
  real Pt = MAX(0.1, (op_pres+C_P(c,t))/101325);
  real Re, vrel, N_sherwood, rd;
  real D_p = C_PHASE_DIAMETER(c,ts); /* read in later ssp*/
  real y_carbon, y_ash;
  real ash_ar = 12., fc_ar = 45.;

  real factor;
  /* Void Fraction of Ash Layer */
  real ep_a = 0.25 + 0.75*(1-ash_ar/100.);
  real f_ep_a = pow(ep_a,2.5);

  /*
  !           2C + O2 --> 2CO           kg-mole/(m^3.s)
  !
  !           Wen at al. (1982), Syamlal and Bissett (1992), Syamlal (1993)
  !           Intrinsic rate from Desai and Wen (1978), originally from
  !           Sergeant and Smith (1973).
  !
  */

  *rr = 0;

  T = MIN(T,TMAX);

```

```

T_s = MIN(T_s, TMAX);
if(C_VOF(c, tp) < eps_g_small && yi[INDEX_PHASE_C][INDEX_SPECIES_C] > spe_small
&& yi[INDEX_PHASE_O2][INDEX_SPECIES_O2] > spe_small)
{
    y_carbon = yi[INDEX_PHASE_C][INDEX_SPECIES_C];
    y_ash = yi[INDEX_PHASE_ASH][INDEX_SPECIES_ASH];

    p_o2 =
C_R(c, tp)*UNIVERSAL_GAS_CONSTANT*C_T(c, tp)*yi[INDEX_PHASE_O2][INDEX_SPECIES_O2]
    /mw[INDEX_PHASE_O2][INDEX_SPECIES_O2] / 101325.;

    if(fc_ar > 0.)
    {
        if (y_carbon > 0.)
        {
            rd = pow( (y_carbon * ash_ar/100.)/(y_ash * fc_ar/100.), (1./3.)
);
            rd = MIN(1., rd);
        }
        else rd = 0.;
    }
    else rd = 0.;

    diff = 4.26 * pow((T/1800.), 1.75)/Pt; /* cm^2/s */
    diff = MAX(diff, 1.e-10);
    Sc103 = pow(C_MU_L(c, tp)/(C_R(c, tp) * diff * 1.e-4), 1./3.);
    vrel = pow(( (C_U(c, tp)-C_U(c, ts))*(C_U(c, tp)-C_U(c, ts)) +
        (C_V(c, tp)-C_V(c, ts))*(C_V(c, tp)-C_V(c, ts)) +
        (C_W(c, tp)-C_W(c, ts))*(C_W(c, tp)-C_W(c, ts)) ), 0.5);
    Re = C_VOF(c, tp) * D_p * vrel * C_R(c, tp)/(C_MU_L(c, tp)+SMALL_S);
    N_sherwood = 4.; /*(7. - 10. * C_VOF(c, tp) + 5. * C_VOF(c, tp) * C_VOF(c, tp)
)*
        (1. + 0.7 * pow(Re, 0.2) * Sc103)
        +
        (1.33 - 2.4 * C_VOF(c, tp) + 1.2 * C_VOF(c, tp) * C_VOF(c, tp)) *
        pow(Re, 0.7) * Sc103; */
    if ( rd <= 0. || C_VOF(c, ts) <= 0. )
    {
        *rr = 0.;
    }
    else
    {
        T_f = 0.5 * ( C_T(c, tp) + C_T(c, ts) );
        T_f = MIN(T_f, TMAX);
        k_f = diff * N_sherwood / (D_p * 1.e+2 *
Rgas/mw[INDEX_PHASE_O2][INDEX_SPECIES_O2] * T_f );
        k_r = 8710. * exp( -27000/1.987/T_s ) * rd * rd;
        if ( rd >= 1.)
        {
            *rr = 1. / (1./k_f + 1./k_r);
        }
        else
        {
            k_a = 2. * rd * diff * f_ep_a / (D_p * 1.e+2 * (1.-rd) *
Rgas/mw[INDEX_PHASE_O2][INDEX_SPECIES_O2] * T_s );
            *rr = 1. / (1./k_f + 1./k_r + 1./k_a);
        }
        factor = y_carbon / (y_carbon + 1.e-6);
        *rr = *rr * p_o2 * 6. * C_VOF(c, ts) * factor / (D_p * 1.e+2 * 32.);
/* mol/(cm^3 .s) */
        *rr = c_char_comb * *rr * 1000.; /* kmol/(m^3 .s) */
    }
}

```

```

    }
}

DEFINE_HET_RXN_RATE(steamr,c,t,hr,mw,yi,rr,rr_t)
{
    Thread **pt = THREAD_SUB_THREADS(t);
    Thread *tp = pt[0]; /* gas phase */
    Thread *ts = pt[1]; /* solid phase */

    real prodst;
    real x0_star1 = 0., x_star1 =0.;
    real T = MAX(273.,C_T(c,ts));
    real T_SAT = 373.15;

    *rr = 0;
    prodst =0.;
    if(T>TMAX) T = TMAX;
    if(T > T_SAT)
    {
        if(C_VOF(c, tp) < eps_g_small && yi[INDEX_PHASE_H2O][INDEX_SPECIES_H2O] >
spe_small)
        {
            prodst = (yi[INDEX_PHASE_H2O][INDEX_SPECIES_H2O]-
x_star1)*C_R(c,ts)/mw[INDEX_PHASE_H2O][INDEX_SPECIES_H2O];

            *rr = Arrhenius_steamr *
                exp(E_Activation_steamr/(UNIVERSAL_GAS_CONSTANT*T))
                * prodst*C_VOF(c, tp); /* kmol/(m3.s) */
        }
    }
}
}

```

```

DEFINE_HET_RXN_RATE(dryr1,c,t,hr,mw,yi,rr,rr_t)
{
    Thread **pt = THREAD_SUB_THREADS(t);
    Thread *tp = pt[0]; /* gas phase */
    Thread *ts = pt[1]; /* solid phase */

    real prodst1;
    real x0_star1 = 0., x_star1 =0.;
    real T = MAX(273.,C_T(c,ts));
    real T_SAT = 373.15;

    *rr = 0;
    prodst1 =0.;
    if(T>TMAX) T = TMAX;
    if(T > T_SAT)
    {
        if(C_VOF(c, tp) < eps_g_small && yi[INDEX_PHASE_CO2][INDEX_SPECIES_CO2] >
spe_small)
        {

```

```

        prodst1 = (yi[INDEX_PHASE_CO2][INDEX_SPECIES_CO2]-
x_star1)*C_R(c,ts)/mw[INDEX_PHASE_CO2][INDEX_SPECIES_CO2];

        *rr = Arrhenius_dryr1 *
        exp(E_Activation_dryr1/(UNIVERSAL_GAS_CONSTANT*T))
        * prodst1*C_VOF(c, tp); /* kmol/(m3.s) */
    }
}

DEFINE_HET_RXN_RATE(Hydrogasr2, c, t, hr, mw, yi, rr, rr_t)
{
    Thread **pt = THREAD_SUB_THREADS(t);
    Thread *tp = pt[0]; /* gas phase */
    Thread *ts = pt[1]; /* solid phase */

    real prodst2;
    real x0_star1 = 0., x_star1 =0.;
    real T = MAX(273.,C_T(c,ts));
    real T_SAT = 373.15;

    *rr = 0;
    prodst2 =0.;
    if(T>TMAX) T = TMAX;
    if(T > T_SAT)
    {
        if(C_VOF(c, tp) < eps_g_small && yi[INDEX_PHASE_H2][INDEX_SPECIES_H2] >
spe_small)
        {
            prodst2 = (yi[INDEX_PHASE_H2][INDEX_SPECIES_H2]-
x_star1)*C_R(c,ts)/mw[INDEX_PHASE_H2][INDEX_SPECIES_H2];

            *rr = Arrhenius_Hydrogasr2 *
            exp(E_Activation_Hydrogasr2 / (UNIVERSAL_GAS_CONSTANT*T))
            * prodst2*C_VOF(c, tp); /* kmol/(m3.s) */
        }
    }
}

```

Heat flux code

```

/*****
/* heatfluxwallprofile.c */
/* UDF for specifying heat flux boundary condition for non-homogeneous parabolic
trough absorber wall obtained from MCRT method */
/*****
#include "udf.h"

DEFINE_PROFILE(bottomwall_x_profile, thread, position)
{
    real x[ND_ND]; /* this will hold the position vector */
    real x0;
    face_t f;

    begin_f_loop(f, thread)

```

```

{
    F_CENTROID(x,f,thread);
    x0 = x[0];

    if (x0 >= 0 )
        F_PROFILE(f, thread, position) = (2e+11 * pow(x0, 4)) - (2e+10 * pow(x0, 3)) +
(4e+8 * pow(x0, 2)) - (1e+6 * x0) + 41906;
    else
        F_PROFILE(f, thread, position) = (2e+11 * pow(x0, 4)) + (2e+10 * pow(x0, 3))
+ (4e+8 * pow(x0, 2)) + (1e+6 * x0) + 41906;
}
end_f_loop(f, thread)
}

DEFINE_PROFILE(topwall_x_profile, thread, position)
{
    real x[ND_ND];          /* this will hold the position vector */
    real x0;
    face_t f;

    begin_f_loop(f, thread)
    {
        F_CENTROID(x,f,thread);
        x0 = x[0];

        if (x0 >= 0 )
            F_PROFILE(f, thread, position) = - (5e+6 * pow(x0, 3)) - (462810 * pow(x0, 2)) -
(7969.7 * x0) + 950;
        else
            F_PROFILE(f, thread, position) = (5e+6 * pow(x0, 3)) - (462810 * pow(x0, 2))
+ (7969.7 * x0) + 950;
    }
    end_f_loop(f, thread)
}

/*****
/* heatfluxwallprofile.c */
/* UDF for specifying heat flux boundary condition for improved parabolic trough
absorber wall obtained from MCRT method */
*****/
#include "udf.h"

DEFINE_PROFILE(bottomwallimp_x_profile, thread, position)
{
    real x[ND_ND];          /* this will hold the position vector */
    real x0;
    face_t f;

    begin_f_loop(f, thread)
    {
        F_CENTROID(x,f,thread);
        x0 = x[0];

        if (x0 >= 0 )
            F_PROFILE(f, thread, position) = (6e+14 * pow(x0, 6)) - (7e+13 * pow(x0, 5)) +
(3e+12 * pow(x0, 4)) - (5e+10 * pow(x0, 3)) + (4e+8 * pow(x0, 2)) - (649350 * x0) +
14974;
        else
            F_PROFILE(f, thread, position) = (6e+14 * pow(x0, 6)) + (7e+13 * pow(x0, 5))
+ (3e+12 * pow(x0, 4)) + (5e+10 * pow(x0, 3)) + (4e+8 * pow(x0, 2)) + (649350 * x0) +
14974;
    }
}

```

```

    }
    end_f_loop(f, thread)
}

DEFINE_PROFILE(topwall2_x_profile, thread, position)
{
    real x[ND_ND];          /* this will hold the position vector */
    real x0;
    face_t f;

    begin_f_loop(f, thread)
    {
        F_CENTROID(x,f,thread);
        x0 = x[0];

        if (x0 >= 0)
            F_PROFILE(f, thread, position) = (3e+15 * pow(x0, 6)) - (3e+14 * pow(x0, 5)) +
            (1e+13 * pow(x0, 4)) - (2e+11 * pow(x0, 3)) + (1e+9 * pow(x0, 2)) - (2e+6 * x0) +
            12926;
        else
            F_PROFILE(f, thread, position) = (3e+15 * pow(x0, 6)) + (3e+14 * pow(x0, 5))
            + (1e+13 * pow(x0, 4)) + (2e+11 * pow(x0, 3)) + (1e+9 * pow(x0, 2)) + (2e+6 * x0) +
            12926;
    }
    end_f_loop(f, thread)
}

```

APPENDIX B: List of Publications

Journal articles

Bashir, M.; Yu, X. & Makkawi, Y. (2016) *CFD Modelling of biomass fast pyrolysis using a solar-thermal receiver/reactor*; ACS Sustainable Chemistry & Engineering. (Accepted)

Bashir, M.; Makkawi, Y. & Generalis, S. (2017) *Modelling of char gasification in a circulating fluidised bed*. ACS Sustainable Chemistry & Engineering (Submitted)

Conference proceedings

Bashir, M. & Makkawi, Y. *CFD Modelling of biomass fast pyrolysis in a solar trough receiver/reactor*; In proceedings of 2nd International Symposium on Energy Challenges and Mechanics, Aberdeen, UK, August 2014

Bashir, M. & Makkawi, Y. *Modelling of a solar-thermal reactor for biomass fast pyrolysis*; In proceedings of AIChE Spring Meeting, Austin, USA, April 2015

Bashir, M. & Makkawi, Y. *Modelling of steam gasification of char in a circulating fluidised bed*; In proceedings of 3rd World Congress on Petrochemistry and Chemical Engineering, Atlanta, USA, January 2016

